Research & Development towards Undulator Designs Dedicated to Laser Plasma Accelerator Beam Lines

Dissertation

zur Erlangung des Doktorgrades

an der Fakultät für Mathematik, Informatik und Naturwissenschaften

Fachbereich Physik

der

Universität Hamburg

Vorgelegt von:

Florian Holy

aus:

Berlin

Hamburg

2018

Eidesstattliche Versicherung / Declaration on oath

Hiermit versichere ich an Eides statt, die vorliegende Dissertationsschrift selbst verfasst und keine anderen als die angegebenen Hilfsmittel und Quellen benutzt zu haben.

Die eingereichte schriftliche Fassung entspricht der auf dem elektronischen Speichermedium.

Die Dissertation wurde in der vorgelegten oder einer ähnlichen Form nicht schon einmal in einem früheren Promotionsverfahren angenommen oder als ungenügend beurteilt.

Ort, Datum & Unterschrift:

UNIVERSITÄT HAMBURG

Abstract

Fachbereich Physik
Institut für Experimentalphysik

Doktorarbeit

**Designstudien und spektrale Messungen an Undulatoren für
Laser-Plasma Elektronenbeschleuniger**

von Florian HOLY

Moderne bildgebende Verfahren erlauben die Untersuchung von Materie über die Grenzen des Auflösungsvermögens von sichtbaren Lichtes hinaus [1]. Hierzu geeignetes Licht kann nur von komplexen und teuren Lichtquellen erzeugt werden, deren Verfügbarkeit stark limitiert ist. Der größte Kostenfaktor beim Bau dieser Maschinen ist der Teilchenbeschleuniger, der die benötigten hochrelativistische Elektronenstrahlen bereitstellt. Ein alternatives Beschleuniger-Konzept könnte diesen teilweise ersetzen, der sogenannte Laser-Plasma Beschleuniger (PWA) [2]. Dieser nutzt die elektrischen Felder in laserinduzierten Plasmen geringer Dichte, welche um etwa drei Größenordnungen höher sind und damit Größe und Kosten des Beschleunigers bei gleicher Elektronenenergie signifikant reduzieren. Die entstehenden Elektronenwolken sind extrem kompakt (Pulslängen von unter einer Femtosekunde), bieten enorme Elektronendichten und Ströme bei geringen Emitanzen [3]. Gleichzeitig leidet die noch junge Technologie aber unter Instabilitäten bei Strahlposition und Richtung und in der Breite der Elektronenenergieverteilung.

Um die Vorteile des neuen Beschleunigerkonzeptes für die Erzeugung von Licht durch sogenannte Undulatoren nutzen zu können (magnetische Strukturen in denen hochenergetische Elektronen konstruktiv interferierendes Licht emittieren indem sie durch relativistische Lorentz-Kräfte auf eine Wellenartige Bahn gelenkt werden), ist es notwendig das Design dieser Undulatoren auf die Besonderheiten des PWA Elektronenstrahls anzupassen. In dieser Arbeit werden hierzu zwei verschiedene Undulatordesigns besprochen. Eines ist für die spontane Erzeugung von Licht durch einen relativ kurzen 0.5 m langen Undulator optimiert, das Andere für die Erzeugung von selbstverstärktem, laserartigen Licht eines sogenannten Freien-Elektronen Lasers (FEL). Für den ersten Fall wurde das magnetische Design geplant, simuliert und auf das zu erzeugende Spektrum hin optimiert. Im zweiten Fall wurden in einer Machbarkeitsstudie die zu erwartenden Fertigungstoleranzen dahingehend überprüft, ob ein erstes Experiment zur Erzeugung von PWA getriebener FEL Strahlung möglich ist. Die zu erreichende Genauigkeit und Qualität des magnetischen Feldes des Undulators wurden in einer Start-Ende Simulation von T. Seggebrock berechnet [4]. Im letzten Teil der Arbeit wurde das Spektrum eines kryogenen Undulator-Prototypen analysiert, als erster Feldtest zur Realisierung der weltweit ersten PWA getrieben FEL Beamline.

Abstract

Research & Development towards Undulator Designs Dedicated to Laser Plasma Accelerator Beam Lines

by Florian HOLY

Most advanced light sources enabling modern scientific imaging methods for the exploration of matter, beyond the limits of resolution in the visible spectrum [1], have become inconceivably complex and cost intense machines and access to these light sources - due to limited and expensive beam times - is rigorously restricted to only a small number of applicants. The highest cost impact of these machines, the particle accelerator, used to generate free moving, highly relativistic electron beams, could be replaced or at least supported by an alternative accelerator concept, the Plasma Wake-field Acceleration (PWA) [2]. Using accelerating fields generated in low-density plasmas, the length of the accelerator can be tremendously reduced, and with it size and costs, by about three orders of magnitude. The electron bunches injected by lasers into these plasma waves, stand out due to their compactness (sub fs scale) providing highest electron densities and peak currents and promise low emittance [3] at the same time. Along with the advantages - so far - the PWA electron beams suffer from severe instabilities in position and direction, as well as in absolute energy and relative energy spread.

In order to be able to make use of this acceleration concept for the generation of light in undulators anyway (periodic magnetic structures where electrons emit constructive interfering light transversally accelerated by the Lorentz force), it is necessary to adapt the design of the undulators to the described characteristics of PWA electron beams. In this work two different undulator designs are discussed, one dedicated for the spontaneous emission of light in a short undulator of 0.5 m length and one tailored for the stimulated emission in a Free Electron Laser, both driven by PWA electron beams. In the first case the geometric design was simulated and discussed, to optimize the spectral output, and the final magnetic design was specified. In the second case the manufacturing tolerances, were simulated with their consequences to the required magnetic field conformity resulted from a start-to-end simulation [4] and thus conceptual feasibility could be approved. In the last part of his work, the spectrum of a cryogenic prototype undulator was analyzed, as a field test for the realization of the worlds first PWA driven FEL beam line.

Contents

List of Figures

List of Tables

Abbreviations

ARPES   **A**ngle-**R**esolved **P**hotoemission **S**pectroscopy

DESY   **D**eutsche **E**lektronen-**SY**nchrotron

EXAFS   **E**xtended **X**-ray **A**bsorption **F**ine-structure **S**pectroscopy

FEL   **F**ree **E**lectron **L**asers

FEM   **F**inite **E**lement **M**ethod

FFT   **F**ast **F**ourier **T**ransformation

FWHM   **F**ull **W**idth **H**alf **M**aximum

GBD   **G**rain **B**oundary **D**iffusion

GeD   **Ge**rmanium diode **D**etector

HRE   **H**eavy **R**are **E**arth atoms

HZB   **H**elmholtz-**Z**entrum **B**erlin für Materialien und Energie

JASRI   **JA**pan **S**ynchrotron **R**adiation Research Institute

LCLS   **L**inac **C**oherent **L**ight **S**ource

LBNL   **L**awrence **B**erkeley **N**ational **L**aboratory

MAMI   **MA**inzer **MI**krotron

OFHC   **O**xygen **F**ree **H**igh **C**onductivity copper

PSI   **P**aul **S**cherrer **I**nstitut

PWA   **P**lasma-**W**akefield **A**ccelerators

RMS   **R**oot **M**ean **S**quare

RF   **R**adio **F**requency

RT   **R**oom **T**emperature

SACLA   **S**Pring-8 **A**ngstrom **C**ompact free electron **LA**ser

SASE-FEL   **S**elf **A**mplified **S**pontaneous **E**mission - **F**ree **E**lectron **L**aser

SLAC   **S**tanford **L**inear **A**ccelerator **C**enter

SR   **S**ynchrotron **R**adiation

TGS   **T**ransmission **G**rating **S**pectrometer

UR   **U**ndulator **R**adiation

VUV   **V**acuum **U**ltra**V**iolet

XFEL   European **X**-ray **F**ree **E**lectron **L**aser

Dedicated to my father,
who already left.

Dedicated to life,
which is short and unique for the lively.
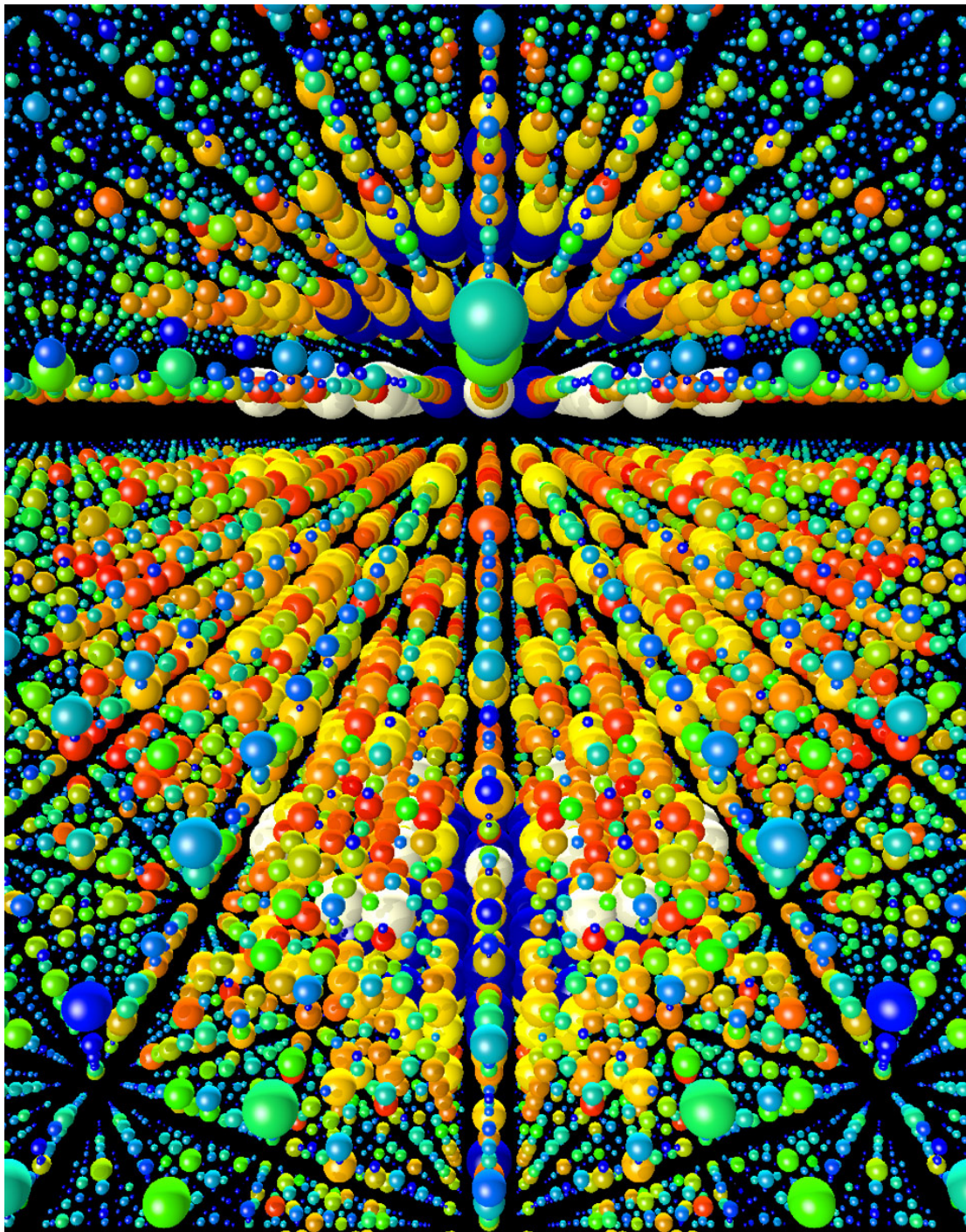
FIGURE 1: Three-dimensional rendering of the X-ray diffraction pattern for the Photosystem I protein, reconstructed from more than 15,000 single nanocrystals. Snapshots taken from experiments performed at the Linac Coherent Light Source (LCLS) based the Stanford Linear Accelerator Center (SLAC). Credit: Thomas White [5]

"Science cannot solve the ultimate mystery of nature. And that is because, in the last analysis, we ourselves are a part of the mystery that we are trying to solve."

Max Planck

Chapter 1

Introduction

Most of the technological challenges in our days, including the development of sustainable energy sources as well as improvements in medicine and health of all kind of creatures - including their biospheres - are predicated on an advanced understanding and the precise control of matter.

Visualization and manipulation on the scale of atoms, electrons and spins - where contributors move on quantum mechanic courts - become therefore an essential factor for scientific developments in the twenty-first century. With the aim to serve the entire range of natural sciences, light sources are refined to regions of smallest possible spatial and temporal resolutions, reaching shorter wavelengths and bandwidths and higher intensities at timescales beyond the limits of imagination. As an example for the unprecedented abilities of a newly developed technology, the X-ray Free Electron Laser (X-ray FEL), figure 1 demonstrates the molecular structure of the Photosystem 1, which allows for a deeper understanding of the processes taking part during the photosynthesis.

In this introduction the historical development of scientific light sources based on particle accelerators should be delineated, to introduce the reader to a revolutionary, ground breaking technology which cuts the costs of the inconceivably complex machines and imaging technologies of today, and hopefully enables to give access to these tools to a broad scientific community.

1.1   Short history of accelerator-based light sources

The principles of the nature of light beyond simple geometric optics, the theoretic background of electromagnetism and electromagnetic waves, were condensed by Maxwell in 1865 [6], but most of the equations were known even before. However, Maxwell completed an impressive collection of empirical works, combining them to one of the most beautiful theoretical concepts in physics - the theory of electromagnetic fields. The structure was taken as ideal paragon for modern field theories which still holds true in its forward-looking statements.

For many years, the theory remained untouched, professing without better knowledge an unknown, invisible 'luminiferous aether' with strange characteristics. As the carrier medium for

FIGURE 1.1: Engraving from a photograph of J.C. Maxwell (Source: [7])
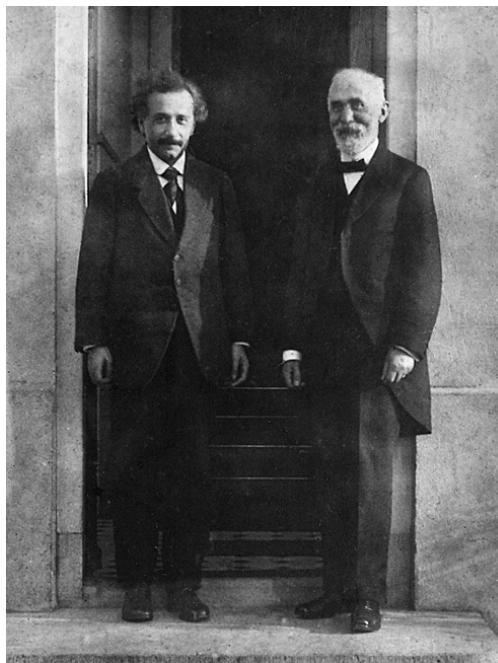
FIGURE 1.2: A. Einstein and H.A. Lorentz (Source: [8])
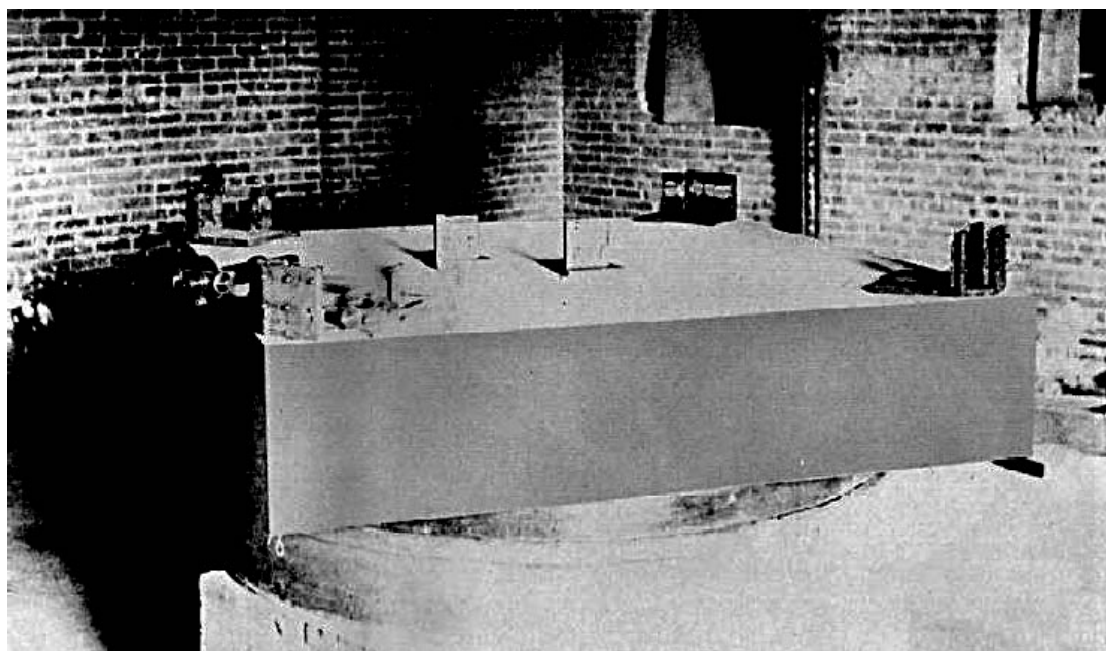
FIGURE 1.3: Michelson and Morley's interferometric setup, mounted on a stone slab that floats in an annular trough of mercury. (Source: [9])

the electromagnetic fields, it should permeate everything while being a fix-point, an absolute reference for all positions. In other words, it should not move at all.

This indiscriminate and indeterminable specification was more and more questioned by physicists and with Michelson and Morley's experiment in 1887, where the comparison of the speed of light in perpendicular directions was measured to be the same, even though the rotation and

translation of earth should have been added to at least one direction, the theory of aether was not longer tenable.

With the dawn of the 20th century, H. Lorentz and J. Lamor derived the Lorentz transformation under which the Maxwell equations were invariant, when transformed from the aether to a moving frame. They found out that not only spatial extents must be distorted, but also time when a system is observed from another inertial reference frame.

With the achievements of Lienard [10] and Wiechert [11] who independently developed the method of retarded potentials, the road was paved to drop the aether completely but nevertheless it was not until the year 1905 that A. Einstein published his theory of special relativity [12]. His works were shaking the laws of physics to their very foundations, since not only the controversial and unloved aether was disproved, but some revolutionary and provocative predictions followed with his theory. His principles of relativity affected not only space and time, but showed the relativistic character of mass and its equivalence to energy.

A proof of that predictions was found with the evolution of electron accelerators. The first concepts used electric fields repeatedly for acceleration. Leading the electrons on circular paths and several times through the same electric field, relativistic electron energies (energies at the scale of the particles rest mass) could have been reached this way. As a side note, The method revealed a constant loss of energy of the electrons. This loss was expected and predicted by Maxwell's equations as the circular path of the electrons, required a transverse, radiation generating acceleration of charged matter. One of the first experiments was a betatron operated at about 100 MeV by General Electrics. 1946 the physicist Blewett concluded correctly that radiation must be emitted in that electron accelerator [13], by observing a smaller circumference of the electron path inside the betatron than expected, but searching for the radiation revealed nothing but the characteristic background. In the beginning he was not able to detect the electromagnetic waves. This was due to the fact that he wasn't aware of the relativistic Doppler effect. Not thinking about Einstein's Special Relativity consequently, he initially searched for the radiation at the wrong wavelengths, and the glass window he used to extract the radiation out of the vacuum chamber was opaque in the actually required wavelength region. Not giving up, as the evidence of the measured loss of electron energy was clear, he found the radiation then one year later [14].

Another development took place in the early 20th century. The discovery of X-rays 1895 by Röntgen [16] promised the possibility to look not only at the surface but into matter with an increased resolution. From then on, the development of theoretical methods and technical evolutions stimulated and challenged each other. It triggered the development of several imaging techniques for the advanced investigation of matter as well as a number of technical revolutions.

Additionally to the simple X-ray imaging first demonstrated by Röntgen himself, which is still widely used in medicine, several methods were developed over the years, including X-ray diffraction, which revealed the atomic structure of matter and was pioneered by von Laue and Bragg, the X-ray absorption and emission spectroscopy developed by Barkla, which unveiled the complete electronic shell structure of atoms, the inelastic x-ray scattering, which was first demonstrated by Compton and proved indispensable later on for measuring collective excitations and vibrational and elastic properties of matter and the magnetic properties and valence states of iron,
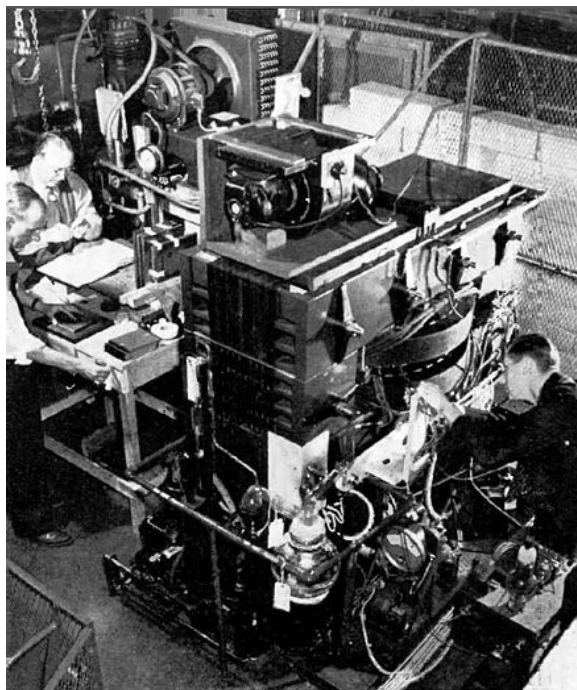
FIGURE 1.4: Betatron particle accelerator at University of Illinois. Consisting of a 4 ton electromagnet 24 Mev electrons were produced. (Source: [15])

the photo-electron spectroscopy, which revealed the signature of bonding in molecules and solids, pioneered by Siegbahn, Spicer, and Turner, followed by the demonstration of its spin dependence by Siegmann and other less known methods.

On the technical side, it was only after the development of electron accelerator-based light sources, providing photons at higher energies, intensities, shorter pulse durations, that it was possible to probe nature's fabric at the next level of accuracy. The technical evolution from the so-called first generation of Synchrotron Radiation (SR) sources, where bending magnets generated X-rays for parasitic measurements, was heading then for the first storage rings, where electron bunches were injected into ring beam lines and constantly accelerated to produce higher electron currents and with it more light. After that, the second generation of storage rings took place, which were dedicated to the production of X rays using higher electron energies and providing even higher beam currents at a higher accuracy and beam stability. This was made possible by some developments on the theoretical side. Schwinger [18] simplified the SR equations by introducing the Bessel functions to it (**??**). Schwingers equations motivated the development of undulators [19] subsequently and with it the experimental production of undulator radiation in both visible and millimeter wavelength [20] could be achieved. One has to mention that simultaneously, the theoretical background was developed in the Soviet Union [21, 22]. Four years before Motz, Ginzburg - a Russian physicist - proposed a periodic magnetic structure, in our days called undulator, in his theoretical work [23], as a source for radiation inspired by his earlier work on transition radiation [24].

After this step, the development moved on to the actual third generation of accelerator-based light sources, which were now fully dedicated to the production of light. The so-called advanced

storage rings are equipped with undulators [25] increasing the Brilliance by about 3 orders of magnitude. The so-called Brilliance is defined with its units by:

$$\mathcal{B} = \frac{\text{photons}}{\text{s} \cdot \text{mrad}^2 \cdot \text{mm}^2 \cdot 0.1\%\text{BW}}$$

considering the number of photons produced per second, divided by the angular divergence of the photons, the width of the cross-sectional area of the beam and the number of photons within a bandwidth (BW) of 0.1% of the central wavelength. Further, the development of undulators enabled additional imaging techniques using polarized light at higher intensities. With it even more advanced methods and techniques, using spectral properties of emitted light for the investigation of matter become feasible. Two better known examples are the Angle-Resolved Photo-Emission Spectroscopy (ARPES) or the Extended X-ray Absorption Fine-structure Spectroscopy (EXAFS). Both allowed protein crystallography to be extended to small, difficult to grow, or otherwise unstable protein samples, which still are of high interest in biology, medicine and pharmacy.

The actual state-of-the-art, the so-called fourth generation light sources, brought another major step in terms of Brilliance, which was introduced above as sophisticated measure for the photon density at the source. That Brilliance became a sextillion times higher than that of the sun,
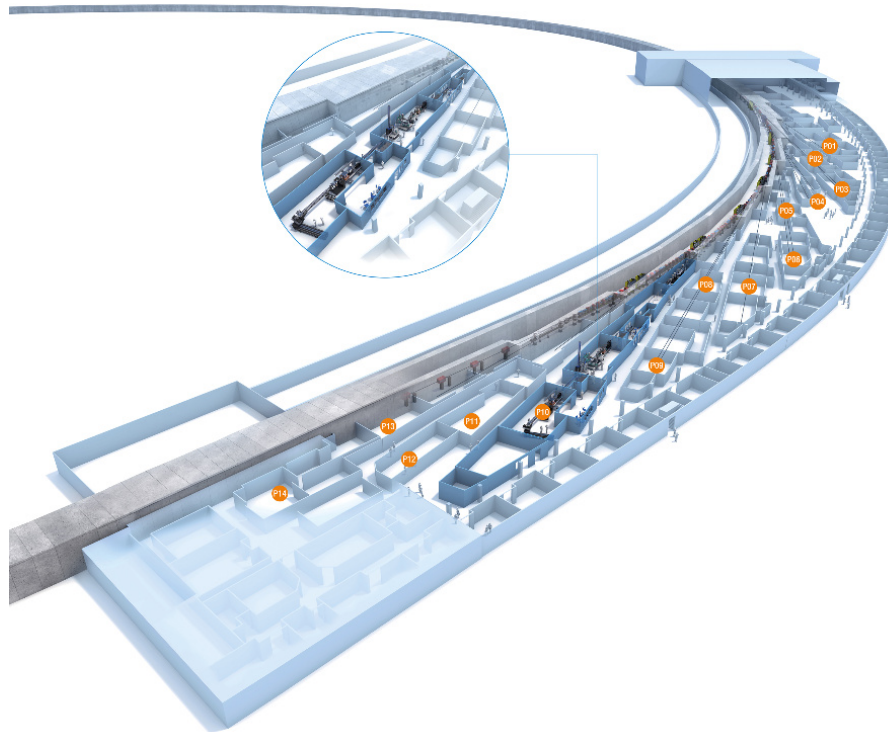
FIGURE 1.5: General diagram of Synchrotron PETRA III at DESY. The outer ring is the actual synchrotron, i.e. a particle accelerator that brings electrons to energies of 6 GeV, with a beam current of 100 mA and a normalized emittance of 1 nmrad. In 2017 17 photon beam lines are equipped with different, independently tunable insertion devices, basically undulators. (Source: [17]).

FIGURE 1.6: Electron accelerator beam line of the XFEL. (Source: [26])

providing coherent radiation. The machines providing this kind of light are called X-ray Free Electron Lasers (X-FEL's) which are the most advanced light sources built so far.

With every new generation of light sources, not only the photon Brilliance could have been increased but also the spatial, time and energetic resolution of the measurements. However, along with it, new challenges in both the financial and engineering requirements arose. The size of these facilities grew to the lengths of several kilometers for the particle accelerator itself, followed by - in some cases - more than hundred meters of magnetic structures, the undulators, where parts of the electron energy are transformed into radiation. The combination of these vast dimensions and the fact that at the same time technical parts of the beam line require a positioning accuracy at the micrometer scale, made it an enormous challenge to build such machines. Therefore only few X-FEL facilities were realized, most of them within the last years: the Linac Coherent Light Source (LCLS) in 2009 - USA, the SPring-8 Angstrom Compact free electron LAser (SACLA) in 2011 - Japan, the SwissFEL of the Paul Scherrer Institut (PSI) in Switzerland and the European X-ray Free Electron Laser (XFEL) in Germany, both at the end of 2016.

1.2 Development of Plasma Wake-field Accelerators

To decrease size and costs of these scientific instruments (several kilometers and about a billion of Dollars), and to make these fascinating imaging methods accessible to a broader scientific community, e.g. hospitals and also researching companies, a revolutionary method for particle acceleration has been tried to be adapted to the needs of the generation of light.

FIGURE 1.7: XFEL facility from above crossing the border of the federal county. The electron gun is located at the DESY campus in Bahrenfeld, the undulators and photon beam lines are in Schenefeld. The over all length is 3.4 km. (Source: [27])

An encouraging theoretical concept was developed by T. Tajima and J.M. Dawson [28] already in 1979. They proposed the application of high power lasers to generate a plasma as a source for the accelerating field. Within such plasmas, electric field gradients where thinkable to reach about one TV/m, thereby exceeding those of conventional accelerators by three orders of magnitude. This allows to achieve comparable electron energies within acceleration distances decreased by the same factor, decreasing size and costs at the same time. The first high power lasers strong enough to create such plasmas were built in the nineties of the past century and first experiments showed the conceptual feasibility [29–31] of the so-called Plasma Wake-Field Accelerators (PWAs).

However, it took about 20 years to increase the particle energies into a regime which makes their potential for the generation of light usable . Nowadays, multi GeV electron beams are possible by the use of Peta-Watt laser systems [33] delivering unprecedented electron peak currents due to high electron densities at ultra short bunch lengths. Especially these properties promise key advantages compared to conventional accelerators beyond the fact that PWAs are less costly and smaller in extent. Nevertheless, several drawbacks still remain. One major difficulty is the control of the high electron densities (space charge) in combination with the extreme field gradients from the plasma causing severe instabilities. These instabilities affect direction and position of the electron beam as well as the average energy and the energy spread of the electron bunch.

In the last 10 years, some progress could have been achieved for the use of PWA's for the production of UV and soft X-ray radiation [34]. The latest development is the combination of a classical electron accelerators to generate a properly controllable and well defined plasma wave

for the acceleration and a laser for the induction of electrons into the accelerating field [3]. These developments promise to combine the best of both worlds, compact accelerators providing ultra short bunches (sub fs scale) accelerated by multi-GV/m electric plasma fields with a normalized emittance of about 10^{-9} mrad.

The aim of this work was to develop undulator designs and to test their conceptual ability to be used in combination with a PWA, driven by a high power laser, meeting the challenges of the PWA electron beam properties described in the next section.

1.3 Design goals for undulators at laser plasma accelerators

As described above, the PWA concept bears some drawbacks compared to conventional electron accelerators, mostly in the field of spatial stability and energetic definedness (accuracy) but also given by the lower absolute electron bunch charge, decreasing the total number of emitted photons described in section 2.2.5.6 and the limited electron beam energy, increasing the wavelength of the emitted light, see section 2.2.5.2.

The specifications of the PWA electrons demand for an undulator design, adapted to the needs of the alternative concept. In this work, two different scenarios are examined. One scenario is the use of PWAs for the generation of spontaneous undulator radiation in chapter 3, the other
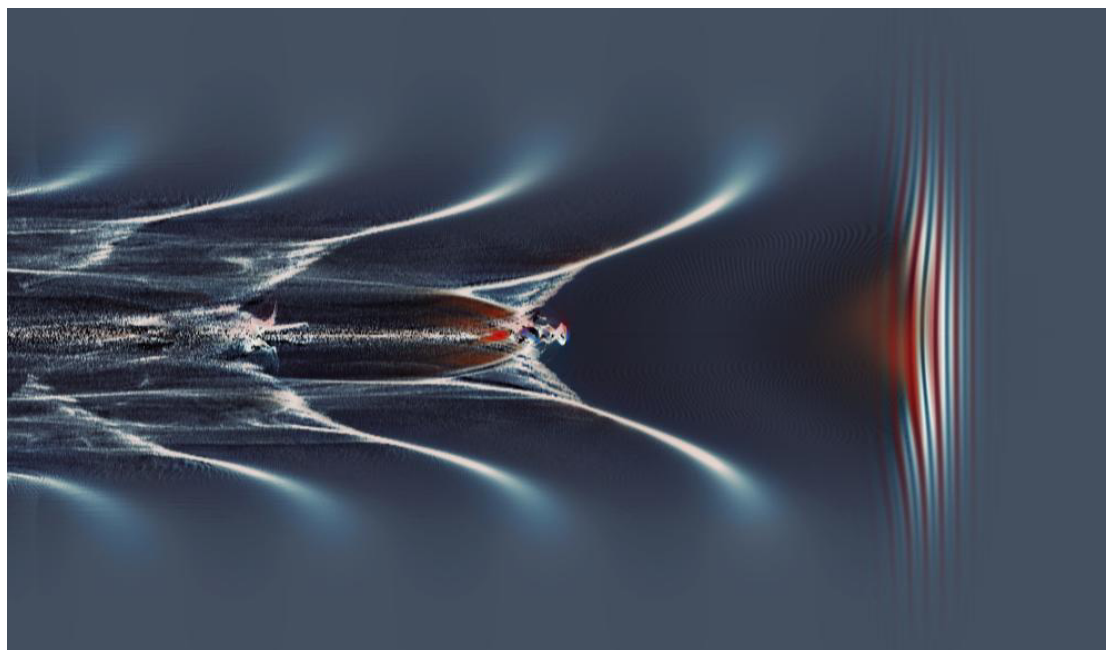
FIGURE 1.8: A particle-in-cell (PIC) simulation shows the electron densities within a PWA Hydrogen gas target. Coming from the left, a high power laser pulse has stripped former bound electrons from their nuclei, creating a plasma. The electron density distribution reminds on the stern wave of a boat. Electrons situated directly behind the positively charged, quasi electron free zone are now accelerated by the electric field towards the space were the laser pulse has left a quasi electron free bubble. Credit: Sören Jalas/Universität Hamburg [32]

is the use of a PWA as electron source for an FEL, discussed in chapter 4. In the last chapter of this work, chapter 5, a cryogenic undulator prototype was used for the generation of light at a conventional accelerator to prove the cryogenic design as a concept for its use as an FEL undulator.

In both scenarios, the main task was to compensate the lower electron energy and absolute number by using exceptionally strong magnetic materials not neglecting the fact that the material must withstand the possible irradiation with ionizing irradiation (high energy electrons) caused by possible electron instabilities. Due to the challenge to further decrease the length of the PWA-driven FEL, in the second scenario, the use of cryogenic magnetic material was decided to further increase both the undulator's magnetic flux density and the resistivity of the magnetic material against irradiation.

Chapter 2

Theoretic Background

2.1 Introduction to permanent magnet material

The following section on permanent magnets follows the introduction given in James A Clarke's book about undulator and wiggler technology [35]. A more complete discussion of this field can be found in other texts [36, 37].

The sources of the magnetic field of permanent magnets are magnetic dipole moments generated by microscopic currents. These currents are born by the inner atomic motion of electrons. In most cases, the resulting magnetic dipole moments within an atom is zero. That is because in most cases, it is neutralized by electrons in the same atomic shell generating magnetic dipole moments of the same strength but in opposing direction. In case of some of the transition metals in the d-block of the periodic table (Fe, Co, or Ni) and some of the Lanthanides in the f-block (including all rare earth elements) one finds atoms with unfilled inner shells. These atoms share a net magnetic dipole moment and are commonly used as key components in permanent magnet materials.

If these atoms are aligned along a single direction a macroscopic magnetization can be generated. Landau and Lifschitz showed that this alignment is a natural consequence of the interplay of forces [38]. Three energies assess the final state: the quantum-mechanical *exchange energy*, the *magnetocrystalline anisotropy* or simply *magnetic anisotropy* and the magnetic energy.

The regions where the magnetizations of individual atoms show in exactly the same direction are called magnetic domains. In general, this alignment is achieved by including atoms with such magnetic moments into a crystalline structure with a preferred direction for those magnetic moments. These directions are often called *easy magnetization direction* or *easy axis*.

In the production process of rare earth permanent magnets first the single elements are molten together under high temperatures in a vacuum containment. Magnetic domains are establishing. The product is crushed and ground to a fine powder which is then placed in a mold. The size of the grains is nearly the size of the domains . At the same time, an external magnetic field aligns the crystals and temperature and pressure is increased to press the material within the preferred

geometry and shape. Cooling down inside a constant external magnetic field, the magnetization becomes permanent.

With the development of Samarium-Cobalt magnets $\mathrm{Sm_2(Co, Cu, Fe, Zr)_{17}}$ and further with Rare-Earth magnets like Neodymium-Iron-Boron $\mathrm{Nd_2Fe_{14}B}$ permanent magnets prevailed in accelerator technology over electromagnetic sources due to their superior performance and price. Until now they are the most common, most elaborate source of magnetic fields.

The theory of electromagnetic phenomena is well understood. In principle, all electric and magnetic problems can be described by the famous Maxwell equations. In case of macroscopic systems all involved matter reacts to electric and magnetic fields. The resulting equations average over the internal microscopic charges and currents by introducing auxiliary fields:

$$\nabla \cdot \vec{D} = \rho \qquad\qquad \nabla \cdot \vec{B} = 0$$
$$\nabla \times \vec{E} = -\frac{\partial \vec{B}}{\partial t} \qquad\qquad \nabla \times \vec{H} = \frac{\partial \vec{D}}{\partial t} + \vec{J}. \tag{2.1}$$

With $\vec{D} = \epsilon_0 \vec{E} + \vec{\mathcal{P}}$ the dielectric displacement consisting of the electric field $\vec{E}$ and the (macroscopic) density of the permanent and induced electric dipole moments in the material, called the polarization density $\vec{\mathcal{P}}$ and another auxiliary field $\vec{H} = \vec{B}/\mu - \vec{M}$. μ is the magnetic susceptibility which will be discussed in section 2.1.1.1.

In the beginning of the exploration of electromagnetic phenomena $\vec{H}$ and $\vec{B}$ could not be distinguished. Therefore unfortunately both have not only many but sometimes also the same names in literature. An overview is given in table 2.1.

To avoid misconceptions, in this work $\vec{H}$ will be described by the term 'magnetic field strength' whereas $\vec{B}$ will be termed 'magnetic flux density'. The electric charge and current density are here written as ρ and $\vec{J}$.

$\vec{H}$ [A/m]	$\vec{B}$ [T]
Magnetic field strength	**Magnetic flux density**
Magnetic field	Magnetic field
Magnetizing field	Magnetic induction
Magnetic field intensity	

TABLE 2.1: Historically used names for the vector fields $\vec{H}$ and $\vec{B}$. To avoid misconceptions, in this work $\vec{H}$ and $\vec{B}$ will be termed by the names printed bold.

Another macroscopic property is the magnetization $\vec{M}$ which is defined by $\vec{M}(\vec{x}) = \sum_i N_i \langle m_i \rangle$ with N_i the averaged number of molecules of type i with the mean magnetic dipole moments m_i at the positions $\vec{x_i}$. This defines then the effective averaged current density $J_M = \nabla \times \vec{M}$.

As this part of the work will focus on permanent magnets and thereby handle with magnetostatic phenomena without electric charges and fields, the two Maxwell equations on the right hand side are sufficient for the derivation of the used formulas in the following discussion.

$$\boxed{\nabla \cdot \vec{B} = 0,} \tag{2.2}$$

$$\boxed{\nabla \times \vec{H} = \vec{J}.} \tag{2.3}$$

2.1.1 Characteristic properties of permanent magnets

In order to understand permanent magnets one needs to understand their key properties. These are often used to compare the performance and the usability of different types of magnets for special purposes. The most important key properties can be found as specific points in the hysteresis loop of a permanent magnet, figure 2.1.

2.1.1.1 Hysteresis of permanent magnets

The hysteresis loop of a ferromagnetic material describes the response of the magnet to external magnetic fields. In fact - for ferromagnets - it is a nonlinear function. The magnetic flux density $\vec{B}$ depends not only on the external magnetic field strength $\vec{H}$ but also on the inner state of the magnet. Depending on the inner state of the magnet, or rather its magnetization $\vec{M}$, the external field strength $\vec{H}$ can be amplified or attenuated.

Furthermore, external fields can change the inner state, the magnetization of a ferromagnet itself. To a certain limit of the external field strength the induced changes of the magnetization are reversible. However, if the external field strength surpasses a particular threshold, the magnetization of the magnet changes permanently.
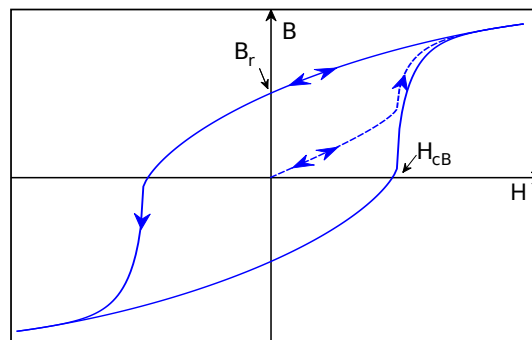
FIGURE 2.1: Theoretical slope of a hysteresis curve - Stoner Wolfarth model

If one takes a closer look to these demagnetizing processes, one can distinguish between two different processes participating [39]:

1. External fields with low strengths lead to an increase of the volume of domains which show the same magnetization direction as the external field strengths. These shifts of the domain walls are reversible in the beginning but can become irreversible after a certain threshold of the external field strength $\vec{H}$.

2. Strong external field strengths turn the magnetization $\vec{M}$ of the domains in the direction of the external field. This the same process as the initial magnetization and of course irreversible.

The graph in figure 2.2 shows a demagnetization curve. In this figure a fully magnetized magnet is affected by an external field. The first effect is a fully reversible decrease of the magnetization. Then both irreversible effects take place. All effects are marked and, one can see their dependency to the strength of the external field $\vec{H}$. A double arrow marks a reversible process and a single arrow an irreversible.

A full hysteresis circle of a permanent magnet is shown in figure 2.1. In this figure the magnetic flux density $\vec{B}$ of the permanent magnet is given as a function of an external field strength $\vec{H}$. Both, $\vec{H}$ and $\vec{B}$ point in the same direction and when $\vec{H}$ is negative its direction is exactly the opposite of the direction of $\vec{B}$ per definition. The dashed line in the middle of the graph shows the initial magnetization of an unmagnetized sample. Again, a single blue arrow marks an irreversible process, a double arrow a reversible one.

The fact that the magnetization can be changed irreversibly and thus stays permanently also when the external field is removed was the basic requirement for magnetic storage. In case of undulator magnets, this characteristic is less desirable. Nevertheless, permanent magnets are the most common and most elaborate sources of magnetic fields. They are used whenever high magnetic flux densities are demanded. To characterize permanent magnets and evaluate their
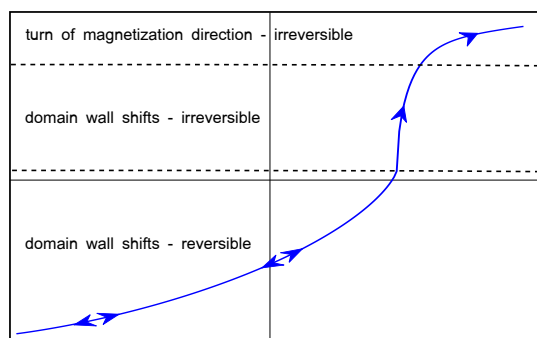
FIGURE 2.2: Demagnetization curve. A fully magnetized ferromagnet is demagnetized by an external field strength $\vec{H}$. A double arrow marks a reversible process and a single arrow an irreversible. Depending on the intensity of $\vec{H}$ different demagnetizing effects take place further described in the text.

usability for different applications two characteristic points become apparent in figure 2.1. Both characteristics are described in the following sections.

2.1.1.2 Remanent flux density of permanent magnets

The remanent flux density B_r (also called remanence, remanent magnetization or residual magnetism) is one key property of permanent magnets. It characterizes the magnetic flux density once the external magnetic field is zero. The density of the magnetic field flux is proportional to the magnetic force a magnet can generate. In case one needs high flux densities from small sources, without focusing the field lines using a magnetic pole material, one has to use magnetic materials with a high remanence. This makes the remanent flux density B_r an important property for undulator engineering.

2.1.1.3 Coercive field of permanent magnets

The coercivity (also called the magnetic coercivity, coercive field or coercive force) is a characteristic for ferromagnetic materials which describes their ability to withstand external magnetic field strengths without becoming demagnetized. It is often abbreviated by H_{cB} and is defined by the zero crossing of the hysteresis loop, as shown in figure 2.1. At this external field strength the magnetic flux density inside the magnet sample becomes zero. The higher H_{cB} the more resistive is the magnetic material against demagnetization. Sometimes the coercivity is given by a slightly different definition. One can also observe the so-called magnetic polarization J, according to this the value of H_{cJ} gives the value of the external magnetic field strength $\vec{H}$ at which the magnetic polarization of the sample becomes zero.

Both properties can be found in literature and are given by manufacturers of magnet materials. Especially for undulator magnets these characteristics are important since the working environment of undulators in general is highly demanding. Ionizing radiation, high energy particles, possible high temperatures due to the lack of cooling within the vacuum and strong opposing magnetic fields cause high dangers of demagnetization. These processes and their consequence is discussed in more detail in the next section.

2.1.2 Demagnetization

The mechanisms of demagnetization are still subject of research and with the dissemination of electric motors in cars, wind power plants and robotics the industry gives more and more attention to that topic. Several models describing different processes of demagnetization were developed in the past which take a variety of determining factors into account.

Driven by space exploration programs and particle accelerator science, several studies were conducted concerning demagnetization due to irradiation with relativistic electrons, gamma photons and fast neutrons, e.g. [40–46].

In the hazardous environment of an undulator beam line two kinds of radiation prevail which are the main factors of demagnetization: electrons with energies of up to several GeV, and photons generated by the undulator itself, with energies of several keV. The mechanisms of energy deposition differ from each other due to the specific characteristics of the radiation. These two different types of radiation determine two different mechanisms for the demagnetization process. A recent review article [47] summarizes and describes these mechanisms and presents appropriate countermeasures against demagnetization. An overview on the conclusions is given in the next sections after the presentation of the basic properties of the predominant radiation types and their interaction with matter.

2.1.2.1 Demagnetization by opposing fields

The highest opposing fields affect undulator magnets during assembly, when single magnets are inserted into an array with alternating polarization. The field strength of this external magnetic field seen by the magnets during assembly has to be simulated to prevent the magnets from damage before the undulator even exists.

For the fully assembled device the counterfields are smaller and the risk of demagnetization by opposing fields is given only if external fields are applied. But demagnetization is also possible if external energy is induced into the magnets. This can happen by uncharged particles, in our case mainly photons, or charged particles like electrons. These mechanisms are introduced in the following sections.

2.1.2.2 Photon interaction

Photons are electromagnetic radiation only existing while moving with the speed of light c. Because they are electrically neutral, they do not steadily lose energy via Coulomb interactions with atomic electrons, as do charged particles. Thus, photons travel some considerable distance before undergoing a more "catastrophic" interaction leading to partial or total transfer of the photon the energy to particles in their way. These secondary particles, most probably electrons, will ultimately deposit their absorbed energy in the medium. The attenuation length of photons with energies up to 10 keV is about 10 microns [48]. The energy deposition mechanisms are the photoelectric effect which is most probable for energies up to a few keV as produced in the undulator, Compton scattering (dominant for energies between 10 keV and 10 MeV) and for energies above 10 MeV pair production.

2.1.2.3 Electron interaction

The interactions between fast charged particles with speed $\beta = \frac{v}{c}$ or momentum $p = Mc\beta\gamma$ and matter can generally be described as the occurrence of random individual collisions [49] in each of which the particle loses a random amount of energy E. After approximately one centimeter, a primary electron with the energy of 1 GeV loses circa half its energy [50, 51]. The energy is transferred to secondary particles and photons and a cascade of Bremsstrahlung is generated.

Many different interaction schemes are possible for the products, the probability (represented by the cross section) for each depends on energy of the incident particle and density and type of the irradiated matter. The spectrum of Bremsstrahlung has a minimum wavelength given by the energy of the incident electron, which is $\lambda_{min} = \frac{hc}{E_e}$ [52]. Together with secondary particles, a shower diffuses in the material dissipating its initial energy along its pathway. This shower can be simulated by Monte-Carlo codes like *FLUKA* [53, 54] or *GEANT* [55].

2.1.2.4 Demagnetization mechanism 1 - magnetic moment instability

The first model describes the demagnetization of a wide unstable region, similar to the demagnetization caused by heat or reversal magnetic fields. In our case, this process is actuated by an energy transfer from photons, and low energy electrons (from the low energy tail of the electron bunch) or neutrons to the magnet material which causes a destabilization of the magnetic moments in a wide region around the impact area. The process occurs as follows:

1. The magnetic anisotropy well is decreased in a wide region of the magnetic material due to the energy transfer. Photons with energies up to few keV are absorbed within few µm predominately by the photo electric effect, emitting a cascade of low energy electrons which can ionize again until the remaining energy is to small. Thus, the absorbed energy is equivalent to the incident photon energy, distributed to a larger volume of the magnet material effecting a long ranging interaction.

2. The magnetization near the grain boundaries of the magnet where the anisotropy is the lowest tips over and nucleates - arouses and spreads - from that point to the whole domain. Thus, an inverse magnetic domain is generated within the grain.

3. The wall of this domain permeates throughout the grain and an inverse magnetized region is generated, decreasing the cumulative magnetization of the magnet.

Since this process is similar to the magnetization reversal by opposing magnetic fields or heat, the same engineering countermeasures were successfully tested and are suggested for application. For this purpose, the magnets can be stabilized by an artificial aging process, which is generated by the controlled application of an opposing field and/or heat to the magnets [56] in an open circuit condition before they are put together in the insertion device.

2.1.2.5 Demagnetization mechanism 2 - local hot spot demagnetization

High energy electrons can generate high energy photoneutrons while interacting with hadronic matter. These photo neutrons carry enough momentum to kick out single atoms from the magnets crystal lattice. This can be interpreted as a thermal spike within a small region around the 'knocked-out atom' where the thermal energy is transferred to a sphere around the impact region. Thereby, the temperature is almost instantaneously locally increased above the melting point and the demagnetization process initiates. If one calculates the temperature in the region of dense collisions by using the basic equation $E = 3/2nk_BT$ one finds that the kinetic energy

FIGURE 2.3: An interesting image shows grains and structure of magnetization (domains) of iron in the above figure, published in [59].

in units of temperature is initially of the order of 10,000 K. After the impact, the heat spikes cool down to the ambient temperatures within only few picoseconds time, which is definitely not corresponding to a thermodynamic equilibrium temperature. However, it has been shown that after about 3 lattice vibrations, the kinetic energy distribution of the atoms in a heat spike has the Maxwell–Boltzmann distribution [57], making the use of the concept of temperature justifiable. Moreover, experiments have shown that a heat spike can induce a phase transition which is known to require a very high temperature [58], showing that the concept of a (non-equilibrium) temperature is indeed useful in describing collision cascades. This process occurs as follows:

1. Energy from the central hot spot dissipates into a sphere around the impact zone.

2. The heat decreases the magnetic anisotropy well. A small domain is generated where the spins are flipped and the magnetization is opposed to the surrounding grains.

3. The inverse domain wall expands in the region where the anisotropy energy is low; grains and domains are shown in figure 2.3.

4. The anisotropy energy increases with the distance from the impact region until the thermal energy does not last out to flip additional spins.

Especially in this model, a high coercivity restricts the demagnetization of the magnets since for high coercive materials the size of the sphere where the anisotropy energy gets below the demagnetization limit is decreased.

2.1.3 Manufacture and processing of permanent magnets

In 1982, industrial approaches for the manufacturing of tetragonal crystal structures with Neodymium ($Nd_2Fe_{14}B$) were developed and took the place of the previously used Samarium Cobalt-based magnets which are costly and less powerful. The new materials showed an exceptionally

high uni-axial magneto-crystalline anisotropy and with it remanent fields of up to 1.3 T together with coercive fields of more than 2000 kA/m. There are mainly two fabrication processes the classical powder metallurgy or sintered magnet process and the so-called rapid solidification or bonded magnet process. A short description is given here:

1. Mixing the materials with the exact proportions of the final alloy, put into furnace and create the alloy by melting together the raw ingredients.

2. Grinding of the primary alloy to a very fine powder again. The less the grain size of the powder the higher the coercivity and the better the final surface structure [60]. Grain sizes below 2 µm are possible.

3. Material is pressed into a mold under a strong magnetic field to align Bloch domains.

4. Sintering at about 1100°C.

5. Polishing the outer boundaries, machining, cutting of the final geometry.

6. Surface coating for applications which is inevitably required since Rare-Earth magnet materials are highly corrosive and show outgassing [61] in UHV environments.

7. Final magnetization to saturation and special coercivity enhancing treatments.

Some special treatments are possible to homogenize the magnetization of the magnet charge and to enhance the coercivity further. This is not part of the standard process and described in the following.

2.1.3.1 Heat treatment

Applications with a high demand on the homogeneity of the magnetic field - like undulators - often need a high number of magnets with the exact same properties in magnetic field strength and direction. This can be achieved by producing more magnets than demanded, characterizing every single magnet in its properties in a magnetometer, and then choose a selection of magnets with high degree of similarity. This method, often referred to as *Surplus and Sorting*, is used by many magnet manufacturers, i.a. [62]. Depending on the degree of similarity, a multiple of the initially required number has to be produced which is costly and time consuming.

Another option is to treat the magnets with heat after the final magnetization. What happens then is a kind of artificial aging process. The magnets with a higher magnetic field strength demagnetize more easily and by the expense of a slightly decreased peak value of the magnetic field strength of the whole pile of magnets one gets a higher degree of conformity.

2.1.3.2 Grain boundary diffusion

The Grain Boundary Diffusion (GBD) process increases the coercivity of magnets without decreasing their remanent magnetic field strength [63–66]. As the name suggests during this treatment a higher coercive material (like Dysprosium) permeates through the surface of the magnets

by a diffusion process under heat and accumulates near the grain boundaries of the material and increases thereby the stability of the domain walls of the magnet without losing the remanent magnetic field strength. The process affects only a few tenths of a millimeter below the surface of the magnet. Thereby it is well suited for magnets with small dimensions and large surfaces like these used in undulators.

2.2 Introduction to undulator physics

As introduced in chapter 1, undulators range among the most versatile and powerful light sources used in science. In undulators, the light is generated by an electron beam traversing a periodic structure of magnets with alternating magnetization. The name undulator comes from the Latin word 'undula' which means small wave. It refers to the 'undulating' track of the electrons inside the structure which results from the Lorentz force generated by the periodic magnetic field.

Looking more into the details of engineering of an undulator, one can find several different types of design. First, one can distinguish between planar and circular undulators, where the oscillation of the electrons is either in one flat plane (planar) or on a helical track (circular). This causes the emission of planar or circular polarized light. Although the principle of an undulator itself is very simple, there are different ways of construction in each group. For more information on this topic see [68].

FIGURE 2.4: Permanent magnet undulator at *DESY*. (Source: [67])

Material	Electromagnets	Permanent magnets	Superconducters
Magnetic flux density	low	high	ultra high
Demagnetization	low	high	unknown
Field tuning	adjustable by currents	adjustable by gap	unknown
Operating temperature	293 K	10-293 K	<4 K

TABLE 2.2: Sources of magnetic fields and their advantages and disadvantages for use in undulators.

Also the source of the magnetic field itself can be various. Beginning from electromagnets to permanent magnets and superconducting materials, everything has been used in undulator engineering. A comparison between advantages and disadvantages between the materials is shown in table 2.2.

For different cases of application, different technologies are advantageous. In the scientific case of our research group - to build an undulator for a laser-plasma accelerator driven light source - a comparably short undulator period length in combination with a high magnetic flux density is desired, as described in section 2.5. Moreover, the field error has to be essentially low and the undulator gap, which is the distance between the upper and lower girder holding the magnetic sources, should not to be to close. This requires even higher magnetic flux densities since the field is reduced by the increased distance of the field sources, the undulator jaws.

First of all, this combination of requirements excepts electro-magnets since the generation of high magnetic flux densities with this technology requires large coils to conduct extremely strong electric currents. This fact makes it impossible to build small electromagnets as source of strong magnetic fields and thereby also short alternating undulator periods where the distance between two successive sources is very low (about 2.5 to 10 mm).

At the first glance, the demand for a high magnetic flux density inside the undulator clearly favors superconducting materials. The study of the latest papers on this technology shows that several problems are still unresolved [69]. Especially the necessity to hold the field deviations between the single undulator periods below a certain limit seems difficult with superconducting materials. First, this comes from the fact that the operation temperature of such devices is in general very low, which creates strong thermal stresses within the girder. Second, there is still no approved method to correct existing field errors from manufacturing tolerances either.

On the other hand: permanent magnets show improved magnetic performances being cooled down to cryogenic temperatures [70–73]. The fact that the required temperatures are above 30 K reduces mechanical stresses and thereby field errors effected by thermal distortions. Using moderatly cooled permanent magnets in combination with a distinct undulator design, the field errors should thereby be reduced to an acceptable level. To obtain nevertheless a high magnetic flux density, a hybrid design is chosen where the magnetic flux is additionally concentrated by using pole material with saturation magnetizations exceeding the magnetization of the used permanent magnets. All this is explained in more detail in chapter 4.

2.2.1   Electric field produced by a single electron

The following approach to calculate the characteristics of the Undulator Radiation (UR) is inherited for the most part from the book of H.Onuki and P.Elleaume [68]. From the general case of the electric field emitted by an accelerated charged particle, finally intensity and spatial distribution of an electron beam passing an undulator will be derived.

An accelerated charged particle emits an electromagnetic wave. The acceleration depends on the local force acting on the particle. Most of the special characteristics of undulator radiation arise from the fact that the emitting particles travel almost at the speed of light c while the source of the constitutive force, the magnetic field of the undulator, is at rest in the laboratory frame (as well as the observer of the radiation). In the following, the position of the particle $\vec{R}(\tau)$ is given at time τ in the local system of the moving particle. The irradiated light will arrive at the observer with the position $\vec{r}$ at time t in the laboratory system. If $S = |\vec{r} - \vec{R}(\tau)|$ is the distance between observer and particle, the time t can be calculated by the following expression

$$t = \tau + \frac{S(\tau)}{c} \; .$$

(2.4)

This equation relates the observer time t to the particle time τ (also called retarded time). The unit vector $\hat{n}$ pointing from particle towards observer is defined as

$$\hat{n} = \frac{\vec{r} - \vec{R}(\tau)}{|\vec{r} - \vec{R}(\tau)|} \; .$$

(2.5)

With these two definitions, the electric and magnetic field of any moving charge can be derived from the Liénard-Wiechert potentials [74, 75]. The specific fields for an electron with its electric and magnetic field $\vec{E}$ and $\vec{B}$ can be expressed then [68] as

$$\vec{E}(\vec{r}, \omega) = \frac{\mathrm{i}e\omega}{4\pi c\varepsilon_0} \int_{-\infty}^{\infty} \frac{\vec{\beta} - \hat{n}(1 + \mathrm{i}c/\omega S(\tau))}{S(\tau)} \exp\left[\mathrm{i}\omega\left(\tau + \frac{S(\tau)}{c}\right)\right] \mathrm{d}\tau$$
$$\vec{B}(\vec{r}, \omega) = \frac{-\mathrm{i}e\omega}{4\pi c^2\varepsilon_0} \int_{-\infty}^{\infty} \frac{\vec{\beta} \times \hat{n}(1 + \mathrm{i}c/\omega S(\tau))}{S(\tau)} \exp\left[\mathrm{i}\omega\left(\tau + \frac{S(\tau)}{c}\right)\right] \mathrm{d}\tau$$

(2.6)

with $\beta = v_\mathrm{e}/c$ the normalized electron velocity. This equation can numerically be solved using the Fast Fourier Transform algorithm (FFT) as done by many synchrotron radiation calculation codes (e.g. *URGENT* [76], *SRW* [77] or *SPECTRA* [78]).

However, an analytical approach is only possible using the so-called far-field approximation which neglects the part of the solution decreasing with $1/S^2$ (the so-called velocity field). The second part, proportional to $1/S$, describes the acceleration field because it vanishes for a particle at constant velocity. Only this part is used for the so-called far field approximation, which neglects the velocity field and assumes all magnetic and electric fields orthogonal to each other as well as

to the direction of observation, which only holds true for distances far away from the radiation source.

For an electron with electron energy $E = \gamma m_\mathrm{e} c^2$, invariant (rest) mass m_e and charge e, one can define now an orthogonal set of axis x, z and s where x and z are the horizontal and vertical transverse axes while s is the longitudinal regarding the electrons motion, one can split the electrons velocity vector β in three components: ϑ_x, ϑ_z and β_s where only the latter is close to the speed of light. If one assumes therefore $\vartheta_x, \vartheta_z \ll 1$ (transverse velocities of the electron) as well as $\theta_x, \theta_z \ll 1$ the angle between s the direction of the electron's main motion and $\hat{n}$ the direction of observation, another approximation can be made: the so-called small angle approximation. With it $\vec{R} = (x, z, s) \approx (0, 0, c\tau)$ holds true and the assumption that both electric and magnetic field, are orthogonal to $\hat{n}$. Then the electric field of the electron can be written as

$$\vec{E}(x, z, s, \omega) = \frac{\mathrm{i}e}{2c\varepsilon_0 s} \exp\left(\mathrm{i}\frac{\omega}{c}s\left(1 + \frac{x^2}{2s^2} + \frac{z^2}{2s^2}\right)\right) \vec{H}\left(\frac{x}{s}, \frac{z}{s}, \omega\right), \tag{2.7}$$

with c the speed of light, ε_0 the vacuum permeability, and $\vec{H}$ a 2-dimensional field vector, given by the following expression

$$
\begin{aligned}
\vec{H}(\theta_x, \theta_z, \omega) \;=\; & \frac{\omega}{2\pi c} \int_{-\infty}^{\infty} \begin{bmatrix} \vartheta_x(s) - \theta_x \\ \vartheta_z(s) - \theta_z \end{bmatrix} \\
& \times \exp\left(\mathrm{i}\frac{\omega}{2c\gamma^2} \int_0^s \left(1 + \gamma^2(\vartheta_x(s') - \theta_x)^2 + \gamma^2(\vartheta_z(s') - \theta_z)^2\right) \mathrm{d}s'\right) \mathrm{d}s,
\end{aligned}
\tag{2.8}
$$

with the Lorentz factor γ by which time, length and relativistic mass change for a moving object. The Lorentz factor is defined by $\gamma = \mathrm{d}t/\mathrm{d}\tau = 1/\sqrt{1-\beta^2}$. Almost all physical quantities of the undulator radiation can be expressed as functions of this dimensionless field vector. In order to do so, it is useful to simplify this vector.

One can express the transverse velocities as functions of the transverse horizontal and vertical magnetic field components of the undulator B_x, B_z which are passed by the electron moving along the undulator axis

$$\vartheta_x(s) = \frac{e}{\gamma m_e c} \int_{-\infty}^{s} B_z(s')\mathrm{d}s \qquad\qquad \vartheta_z(s) = \frac{-e}{\gamma m_e c} \int_{-\infty}^{s} B_x(s')\mathrm{d}s. \tag{2.9}$$

These equations allow for any kind of magnetic field distribution inside along the electron path through the undulator. This generality can be maintained through the following sections. In section 2.2.5, a set of equations is presented for everyday life and in order to do that - for the sake of simplicity - the field is assumed to be sinusoidal then, with the field amplitude $B_{\updownarrow}$. This is necessary to solve the equations of motion which allows to deduce some important properties

of the undulator radiation. Coming back to this section, the only assumption here is that the transversal field integrals over one period vanish:

$$\int_0^{\lambda_u} B_x(s')\mathrm{d}s' = \int_0^{\lambda_u} B_z(s')\mathrm{d}s' = 0 .$$

Due to the periodicity of the undulator fields B_x, B_z with the period length λ_u, one can split the integral in equation (2.8) into a sum of integrals over each period. If the undulator center is placed at the origin of the coordinate system, one can express the field vector $\vec{H}$ as

$$
\begin{aligned}
\vec{H}(\theta_x, \theta_z, \omega) &= \vec{h}(\theta_x, \theta_z, \omega) \left(\sum_{q=-(N_u-1)/2}^{(N_u-1)/2} \exp\left(2\mathrm{i}\pi q \frac{\omega}{\omega_1}\right) \right) \\
&= N_u \vec{h}(\theta_x, \theta_z, \omega) \frac{\sin\left(\pi N_u(\omega/\omega_1)\right)}{N_u \sin(\pi\omega/\omega_1)} ,
\end{aligned}
\tag{2.10}
$$

where N_u is the number of undulator periods and ω_1 the fundamental resonance frequency. ω_1 depends on the direction of observation (θ_x, θ_z) and can be expressed as

$$
\begin{aligned}
\omega_1(\theta_x, \theta_z) &= \frac{4\pi c \gamma^2}{\int_0^{\lambda_u} \left(1 + \gamma^2(\vartheta_x(s) - \theta_x)^2 + \gamma^2(\vartheta_z(s) - \theta_z)^2\right) \mathrm{d}s} \\
&= \frac{4\pi c \gamma^2}{\lambda_u \left(1 + K_x^2/2 + K_z^2/2 + \gamma^2\theta_x^2 + \gamma^2\theta_z^2\right)} .
\end{aligned}
\tag{2.11}
$$

with the dimensionless deflection parameters K_x and K_z defined as:

$$
K_x = \sqrt{\frac{2\gamma^2}{\lambda_u} \int_0^{\lambda_u} \vartheta_x^2 \mathrm{d}s} \qquad\qquad K_z = \sqrt{\frac{2\gamma^2}{\lambda_u} \int_0^{\lambda_u} \vartheta_z^2 \mathrm{d}s} .
\tag{2.12}
$$

An interesting fact follows from (2.9) and (2.12). The deflection parameters are independent of the electron energy, they only depend on the magnetic field.

From the resonant frequency, one can now derive the associated resonant wavelength which characterizes the typical undulator spectrum, as will be seen in the following. The related wavelength is defined by:

$$
\lambda_1 = \frac{2\pi c}{\omega_1} = \frac{\lambda_u}{2\gamma^2} \left(1 + \frac{K_x^2}{2} + \frac{K_z^2}{2} + \gamma^2\theta_x^2 + \gamma^2\theta_z^2 \right) .
\tag{2.13}
$$

Furthermore, coming back to equation (2.10) again, one can see a non normalized sinc function as factor at the end. This factor (sometimes referred to as interference term or as 'grating' function [35]) determines the spectral properties of the radiation. For large numbers of N_u it can be written as:

$$\frac{\sin\left(\pi N_u(\omega/\omega_1)\right)}{N_u \sin(\pi\omega/\omega_1)} \approx \sum_{n=1}^{\infty} (-1)^{n(N_u-1)} \frac{\sin\left(\pi N_u((\omega/\omega_1)-n)\right)}{\pi N_u((\omega/\omega_1)-n)} . \tag{2.14}$$

This way, the radiation is bundled into a series of narrow bands in the frequency domain shown in figure 2.5. Furthermore, the dimensionless vector field $\vec{H}$ can be written as:

$$\vec{H}(\theta_x, \theta_z, \omega) \approx N_u \sum_{n=1}^{\infty} (-1)^{n(N_u-1)} \vec{h}_n(\theta_x, \theta_z) \frac{\sin\left(\pi N_u((\omega/\omega_1)-n)\right)}{\pi N_u((\omega/\omega_1)-n)} \tag{2.15}$$

with $\vec{h}_n(\theta_x, \theta_z) = \vec{h}_n(\theta_x, \theta_z, n\omega_1)$ representing the contribution to the electric field of the nth harmonic which can be derived from equation (2.8):

$$\vec{h}_n(\theta_x, \theta_z) = \frac{n}{\lambda_1} \int_{-\lambda/2}^{-\lambda/2} \begin{bmatrix} \vartheta_x(s) - \theta_x \\ \vartheta_z(s) - \theta_z \end{bmatrix} \tag{2.16}$$

$$\times \exp\left(\frac{2i\pi n}{\lambda_u} \int_0^s \frac{1 + \gamma^2(\vartheta_x(s')-\theta_x)^2 + \gamma^2(\vartheta_z(s')-\theta_z)^2}{1 + K_x^2/2 + K_z^2/2 + \gamma^2\theta_x^2 + \gamma^2\theta_z^2} ds'\right) ds .$$

with λ_1 the resonance wavelength defined by equation (2.13), K_x and K_z being the deflection parameters defined in equation (2.12) and ϑ_x and ϑ_z the transversal velocities which can be calculated for each transverse magnetic field distribution using equation (2.9). For any magnetic field independent of its exact form, one can conclude as a general rule that only the set of discrete
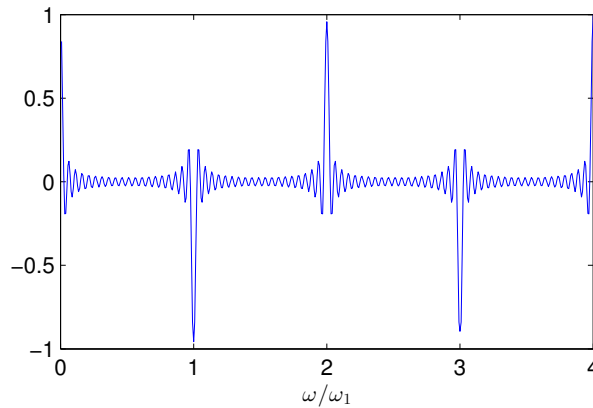
FIGURE 2.5: Interference term of equation (2.10)- $\sin(\pi N_u(\omega/\omega_1))/N_u \sin(\pi\omega/\omega_1)$ - defines narrow bands in the frequency domain. Here, it is shown for a 40 period undulator as a function of the resonance frequency ω/ω_1 defined in equation (2.11).

vectors given by $\vec{h}_n(\theta_x, \theta_z)$ (with $n = 1, 2, 3, ...$ only depending on the viewing direction defined by θ_x and θ_z) determines the electric field irradiated by the electrons. The general expression for the electric field emitted by a single electron can now be derived from equation (2.7) and equation (2.15):

$$
\begin{aligned}
\vec{E}(x, z, s, \omega) &= \frac{\mathrm{i}e\omega N_{\mathrm{u}}}{4\pi\varepsilon_0 c^2} \sum_{n=1}^{\infty} (-1)^{n(N_{\mathrm{u}}-1)} \int_{-\infty}^{\infty} \int_{-\infty}^{\infty} \vec{h}_n(\theta_x, \theta_z) \frac{\sin(\pi N_{\mathrm{u}}((\omega/\omega_1) - n))}{\pi N_{\mathrm{u}}((\omega/\omega_1) - n)} \\
&\quad \times \exp\left(\mathrm{i}\frac{\omega}{c}\left(\theta_x x + \theta_z z + s\left(1 + \frac{\theta_x^2}{2} + \frac{\theta_z^2}{2}\right)\right)\right) \mathrm{d}\theta_x \mathrm{d}\theta_z \,.
\end{aligned}
\tag{2.17}
$$

One can see that the resonance frequency ω_1 depending on the directions θ_x and θ_z (see equation (2.11)) finally determines a strong relation between the spatial and the spectral distribution. The far field approximation allows the integration over these angles:

$$
\begin{aligned}
\vec{E}(x, z, s, \omega) &\approx \frac{eN_{\mathrm{u}}}{2c\varepsilon_0 s} \exp\left(\mathrm{i}\frac{\omega}{c}s\left(1 + \frac{x^2}{2s^2} + \frac{z^2}{2s^2}\right)\right) \\
&\quad \times \sum_{n=1}^{\infty} (-1)^{n(N_{\mathrm{u}}-1)} \vec{h}_n(x/s, z/s) \frac{\sin(\pi N_{\mathrm{u}}(\omega/\omega_1(x/s, z/s) - n))}{\pi N_{\mathrm{u}}(\omega/\omega_1(x/s, z/s) - n)} \,,
\end{aligned}
\tag{2.18}
$$

with $\vec{h}_n(\theta_x, \theta_z)$ given by equation (2.16). Until this point, we only derived expressions for the emitted field vectors. In the next section, these fields will be translated into expressions describing the photon output of an undulator.

2.2.2 Angular distribution of undulator radiation

The energy per time and area of the electromagnetic irradiation can be calculated by the Poynting vector $\vec{S} = 1/\mu_0 \, \vec{E} \times \vec{B}$ which can be rewritten as $\vec{S} = \varepsilon_0 c E^2 \hat{n}$ combining the expressions in (2.6). If the area is then defined by the solid angle $\Delta\Omega$, one can calculate the energy at this area to be $W = (\hat{n}\vec{S})\Delta t R^2 \Delta\Omega = \varepsilon_0 c E^2 R^2 \Delta t \Delta\Omega$ and thereby the power to be $P = \mathrm{d}W/\mathrm{d}t = \int \varepsilon_0 c E^2 R^2 \mathrm{d}\Omega$. After the Fourier transformation to the frequency domain one gets two expressions for the power irradiated per unit solid angle $\mathrm{d}\Omega$ and frequency $\mathrm{d}\omega$ and the spectral flux per unit solid angle in the direction of $\hat{n}$:

$$
\begin{aligned}
\frac{\mathrm{d}P}{\mathrm{d}\Omega\mathrm{d}\Phi}(\hat{n}, \omega) &= \frac{h\alpha}{2\pi} \frac{I}{e} |\vec{H}(\hat{n}, \omega)|^2 \tag{2.19} \\
\frac{\mathrm{d}\Phi}{\mathrm{d}\Omega}(\hat{n}, \omega) &= \frac{2\pi\omega}{h\omega} \frac{\mathrm{d}P}{\mathrm{d}\Omega\mathrm{d}\omega}(\hat{n}, \omega) = \alpha\frac{I}{e}|\vec{H}(\hat{n}, \omega)|^2, \tag{2.20}
\end{aligned}
$$

where $\alpha = e^2/2\varepsilon_0 hc = 1/137$ is the fine structure constant. With these expressions, one can derive equations for the angular distribution of the radiation. For an idealized filament electron beam, the photon flux in direction (θ_x, θ_z) at frequency ω is

$$
\begin{aligned}
\frac{\mathrm{d}\Phi}{\mathrm{d}\Omega}\left(\theta_x, \theta_z, \omega, \hat{u}^*\right) &= \alpha\frac{I_\mathrm{e}}{e}|\vec{H}(\theta_x, \theta_z, \omega)\hat{u}^*|^2 \\
&\approx \alpha\frac{I_\mathrm{e}}{e}\sum_{n=1}^{\infty}\left|N_\mathrm{u}\vec{h}_n(\theta_x, \theta_z)\hat{u}^*\left(\frac{\sin(\pi N_\mathrm{u}((\omega/\omega_1)-n))}{\pi N_\mathrm{u}((\omega/\omega_1)-n)}\right)\right|^2 \\
&\approx \sum_{n=1}^{\infty}\frac{\mathrm{d}\Phi_n}{\mathrm{d}\Omega}\left(\theta_x, \theta_z, \omega, \hat{u}\right) \ ,
\end{aligned}
\tag{2.21}
$$

with $\mathrm{d}\Phi_n/\mathrm{d}\Omega\left(\theta_x, \theta_z, \omega, \hat{u}\right)$ the angular spectral flux of the n-th harmonic. This is defined by

$$
\frac{\mathrm{d}\Phi_n}{\mathrm{d}\Omega}\left(\theta_x, \theta_z, \omega, \hat{u}\right) = \alpha\frac{I_\mathrm{e}}{e}N_\mathrm{u}^2 \underbrace{\left|\vec{h}_n(\theta_x, \theta_z)\hat{u}^*\right|^2}_{\substack{\text{Lobe function -}\\\text{spatial shape}}} \underbrace{\left(\frac{\sin(\pi N_\mathrm{u}((\omega/\omega_1)-n))}{\pi N_\mathrm{u}((\omega/\omega_1)-n)}\right)^2}_{\substack{\text{Interference function -}\\\text{spectral line shape}}} .
\tag{2.22}
$$

The first factor describes the spatial distribution of the radiation lobe which depends on the magnetic field of the undulator by equation (2.9), the rear factor determines the spectral line shape which is independent from the exact undulator field. If the case is simplified to the n-th harmonic (with resonance frequencies $n\omega_1$ defined by equation (2.11)), one gets

$$
\frac{\mathrm{d}\Phi_n}{\mathrm{d}\Omega}\left(\theta_x, \theta_z, n\omega_1, \hat{u}\right) = \alpha\frac{I_\mathrm{e}}{e}N_\mathrm{u}^2\left|\vec{h}_n(\theta_x, \theta_z)\hat{u}^*\right|^2.
\tag{2.23}
$$

This equation is proportional to the square of the number of periods. From equations (2.10) and (2.23), one can calculate the angular distribution of the undulator radiation. The radiation is distributed in some narrow cones centered along the direction of the electron beam, this way
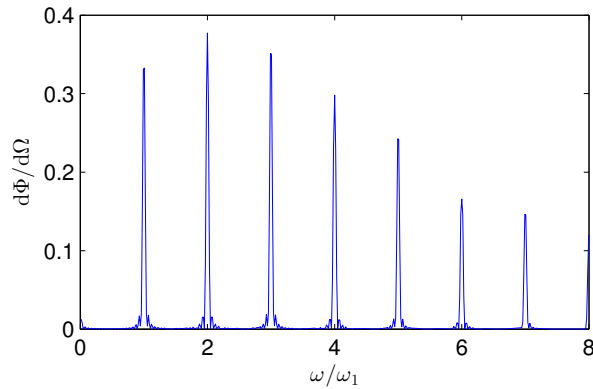
FIGURE 2.6: Graph of the angular spectral flux $\mathrm{d}\Phi/\mathrm{d}\Omega$ as a function of the frequency given as multiples of the resonance frequency ω_1. The spectrum is shown for a planar undulator with 20 periods and a K parameter of 1.5 (see eq. (2.12)).

spatially structured. The interference function structures the radiation spectrally to narrow bands of frequency, see figure 2.6.

With this, one can now develop a set of useful equations helping to calculate the main properties of undulator radiation fast and easily. The following set of equations thereby serve as a toolbox in the everyday life of a scientist working with undulators, using their radiation.

2.2.3 Angle integrated spectral flux

If we now integrate over the whole 4π angle range we get the angle integrated photon flux. This can be calculated by using equation (2.22)

$$
\begin{aligned}
\Phi_n\left(\omega, \hat{u}\right) &= \int_{-\infty}^{\infty} \int_{-\infty}^{\infty} \frac{\mathrm{d}\Phi_n}{\mathrm{d}\Omega}\left(\theta_x, \theta_z, \omega, \hat{u}\right) \mathrm{d}\theta_x \mathrm{d}\theta_z & (2.24) \\
&= \alpha \frac{I_\mathrm{e}}{e} N_\mathrm{u}^2 \int_{-\infty}^{\infty} \int_{-\infty}^{\infty} \left|\vec{h}_n(\theta_x, \theta_z)\hat{u}^*\right|^2 \left(\frac{\sin\left(\pi N_\mathrm{u}\left((\omega/\omega_1) - n\right)\right)}{\pi N_\mathrm{u}\left((\omega/\omega_1) - n\right)}\right)^2 \mathrm{d}\theta_x \mathrm{d}\theta_z . & (2.25)
\end{aligned}
$$

Using the fact that the undulator radiation consists of a series of thin spikes in the frequency domain with $\omega' = \omega\left(1 - 1/nN_\mathrm{u}\right)$ a frequency slightly below the resonant frequency, one can simplify the expression to the following approximation

$$
\Phi_n\left(\omega', \hat{u}\right) \approx 2\Phi_n\left(\omega_n, \hat{u}\right) = \pi\alpha \frac{I_\mathrm{e}}{e} \frac{N_\mathrm{u}}{n}\left(1 + \frac{K_x^2}{2} + \frac{K_z^2}{2}\right)\frac{1}{\gamma^2}\left|\vec{h}_n(0,0)\hat{u}\right|^2 . \qquad (2.26)
$$

Contrary to the frequencies ω_n growing quadratically with the electron energy, the flux $\Phi_n\left(\omega_n, \hat{u}\right)$ is independent from the electron energy. The integrated photon flux Φ_n only depends on the undulator period number N_u and the electron current I_e.

2.2.4 Electron transverse motion inside the undulator field

Until this point, all calculations were independent from the actual magnetic field distribution inside the undulator. The only assumption was that the field is periodic. At this point we leave the general approach in order to make some simplifications leading to a set of simple equations which are useful in the every day life of an undulator radiation physicist.

The relativistic Lorentz force gives us the equations of motion for an electron traveling with nearly the speed of light along s in the laboratory frame. This approach is described in most of the books, for instance in [79], [68] or [35]. From equation (2.9), for small angular deflections from s $(\vartheta_x, \vartheta_z \ll 1)$, one can write for the curvature $\alpha_{x/z}$:

$$\alpha_x = \frac{\mathrm{d}\vartheta_x(s)}{\mathrm{d}s} = \frac{e}{\gamma m_e c}(B_z - \dot{z}B_s) \tag{2.27}$$

$$\alpha_z = \frac{\mathrm{d}\vartheta_z(s)}{\mathrm{d}s} = \frac{e}{\gamma m_e c}(\dot{x}B_s - B_x) \, , \tag{2.28}$$

with m_e the electrons rest mass. For the sake of simplicity, we treat here the field distribution of the most common type of undulators - the planar undulator. This undulator consists of two parallel girders each holding a row of magnets with alternating direction of magnetization. A typical planar undulator can be seen in figure 4.1. The magnetic field of these kind of undulators have only vertical components along the central plane ($z = 0$) between the two girders, where $B_x(x, 0, s) = B_s(x, 0, s) = 0$ holds true for reasons of symmetry. Thus we get

$$\alpha_x = \frac{eB_z}{\gamma m_e c} \tag{2.29}$$

$$\alpha_z = 0 \, . \tag{2.30}$$

Ideally the field of such undulator is sinusoidal and can be described by:

$$B_z(s) = -B_\updownarrow \sin\left(\frac{2\pi}{\lambda_\mathrm{u}}s\right) \, , \tag{2.31}$$

where λ_u is the undulator period length. With this field distribution integration is possible and one gets:

$$\vartheta_x(s) = -\int \frac{B_\updownarrow e}{\gamma m_e c} \sin\left(\frac{2\pi}{\lambda_\mathrm{u}}s\right) \mathrm{d}s \tag{2.32}$$

$$= \frac{B_\updownarrow e}{\gamma m_e c} \frac{\lambda_\mathrm{u}}{2\pi} \cos\left(\frac{2\pi}{\lambda_\mathrm{u}}s\right) + const. \tag{2.33}$$

Considering (2.12) this can be simplified to:

$$\vartheta_x(s) = \frac{K_z}{\gamma} \cos\left(\frac{2\pi}{\lambda_\mathrm{u}}s\right) \, . \tag{2.34}$$

Another integration leads to the transverse position along s;

$$x(s) = \frac{K_z}{\gamma} \int \cos\left(\frac{2\pi}{\lambda_\mathrm{u}}s\right) \mathrm{d}s \tag{2.35}$$

$$= \frac{K_z}{\gamma} \frac{\lambda_\mathrm{u}}{2\pi} \sin\left(\frac{2\pi}{\lambda_\mathrm{u}}s\right) + const. \tag{2.36}$$

In all results, integration constants were chosen to be zero. This is reasonable if one assumes that the transverse position and the angle of deflection is ideally zero at the beginning of the undulator were $s = 0$.

2.2.4.1 Radiation field in the frequency domain

From equation (2.16) and equation (2.34), one can derive the radiation field in the frequency domain:

$$
\vec{h}_n(\theta_x, \theta_z) = \frac{n}{\lambda_1} \int_0^{\lambda_{\mathrm{u}}} \begin{bmatrix} K_z/\gamma \cos\left(2\pi(s/\lambda_{\mathrm{u}})\right) - \theta_x \\ -\theta_z \end{bmatrix} \tag{2.37}
$$
$$
\times \exp\left(2\mathrm{i}\pi n \left(\frac{s}{\lambda_{\mathrm{u}}} + \frac{-2\gamma\theta_x K \sin(2\pi(s/\lambda_{\mathrm{u}})) + K^2/4 \sin(4\pi(s/\lambda_{\mathrm{u}}))}{2\pi\left(1 + K^2/2 + \gamma^2\left(\theta_x^2 + \theta_z^2\right)\right)}\right)\right) \mathrm{d}s .
$$

with λ_1 defined by equation (2.13). On axis, integration is possible using a modified Bessel Function of the first kind. This reads then

for odd harmonics $n = 1, 3, 5, ...$
$$
\vec{h}_n(0,0) = \gamma\hat{u}_x \frac{nK_z}{1 + K_z^2/2} \left[J_{(n+1)/2}\frac{nK_z^2}{4 + 2K_z^2} - J_{(n-1)/2}\frac{nK_z^2}{4 + 2K_z^2} \right] \tag{2.38}
$$
for even harmonics $n = 2, 4, 6, ...$
$$
\vec{h}_n(0,0) = 0 .
$$

Here, $\hat{u}_x$ is the unit vector parallel to the x-axis, transversal (horizontal) to the averaged direction of electron motion. One can see that the even harmonics disappear on axis where the angle of observation is zero. This is due to the fact that the pulses of positive and negative electric fields are equidistant in the time domain [68]. From that equation, one can derive equations to estimate the expected photon yield of planar undulators, shown in section 2.2.5.5.

2.2.5 Undulator radiation toolbox

Using the results we got so far in section 2.2, we can deduce now a set of handy equations describing the most important properties of the undulator radiation for planar undulators.

2.2.5.1 *K* parameter

The so-called K parameter defined by equation (2.12) characterizes not only the electron motion within the undulator but gives at the same time a figure of merit for the spectral properties of the generated undulator radiation. For the sinusoidal magnetic field of a planar undulator, as

discussed in this work, it can be deduced from (2.12) by integrating over the field over a complete period length from zero to λ_u. For a magnetic field with amplitude $B_\updownarrow$, it can be written in a more handy notation, given by:

$$K = \frac{\lambda_\mathrm{u} e B_\updownarrow}{2\pi m_\mathrm{e} c} \approx 0.09336 \ B[T] \ \lambda_\mathrm{u}[mm].$$ (2.39)

2.2.5.2 Peak wavelength

From equation (2.13), one can derive an equation for the wavelengths of the radiation bands. These so-called undulator radiation harmonics are determined by the undulator resonance equation [68] which reads for a planar undulator with only one transverse field vector at the central plane:

$$\lambda_\mathrm{ph} = \frac{\lambda_\mathrm{u}}{2n\gamma^2} \left(1 + \frac{K^2}{2} + \theta_x^2 \gamma^2 + \theta_z^2 \gamma^2\right)$$ (2.40)

Here, λ_ph is the emitted photon wavelength, λ_u the period length of the undulator, K the characteristic undulator parameter and $\gamma = 1 + E_\mathrm{e}/(m_e c^2)$ the Lorentz factor describing the total energy of the electrons in the beam. $n = 1, 2, 3, ...$ is the harmonic number. The last term of eq. (2.40) describes the redshift due to the relativistic Doppler effect at observation angles θ.

This has some effects on undulator radiation measurements. Due to the extent of the spectrometers aperture a certain amount of radiation with red shifted peak wavelengths gets through to the detector. An approximation of the most intense wavelength, the peak wavelength of the worst case, when no slit is used and all of the undulator radiation is detected (integrated over the whole radiation cone) is described by the following equation:

$$\lambda_\mathrm{peak} = \frac{\lambda_1}{n(1 - 1/nN_\mathrm{u})}$$ (2.41)

where N_u is the number of undulator periods and λ_1 the fundamental wavelength of the radiation spectrum [35].

2.2.5.3 Opening angle

From the term of equation (2.22) which determines the spatial distribution, one can derive a general expression for the RMS divergence for filament electron beams. In case of realistic beams this angle has to be quadratically summed with the divergence of the electrons. From equation (2.15) for small angles of observation ($\theta_x, \theta_z \ll 1/\gamma$ and a large number of periods $N \gg 1$), one can approximate the field vector $\vec{H}$ by:

$$
\vec{H}(\theta_x, \theta_z, \omega) = N_{\mathrm{u}} \sum_{n=1}^{\infty} (-1)^{n(N_{\mathrm{u}}-1)} \, \vec{h}_n(0,0) \, \frac{\sin\left(\Gamma(\theta_x, \theta_z)\right)}{\Gamma(\theta_x, \theta_z)} \quad \text{with} \tag{2.42}
$$

$$
\Gamma(\theta_x, \theta_z) = \pi n \, \frac{\theta_x^2 + \theta_z^2}{2} \, \frac{L}{\lambda_1(0,0)} + \pi N \left(\frac{\lambda_1(0,0)}{\lambda} - n \right).
$$

Here, λ_1 is the resonance wavelength obtained on axis ($\theta_x, \theta_z = 0$) and $L = \lambda_{\mathrm{u}} N$ is the length of the undulator. When the results of equation (2.42) are fit by a gaussian ($\exp\left(\theta^2/2\sigma^2\right)$) one gets the opening angle of the central cone:

$$
\sigma_{\angle} \approx 0.69 \sqrt{\frac{\lambda_n}{L_{\mathrm{u}}}} \approx \sqrt{\frac{\lambda_n}{2 L_{\mathrm{u}}}} \ . \tag{2.43}
$$

Here, L_{u} is the total length of the undulator. This is true for the resonant wavelengths $\lambda_n = n \lambda_1$. For the peak wavelength, described by (2.41) the opening angle is twice as wide and the the photon number is doubled as well. Substituting equation (2.40) in (2.43) one gets another expression for the opening angle in terms of K

$$
\boxed{\sigma_{\angle} \approx \frac{1}{2\gamma} \sqrt{\frac{1}{n N_{\mathrm{u}}} \left(1 + \frac{K^2}{2} \right)}} \tag{2.44}
$$

For a large number of periods, the opening angle becomes much narrower than $1/\gamma$ which is the opening angle of a typical bending magnet. This is due to the constructive interference of the light emitted from the subsequent periods which also leads to the fact that for odd harmonic numbers n the photons are emitted in a cone of light around the electrons direction of motion, whereas the even harmonics do not appear on-axis.

2.2.5.4 Bandwidth

From the interference condition of the UR, emitted at every period over the whole undulator length, one obtains the intrinsic bandwidth of each harmonic peak [68]:

$$
\left(\frac{\Delta \lambda}{\lambda} \right)_{\mathrm{u}} = \frac{1}{n_{\mathrm{u}} N_{\mathrm{u}}} \quad (\text{for } n_{\mathrm{u}} = 1, 3, 5, \dots) \ . \tag{2.45}
$$

Additionally, one gets a contribution from magnetic field errors ΔB. From eq.(2.40) and $\Delta B / B \approx \frac{\Delta K}{K}$ follows

$$
\left(\frac{\Delta \lambda}{\lambda} \right)_B = \frac{K^2}{\left(1 + \frac{K^2}{2} \right)} \frac{\Delta B}{B} \ . \tag{2.46}
$$

A third contribution is given by the electron energy spread which can be significant (about 10% and higher) for PWA electron beam lines

$$\left(\frac{\Delta\lambda}{\lambda}\right)_{e} = 2\frac{\Delta\gamma}{\gamma} \,. \tag{2.47}$$

Another contribution is given by the electron beam divergence and a non ideal entrance slit of the used spectrometer or the experimental sample. This leads to a certain range in the angle of incidence of the radiation and thereby to a partial red shift of the incident light pulse. The effect can be described by the following expression [80]

$$\left(\frac{\Delta\lambda}{\lambda}\right)_{\sigma',\theta} = \frac{(\gamma\sigma_{x'})^2 + (\gamma\sigma_{y'})^2 + (\gamma\theta_{ap,x})^2 + (\gamma\theta_{ap,y})^2}{1 + K^2/2} \,. \tag{2.48}$$

Since all bandwidth broadening effects are statistically independent, the total bandwidth of UR on-axis is given by a quadratic sum over all expressions, from (2.45) to (2.48).

$$\boxed{\left(\frac{\Delta\lambda}{\lambda}\right)_{tot} \approx \sqrt{\left(\frac{\Delta\lambda}{\lambda}\right)_u^2 + \left(\frac{\Delta\lambda}{\lambda}\right)_B^2 + \left(\frac{\Delta\lambda}{\lambda}\right)_e^2 + \left(\frac{\Delta\lambda}{\lambda}\right)_{\sigma',\theta}^2}} \tag{2.49}$$

This summary still neglects diffraction effects, further described in appendix B.

2.2.5.5 On-axis photon flux density

The on-axis ($\theta = 0$) photon flux density in units of photons per solid angle, second and 0.1% bandwidth for an electron beam with zero divergence ($\sigma_{x'} = \sigma_{z'} = 0$) can be derived from (2.22) substituting equation (2.38) [68] and using the 'On-axis angular density' function:expression

$$F_n(K) = \frac{n^2 K^2}{(1 + K^2/2)^2} \left(J_{(n-1)/2}\left(\frac{nK^2}{4 + 2K^2}\right) - J_{(n+1)/2}\left(\frac{nK^2}{4 + 2K^2}\right)\right)^2 \,, \tag{2.50}$$

again with modified Bessel Functions $J_{(n+1)/2}$ and $J_{(n-1)/2}$ the harmonic number n and the undulator parameter K. In the end we get a handy expression which reads

$$\boxed{\left.\frac{d\Phi}{d\Omega}\right|_{\theta=0}^{n} \approx 1.74 \times 10^{14}\, N_u^2\, E_e^2\, I_e\, F_n(K) \,.} \tag{2.51}$$

Here, $d\Phi/d\Omega|_{\theta=0}^{n}$ is shortly written for $d\Phi/d\Omega\,(0,0,n\omega_1,\hat{u})$, the number of photons per solid angle $d\Omega$ per second at observation angle $\theta = 0$ which means directly on-axis, given for the n-th harmonic. E_e is the electron energy to be inserted in [GeV], I_e the average electron beam
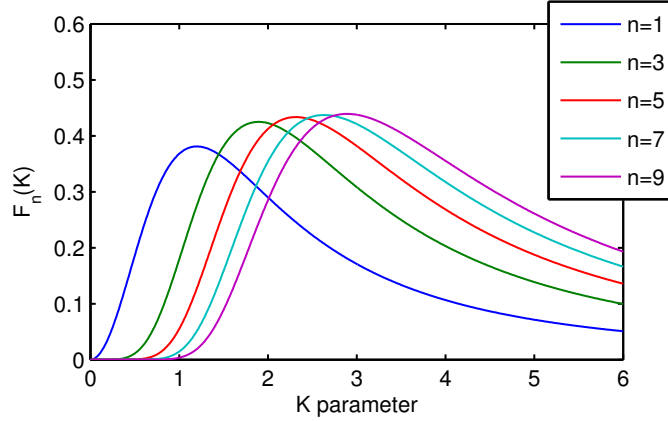
FIGURE 2.7: Graph of the 'On-axis angular density' function $F_n(K)$ which is defined by equation (2.50). One can see distinct maxima for specific values of K.

current in [A] and $F_n(K)$ given by (2.50). Figure 2.7 shows a plot of $F_n(K)$ which gives a general form of equation (2.51).

At a K parameter of 1, the highest possible on-axis photon flux density for the fundamental is reached, shown in figure 2.7, whereas a K parameter of 2 enables the highest possible on-axis photon flux density for the third harmonic spectral order followed by the maxima of the higher harmonics in shorter pitches.

However, equation (2.51) describes undulator radiation generated by zero divergence electron beams only. For divergent electron beams, a modification of equation (2.51) must be made, as suggested by P. Elleaume [68]:

$$\frac{\mathrm{d}\Phi}{\mathrm{d}\Omega}\bigg|_{\theta=0}^{n} (\sigma_{x'}, \sigma_{z'}) \approx \frac{\mathrm{d}\Phi}{\mathrm{d}\Omega}\bigg|_{\theta=0}^{n} \times \left[\left(1 + \frac{L\sigma_{x'}^2}{2\lambda_{\mathrm{ph}}}\right)\left(1 + \frac{L\sigma_{z'}^2}{2\lambda_{\mathrm{ph}}}\right)\right]^{-1}. \tag{2.52}$$

Here, $\sigma_{x'}$ and $\sigma_{z'}$ are the horizontal and vertical electron divergences, L the undulator length and λ_{ph} the photon wavelength.

2.2.5.6 Angular integrated photon flux

Substituting equation (2.26) in equation (2.38) and an expression for the modified Bessel Function using,

for odd harmonics ($n = 1,3,5,...$):

$$Q_n(K) = \frac{nK^2}{1 + K^2/2}\left(J_{(n-1)/2}\left(\frac{nK^2}{4 + 2K^2}\right) - J_{(n+1)/2}\left(\frac{nK^2}{4 + 2K^2}\right)\right)^2$$
$$= \left(1 + \frac{K^2}{2}\right)\frac{F_n(K)}{n} \tag{2.53}$$
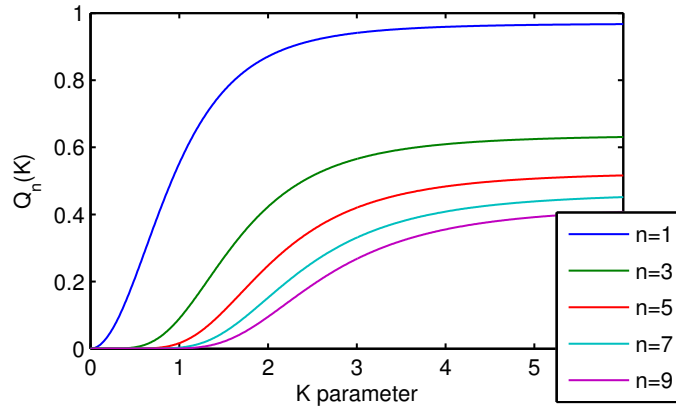
FIGURE 2.8: Graph of 'Integrated Flux' function $Q_n(K)$, defined by (2.53), gives an impression on the dependence of the integrated photon flux Φ_n to the undulator parameter K. One can see that an effective production of higher harmonics starts beyond $K = 1$ and shows asymptotic behavior for higher values of K.

and for even harmonics ($n = 2,4,6,...$):

$$Q_n(K) = 0 \; .$$

The 'Integrated Flux' $Q_n(K)$ tends towards 1 for higher values of K, as shown in figure 2.8. Thus it follows that the integrated photon flux can never exceed the threshold $\pi\alpha N_\mathrm{u} I_\mathrm{e}/e$, which is a kind of conversion limit, depending linearly on the number of periods and the number of electrons in the bunch. After the substitution, one gets an equation for the integrated photon flux:

$$\Phi_n \approx \pi\alpha N_\mathrm{u}\frac{I_\mathrm{e}}{e}Q_n(K)|\hat{u}_x\hat{u}^*|^2 \; . \tag{2.54}$$

Combining the constants, one can write down a simple expression instead

$$\boxed{\Phi_n \approx 1.431 \times 10^{14}\, N_\mathrm{u}\, I_\mathrm{e}\, Q_n(K) \; ,} \tag{2.55}$$

where, as before, N_u is the undulator period number and I_e is the electron beam current which has to be inserted in [A]. The integrated photon flux Φ_n is then given as photons per second and 0.1% bandwidth.

2.3 Field measurements, deviations and consequences

In the following section, typical undulator errors and their influence on field and spectrum of the UR will be shown. Furthermore, it should be pointed out that this far the undulator field was assumed to be sinusoidal to allow for simplifications and integrations for the sake of simplicity.

This was done to get some insights to the general behavior of undulator radiation gaining the possibility to derive some rules of thumb.

In particular the undulator K parameter, as a characteristic property describing most of the radiation-related properties, is calculated amongst others by the amplitude of the sine curve of the magnetic flux density of the undulator. Since the slope of the magnetic flux density defers from the perfect sine shape for most of the undulator designs we will derive another characteristic property significant for the undulator radiation of real devices.

2.3.1 Effective field and *K* parameter

The calculation of the spectral output of an undulator is complex for real undulators, where the slope of the magnetic field defers from the ideal sinusoidal trace and the analytic expressions are not sufficient anymore. In these cases, it does not simply suffice to use the field amplitudes for the calculation of K. A simple and adequate method for most cases is to calculate the spectral output of a real undulator using the so-called effective field amplitude. There are several ways to get the field approximation, here two of them will be described.

The first follows the idea to average the magnetic field by calculating the slippage which follows from the difference between velocities of electron bunch and light field in the direction of the beam. After every undulator period, the electron bunch falls back behind the initially generated light pulse by approximately one wavelength of the light itself. If this is now done for every period of the undulator, one can use the linear fit over all subsequent slippage distances to get an average and calculate the effective field and K parameter from that [81] with the formulas:

$$\Delta S_s = \int_{s_1}^{s_2} \left(\frac{1}{2\gamma^2} + \frac{1}{2}\vartheta_x^2(s) \right) \mathrm{d}s. \tag{2.56}$$

ϑ_x given by (2.9) can be calculated from the first field integral. The effective undulator parameter K_{eff} is then calculated from the gradient of the linear fit of S_s along s:

$$K_{eff} = \sqrt{2(m_{fit} - 1)} \tag{2.57}$$

and accordingly follows the calculation of the effective field (2.39):

$$B_{eff} = -\frac{2\pi m_e c}{\lambda_u e} K_{eff}. \tag{2.58}$$

The second method calculates the effective magnetic field by calculating the Fourier series of the measured magnetic field and cut off some higher orders. This method was used within the thesis in hand, all terms above the ninth harmonic [82, 83] were cut off. Both ways allow to determine the effective undulator parameter K_{eff} using equation (2.39) and use this for the calculation of the undulator radiation.

2.3.2 Undulator field deviations

As mentioned above, there are mainly two types of undulator field errors being significant for FEL applications. The effect on electron bunch and light generation of both is described in detail in the next sections.

2.3.2.1 Relative error of the K parameter

The relative error of the K parameter is due to its definition (2.39) given by:

$$\Delta K / K = \sqrt{\left(\Delta B / B\right)^2 + \left(\Delta \lambda_{\mathrm{u}} / \lambda_{\mathrm{u}}\right)^2}.$$

Since $\Delta \lambda_{\mathrm{u}} / \lambda_{\mathrm{u}}$ is usually small compared to $\Delta B / B$, $\Delta K / K$ is intuitively understandable and it can be measured easily by determining the amplitudes of the magnetic induction inside the undulator. But beside its comprehensibility, the use of $\Delta K / K$ has a major drawback: the correlation to the undulator photon performance is poor [84]. Hence, this property might be used to explain a possible broadening of the peaks within the undulator harmonic spectrum but it might not predict the expected performance of the undulator in terms of photon radiation intensity. Thus, it is a less useful figure of merit to evaluate the feasibility of the required FEL undulator.

Nevertheless, $\Delta K / K$ will be observed in this study. If one thinks about the interaction between electrons and light pulse during their track through the undulator, which depends on the phase relation between both one could imagine that this phase relation develops like a random walk phenomenon. In this picture, the mean deviation of K would be the mean step size of the one dimensional random walk of the phase relation and this value would describe the evolution of the phase relation between electron bunch and light pulse.

Thus, $\Delta K / K$ can be interpreted as a kind of key figure for the averaged evolution of another, more important kind of field error of the undulator: the phase shake or RMS phase error, which is described in the next section.

2.3.2.2 Undulator phase error and phase shake

The phase error is the difference in the phase relations of the average phase of the already emitted light field and the electrons in the magnetic field of a successive undulator period.

Light field and electron bunch travel with approximately the same speed c. Due to the differences in path lengths between light and electrons, every subsequent period the electrons fall back behind the light pulse. According to the electrons equation of motion (2.36), the difference in path lengths is given by:

$$s_l = \frac{\lambda_1}{2} = \frac{\lambda_{\mathrm{u}}}{4\gamma^2}\left(1 + \frac{K^2}{2}\right) \tag{2.59}$$

per undulator half period in ideal conditions. This way, the electrons fall back a full wavelength of the resonant light wave λ_1. Thus, the light emitted at the successive period, is interfering constructively with the light pulse emitted before.

From that equation it becomes apparent that a variation in the undulator parameter K not only leads to a broadening of the bandwidth, as described by equation (2.46), but also to a disturbed phase relation between emitted light and the previously emitted light pulse. This way an additional, small variation of the ideal, harmonic difference in the path lengths (of exactly one wavelength) can be calculated:

$$\Delta s_l = \frac{\lambda_{\mathrm{u}}}{4\gamma^2}\left(\frac{K_i^2}{2} - \frac{K_0^2}{2}\right),\tag{2.60}$$

with K_i the individual undulator parameter of the i-th half period and K_0 the ideal undulator parameter. The calculation of the phase shift can then be carried out with the following relation:

$$\Delta\Psi_i = k_l\Delta s_l = k_l\frac{\lambda_{\mathrm{u}}}{4\gamma^2}\left(\frac{K_i^2}{2} - \frac{K_0^2}{2}\right).\tag{2.61}$$

Here, k_l is the wavenumber of the light field. Finally, one can calculate the sum over all phase errors at the n-th period along the undulator given by:

$$\Delta\Psi_n = \sum_{i=1}^{n}\Delta\Psi_n = k_l\frac{\lambda_{\mathrm{u}}}{4\gamma^2}\sum_{i=1}^{n}\left(\frac{K_i^2}{2} - \frac{K_0^2}{2}\right).\tag{2.62}$$

This sum is often called phase error or phase shake and a convenient figure of merit in FEL design is the RMS value of the complete undulator:

$$\Psi = \sqrt{\frac{1}{2N_{\mathrm{u}}}\sum_{i=1}^{2N_{\mathrm{u}}}\Delta\Psi_n^2},\tag{2.63}$$

with N_{u} the number of undulator periods.

It is stronger correlated to FEL performance than the relative error in K [84]. This is intuitively clear since the stimulated amplification of the FEL signal depends on the interaction and thus on the phase relation between electron bunch and photon beam.

2.3.3 Electron beam wander

For both concepts, spontaneous undulator radiation and FELs, an important consequence follows from undulator field errors, the so-called beam wander. The beam wander is the transversal offset of the electron beam which is generated any time a stronger undulator half period with higher magnetic flux densities follows a weaker half period or vice versa. Then, the electron trajectory is deflected from the initial beam axis.

The final trajectory or rather their maximum distance from initial beam axis can be estimated by a 1-d random walk theory [85]. Besides that, there is a correlation between phase shake and beam wander, as the electron path passes regions where the magnetic field flux differs from the ideal. Moreover, if the electron bunch drifts away from the light pulse, the interaction between both fields is weakened and thereby the FEL performance [84]. Further information about the consequences to the spectral output can be found in e.g. [86].

2.4 Brief introduction to the principles of Free electron lasers

This section will concentrate on one scheme of the theory, the so-called Self Amplified Spontaneous Emission - Free Electron Laser (SASE-FEL). This is a unique type of laser which uses highly relativistic, quasi monoenergetic electron bunches as lasing medium. The word *free* refers to the unbound electrons, which are other than usual unattached to atomic orbitals. In the following section the basic principles of a SASE-FEL will be described. The introduction is oriented at the discussion found in [87].

Whereas the underlying principle of the generation of synchrotron light is the same for the FEL and for spontaneous undulator radiation, as described before in section 2.2, there is an additional process involved, which leads to the generation of highly coherent light, with an exponential scaling of the radiation power. This process emerges from the interaction of electrons with previously (more upstream) emitted light. The phase relation between light waves and individual electrons determines whether the electron gains or loses energy in the electric field of the radiation. This effect is described by a simple formula [88]:

$$\frac{\mathrm{d}W}{\mathrm{d}t} = \vec{v} \cdot \vec{F} = -ev_z E_z \tag{2.64}$$

with v_z the transverse electron velocity and E_z the electric field of the radiation along the same axis. All electrons with shares of their velocities pointing in the same direction the field vector of the radiation field points to, gain energy, and in case of opposing directions lose energy accordingly. Thereby an energy modulation on the scale of the wavelength of the light emerges during the electrons journey through the undulator.

Additionally, the undulator works as a dispersive medium for the electrons. This is due to the fact that the energy of the electron determines their trajectory according to the Lorentz force. As a matter of fact the amplitude of electrons with higher energies is smaller and vice versa. Together with the higher velocity of the 'high energy' electrons, these electrons are moving ahead and these with lower energy are falling in behind. This way, an energy dependent local separation is generated with a separation length matching the periodicity of the electric field of the light wave of the emitted light. This energy-depending changes of motion quantities in optical systems are called dispersion in general.
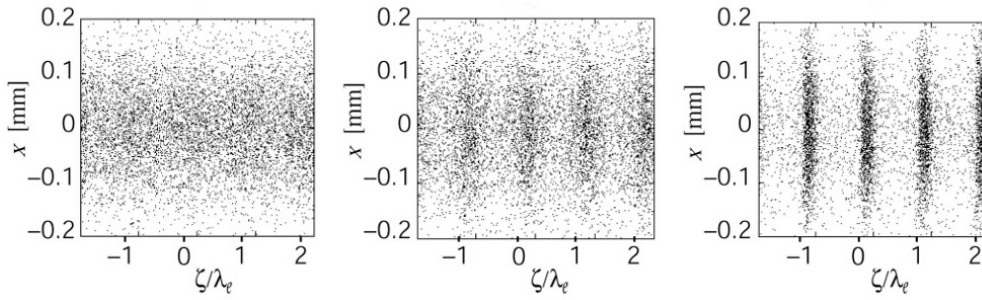
FIGURE 2.9: Development of the electron density after passing hundreds of undulator periods. Here, the power modulation coming from the electrons interaction with the emitted light field generates a density modulation at the scale of the wavelength of the light λ_l. (Source: [89])

The resulting modulation of electron density is often called microbunching. With the ongoing amplification of the spatial separation matching exactly the distance of one wavelength of the emitted light, the electrons - as source of the undulator radiation - emit more and more in phase or rather more and more coherently. The gain in coherence leads to stronger electric fields of the light pulse and this to a boost of the so-called ponderomotive force which is the name of the separating force and the root of the amplification process. This again leads to stronger microbunching and in turn to a stronger emission. By that, an exponential growth of the undulator radiation along the length of the undulator is created.

The SASE (spontaneous amplification of stimulated emission) regime described here, starts at the beginning of the undulator with an electron bunch featuring a slightly disturbed Gaussian distribution (noise). From that point, the microbunching evolves into a state where saturation is reached, when the ponderomotive force and the coulomb interaction between the electrons reach an equilibrium. In case of X-ray FELs, the length of the undulator must be tens of meters to reach this state, where the radiation intensity is the highest.

A simplified 1D approach of the problem shows that the emitted radiation power can be described by [88]:

$$P = \exp\left(\frac{s}{L_{g0}}\right) , \tag{2.65}$$

with s the position along the beam and undulator axis and the so-called power gain length L_{g0}. This is defined by:

$$L_{g0} = \frac{1}{4\pi\sqrt{3}}\frac{\lambda_{\mathrm{u}}}{\varrho} , \tag{2.66}$$

including the Pierce parameter ϱ which is a characteristic property of an FEL. It is defined by:

$$\varrho = \frac{1}{2\gamma}\left[\frac{I_{\mathrm{peak}}}{I_A}\left(\frac{A_{\mathrm{u}}\lambda_{\mathrm{u}}}{2\pi\sigma_{\mathrm{r}}}\right)^2\right]^{1/3} \propto \frac{1}{\gamma}\left(\frac{I_{\mathrm{peak}}}{I_A}\right)^{1/3}\lambda_{\mathrm{u}}^{4/3} , \tag{2.67}$$

where γ is - as before - the relativistic Lorentz factor. The normalized electrical current I_{peak}/I_A with the constant $I_A := 17\mathrm{kA}$, the so-called Alfvén current. λ_{u} is as in the sections before the undulator period length and σ_{r} the standard deviation of the transverse diameter of the electron bunch. A_{u} is a dimensionless factor defined by a modified Bessel function which reads $A_{\mathrm{u}} = K/\sqrt{2}[J_0(\xi) - J_1(\xi)]$, where J are Bessel functions with the argument $\xi = K^2/(4+2K^2)$ as already known from the previous section in equation (2.50). On the right hand side, the second expression shows a rough scaling of the Pierce parameter ϱ which only accounts if the following assumptions could be made. The amplitude of the magnetic induction $B_{\updownarrow}$ must be independent of the undulator period length λ_{u} which we will see in section 3.6.1 is not the case in general. Nevertheless, the right hand side of equation (2.67), leaving γ, λ_{u} and I_{peak} as free parameters can serve here as rough approximation of the scaling. Another fact is that σ_{r} has to be matched to the beam optics of the beam line, to reach a high average electron beam current density along the path through the undulator.

In a distinct FEL design [4] which is adapted to electron beams generated by state-of-the-art Plasma-Wakefield Accelerators (PWA), a constantly shifting focus position is suggested in combination with a tapered undulator. The electron beams from PWAs show conceptually significant energy spreads due to the accelerating process. The chromaticism of the beam optics smears out the focal spot which would lead to a reduced electron current density as every electron energy would have another focal length. This degrading effect (the lower average electron density) can now be minimized by matching the undulators K parameter to the electrons energy at each position along the line focus inside the undulator.

Typically the length of an FEL undulator is 15 to 25 times the power gain length L_{g0}. After this length microbunching reaches saturation and with it the highest photon flux densities are possible. As can be seen from equations 2.66 and (2.67) a high pierce parameter and a short undulator period length is needed to reduce the gain length. To save building costs of such a light source one naturally aims to reduce the size of both the undulator and the accelerator. As we will see in the next section, a Laser-based accelerator concept, incomparably small, generating accelerating fields outnumbering these of conventional accelerators to about two orders of magnitude ($\approx 1T\mathrm{V}$), so-called Plasma-Wakefield Accelerators, provide a couple of features promoting the Pierce parameter as they deliver high electron currents but bring along some difficulties due to the unwieldy accelerator field strengths.

2.5 Brief introduction to the principles of Plasma-Wakefield Acceleration

To hold this section short, the discussion of the Plasma-Wakefield Acceleration (PWA) will be concentrated on the phenomenological side of the concept. In general, PWAs use strong electric field gradients generated in plasmas to accelerate charged particles. These plasmas are generated ionizing gas with high power laser pulses. The laser system at the UHH is a 200 TW laser, providing a 25 fs pulse length, which can run at a repetition rate of 5 Hz.

The principles of the theory were already found in 1979 [28] and first experiments followed in 1984 at the UCLA [29] showing electrical field gradients which were several orders of magnitude higher than those of conventional accelerators. Due to this fact, the acceleration distance could be decreased at the same scale, still reaching comparable kinetic energies of the particles. This is the reason why several research groups are developing experiments in that field of technology these days, increasing the energy and bunch charge from year to year. In 2014, electron energies of 4.25 GeV were achieved at Lawrence Berkeley National Laboratory (LBNL) [33] using a high power laser system for the generation of the plasma. In that case, the laser pulse delivered a power of 1 PW with a pulse energy of 42.2 J in about 40 fs.

Despite recent developments in this field still, the stability of the electron beam in terms of pointing, charge and energy spread are significant weaknesses, so far. Powerful focusing fields within the plasma lead to a high divergence after the acceleration region and the strong acceleration gradients effect a huge energy spread, with a strong correlation to the bunch internal longitudinal position (chirp). However, to make use of these electrons for the generation of light nevertheless, one needs to adapt the beam optic as well as the insertion devices (undulators and wigglers) to these specifics of the electron beam. The aim of this work is to find undulator designs for different PWA-based undulator scenarios. In chapter 3, the focus lies on undulator designs tailored for the production of spontaneous emission, in chapter 4 on manufacturing tolerances of undulators dedicated for a PWA based X-ray FEL and in chapter 5 spectral measurements of a prototype, cryogenic undulator are presented.

FIGURE 2.10: The laser system of the LUX group operates an 200 TW, 25 fs laser named *ANGUS*, which could run with a repetition rate of up to 5 Hz. The focus on design of laser system and beam line was on reliability and reproducibility. A high degree on automatization, such as auto-alignment procedures and continuous data acquisition including environmental conditions, enables a stable every-day operation with a high statistical determination of experiments. (Source: [90])

Chapter 3

Short period undulator design dedicated to PWA electron beam lines

Major questions of natural sciences are connected with processes at the scale of atoms and electrons and their complex and fast interactions. An immensely important research tool to observe these processes is light in the VUV and soft X-ray range. The demand for scientific light sources in that range has constantly been increasing over the past years and synchrotrons and Free Electron Lasers (FELs) all over the world are frequented beyond their capacities.

A fundamental component of these light sources is an electron accelerator. The particles draw their energy from successive Radio Frequency (RF) cavities. Over the past decade, an alternative accelerator scheme has moved into spotlight, promising exceptional electron beam properties with a smaller footprint in size and costs compared to conventional synchrotron light facilities. By using plasmas as source of the accelerating electric field, the attainable field gradients exceed those of the prevailing accelerator technology by several orders of magnitude. These plasmas are generated by focusing high power laser beams or alternatively low energy electron pulses into gases. Different gas targets were developed for this purpose. The technical complexity of these targets ranges from simple gas jets to complex targets. A simple form is the supersonic gas jet, streaming from 'de Laval' nozzles into the vacuum chamber optionally equipped with razor blades causing a hard drop in the density distribution of the gas (which creates a distinct region for the injection of electrons in the plasma bubble and reduces this way the energy spread of the electron bunch). More complex targets are e.g. steady-state-flow gas cells with variable length or complex capillary designs with defined pressure and density zones for an optimized electron injection. Both can be equipped with stabilizing features like guiding discharge mechanisms [91]. More on Plasma-Wakefield Accelerators (PWAs) can be found in the review paper of Esarey, Schroeder and Leemans [92].

Triggered by the hope to increase experimental accessibility to accelerator-based light sources for an interdisciplinary scientific community [93], an increasing number of these PWA electron

beam lines are currently under construction, explicitly dedicated to the generation of VUV and soft X-radiation [94–97]. However, before these PWA beam lines might become a mature standard technology of particle accelerators, several technical problems have to be mastered. One of a few drawbacks of the new technology is connected with the control of the plasma, which is challenging to establish due to the small scales and extremely high field gradients. In addition to that, instabilities of the used high power laser systems, induced by temperature fluctuations and vibrations of the environment and impurifications or even attritions of the optics etc. cause degradations of the laser pulse quality and thereby pointing, tilts, energy jitters and other irregularities of the electron beam. Furthermore, even if state-of-the-art PWA electron beam lines reach energies up to 4.2 GeV [98], they are still suffering from a notable energy spread in addition to positional and directional instabilities. Although the comparison of actual PWA beam lines to conventional accelerators might paint an unappealing picture, especially concerning the electron energy spread of still more than 1%, one has to keep in mind the young age of the technology, see the fast developments of the last few years, and the great perspectives connected with it. Finally due to the above described reasons it is necessary to develop undulators with properties specifically adapted to these particular PWA electron characteristics.

3.1 Overview

In the first section 3.2 the design goals of the PWA undulator development are summarized. Then preliminary considerations are made, in order to define essentials for the material selection of the magnetic components of the undulator.

In section 3.3 the decision process for the permanent magnet material choice is described in detail. A main task is to minimize the risk of demagnetization while keeping the magnetic flux density strong. Therefore the expected electron beam loss due to daily operation is estimated in 3.3.1 and a subsequent risk assessment for demagnetization is given in section 3.3.2. The absorbed dose simulated explicitly for the PWA scenario implies the demand for a high coercive magnet material. Based on that analysis a material is chosen conclusively in section 3.3.3, providing the highest coercivity commercially available these days. To further increase the material's radiation resistivity special treatments (GBD and artificial aging) are applied, described in the back part of section 3.3.4. Conclusively magnet specifications of the chosen material are presented.

To achieve the best possible performance, the choice of the pole material is important as well. A high saturation magnetization must be chosen to achieve the highest magnetic flux density. The specifications of the chosen pole material are presented in section 3.4.

In section 3.5 different kinds of undulator types, with differing magnet arrangements, are compared, regarding their applicability to PWA beam lines and the choice is presented.

With the chosen material and undulator type, parametric scans over a range of undulator period lengths and gap sizes are performed to find the maximum on-axis magnetic flux density and the associated K parameter, by means of empiric formulas, which are introduced in section 3.6.1. This data is then used to estimate integrated photon flux and on-axis flux density for undulators, scanning over a range of undulator period lengths and gap sizes, shown in section 3.6.3. The

aim is to find the ideal setup with achieving high photon energies at high flux rates. After that, a comparison of three specific undulator period lengths with 5, 8 and 11 mm is presented in the section 3.6.4. These were selected to illustrate assets and drawbacks resulting from the choice of the undulator period length. Magnetic fields, resulting K parameters and photon performances are compared for a gap range between 1 and 6 mm. Also tuning curves are analyzed, representing the photon flux with respect to the photon energy. These are compared for the same set of period lengths and undulator gap sizes. Finally the photon performance of undulators with 5, 8 and 11 mm at 2 mm gap size is simulated for realistic PWA electron bunches, regarding observed emittance and energy spread for an optimized electron beam optic.

In section 3.6.4.4 the implications of diffraction to the undulator radiation are discussed. Even though the PWA electrons provide a low emittance [99] the generated light is partly affected by the diffraction limit, depending on the wavelength of the emitted radiation.

The performed parameter scans result in specific design parameters, presented in section 3.7. Based on these parameters, FEM simulations are performed to optimize the projected undulator design, now considering real geometric dimensions and shapes. These are presented in section 3.8.

For this purpose, the chosen materials and parameter settings were used to simulate a realistic, geometrically parametrized undulator model. This model then was optimized in terms of the effective undulator field and as a result the final geometry is presented in section 3.9, ready to be manufactured.

3.2 Design goals

The undulator technology itself is a well approved technology, built and used for decades at synchrotron light sources. These light sources are usually based on conventional electron accelerators. However, as described in the section above, these accelerators provide electrons, other than PWA beam lines, with electron energy spreads below 1‰ and a high temporal stability in mean energy and position. Thus, it is inevitably important to target the undulator design to the specific PWA electron beam characteristics.

The first adaption concerns the **undulator period length** λ_u. The PWA beam lines of our group are currently equipped with laser systems providing up to 300 TW power. With these lasers, electron energies up to 600 MeV on average (up to 800 MeV within single events) were achieved in the recent past [100]. As can be seen by the undulator resonance equation (2.40) the wavelength of the emitted radiation is directly proportional to the undulator period length λ_u. Thus an undulator design with a short period is desirable to reach short photon wavelengths, using these relatively low energy electrons.

Unfortunately, making the undulator period shorter implies that the on-axis magnetic flux density will decrease because the longitudinal size of the magnets shrinks inevitably and with it the source size of the magnetic flux. This decreases the undulator K parameter, see equation (2.39), in two different ways: First, directly by the shorter period length λ_u, and second indirectly by

the weakening of the on-axis magnetic flux density B. Thereby, both the on-axis photon flux density (2.51) and the integrated photon flux (2.55) decrease, especially for the higher harmonic portion of the spectrum.

Due to the fact that PWA electron beam lines, other than electron synchrotrons, are single pass machines, the decrease of the on-axis flux density can be partly compensated by reducing the **undulator gap** g (distance between undulator girders), decreasing thereby the loss of magnetic flux. In synchrotron smaller gaps cause problems. The repetitional influence of disturbances of the electron trajectory escalate and high energy losses due to wakefields are inevitable. However, this also reduces the aperture (free space) of the undulator where the electron beam can propagate and thus, the danger of demagnetization is increased. The possible impact of relativistic electrons and high energy photons into the permanent magnets would damage the undulator magnets. The electron bunch diameter together with the instabilities make a certain distance between the undulator girders indispensable and thus a minimum gap size.

The aim for a high magnetic field decreases the gap to a minimum. This implies that an important property of the PWA optimized undulator is its ability to resist against these damages, guaranteeing a reliable operation and a long lifetime within a highly radiative environment. The resistivity against these damages is given by several factors connected to the choice of the magnet material, possible material processing methods and treatments.

To sum the goals up, the undulator design aims for:

- A possibly short undulator period length, providing high photon energies.

- A possibly small undulator gap as it compensates the loss of magnetic flux density due to the short undulator period and assures thereby a sufficient photon yield.

- A strong resistivity against demagnetization due to irradiation by incident particles, especially for a small gap undulator design.

As a result, the choice of magnet material seems to be a key factor for all three design goals: energy, flux and resistivity. Thus, the aim of the following chapter is to find a suitable magnet material and with it an optimum undulator parameter set, which fulfills the demands of an insertion device dedicated for PWA beam lines and provides the best photon flux performance and sufficient demagnetization resistivity. After that we will look for the optimum period length and the specific geometry.

3.3   Choice of magnet material

Before the analysis of the parameter scan can be performed over the basic undulator design parameters (period length and gap size) and the resulting photon performance, one has to choose suitable materials for magnets and poles, which determine the coefficients of the used formulas. One has to emphasize that the choice of the magnet material is a key factor for the performance of

the whole photon beamline. There are mainly two characteristics of permanent magnet materials used for insertion devices, describing performance and suitability of the material.

First key property is the **remanence**. A magnetic material with a high remanent field increases the on-axis flux density of the undulator and with it the generated photon flux, especially at the higher harmonic part of the spectrum. This is particularly interesting for experimental applications with thick nanoscopic targets, due to the higher penetrating and resolving power.

Second key property is the **coercivity**. The coercivity is a measure for the resistivity of the magnet against demagnetization by external magnetic fields and irradiation.

It commonly applies for permanent magnet materials that a higher remanence implies a weaker coercivity. This is caused by a changed material mix. A higher content of dysprosium increases the coercivity but does not provide as much magnetic flux density as using neodymium (at room temperature). Therefore, typically coercivity and remanence are roughly inversely proportional for different rare earth magnet types sharing different ratios of neodymium and dysprosium.

As the coercivity is strongly related to the magnets resistivity against demagnetization, a reliable longterm operation of the insertion device at a PWA beam line can not be guaranteed if the coercivity is to low. Thus the material choice is a tradeoff between strong magnetic flux density and strong resistance against demagnetization. This lesson was learned from the first undulator built in our group, which was significantly demagnetized after only a few beam times, see section 3.3.6. The decision process which material has to be used for the undulator is therefore based on estimations about the demagnetization risks, carried out in the following.

3.3.1 Demagnetization risk assessment

The risk of demagnetization is difficult to be determined exactly. This is due to the fact that even the demagnetization process itself is still not well understood but rather continues to be focus of actual studies. Thus, the risk assessment can only be based on estimations concerning the expected beam loss determined by the stability of the newly built electron source, the frequency of usage of the undulator at the beam line and finally the potential resistance of the material itself. The approximation is therefor subdivided into the following steps:

- Approximation of beam loss due to daily operation,

- Approximation of dose due to beam loss,

- Approximation of demagnetization due to annual dose,

and a detailed description of the approximations is given in the following subsections of this chapter.

3.3.1.1 Approximation of beam loss due to daily operation at a PWA beam line

In order to approximate the irradiation dose causing demagnetization several approaches can be done. A theoretical approach would estimate the pointing and tilts of the incident electron beam generated by the PWA beam line. This depends on many specific details of the experimental setup and will hardly meet reality in particular as the beam line specifications for the group's new electron beamline in Hamburg (at DESY) are up to the time this thesis was written, not evident. Nevertheless, to present at least the method a theoretical approximation calculated by the equations of motion inside the undulator is given in appendix A. In the following we proceed with an empirical approach based on beam characteristics measured during a experimental campaign in 2012.

The setup of a beam time made by our group at MPQ described in the paper of R. Weingartner et al. [99, 101] has shown a measured electron spot size of about 940 µm FWHM averaged over 47 consecutive shots. This was achieved although the electron bunch had a large energy distribution (from 260 MeV peak energy to below 150 MeV in the low energy tail) which broadens the focus of the quadrupole lenses due to their chromaticity. After conversion to the standard deviation $\sigma_{x,z}$ and the deconvolution of the resolution of detector and optical system (approximately $\sigma_{\mathrm{det}} = 160$ µm due to the graininess of the phosphor screen plus the resolution of the optical imaging system observing the beam size screen), the accumulated spot size turned out to be approximately $\sigma_{x,z} = 367$ µm. Thus, a beam channel of $\pm 3.4\sigma_{x,z} = 2500$ µm should contain 99.9% of the electrons and a gap size of 2.5 mm should feasible. Aspiring a high undulator peak field also smaller undulator gap sizes are desired. At a gap size of 1600 µm about $\pm 2.18\sigma_{x,z}$ of the beam would pass the (perfectly aligned) undulator dumping 3% of the bunch charge into the insertion device. These values will serve as basis for the following approximation of the annual beam loss presented in table 3.1.

Electron dumping estimation

Operation time	$52\mathrm{w} \times 5\mathrm{d} \times 10\mathrm{h} \times 60\mathrm{min} \times 60\mathrm{sec} = 9.36 \times 10^6$ sec
Repetition rate	$5/\mathrm{sec} \Rightarrow 4.68 \times 10^7$ shots
Bunch charge	50 pC, assuming 3% dumped in the undulator
Absorbed charge	$1.5\mathrm{pC} \times 4.68 \times 10^7$ shots $= 7 \times 10^7$ pC or
# of electrons	4.4×10^{14} electrons

TABLE 3.1: Estimation of possible beam losses at an PWA electron beam line.

Thus, if we assume a 3% loss of the electrons per shot at maximum, which would take place if the electron beam stability would be as measured during the described beam time and the small gap size would be chosen, 4.4×10^{14} electrons would hit the undulator during one year of operation. On account of these numbers an accumulated dose and corresponding neutron fluence as well as the star density (neutron generation due to photon-atom interactions, see 3.3.1.2), all three crucial measures for the demagnetization of permanent magnets, can be approximated based on simulations presented in the next section.

3.3.1.2 Approximation of electron dose, neutron flux and star events

For the discussion in this section the code *FLUKA* [53, 54] was used to perform Monte Carlo simulations of the resulting impact of the electron bunch to the undulator magnet material. These dose calculations were performed by F. S. Englbrecht and are used to enhance the comparability of the projected PWA scenario design to several studies described in table 3.2. This was necessary since the electron energies of the studies and the PWA scenario are differing significantly. All experiments/simulations featured an electron beam hitting an undulator magnet array from the face of the front side.

As described in chapter 2.1.2 the demagnetization is caused by the energy deposition of an incident electron bunch, which generates a shower of bremsstrahlung particles. The shower's main constituents are electrons, gamma rays and photo-neutrons. The effects of each type of particle were analyzed by several studies. It can be summarized by the following list of facts:

- Main contributor to demagnetization are electrons shown by quantified correlations and measured by several studies, e.g. at ESRF for magnets with a coercivity H_{cJ} of 1800 kA/m. It was stated that there exists an energy threshold of 50 MeV [102], below that no demagnetization was measured.

- The dose induced by photons is irrelevant in our use case, because of a penetration depth of about 1 μm due to a high attenuation coefficient value which results from photoelectric interactions beeing highly probable at this energy. See e.g. Okuda [103].

- Dose by neutrons above a specific energy threshold is significant on demagnetization. Therefore the 1 MeV neutron equivalent fluence, which reflects the non-ionizing energy losses in the bulk of electronic components [43, 104] is simulated by some studies. Also the star density [105] with a threshold of 100 MeV generated by photo-neutrons is relevant [47].

Hence, in this work the focus is concentrated on electron dose, neutron flux and star density as crucial parameters. In the following, the simulation of the dose induced into the magnets along the undulator array is presented, averaged over the first sequential magnets. The resulting mean dose per magnet is shown in figure 3.1. Additionally, the star density measured in events per cm^3 averaged over a single magnet (see figure 3.3) and the so called 1 MeV equivalent neutron flux $D_{\mathrm{eq,1MeV}}$ measured in events per cm^2 is shown in figure 3.2 respectively. With this a comparison to other studies measuring the demagnetization at different electron energies is possible, following in the next section.

3.3.1.3 Demagnetization approximation due to radiation dose and energy

According to Temnykh et. al. [45] an approximation of the relative demagnetization of the magnets can be made by the following formula, independently from the distribution of the incident dose:

$$\frac{\mathrm{d}B}{B} = -\frac{D}{D^\star} \times 10^{-T_{\max}/\bar{T}} , \tag{3.1}$$

with D the average dose per magnet, $T_{\max}$ the demagnetization temperature depending on the used magnets and their working point (permeance coefficient) on the demagnetization curve and $D^\star = 0.25 \pm 0.14$ MRad (corresponds to $D^\star = 2.5 \pm 1.4$ kGy) and $\bar{T} = 41.4 \pm 4$ °C two fit parameters. In our case $T_{\max}$ is 180 °C which is the demagnetization temperature regarding permeance coefficient and working point, post hoc determined for the actual undulator design in the last section of this chapter, see 3.8.3.

As mentioned above Temnykh stated the fact that the distribution of the dose had no significant influence on the demagnetization. This may seem not reasonable for extreme cases, e.g. when only a microscopic fraction of a magnet is irradiated. However, Temnykh's data was measured for an array of magnets and the observed correlation was the same for all of these magnets in the array, independently of their position in the stack. The fact that the magnets at the end of the array, which should have experienced a scattered, flared beam, show the same losses in magnetization as those in the front, support his thesis. On the other hand it must be taken into account that he measured the resulting dose by a rather inaccurate method. He only observed the temperature increase of the samples after irradiation, implying that the raise in temperature is effected only by the irradiation. In fact, thermal conduction could have lead to a balanced temperature distribution and it seems that his results have to be considered with caution.

Qiu et.al. [43] used two different scattering targets, one made from copper, the other from tantalum, to widen the incident electron beam before hitting the magnets. And by comparing these experiments with targets another effect became apparent which plays a major role for demagnetization of irradiated magnets - the neutron fluence. Qiu normalized the neutron flux by calculating the so-called 1 MeV equivalent neutron fluence, which is often used in the analysis of irradiation damages of electronics. It is defined by:
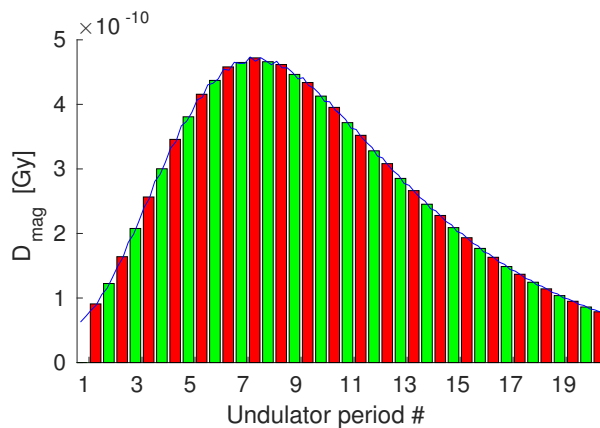
FIGURE 3.1: Mean irradiation dose D_{mag} per magnet. The dose per pole is not shown (but lower) and without relevance for demagnetization processes.

$$\Phi_{\mathrm{eq,1MeV}} = \frac{\int_0^\infty \Phi(E)\kappa(E)\mathrm{d}E}{D_{\mathrm{eq,1MeV}}} \,, \tag{3.2}$$

where $\Phi(E)$ is the neutron energy spectrum and $\kappa(E)$ is the neutron displacement kerma factor for Si. kerma is an abbreviation for 'kinetic energy released per unit mass' and $\kappa(E)$ is given here in units of MeV mb. Two different targets resulted in two differing fit formulas, one for each target material:

$$\left.\frac{\mathrm{d}B}{B}\right|_{\mathrm{Cu}} = \left(a_{\mathrm{Cu}}\ln(10^{12} \times D) + b_{\mathrm{Cu}}\Phi_{\mathrm{eq,1MeV}}\right)N_{\mathrm{e}} \,, \tag{3.3}$$

$$\left.\frac{\mathrm{d}B}{B}\right|_{\mathrm{Ta}} = \left(a_{\mathrm{Ta}}D + b_{\mathrm{Ta}}\Phi_{\mathrm{eq,1MeV}}\right)N_{\mathrm{e}} \,. \tag{3.4}$$

with N_e the of number of impact electrons. For the copper target $a_{\mathrm{Cu}} = 4.94 \times 10^{-17}$ and $b_{\mathrm{Cu}} = 2.21 \times 10^{-14}$ were found, with the dose per electron D given in Gy and the 1 MeV equivalent neutron fluence $\Phi_{\mathrm{eq,1MeV}}$ given in neutron per cm^2 and electron. For the tantalum target $a_{\mathrm{Ta}} = 2.07 \times 10^{-7}$ and $b_{\mathrm{Ta}} = 9.42 \times 10^{-16}$ were found. The differing fit parameters a and b suggest that different demagnetization processes were occurring. The two target materials produce specific bremsstrahlung spectra. In case of the copper target the spectra show more electron flux and less neutron flux at matching energies. The simulation of the Cu target showed an electromagnetic dose D induced in the magnet, contributed by one primary electron, of 6.5×10^{-10} Gy. In the Ta target case, the electromagnetic dose D in the magnet contributed by one primary electron was only 2.4×10^{-10} Gy.

Comparing these results to our case a dose D of 4.7×10^{-10} Gy per primary electron was simulated at maximum, which lies in between the two cases of the paper of Qiu. This maximum flux rate was reached at the 7th undulator period. The value of the electron dose and the 1 MeV equivalent neutron flux rate determined by our simulation were used to calculate the possible demagnetization in figure 3.4, were all described estimations are illustrated and compared. The
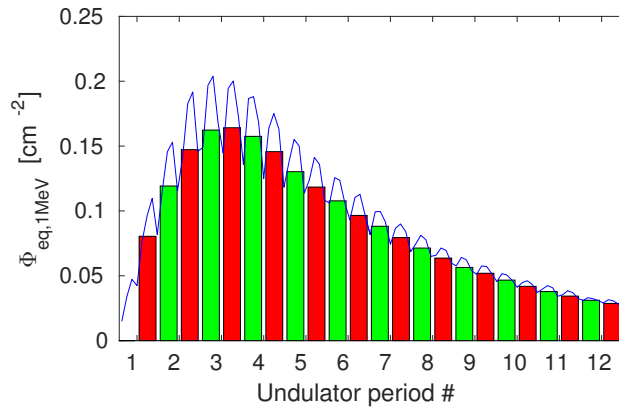
FIGURE 3.2: Mean 1 MeV equivalent neutron flux $\Phi_{\mathrm{eq,1MeV}}$. The blue line shows the actual, non averaged values. One can see that the neutron flux is lower within the pole material.

green area is span using both fit formulas as limits and overlaps the red area span by Temnykh's formula. One would expect the demagnetization in our case to be in between both near the centerline of the area since the simulated dose value and flux density lies in between both target cases.

Another estimation is given by Bizen [42]. He analyzes the contribution of the electron beam energy to the demagnetization. His experiment shows a proportionality between electron number (and thus dose), electron energy and demagnetization described by the following formula:

$$\frac{\mathrm{d}B}{B} = \left(-a + be^{-cE_\mathrm{e}}\right) N_\mathrm{e} \text{ with}$$
$$a = 2.8 \times 10^{-15}, \, b = 5.2 \times 10^{-15} \text{ and } c = 3.66 \times 10^{-1} \tag{3.5}$$

with N_e the electron number and E_e the electron beam energy in GeV. The lowest energy Bizen used was 2 GeV, which is almost three times the expected PWA electron beam energy. At these high energies core reactions of photo-neutrons and the magnetic material so-called stars become more likely, which are crucially effective in the demagnetization process. Thus, this formula should overestimate the expected demagnetization for our scenario, as the expected energies are only a third of those analyzed by Bizen.

However, also for the PWA scenario multi-GeV energies seem achievable as shown by Leemans [98] and they could be standard for the daily work at PWAs in the future. Therefore, this formula describes an electron energy scenario which is not attained yet but could be reached soon and is taken here as a kind of future case scenario. Another study focuses on the star events, described in the next section.

3.3.1.4 Demagnetization approximation due to star events

There are also efforts made, to link demagnetization to so-called star events, see e.g. [47, 106]. Stars are defined as events, in which photo-neutrons are generated from interactions of high energy photons from the shower of Bremsstrahlung particles. Since these events mark mutations of the atomic structure, the resulting damages of the material are irreversible and the magnetic flux density can not be fully recovered by newly magnetizing the damaged magnets. From the *FLUKA* simulation it is possible to count the number of star events for each magnet, see figure 3.3.

However, the events are rare at the assumed PWA electron beam energies of 725 MeV. For the simulated undulator, magnets with dimensions comparable to the planned undulator were used having a volume of 0.67 cm^3. With a density of 7.4 g/cm^3 each magnet has a weight of about 5 g. Thereby one can approximate the number of atoms in the magnet. With the molar weight of 1081.19 g/mol (for $Nd_2Fe_{14}B$) one gets about 2.76×10^{21} atoms in one magnet, in order to estimate the percentage of modified atoms in the magnet.
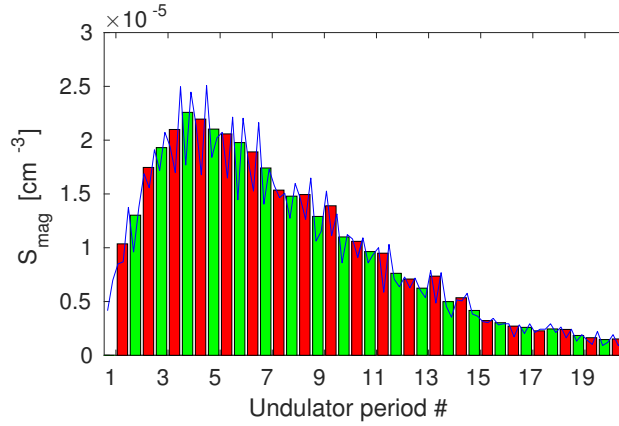
FIGURE 3.3: Mean star density per magnet S_{mag}. The blue line shows the actual, non averaged values.

In figure 3.3 the mean star density is shown. The maximum star density is reached in the 7th magnet with a value of about 2.2×10^{-5} events per cm^{-3} per electron. Thus 1.5×10^{-5} events per electron take place in the 7th magnet. After one year of operation, dumping approximately 4.4×10^{14} (assuming the 1.6 mm gap case) electrons into the magnet, only 6.6×10^9 atoms would be modified by star events.

Thus, even if every atom is hit only once, and no double star events occur, one of 2.4×10^{12} atoms would be affected at maximum. Therefor, this effect seems negligible at low energies. However, in the near future the energy of Plasma-Wakefield Accelerators could exceed several GeV as a matter of routine and for the sake of completeness the demagnetization effect due to star events is described quantitatively in the following paragraphs.

In 2011 Asano et al. [106] found a correlation between the star density and demagnetization, which is modeled by the following formula:

$$\frac{\mathrm{d}B}{B} = 1.9 \times 10^{-11} \, S_{\mathrm{mag}} \, N_{\mathrm{e}} \, , \qquad (3.6)$$

where S_{mag} is the averaged star density with an energy threshold of 100 MeV and N_{e} is the accumulated number of electrons. This approximation is shown and compared to the previously introduced approximations by figure 3.4.

3.3.2 Demagnetization risk assessment

Despite all scientific efforts made so far, the demagnetization processes of permanent magnets are not fully (quantitatively) understood and exact predictions about the expected demagnetization are not possible. It only can be stated that most of the studies agree in the facts that the degree of demagnetization depends on some material and some environment dependent factors, as well as on type, energy and intensity of the radiation the magnets are exposed to. A review on the key points of interest is given by Bizen [47] and is summarized in the following list:

1. **Magnet material**

   - Micro structure, degree of fineness and manufacturing methods
   - Coercivity H_c of the material composition
   - Curie temperature T_c of the material composition

2. **Magnet shape**

   - Permeance coefficient (working point on BH curve)
   - Shape (especially inflection point and edge steepness) of the BH curve

3. **Operation temperature** (concerning beam based heat deposition)

4. **External magnetic fields**

5. **Radiation**

   - Type (determines interaction)
   - Energy (determines cross section of interactions) and resulting dose
   - Star density (determines irreversible damages due to core reactions)

Numbers 1-4 are related to the magnets coercivity or as the case may be to the operation point on the demagnetization curve, which is described by the permeance coefficient, related to the coercivity. The operation point is defined by the *H* field within the magnet, which depends again on the magnets geometry. All of these factors have to be considered in the design process of the insertion device, but since their influence is only qualitatively approved, the decision was made to compare the PWA undulator scenario to all demagnetization studies made in the recent years, which provide a demagnetization approximation formula. This risk assessment and analysis is thereby based on comparison to all these experiments in a meta study.

In table 3.2 the main parameters of the experiments introduced in section 3.3.1.3 are summed up except for the study presented in section 3.3.1.4, since the corresponding paper provides no other information than that the magnets were made from material of the Neomax company for an undulator with 18 mm period length used at the *SACLA* FEL. The other studies instead are compared to the actual design case, shown in the right column.

At a first glance it seems strange that the magnets with the lowest coercivity (used by Temnykh - red line in figure 3.4) show the smallest demagnetization. This immediately suggests itself that the distribution of the irradiation, the size and divergence of the electron beam should, other than claimed by Temnykh, play a more than subordinate role. This fact makes the applicability of the study to our case questionable. Considering the study of Asano (black line in the figure) only poor information is given. Moreover, the key parameter used by him as figure of merit, the star density, seems to be small for PWA electron energies and thus not as significant as the electromagnetic dose.

Especially low energy electrons seem to be the main contributers to the dose and thereby to the evolving damage. This suggests to use the approximations of Bizen and Qiu for the estimation.

Parameter	Bizen [40, 42]	Qiu [43]	Temnykh [45]		Design case (FLUKA sim.)
E_e [GeV]	2-8	2.5	5		0.725
N_e	1.4×10^{15}	1.4×10^{16}	5×10^{14}		6×10^{14}
D_{mag} [MGy]	unknown	2.8	6.4		0.3
Company	Neomax Materials		Stanford Magnets		Vacuumschmelze
Type	NEOMAX-35EH		N40	N40SH	VACODYM890TP
B_r [T]	1.17	1.17	1.27	1.26	1.19
H_{cJ} [kA/m]	1989*	1989	955	1592	2625
$x \times y \times z$ [mm]	$46 \times 8 \times 12$	$46 \times 8 \times 12$	$46 \times 8 \times 12$		$23 \times 1.7 \times 15.6$
$P_c = B_d/\mu_0 H_d$	0.8†	0.8†	0.6		0.12*
$\|\Delta B/B\|_{max}$ [%]	3.5	2.5	15	2.5	2.5

* thermally stabilized at 140 °C for 24 h † analytic calculation [107]   * see section 3.8.3

TABLE 3.2: A comparison of several studies with the actual design case is shown. First characteristics of the incident electron beam like electron energy E_e, electron number N_e, and resulting dose on the magnet D_{mag} are compared. Then properties of the used magnets (remanence B_r, company and type, coercivity H_{cJ}, geometry and permeance coefficient P_c are summed up. The resulting relative demagnetization $\Delta B/B$ range from 2.5% up to 15% for a magnet material with low coercivity. The last column shows simulation results for the PWA undulator design case. The dose calculations were performed by FS Englbrecht using the Monte Carlo code FLUKA [53, 54]. The magnet properties anticipate the outcome of the analysis of the following sections, as well as the permeance coefficient P_c, which was calculated afterwards from results of the optimization simulations in section 3.8. As a result a possible demagnetization of about 2.5 % is estimated for one year of operation for the design case, using Qiu's model as worst case scenario.

Assuming the same incident electron numbers (4.4×10^{14}) as in table 3.1 and the design case in table 3.2, and assuming a density of the magnet material of 7.4 g/cm^3, one gets a maximum dose per magnet of about 0.25 MGy. From the comparison to both the experiments it follows an expected demagnetization of up to 2% for magnets with a coercivity of $H_{cJ} = 1989$ kA/m (providing a remanence of $B_r = 1.17$ T), as used by both groups. This value may be tolerable if the possibility to exchange single magnets of the undulator in case of demagnetization can be guaranteed by the undulator design. It would demand for a service interval of about one year of constant use. In favor of the demagnetization resistivity the choice of a higher remanence B_r of the magnets was renounced, even if achieving higher fields would result in a higher photon output (see chapter 2.2.5.5). This is because a higher remanence would also imply a smaller coercivity H_{cJ} and in that case the demagnetization would be increased. Thus a coercivity of **2000 kA/m is defined as lower limit** for the choice of the magnet material.

Since we do not have the possibility to verify the demagnetization for the estimated dose experimentally on real magnet samples, we have to rely on these rough estimations, not considering geometry, working point and opposing fields of the magnet array. The assumption of loosing 3% of the electrons per shot clipping at the undulator magnets in case of the smaller gap size of 1.6 mm, motivated in appendix A, is a hypothetic scenario unless the obtained electron beam stability could be measured exactly.
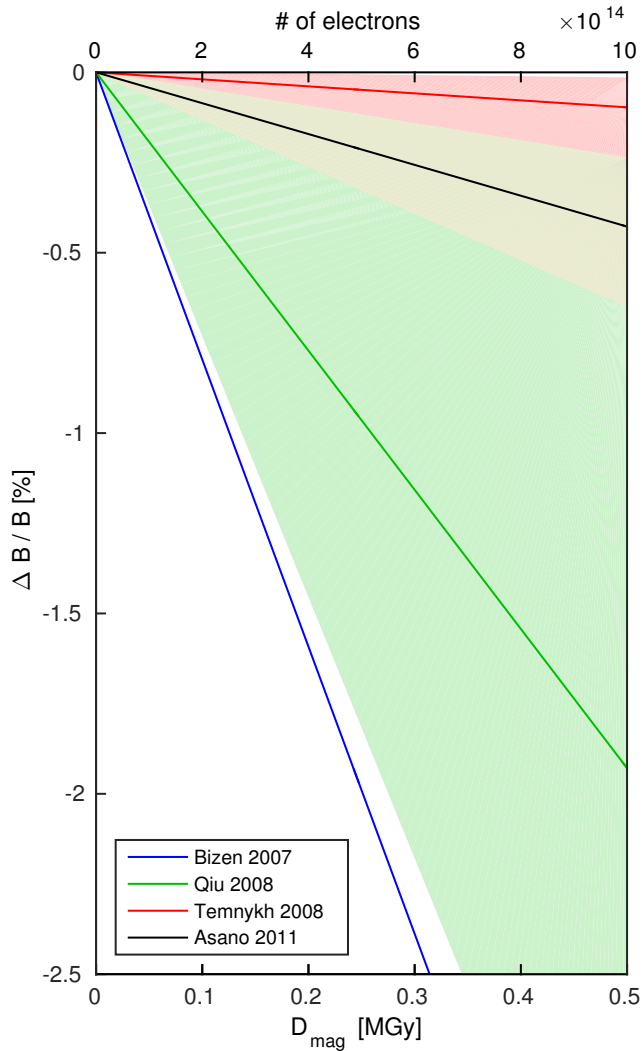
FIGURE 3.4: Empiric studies for the estimation of undulator magnet demagnetization. Models are based on empiric fit formulas of Bizen [42], Qiu [43], Temnykh [45] and Asano [106]. More details to the experimental setups is given in table 3.2. The beige area marks the overlap between Temnykh's and Qiu's formula, for Asano's and Bizen's models no error range is given.

3.3.3 Final choice of the permanent magnet material

The choice of the magnet material was intended to provide at least a coercivity of 2000 kA/m, set as a lower limit in the last section. The choice of VACODYM 890 TP from *Vacuumschmelze* provides an even higher coercivity (30% higher than the lower limit) and thereby a sufficient resistivity against demagnetization providing a remanence of 1.19 T. This emphasis on the resistivity was strongly recommended due to the fact that both of the group's electron sources are currently under development and their stability is not tested yet. Therefore also additional countermeasures against demagnetization were taken, discussed in the next section.

3.3.4 Methods to further increase the demagnetization resistance

The most commonly recommended methods to increase the resistivity against demagnetization of the magnet material are given in the following list, based on several studies performed in the recent years [40–42, 44–47, 56, 63–66, 108] which come in most aspects to the same conclusions:

- Application of stabilization methods to the magnets, e.g. artificial aging using thermal heat or opposing magnetic fields.

- Grain Boundary Diffusion (GBD) using Heavy Rare Earth elements e.g. Terbium (Tb) to increase the coercivity at the domain walls, without loosing magnetic flux density. This method is especially suited for flat magnets as the diffusion process is limited to material near the surface.

- Selecting magnets with high temperature stability (additionally to the high coercivity H_{cJ}).

- Designing a magnetic circuit with an operation point far away from the knee (higher permeance coefficient) see section 2.1.1.1.

- Reducing the operation temperature of the undulator magnets by cryogenic cooling.

Figure 3.5 shows the increase of the coercivity and thus of the resistance (figure 3.6) of irradiated magnets at low temperatures [42]. This follows from the increase of the coercivity with a decreasing temperature as shown by Hara [108] for instance. This cryogenic undulator technology was tested by a prototype undulator described in detail in chapter 5. Major drawbacks of this technology are the expensive cooling equipment and the more complex and time consuming operation as the undulator has to be cooled down for several hours before the experiments can start together with the fact that it is highly questionable if the advantage of a higher coercivity at low temperatures is useful in the impact scenario, where an incident electron beam increases locally the temperature at the impact region drastically.
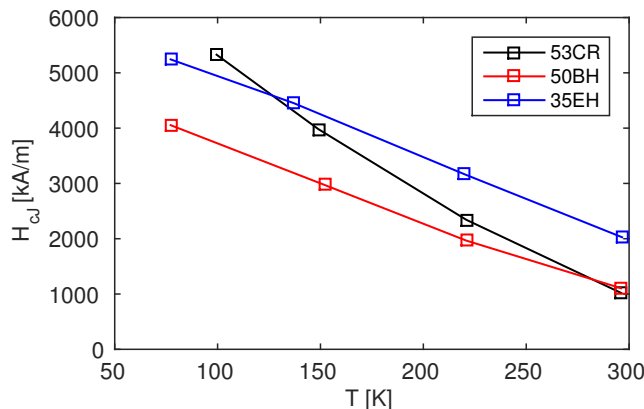
FIGURE 3.5: The effect of the temperature to the coercivity of a selection of typical rare earth magnet materials. The data is based on a review paper of Bizen [47]. All types of magnets show increasing coercivity H_{cJ} values, with a similar gradient. The increased coercivity leads to a higher demagnetization resistivity, shown in figure 3.6.
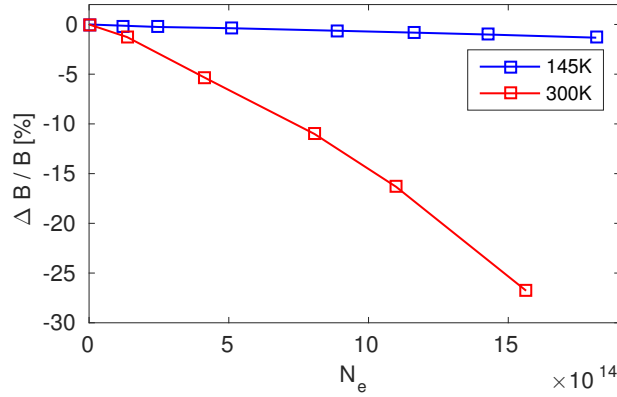
FIGURE 3.6: Demagnetization due to electron irradiation. The data shows measurements of the remaining magnetization after electron exposure for two temperatures, 145 K and 300 K. Data is taken from a review paper of Bizen [47].

Another way to increase the coercivity of a rare earth magnet ($Nd_2Fe_{14}B$) can be achieved by the substitution of heavy rare earth (HRE) elements, e.g. dysprosium (Dy) or terbium (Tb) for neodymium (Nd) in the magnets crystal structure. The HRE accumulates mainly near grain boundaries, thus increasing the coercivity without a significant loss of remanence, if the so-called GBD process is applied [63–66]. The increase depending on the distance from the magnets surface is shown in figure 3.7.

Almost all of the described countermeasures were taken into account. First, the choice of a material with strong coercivity and a high maximum application temperature ($T_{max} = 220°C$ at B/μ_{0H}). Second, an additional GBD with Tb (terbium), which is especially effective for thin magnets as used in our case, since the diffusion rate decreases with the distance to the magnets surface, as metioned before and shown in figure 3.7. Third, an artificial aging process, achieved by heating the magnets to a well controlled temperature (418 K in our case). At this
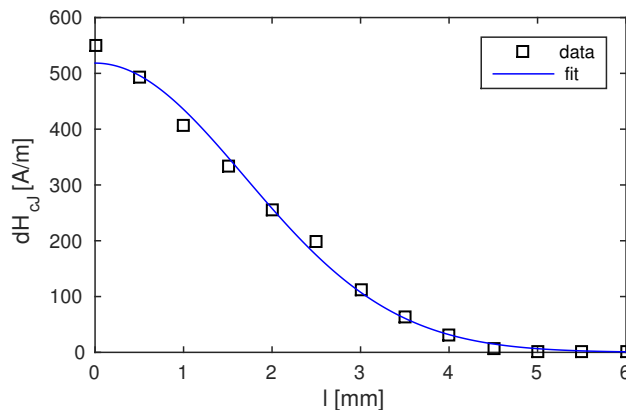
FIGURE 3.7: The figure shows the increase of coercivity due to the grain boundary diffusion process. This process increases the concentration of heavy rare earth (HRE) atoms in the crystal lattice (Terbium in this case) especially at the grain boundaries of the magnets material, where the anisotropy energy is lowest and thereby an overturning of spins is easiest. The concentration of the diffused HRE depends among others on the distance to the magnets surface. The data was provided by *Vacuumschmelze* and fit by a exponential function due to Fick's second law, which can be found e.g. in [109].

temperature a slight decrease of the anisotropy energy is reached and magnetic domains with the highest probability to demagnetize, relax in the magnets self induced counter-field. Thereby two advantages can be achieved at once, one is that the deviations in magnetization of the undulator magnets are smaller within the magnets stack and thus a better field homogeneity is reached, but the main reason in our case is again that the resistivity against demagnetization is increased.

3.3.5 Additional countermeasures for use cases with higher risk of demagnetization

If the stability measurement of the new PWA source reveals, contrary to expectations, an even higher demagnetization risk, an additional countermeasure would be the use of a collimator in front of the undulator to minimize the dose. Another suggestion could be the use of two part magnets using a highly coercive material at the inside edges pointing towards the undulator gap and a highly remanent magnet material for the rest of the magnet, to increase the magnetic flux density to the poles. For future designs, one can also think about 'over saturating' the poles, shifting the optimal ratio between longitudinal magnet and pole length towards thicker magnets. Thus the undulator peak field would be decreased, but a partly demagnetization of a magnet would be compensated intrinsically, as long as still a superabundant field flux is provided by the undamaged part of the magnet, still driving the magnetic flux density inside the pole to saturation.

3.3.6 Comparison of the new permanent magnet material to the material used for the 5 mm BEAST undulator

The group's previous undulator [34] was built with VACODYM 764 TP magnets. These have a higher remanence (1.37 T compared to 1.19 T of VACODYM 890 TP) but a lower coercivity i.e. 1275 kA/m (16 kOe) compared to 2625 kA/m (33 kOe). A comparison of the specific data is shown in detail in tab. 3.3. The GBD treatment, described in section 3.3.4, increases the coercivity further by approximately 6.3 kOe (or 500 kA/m). In the end an absolute coercivity of about 3125 kA/m can be expected for the undulator magnets. The artificial aging process slightly lowers the remanence, about 1% at maximum are expected. These corrections are not

Specifications	B_r [T]	H_{cJ} [kA/m]	$(BH)_{max}$ [kJ/m³]	T_C [°C]	T_{max} [°C]	$\partial B/\partial T$ [%/K]	$\partial H_{cJ}/\partial T$ [%/K]
VACODYM 890 TP	1.19	2625	270	310-370	220	-0.090	-0.500
VACODYM 764 TP	1.37	1275	360	310-370	100	-0.115	-0.700

TABLE 3.3: Specifications of the magnet materials VACODYM 890 TP and VACODYM 764 TP from *Vacuumschmelze*. Listed are, in order from left to right, remanence, coercivity, maximum energy product, Curie temperature, temperature coefficient of the remanence and temperature coefficient of the coercivity, both given at room temperature [110]. The coercivity is further enhanced by GBD and thus increased by approximately 500 kA/m, the remanence instead, is potentially decreased by about 1% due to an additional stabilization process (artificial aging) further described in the text above.

covered by the table since the exact consequences are unknown and the measurements of such high coercivities are not possible according to *Vacuumschmelze*.

As can be seen, the chosen material *VACODYM 890 TP* has a smaller energy product ($BH_{\max}$) and a reduced remanence. However, the new material shows a significant improvement in every demagnetization stability relevant factor. Thus a prolonged life time can be expected and an extensive use as radiation source should be possible.

3.4 Choice of the pole material

The pole material should have the highest possible saturation magnetization to enable the highest possible magnetic on-axis flux density. Recent studies revealed that holmium and monocrystalline dysprosium show flux densities up to 3.5 T [111]. The major drawback of these materials is not only the costs, but also that these high saturation values can only be reached at cryogenic temperatures. Since the planned undulator should operate at room temperature, an iron alloy is chosen. At room temperature alloys of cobalt and iron at the ratio of 50 to 50 or 49 to 51 show the highest saturation values. With these alloys called *permendur* (or *vanadium permendur* if a small ratio of vanadium is added for better workability) a saturation magnetic flux density of up to 2.35 T can be reached. The specifications of two typical materials with slightly differing composition ratios are compared in table 3.4.

In our case VACOFLUX 50 from *Vacuumschmelze* was chosen. Even though there is a slightly higher magnetization of VACOFLUX 48. This is due to the fact that the small advantage in field flux almost vanishes at saturation, and would be on the price of significantly worse mechanical properties, which makes manufacturing especially of small structures like ours, complicated.

For the optimization simulations in section 3.8 the BH-curve shown in figure 3.8 was used. For this purpose the original data, shown as blue squares, was smoothed and interpolated (black line).

Specifications	H [A/m]	300	800	1600	4000	8000	16000
VACOFLUX 48	B [T]	2.05	2.15	2.25	2.27	2.3	
VACOFLUX 50		1.9	2.1	2.2	2.25	2.27	2.35

* typical, static values for 0.35 mm stamped samples

TABLE 3.4: Comparison of the specifications of the pole materials VACOFLUX 48 and 50 from *Vacuumschmelze*. Listed is the magnetic flux density B with respect to the external magnetic field H given in A/m. [112].
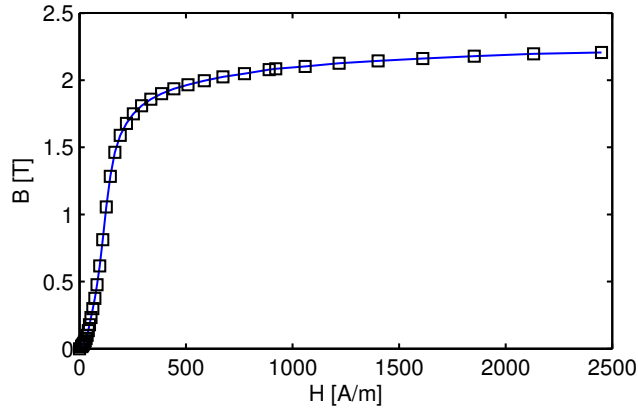
FIGURE 3.8: The figure shows the magnetic flux density B of the used pole material (VA-COFLUX 50) with respect to an external magnetic field strength H. The data is taken from *Vacuumschmelze* and is listed in the appendix C in table C.2.

3.5 Choice of undulator configuration

Mainly two undulator design types are commonly used at synchrotron radiation facilities. The first is the planar undulator, the second is the ellipsoidal undulator. Whereas the planar undulator has a magnetic field which only alternates in one transverse direction, the field of the ellipsoidal undulator alternates along both transverse axis. Sinusoidal horizontal and vertical magnetic field components with the same period length force the electrons on a winding trajectory emitting light with arbitrary elliptical polarized light. The most simple case is the helical undulator where both field components have the same amplitude and a phase difference of $\pi/2$. Comparing the angle integrated flux of a planar undulator $\Phi_{1,P}\left(\omega_1'\right) = \pi\alpha N_u \frac{I}{e} Q_1(K)$, eq. (2.55), to the flux of an helical undulator [68] one gets

$$\Phi_{1,H}(\omega_1') = \pi\alpha N_u \frac{I}{e} \frac{2K^2}{(1+K^2)} \tag{3.7}$$

$$\frac{\Phi_{1,P}}{\Phi_{1,H}} = \frac{1}{2}\left[J_1\frac{K^2}{(4+2K^2)} - J_0\frac{K^2}{(4+2K^2)}\right]^2. \tag{3.8}$$

The ratio ranges from 0.5 for small K parameters to 0.24 for large K parameters. Overall, the helical undulator produces more flux than the planar undulator if the undulators are compared at the same K parameter. This is because the planar undulator spreads its flux over many harmonics on-axis while a helical undulator emits only at the fundamental on-axis. One has to consider too, that the gap size of a helical undulator is larger in general which implies smaller peak fields and thereby smaller K parameters.

Since higher photon energies extend the range of applicability of the undulator radiation the decision was to build a planar undulator intending to use higher harmonics in the undulator spectrum, which favors the hybrid design due to its higher K parameters.

For future PWA sources, delivering higher electron energies with a good controllability in terms of absolute energy, electron trajectory, divergence and stability, the helical design seems to be

a very attractive alternative. If the generated photon energies become sufficiently high to allow the use of only the first harmonic, the use of the first harmonic would allow simple beam optics and detector design.

3.6 Parameter scan over undulator period lengths and possible gap sizes

Based on empiric formulas parameter scans presented in the next sections were performed, to prune the parameter space of the final FEM simulation model of the undulator. The varied parameters are the undulator main parameters: gap size g and period length λ_u leading to general predictions on field flux densities and following from that finally to photon emission performance.

3.6.1 Empiric formula for undulator on-axis fields

Theoretical considerations lead Halbach in 1983 to formulas [113] with which the on-axis flux density of pure permanent magnet undulators could be calculated. Inspired by that, the following empiric formula was proposed by P. Elleaume [114] who extended Halbachs formula to other undulator designs and materials. This gives an approximation of the magnetic on-axis peak field flux of planar undulators:

$$\hat{B} = a \exp\left[\left(-b + c\frac{g}{\lambda_\mathrm{u}}\right)\frac{g}{\lambda_\mathrm{u}}\right]. \tag{3.9}$$

Here g is the undulator gap size, λ_u the period length and a, b, c are empirically determined coefficients.

Although only planar undulator types are described by this formula, providing a vertical magnetic field in the first order and generating thereby linearly polarized photons, several different coefficients can be found in the literature [113–117] for the planar undulator design. These coefficients strongly depend on the remanent field strength of the used magnets, their volumes and their geometry and also on the fact if and when yes, which kind of pole material is used. The choice of permanent magnet materials has grown over the years from samarium–cobalt (SmCo) magnets, used in the beginning, to further advanced materials based on Dy, Nd and Pr. SmCo magnets provide a high Curie temperature up to 800 °C and a strong resistance against demagnetization by irradiation with ionizing radiation, but they are costly and their remanent field is weaker by 20% to 80% compared to state of the art rare earth materials. Those Dy, Nd and Pr based magnets have a Curie temperature of up to 370 °C, are less costly and provide remanent fields up to 1.6 T.

Whereas the formulas of K. Halbach were calculated for undulators based on SmCo magnets, all other model parameter shown table 3.5 are derived for NdFeB magnets, which provide a higher

Type	Material	B_r [T]	a	b	c	Range of validity
K. Halbach [113]						
PPM	SmCo	0.9	1.723	π	0	$0.07 < g/\lambda_u < 0.7$
Hybrid	SmCo/Fe	0.9	3.33	.547	1.8	$0.07 < g/\lambda_u < 0.7$
APS design report [115]						
Hybrid	NdFeB/CoFe	1.1	3.44	5.08	1.54	$0.07 < g/\lambda_u < 0.7$
P. Elleaume [114]						
PPM	NdFeB	1.2	2.076	3.24	0	$0.1 < g/\lambda_u < 1$
Hybrid	NdFeB/Fe	1.2	3.381	4.730	1.198	$0.1 < g/\lambda_u < 1$
Hybrid	NdFeB/CoFe	1.2	3.694	5.068	1.520	$0.1 < g/\lambda_u < 1$
DIAMOND design report [116]						
Hybrid	NdFeB/CoFe	1.3	4.3	6.45	1	$0.04 < g/\lambda_u < 0.2$
DUV-FEL design report [117]						
Hybrid	NdFeB/CoFe	B_r	$0.52\,B_r$ $+2.69$	$-1.95\,B_r$ $+7.23$	$-1.3\,B_r$ $+2.97$	$0.07 < g/\lambda_u < 0.7$

TABLE 3.5: Coefficients for equation (3.9) empirically determined for pure permanent magnet undulator designs as well as for hybrid designs with iron or iron cobalt poles. Magnet materials with remanent fields from 0.9 T up to 1.3 T are described as well as one set of coefficients which can be adapted to the actual remanent field strength of the magnet material.

remanence compared to SmCo. The highest on-axis fields are achieved with the hybrid design using iron cobalt (CoFe) or vanadium permendur (2V) as pole material. The latter is a special iron cobalt alloy with a small amount of vanadium which improves the mechanical properties of the material, making it less brittle. Typical saturation magnetization values are around 2.35 T. To achieve both a high on-axis magnetic flux density and at the same time a good resistivity against demagnetization in particular, a magnet material with a remanence of 1.19 T was chosen providing a coercivity of 2625 kA/m, as described in section 3.3 (VACODYM 890 TP with VACOFLUX 50). This material is best described by the third set of coefficients of P. Elleaume and is used therefore for all calculations in the following sections. With it a parametric scan over the undulator period length and undulator gap size was made in section 3.6.2, resulting in area graphs showing the expected magnetic flux density on-axis and the corresponding K parameter. The data is then used to calculate the expected spectral performance of the undulator in section 3.6.3, performed in order to find the best parameter set for an experimental soft X-ray photon beam line driven by a laser plasma wake field accelerator (PWA).

3.6.2 Parameter scan for undulator magnetic field performance

As described in the last section, equation (3.9) is used to calculate the maximum on-axis flux density $\hat{B}$ (in the following called on-axis peak field or shortly peak field) for undulator periods between 3 and 15 mm and gap sizes between 0.5 and 6 mm. From that value the undulator K parameter can be determined, which sets the spectral characteristics of the insertion device.

Figure 3.9 shows the approximated peak field values within a parameter space which is interesting in particular for the electron bunch attributes achieved with PWA, described in chapter 2. The marked area indicates the range of validity of the used equation (3.9). Whereas the theoretical peak field limit for a PPM undulator is $2\,B_\mathrm{r}$ at maximum (in this case 2.4 T) with the hybrid design even higher peak fields can be reached, but these extreme cases can not be described exactly by the used formula, exceeding its range of validity. On the other hand, the small gap sizes, where these values are reached, below 1.5 mm, are not feasible for the PWA scenario, as learned by experience with the first undulator of the group [71]. This undulator, featuring a gap size of 1.6 mm, was significantly demagnetized after only a few beam times due to irradiations with high energy electrons.

It is intuitively clear that small gaps g produce high flux densities, and larger undulator period lengths mean larger magnets which induce again a higher field flux. Whereas the peak field does not change if the ratio g/λ_u is constant, the K parameter in figure 3.10 increases for higher period lengths even if the ratio is constant. This is caused by the additional contribution of the period length λ_u to the undulator parameter K defined as $K \approx 0.9336\,\hat{B}[\mathrm{T}] \times \lambda_\mathrm{u}[\mathrm{cm}]$. The intended undulator gap size regarding PWA electron beam instabilities is about 2 mm. With further development of the PWAs, regarding laser, beam line and target designs, smaller gaps and thus higher magnetic flux densities and a higher K parameter seem possible. Thus a simple undulator design is preferred, providing the possibility of a subsequent modification of the gap size towards smaller gaps and higher magnetic flux densities.

There are actually two different key figures for the optimization of the undulator photon yield. One is the on-axis photon flux density and the other is the angle integrated photon number. Both of these depend on the undulator parameter K considering equations (2.51) and (2.55) which is therefore an important measure of an undulator. Which of the key figures, flux density or integrated flux, is more meaningful depends on the type of experiments proposed by the scientist.

For the scheduled gap size of 2 mm, a K parameter of 1 would be realized at an undulator period length of about 8 mm. At a K parameter of 1, the highest possible on-axis photon flux density
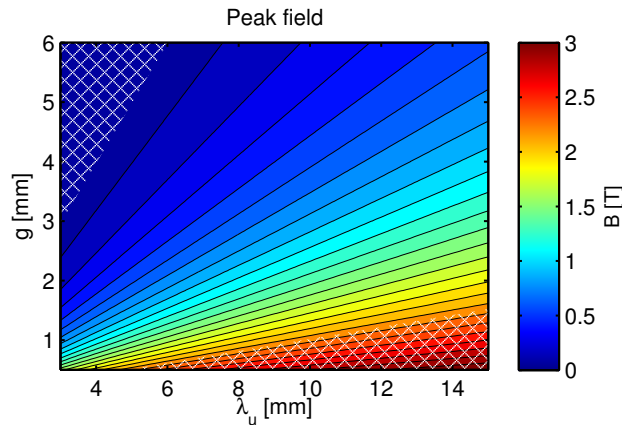
FIGURE 3.9: Parameter scan over gap size g and period length λ_u. Displayed is the peak field $\hat{B}$, calculated with equation (3.9). The equation is valid for the parameter range in between: $0.1 \le g/\lambda_\mathrm{u} \le 1$. The coefficients of equation (3.9) are adapted to values corresponding to hybrid undulators made of NdFeB magnets with a remanence of 1.2 T, according table 3.5.
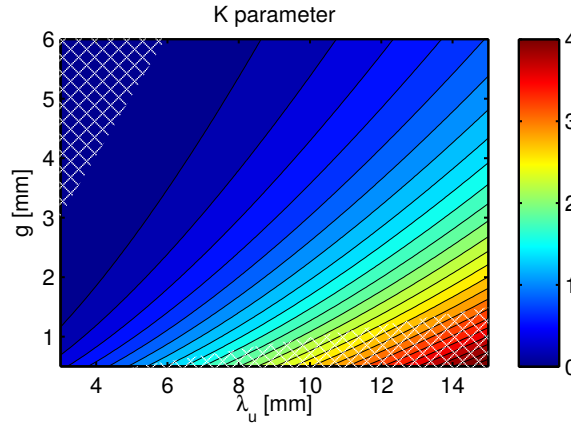
FIGURE 3.10: Parameter scan over gap size g and period length λ_u. Displayed is the K parameter for hybrid undulators made of NdFeB magnets with a remanence of 1.2 T, according to equation (3.9). The equation is valid for $0.1 \leq g/\lambda_u \leq 1$ where g is the undulator gap size and λ_u the period length.

at the fundamental order would be achieved. This follows from the analytic description of the on-axis photon flux density and can be seen in figure 2.7 in section 2.2.5.5. For smaller undulator gap sizes, the optimal period length would decrease. At gap sizes of 1 mm an ideal undulator period length would be about 6 mm, resulting as well in a K parameter of 1. These setups are optimal for maximizing the on-axis photon flux density of the first harmonic.

A K parameter of almost 2 would be realized at a gap size of 2 mm and an undulator period length of 11 mm. A higher K parameter would allow to use especially the higher harmonic part of the spectrum. This particular K parameter of 2 would generate the highest possible on-axis photon flux density for the third harmonic spectral order. This can be comprehended again by looking at figure 2.7 in section 2.2.5.5.

If one would plan a variable gap undulator, where the on-axis magnetic flux density can by varied by moving the undulator girders, a K parameter above two would be desirable, since this would provide a sufficient overlap of the harmonics and thus a certain photon yield over a continuous spectral range. For more information about that, see section 3.6.4.3 and figure 3.16.

3.6.3 Parameter scan for undulator photon flux performance

In the following, a systematic approach will show the expected photon performance of the undulator. First, the integrated photon flux will be studied. Second, the on-axis photon flux densities will be analyzed. Both quantities have their raison d'être depending on the type of planned experiment. Those experiments with samples which have to be excited and observed may prefer a large total number of photons, whereas especially diffraction experiments benefit from a higher flux density. Indeed, the photon beam can be modified also by optics (mirrors etc.), but at short wavelengths, a significant part of the radiation will be absorbed since the efficiency (reflectivity) is usually limited.

All photon numbers are calculated for the following PWA parameters: The high power laser system is expected to work at 5 Hz at 280 TW corresponding to the design goal of the laser

system and laser target of the *DESY* PWA beam line. The electron energy was set to 725 MeV. A bunch charge of 100 pC is assumed, which results at 5 Hz in an average beam current of 500 pA. This value is used to estimate the integrated photon flux and the flux density by equation (2.55) and (2.51) respectively, averaged over one second. It again has to be pointed out that the **length of the undulator** was kept constant at 0.5 m for all calculations to normalize the results and make them comparable. This implies that the number of undulator periods decreases with an increasing period length.

The **peak** photon **flux** density, instead is substantially higher. One has to consider that in case of a PWA electron bunch, the duration of the photon pulse is only a few femtoseconds [118, 119] and not a full second as used for the averaged values. Peak currents of more than 100 kA could be expected [120] from PW class laser systems. To approximate the photon pulse duration, the following issue was addressed. If an electron bunch length of about 0.5 µm is assumed, the pulse would last 1.7 fs in the time domain. Passing the undulator the electrons generate light at every position within the undulator. The light which is emitted first overtakes the electron bunch due to its faster velocity. After every undulator period the bunch drops behind the light pulse by one wavelength. Thus a slight prolongation of the light pulse takes place, resulting in a lengthening depending on undulator period number and radiation wavelength. A prolongation of e.g. 0.1 µm would take place for a 100 period device radiating at a wavelength of about 1.2 nm (ca. 1 keV), which would result then in an additional duration of 0.34 fs. Thus the total pulse length of the emitted light can be estimated to be about 2 fs.

Now the **peak flux** density values can be calculated by dividing the number of photons by 5 to get the photons in a single shot and then dividing it by 2 fs the approximated pulse duration. This results in a factor of 10^{14} which has thus to be multiplied to the values in the graphs.

3.6.3.1 Angle integrated photon flux

In figure 3.11 plots of the angle integrated photon flux of the first and the third harmonic are shown. The flux rates are calculated by equation (2.55), using the results of equation (3.9). The integrated photon flux depends on the number of undulator periods N_{u}, the electron beam current I and the K parameter, which gives the argument of the modified Bessel function $Q_n(K)$. The shape of the curve (2.55) is determined by $Q_n(K)$, which reaches 80% of its maximum value at $K \approx 1.53$, for all spectral harmonics (compare figure 2.8) and shows a slow asymptotic behavior to the maximum values for higher K values. Again, the marked area indicates the range of validity of equation (3.9) and restricts thereby also the meaningful area of the photon flux parameter scans.

The first thing to be noticed in figure 3.11 is that small undulator gap sizes g mean high undulator peak fields and K parameters (compare figure 3.9 and 3.10) and thereby a high photon flux. Second, the integrated photon flux can be maximized at specific undulator period lengths concerning a given gap size g. This is due to the fact that the increase of the undulator period length, increases the K parameter on one hand, but on the other decreases the total number of undulator periods for a given undulator length. As the length is a crucial factor in terms of costs and available space along the beam line, the length of the undulator was kept constant for
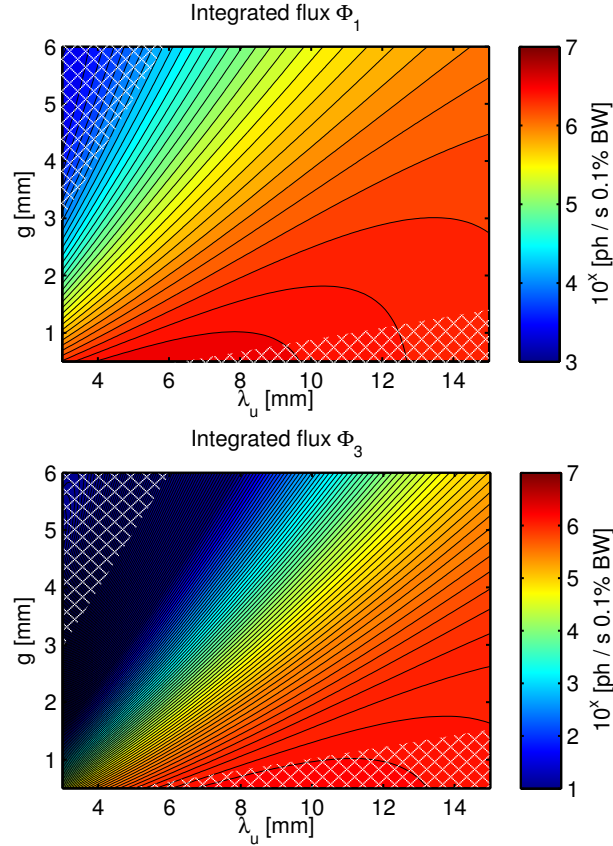
FIGURE 3.11: Parameter scan over gap size g and period length λ_u. Displayed is the integrated photon flux for the fundamental (top) and the third harmonic wavelength ($n = 3$, bottom), according to equation (2.55). The *DESY* PWA beam line works with a 280 TW laser system with a 5 Hz repetition rate. Independent experiments have demonstrated that such laser systems can produce electron bunches with 100 pC charge and electron energies up to 725 MeV, but so far only one of each features could have been achieved at a time. These parameters were used to calculate the integrated flux, defined as photons per second within an energy range of 0.1% of harmonics bandwidth. To calculate the peak flux values one has to multiply the numbers by a factor of 10^{14}, as discussed in the text.

normalization and a better comparison of the results. In the proposed model the absolute length of the undulator is scheduled to a length of 0.5 m. This boundary condition was implemented in the model, to achieve comparability in costs and the limitations in available space along the beam line. Thus the number of periods N_u is given by $N_\mathrm{u} = {}^{L_\mathrm{u}}/\lambda_\mathrm{u}$. Both, N_u and Q_n are functions of λ_u. The integrated flux is proportional to $\Phi_n \propto N_\mathrm{u} Q_n(K)$ and at a gap dependent period length the increase of the value of $Q_n(K(\lambda_\mathrm{u}))$ with the period length becomes smaller than the decrease of the number of undulator periods at this period length. Due to the fact that the undulator length is hold constant, a longer period length implies a smaller number of undulator periods. It turns out that the increase of the K parameter, which follows with a longer period length (see figure 3.10) is overcompensated by the decrease of the period number in equation (2.55) if a certain gap limit is exceeded. An analytical solution would be given by setting the partial derivative of $Q(K(\hat{B}(\lambda_\mathrm{u}))) \times N_\mathrm{u}(\lambda_\mathrm{u})$ with respect to λ_u to zero. This gives as result a gap dependent $\lambda_\mathrm{u,max}(g)$ where the integrated photon flux is at a maximum for a specific g. Unfortunately due to the Bessel function, only a numerical approximation can be

given, which results in the graph of figure 3.11. As stated before, the intended undulator gap size g is 2 mm (3.6.2). At this gap size one gets a maximized flux for an undulator period length of about 11 mm for the fundamental wavelength. For smaller gap sizes the flux maximizing period length (for the first harmonic $n = 1$) becomes shorter. For the higher harmonic part of the radiation, e.g. $n = 3$ as shown in figure 3.11, the optimal period length is at a period length beyond 14 mm.

The photon numbers are calculated for the laser system of *DESY* described in the last section. The peak flux values can be calculated by multiplying the results in figure 3.11 by a factor of 10^{14}. In the end, an integrated peak photon flux of about 10^{20} photons per second within 0.1% bandwidth seems possible, which is unique compared to conventional scientific light sources. It should be mentioned here that Thomson scattering, as another high power laser based light source, could reach comparable values and is target of several research groups today.

3.6.3.2 On-axis photon flux density

In figure 3.12 plots of the on-axis flux density of the first and the third harmonic are shown. Again, like in section 3.6.3.1, the marked area indicates the range of validity of equation (3.9) and restricts thereby also the meaningful area of the photon flux parameter scans.

In contradistinction to the case of the integrated photon flux, here the variation of the gap size implies more complex consequences than a monotonic increase of the on-axis flux density. There is a distinct maximum for every specific undulator period length which follows from the behavior of $F_n(K)$, described in section 2.2.5.5.

As a boundary condition the number of periods N_u is given by $N_u = L_u/\lambda_u$, with L_u the total length of the undulator hold constant. N_u thus decreases with a longer undulator period length λ_u, and since the flux density depends on N_u^2 and $F_n(K)$ is not simply monotonically increasing with a longer undulator period length like $Q_n(K)$ described in section 3.6.3.1, $d\Phi/d\Omega|_{\theta=0}^n$ has a distinctive maximum for any gap dependent period length.

The on-axis photon flux density contour plot is determined by equation (2.51) in section 2.2.5.5. It depends on the squared electron energy E^2, the squared undulator period number N_u^2, the electron beam current I and a modified Bessel function of the first kind. $F_n(K)$ is described in more detail in section 2.2.5.5. In all cases an electron energy of 725 MeV is assumed with a bunch charge of 100 pC at 5 Hz (thus a beam current of 500 pA). This function reaches the highest possible on-axis photon flux density for the fundamental order at a K parameter of 1 (compare figure 2.7 in section 2.2.5.5). For higher values of K, the photon flux density decreases again, due to the fact that the opening angle (the divergence) of the light cone increases with K, given by $\Delta\theta = 1/\gamma \sqrt{\frac{1+K^2/2}{N_u n}}$. The higher harmonic radiation maximizes at higher K parameters, e.g. the 3rd harmonic at $K \approx 2$.

At a 2 mm gap (as intended for the first use) one gets a maximized flux density at an undulator period length of about 8 mm for the fundamental wavelength. For smaller gap sizes this for $n = 1$ optimal undulator period length, becomes radically shorter leading to a 5 mm period length at 1 mm gap size, shown in figure 3.12. For the third harmonic ($n = 3$) the ideal period

length would be at about 11 mm. The maxima are strongly correlated to the K values where the $F_n(K)$ function has its maximum values. A K parameter of 1, realized at a gap size of 2 mm and an undulator period length about 8 mm, maximizes F_n whereas a K parameter of almost 2, realized at a gap size of 2 mm and an undulator period length of 11 mm, would enable the highest possible on-axis photon flux density for the third harmonic spectral order (compare figure 2.7 in section 2.2.5.5).

At this juncture, it must be noted that the numbers are calculated for a 5 Hz operation of the 280 TW laser system of *DESY* as described in 3.6.3. The peak flux density is substantially higher as described in section 3.6.3. A factor of 10^{14} has to be multiplied to the values in the graphs, thus resulting in an on-axis photon flux density of about 10^{27} photons per mrad^2, per second within 0.1% bandwidth.
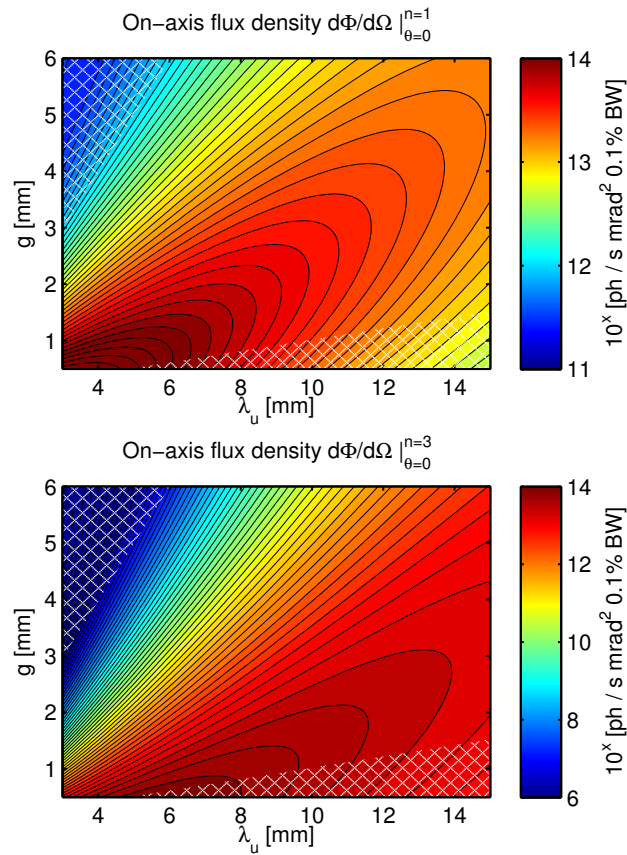
FIGURE 3.12: Parameter scan over gap size g and period length λ_u. Displayed is the on-axis photon flux density for the first ($n = 1$ top) and the third ($n = 3$ bottom) harmonic wavelength, according to equation (2.51). The *DESY* PWA beam line works with a 280 TW laser system with a 5 Hz repetition rate. State-of-the-art experiments have demonstrated that such laser classes can produce electron bunches with more than 100 pC charge and electron energies above 725 MeV. These parameters were used to calculate the integrated flux density, defined as photons per mrad^2 solid angle, per second, within an energy range of 0.1% of the bandwidth.

3.6.4 A case study - comparison of three characteristic subsets

As could be seen in section 3.6.3.1 & 3.6.3.2 there are three interesting undulator period lengths, which will be directly compared in this section. First of all, there is a lower limit of the undulator period length, at which the manufacturing tolerances and the thickness of the dead layer of the magnets become significant in relation to the magnets total sizes. The fact that even if the gap size is chosen to be only 1 mm, thereby maximizing the undulator peak field, the maximum on-axis flux density for the fundamental wavelength would be reached at about 5 mm. However, this small gap size would require a not yet achieved stability of the electron beam line, to guarantee a trouble-free electron beam propagation through the undulator. Two other period lengths are favorable, each with advantages at specific gap sizes.

Photon flux optimized parameter sets

	$\lambda_{\mathrm{u}} = 5$ mm	$\lambda_{\mathrm{u}} = 8$ mm	$\lambda_{\mathrm{u}} = 11$ mm
$g = 1$ mm	$\mathrm{d}\Phi/\mathrm{d}\Omega\big|_{\theta=0}^{n=1}$	$\Phi_{n=1}$	$\Phi_{n=3}$
$g = 2$ mm		$\mathrm{d}\Phi/\mathrm{d}\Omega\big|_{\theta=0}^{n=1}$	$\Phi_{n=1}$ & $\mathrm{d}\Phi/\mathrm{d}\Omega\big|_{\theta=0}^{n=3}$

TABLE 3.6: Specific parameter sets which optimize radiation properties for a hybrid undulator based on magnets with 1.2 T remanent field for the fundamental and the third harmonic part of the undulator spectrum. These combinations of period length λ_{u} and gap sizes g are best to generate a maximum photon flux or flux density at wavelengths according to λ_{u}, g and n. All data is based on equation (3.9) used for solving (2.51) & (2.55). A scan over the complete range is shown in figures 3.11 & 3.12.

At a gap size of 2 mm, which is currently the smallest undulator gap size considering PWA electron beam instabilities, the integrated photon flux of the fundamental $\Phi_{n=1}$ shows a maximum at a period length of 11 mm. At this period length also the on-axis photon flux density of the third harmonic $\mathrm{d}\Phi/\mathrm{d}\Omega\big|_{\theta=0}^{n=3}$ is maximized. However, the on-axis photon flux density of the fundamental $\mathrm{d}\Phi/\mathrm{d}\Omega\big|_{\theta=0}^{n=1}$ at 2 mm gap size is highest at a period length of 8 mm.

Operation at a gap size of 1 mm, which would require a substantial progress considering PWA electron beam instabilities, maximizes the integrated photon flux of the fundamental $\Phi_{n=1}$ at a period length of 8 mm whereas at 1 mm gap size the photon flux of the third harmonic $\Phi_{n=3}$ is maximized at 11 mm. An overview over these properties is given in table 3.6.

For a quantified comparison of the expected undulator performance, these three period lengths, each showing specific advantages, are contrasted particularly in the following section, analyzing the discussed key performance factors of a photon beam line.

3.6.4.1 Magnetic peak field, *K* parameter and fundamental photon energy

In figure 3.13 (top and middle) one can see the change of the undulator peak field and the related *K* parameter, with a variation of the gap size. Figure 3.13 (bottom) shows the expected resonance energy of the fundamental. Assuming an electron energy of 725 MeV one would reach the keV region using radiation of the fundamental with a 5 mm period length at gap sizes above 3 mm.
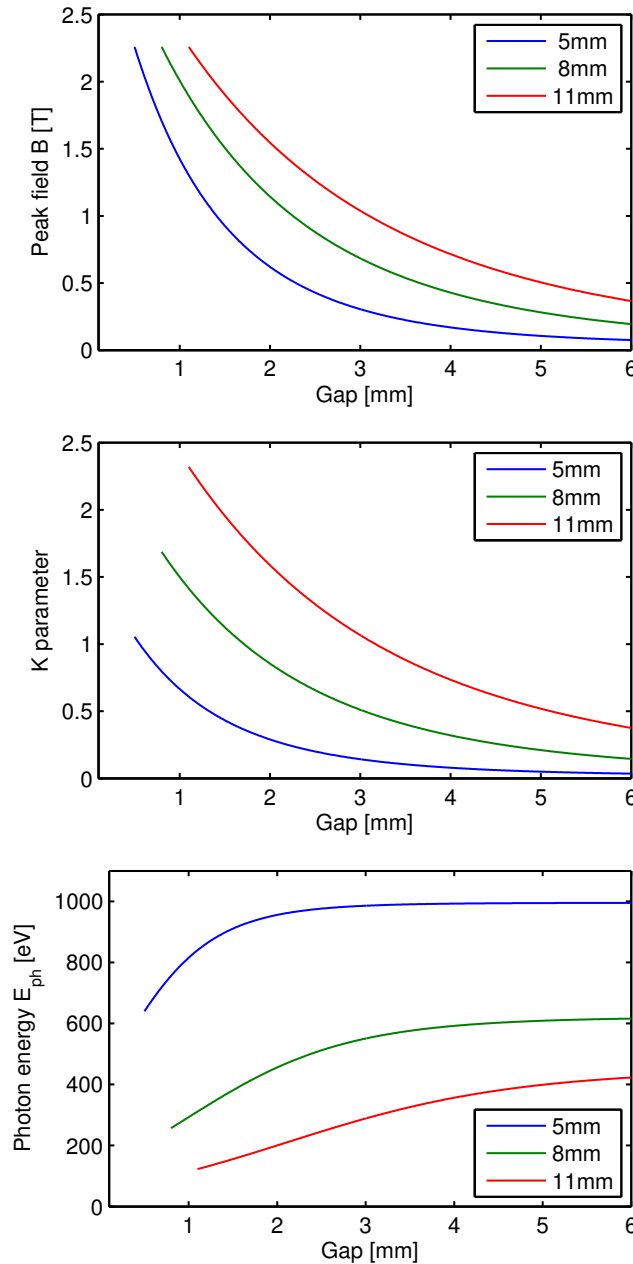
FIGURE 3.13: On-axis peak field (top), *K* parameter (middle) and resulting photon energy of the undulator fundamental (bottom) for undulators with 5, 8 and 11 mm period lengths. The magnetic flux density was calculated by equation (3.9) for magnets with a 1.2 T remanent field, described in more detail in section 3.6.1. Only values within the range of validity ($0.1 < g/\lambda_u < 1$) are shown. The photon energy (bottom) was calculated for an assumed electron energy of 725 MeV.

3.6.4.2 Peak flux of three characteristic undulator subsets

In figure 3.14 it becomes apparent that the differences for the fundamental wavelength are not significant comparing the integrated flux Φ_n for the gap sizes below 1 mm. However, above 3 mm gaps, about one order of magnitude more photons could be expected using an undulator with 8 mm period length when compared to an undulator with 5 mm. The increase of flux considering the third harmonic is even more significant. The flux is increased up to three orders of magnitude, when the 5 mm undulator is compared to the 8 mm period device, at a 2 mm gap size, and almost four orders when compared to the 11 mm device. And even at a gap size of 1 mm, $\Phi_{n=3}$ is one order of magnitude higher at 8 or 11 mm period lengths, compared to a 5 mm period length undulator.
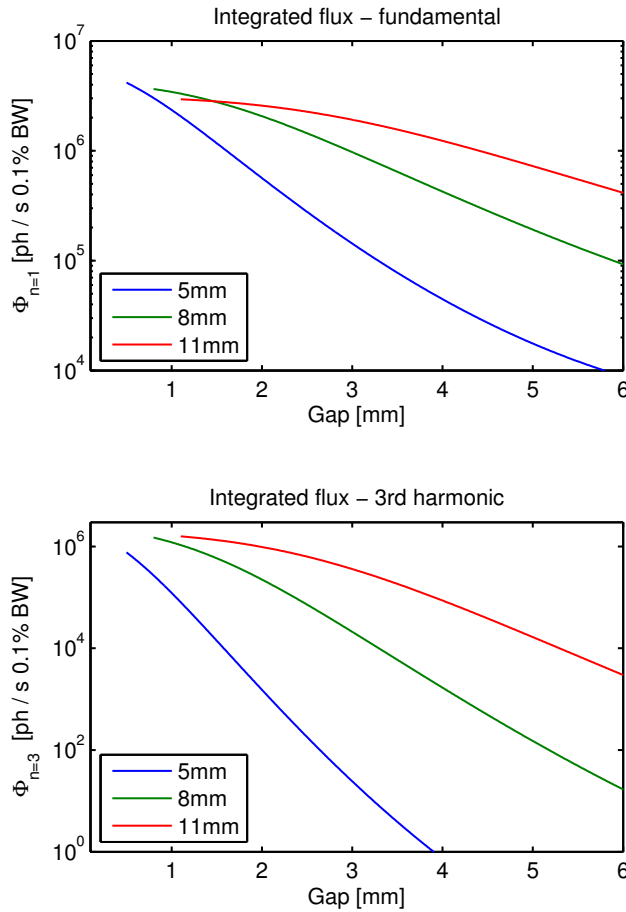
FIGURE 3.14: Integrated photon flux of fundamental and the third harmonic, according to equation (2.55), calculated for a 100 pC electron bunch with a repetition rate of 5 Hz and 725 MeV electron energy. All parameters used to calculate the gap dependent undulator peak field, K parameter and thus the integrated photon flux are described in more detail in section 3.6.3.1. Again, the photon flux is averaged over one second or in this case 5 shots. To get the peak flux densities one has to multiply the Y-axis by 10^{14} for an assumed photon pulse length of 2 fs. The photon energies according to the gap sizes can be found in figure 3.13. For a better overview on the photon flux including information about the photon energies related to the harmonic number, figure 3.16 in section 3.6.4.3 is recommended.

Comparing the on-axis flux density of the fundamental at gap sizes between 1 and 2 mm, shown in figure 3.15, the flux density curves are not clearly favoring larger period lengths. This is due to the fact that the formula used for the analysis, equation (2.51), approximating the on-axis flux density, depends on two undulator related parameters: N_u^2 and $F_n(K)$.

$F_n(K)$ shows, contrary to $Q_n(K)$ (which is a monotonically increasing function), a maximum at $K \approx 1$ for the fundamental wavelength (with harmonic number $n = 1$). Since the 8 mm period undulator reaches this K value at a gap slightly below 2 mm, the flux density is the highest compared to the other devices at this gap size. The 5 mm period undulator dominates for gaps below 1 mm because K tends towards 1 for the 5 mm device, see figure 3.13 (middle), whereas for the 8 and 11 mm period undulator K exceeds 1, and $F_n(K)$ decreases again.

Additionally one has to consider that N_u, the number of undulator periods, depends on the undulator period length due to fact that the total length of the undulator is limited to 0.5 m for
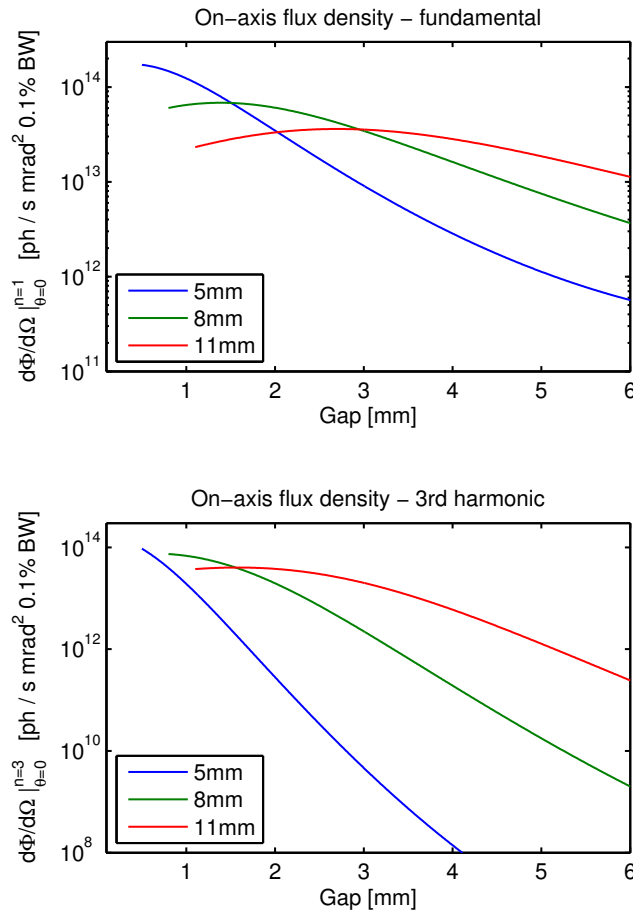
FIGURE 3.15: On-axis photon flux density of fundamental (top) and the third harmonic (bottom), according to equation (2.51), calculated for a 100 pC electron bunch with a repetition rate of 5 Hz and 725 MeV electron energy. All parameters used to calculate the gap dependent undulator peak field, the K parameter and finally the on-axis photon flux density are described in more detail in section 3.6.3.2. Again, the photon flux density is averaged over one second or in this case 5 shots. To get the peak flux densities one has to multiply the photon numbers by 10^{14}, since the graphs represent 5 pulses each with a length of about 2 fs. The photon energies according to each undulator period length depending on the gap size can be found in figure 3.13. For a better overview on the photon flux including information about the photon energies related to the harmonic number, figure 3.16 in section 3.6.4.3 is recommended.

all calculations. The decreasing number of periods for longer period lengths affects on one hand the radiation opening angle, described by equation (2.44), on the other the number of generated photons itself. Both effects point in the same direction, if the number of undulator periods decreases, less photons are generated affecting angle integrated photon number and on-axis flux density. And if the opening angle becomes wider the generated radiation distributes over a larger area decreasing additionally the on-axis flux density.

Expressed in numbers undulators have 100, 62 and 45 periods for the 5, 8 and 11 mm period length and as a consequence, the flux density is the highest for the 5 mm device at particular small gap sizes below 1.5 mm.

3.6.4.3 Tuning curves - photon peak flux and corresponding energies

Undulator tuning curves are commonly used to show the potential output of an undulator with a variable gap size. Since the electron energy of a storage ring is fixed due to several ring design
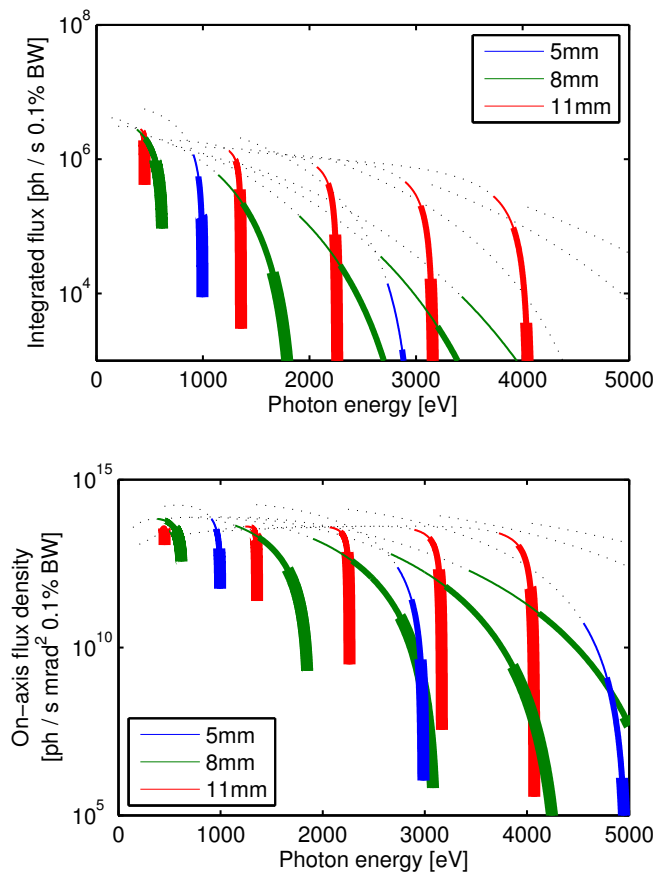
FIGURE 3.16: Integrated photon flux (top) and on-axis photon flux density (bottom) as a function of photon energy, calculated for a variation of the undulator gap. The variation of the gap size is illustrated in simplified terms by the thickness of the lines. The thin line width represents a gap size between 1.5 and 2 mm, the medium line width a gap size ranging from 2 to 3 mm and the thick colored line a gap size up to 6 mm. The flux is calculated according to equation (2.51) for a 100 pC electron bunch with a repetition rate of 5 Hz and 725 MeV electron energy. A more detailed description of these so-called tuning curves is given in the text.

parameters, a variation of the undulator radiation wavelength has to be caused by changing the undulator parameter K, which changes the resonance condition and thereby the wavelength of the emitted light, see equation (2.40). For this purpose the magnetic peak field has to be varied. Permanent magnet undulators can do this by changing the gap size. The possible range of the variation determines the undulators tuning range.

In figure 3.16 one can see the theoretical tuning range of the discussed undulator if the undulator gap would be varied between 1.5 and 6 mm. The graph shows the integrated photon flux and the on-axis flux density with the specific photon energies. The series of same-colored curves presents the sequenced odd harmonics in the undulator spectra, of the discussed undulator selection with 5, 8 or 11 mm period lengths. The variation of the gap size is illustrated in simplified terms by the thickness of the lines. The thin line width represents a gap size between 1.5 and 2 mm, the medium line width a gap size ranging from 2 to 3 mm and the thick colored line a gap size up to 6 mm. One has to be aware, not to confuse these graphs with undulator spectra. The integrated flux and the on-axis flux density is shown only for the resonance wavelength or energy at specific gap sizes, the graphs are not representing the whole spectrum of the undulator output.

One sees in the figures that a high photon flux at high energies is achieved best by using the higher harmonics of the undulator spectra. But one has to keep in mind that these graphs are approximations for electron beams without energy spread and undulators without magnetic field errors, which reduce the photon output of the undulator, described in the next section.

3.6.4.4 Electron beam emittance and diffraction limit

As a final check, if the analytic formulas can be trusted when it comes to the flux density, also diffraction must be considered. Bunches of light waves interfere not only at obstacles, but also with themselves. At small source sizes as found in undulators or lasers in general, wave packages tend to dissolve. This can be expressed by a lower limit for the emittance of the light, depending on its wavelength. If the undulator light source is approximated to the fundamental mode of an optical resonator (Gaussian laser mode) [121, 122], the natural diffraction limit can be assumed by the following [123] with the opening angle given by equation (2.43) and a source size of σ_r it follows that:

$$
\begin{aligned}
2\pi\sigma_r\sigma_\angle &= \frac{\lambda_{\mathrm{ph}}}{2} \Rightarrow \\
\epsilon_{\mathrm{ph}} &\approx 2\frac{\lambda_{\mathrm{ph}}}{4\pi},
\end{aligned}
\tag{3.10}
$$

which is two times the intrinsic emittance of a Gaussian laser pulse. This is related to the fact that UR is not fully coherent, only transversally. Thus, even at negligible electron beam emittances the phase space of the radiation from an undulator itself has a distinct area as minimum due to this diffraction effect. The corresponding emittance of the light beam without electron beam emittance is given by equation (3.10), with λ_{ph} being the wavelength at the undulators harmonic peaks.

An undulator light source is called diffraction limited, if the normalized emittance of the electron beam is smaller than that of the photon beam, since this would lead to a significant increase of the photon beam emittance.

In our case the electron emittance was measured to be $\epsilon_{\mathrm{el}} = 1/\gamma\, 0.21\, \pi\ \mu\mathrm{m}\ \mathrm{rad}$ [99]. If one writes down the equation for the diffraction limit, one gets a relation concerning the wavelength and the energy of the electrons, assuming that the emittance is not changing with the electron energy. At the limit, where ϵ_{el} is at the order of ϵ_{ph} one obtains:

$$\epsilon_{\mathrm{ph}} = \epsilon_{\mathrm{el}} \Rightarrow$$
$$\frac{\lambda_{\mathrm{ph}}}{2\pi} = \frac{1}{\gamma}\, 0.21\, \pi\ \mu\mathrm{m}\ \mathrm{rad}\ ,$$

This gives an upper limit for the wavelength, beneath which the light beam would be forced to diverge by diffraction. This limit is at

$$\lambda_{\mathrm{ph}} \approx \frac{1}{\gamma}\, 0.42\, \pi^2\ \mu\mathrm{m}\ \mathrm{rad}. \tag{3.11}$$

which defines the diffraction limit. Below that limit, the emittance of the electron beam dominates the photon beam emittance. This is shown in figure 3.17. One sees the wavelength of the fundamental in dependence to the electron energy for the three undulator period lengths analyzed in the case study of this section at a gap size of 2 mm. The black dashed line shows the diffraction limit calculated by equation (3.11) for a typical PWA case, numbers taken from [99].
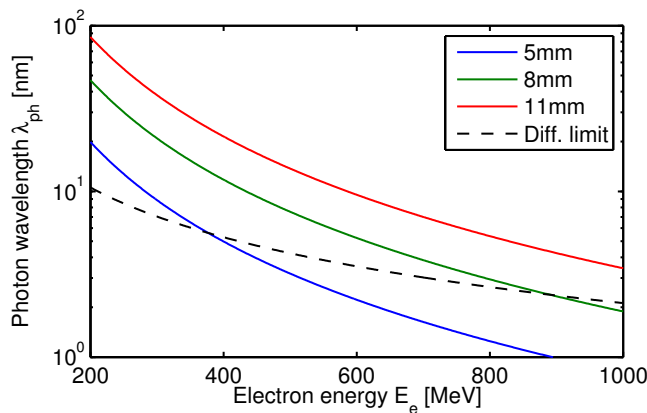
FIGURE 3.17: In the above figure the black dashed line marks the limit when PWA electron bunch and the intrinsic undulator light pulse emittance are the same. If the wavelength of the emitted undulator radiation sinks below that limit, the emittance of the light pulse is dominated by the accelerator specific electron bunch emittance. The emitted wavelengths of the fundamental of all three undulators analyzed in the precedent case study are shown. One can see that the 8 mm and the 11 mm period undulator emit radiation with wavelengths at the fundamental which are not or only partly dominated be the accelerators emittance.

Below the line, the emittance of the photon beam itself becomes smaller than the electron emittance and the photon beam divergence gets a significant contribution to its emittance. This would affect the calculations done so far in this section. One can see that over a range of electron energies from zero to 1 GeV, the undulator radiation emittance of the fundamental of the 5 mm device would significantly increased for electron energies above 400 MeV. It becomes also apparent that higher harmonics of all three cases would suffer from the same effect. Therefor one should consider using simulations including the additional effects of the electron beam properties, which is done in the following section.

3.6.5 Undulator performance with beam optic, emittance and energy spread

Up to this point, all equations, curves and figures describe the theoretical peak flux for a specific harmonic n which is only the peak flux at the specific resonance energy in the undulator spectrum. If one needs to know how the complete spectrum with a continuous range of energies from an undulator looks like, beyond that simple characteristic that every harmonic spike has a bandwidth of $\Delta\omega/\omega = 1/nN_\mathrm{u}$, one has to use computer simulations. Especially if one is interested in spatially resolved results, including a realistic electron bunch with energy spread and emittance as well as electron beam optics.

For this purpose, simulations were performed with the code SPECTRA [78], resulting in predictions on brilliance, angle integrated photon flux and partial flux through a slit, which has the typical dimensions of a grating spectrometer, placed at 1 m distance behind the undulator. The simulations were set up with an emittance value previously measured $\epsilon_\mathrm{el} = 1/\gamma\, 0.21\,\pi\ \mu$m rad [99] and an optimized beam optic setup ($\beta = D$ [68]) with D the distance between undulator and experiment (1 m in this simulation). The beta function is related to the transverse beam size as follows: $\sigma(s) = \sqrt{\epsilon\beta(s)}$ where s is the location along the beam trajectory, $\sigma(s)$ the width of the Gaussian distribution used as fit function. Magnetic field errors or higher order field components were not taken into account for the sake of simplicity. Three different electron beam energy spreads from 5% over 1% to 0% are thereby compared in the following figures 3.18, 3.19 and 3.20.

As a result the more realistic simulations of the achievable photon flux characteristics show numbers consistent to those approximated by the parameter scans in the sections before. The deviations of the integrated flux are highest in case of the 5 mm period length, due to the distinct harmonic structure of its spectrum. This leads to narrow harmonic peaks which are broadened and thus decreased by the energy spread of the electrons.

Also here all numbers are given as average over one second. Since the PWA electron beam is comprised of five ultra short bunches per second, one has to multiply the results by a factor of 10^{14} to get the peak photon flux which is emitted within time ranges of about 2 fs, described in more detail in section 3.6.3.
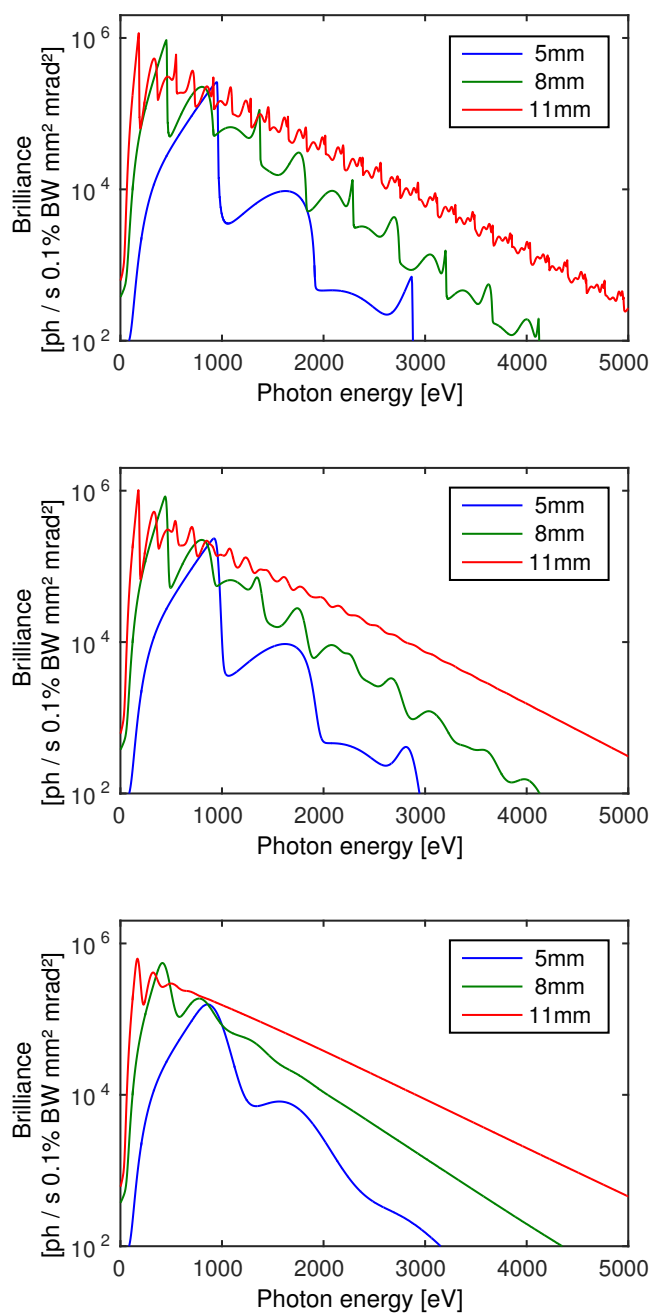
FIGURE 3.18: Simulations of the expected UR Brightness (or sometimes Brilliance) for electron bunches with 0%, 1% and 5% energy spread (from top to bottom), performed with SPECTRA [78]. A 100 pC bunch charge at 5 Hz repetition rate and 725 MeV energy were assumed. The electron beam optics were optimized to maximize the UR flux density. A comparison of 5, 8 and 11 mm period length undulators is shown, with on-axis flux densities of 0.67, 1.27 and 1.67 T respectively at 2 mm gap size is shown, according to figure 3.13 (top). To get the peak Brightness a factor of 10^{14} must be multiplied, which is described in more detail in section 3.6.3.
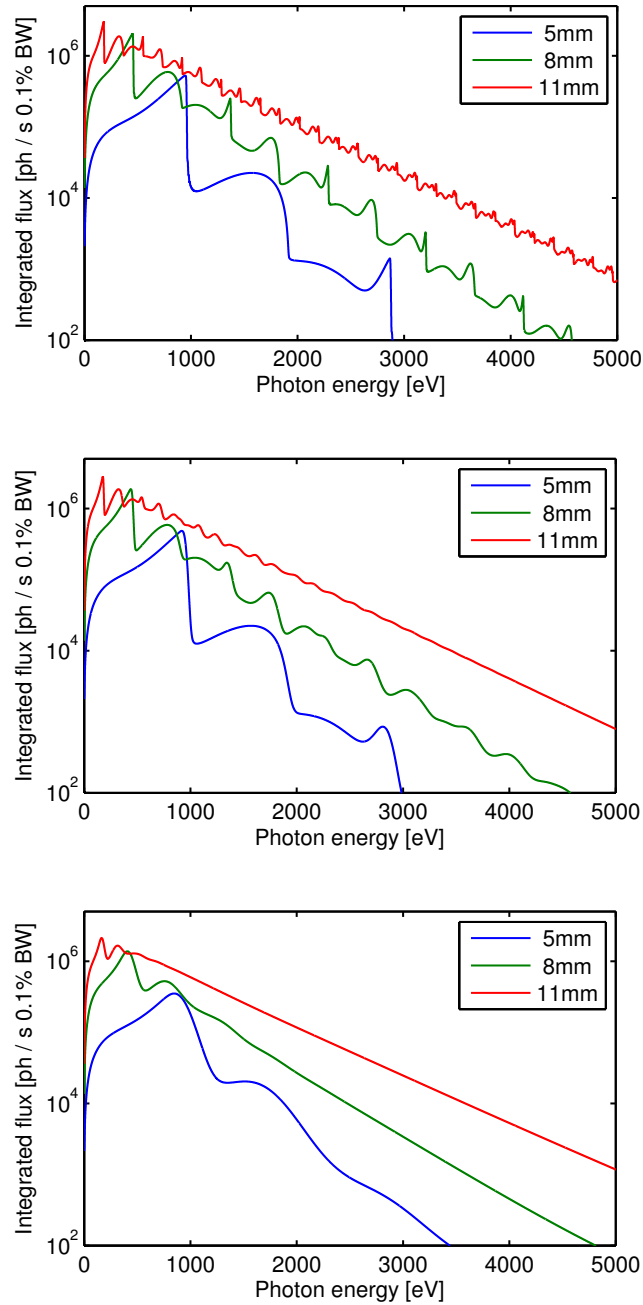
FIGURE 3.19: Simulations of the angle integrated photon flux for electron bunches with 0%, 1% and 5% energy spread (from top to bottom), performed with SPECTRA [78]. A 100 pC bunch charge at 5 Hz repetition rate and 725 MeV energy were assumed. The electron beam optics were optimized to maximize the UR flux density. A comparison of 5, 8 and 11 mm period length undulators is shown, with on-axis flux densities of 0.67, 1.27 and 1.67 T respectively at 2 mm gap size is shown, according to figure 3.13 (top). To get the peak integrated photon flux a factor of 10^{14} must be multiplied, which is described in more detail in section 3.6.3.
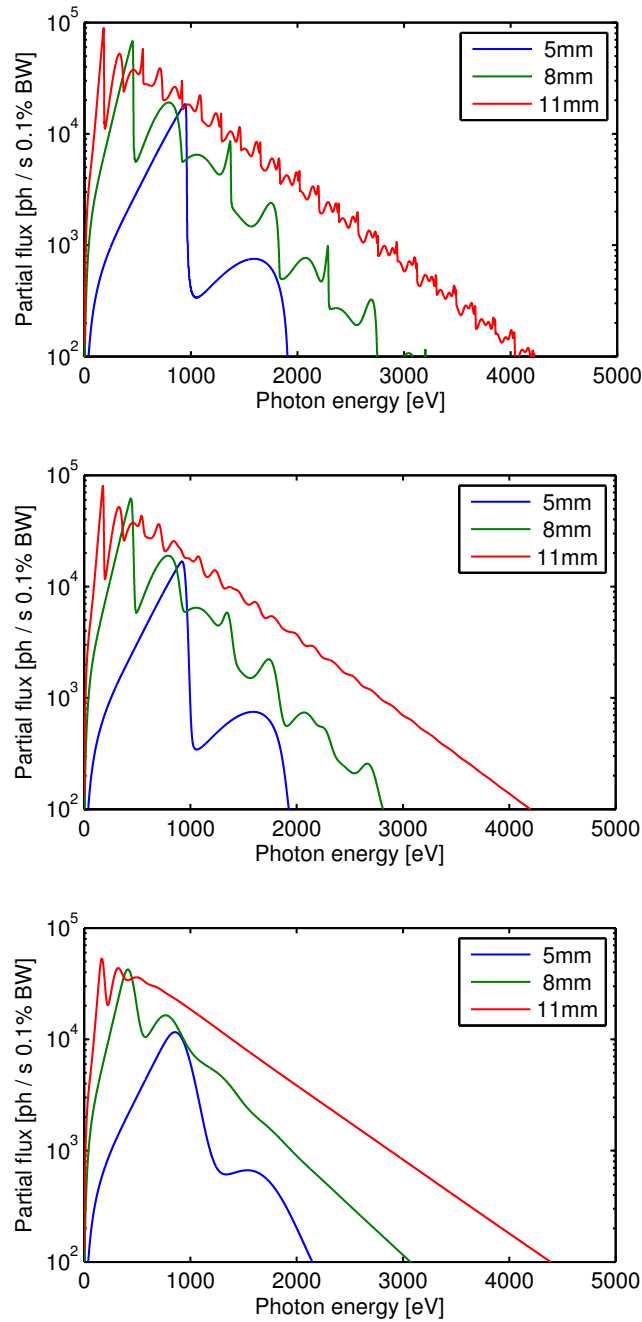
FIGURE 3.20: Simulations of the photon flux through a 100 μm broad (horizontal) and 10 mm high (vertical) slit at 1 m distance for electron bunches with 0%, 1% and 5% energy spread (from top to bottom), performed with SPECTRA [78]. A 100 pC bunch charge at 5 Hz repetition rate and 725 MeV energy were assumed. The electron beam optics were optimized to maximize the UR flux density. A comparison of 5, 8 and 11 mm period length undulators is shown, with on-axis flux densities of 0.67, 1.27 and 1.67 T respectively at 2 mm gap size is shown, according to figure 3.13 (top). To get the peak flux a factor of 10^{14} must be multiplied, which is described in more detail in section 3.6.3.

3.6.6 Effect of undulator field errors on photon flux

So far, in all analytic approaches as well as in the simulations ideal undulators were analyzed, devices with perfectly sinusoidal field slopes and no variations in the peak fields. This assumption was done for the sake of simplicity. In the following we will check if field errors can be critical or not. There is a rule of thumb which approximates the decrease of the photon output which can be found in the literature [35, 68]

$$\Phi_n(\sigma_{\mathrm{u}}) = \Phi_n \times \exp(-n^2\sigma_{\mathrm{u}}^2). \tag{3.12}$$

Here σ_{u} is the standard deviation of the undulator phase error given in degree and n is as usual the harmonic number. As can be seen by equation (3.12), undulator field errors affect mainly higher harmonics, visualized in figure 3.21. This is due to the fact that field errors deteriorate interference. Phase and wavelength of the generated light do not match to the light wave emitted before, if periodicity or amplitude of the magnetic field change along the undulator, and intuitively clear is that especially variations in the period length of the undulator field become larger in relation, when the period length of the radiation field is a third, a fifth or even less than this of the fundamental radiation.

Experiences show that a fixed gap undulator, like the one which is planned in this thesis, can achieve phase errors of about 2-3°, even at small gap sizes, if field correction methods like magnet sorting and shimming are used. The theoretical photon flux losses are shown in figure 3.21.
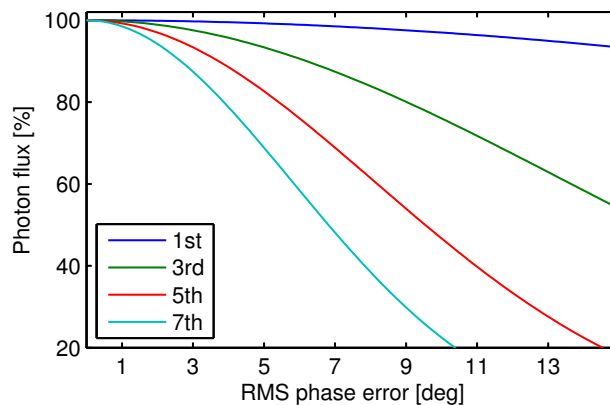
FIGURE 3.21: Reduction of the expected photon flux due to undulator field errors. Especially higher harmonics are affected. According to experiences of the BESSY undulator department, an RMS phase error below 3° should be attainable for fixed gap devices. This would enable to use also higher harmonics since the loss of photon flux is limited to about 3%, 7% and 13% at maximum for the third, fifth and seventh harmonic.

3.7 Resulting undulator parameters from parameter scan

In the last sections parameter scans were performed approximating the magnetic field properties as well as the photon flux and flux density of the planned undulator. This was done to get a preliminary setup suited for further optimization by simulating a magnetically modeled, realistic undulator. This is done by special software and presented in the next sections. The results of the preliminary scans are summarized hereinafter by the following:

- Choice of **magnet material:** due to the fact that PWA beam lines are affected by certain beam instabilities, the decision concerning the magnet material for the planned undulator is based on the demand to maximize the resistivity against demagnetization. Thus a high coercivity was favored over the gain of a few ten percent of magnetic peak field and additional countermeasures were taken to further improve the resistivity. The magnets were processed with dysprosium diffusion which increased the coercivity about 16% and additionally by artificial aging. The aging is accomplished by heating the magnets in an open circuit condition in an oven to about 140 °C.

- The **pole material** VACOFLUX50 with a saturation magnetization of 2.35 T was chosen to maximize the on-axis field flux in the undulator.

- By using empirical formulas, the theoretical undulator performance was calculated over a range of undulator period lengths λ_u and gap sizes g. It turned out that for **gap sizes** g between 1 and 2 mm, three period lengths, shown in table 3.6, maximize the angle integrated photon flux and the on-axis peak flux density. The direct comparison between these period lengths confirmed that for gap sizes g greater than 1.8 mm the longer period lengths are advantageous but for small gap sizes below 1.5 mm a 5 mm period length is preferable. These facts could be confirmed by looking on the undulator tuning curves in figure 3.16

- It was theoretically shown that undulator field errors with the typical magnitudes, decreasing in particular the performance of the higher harmonic output of the undulator, are not critical at all. As described in section 3.6.6 the undulator phase error is assumed to be less than 3° for the fixed gap device, achieved by magnet sorting and shimming.

- Finally, simulations of undulators with realistic PWA scenarios (including electron energy spread and emittance, bunch charge, distribution and beam optic) confirmed the numbers previously calculated by the parameter scans. The simulations further revealed that large energy spreads of the PWA electrons will nearly wipe out the harmonic character of the undulator spectra. The highest flux rates at nearly every energy interval are thus expected at a period length of 11 mm. This includes not only the angle integrated photon flux but also brilliance and the partial flux through a slit at a small distance.

Nevertheless an undulator **period length** of 5 mm is chosen maximizing the photon energy of the radiation fundamental for small gap sizes. At low electron energy spreads the harmonic spectrum is more distinct and diffraction is uncritical for low electron energies at the fundamental wavelength.

3.8 Simulation and optimization of an PWA undulator

As discussed in section 3.7 undulator design, magnet material and period length where chosen. The following approach to find the optimal geometric parameters uses the found parameters as start values for a numerical simulation. Highly accurate FEM simulations were used to improve and optimize the actual design of the undulator. The exact dimensions and shape of magnets and poles were varied systematically to maximize the magnetic on-axis flux density inside the undulator. These fields should be desirably high, to increase the photon yield of the device. Another question was: how strong would be the magnetic forces acting onto the undulators support structure and how strong would be the opposing magnetic field, which possibly could demagnetize the undulator magnets. Especially under the extreme conditions within a particle accelerator beam line, considering irradiation and heat flux (Curie temperature) this fact had to be considered carefully. To clarify these questions a software from Infolytica was used. Since this software was new to the group an approved open source software (RADIA [124, 125]) was used for benchmarking the results.

3.8.1 Software

As mentioned before two software packages were used, one commercially available software suite and one approved open source package for *Mathematica* developed by the *ESRF*. Both are described shortly in the following:

- **Infolytica** (finite element method (FEM) software [126]), divides simulation box by a triangular mesh in small elements. The potentials of the single elements are approximated by simple polynomial functions of the order 1 to three. Thus the problem simplifies to a set of linear equations, which can be numerically solved.

- **RADIA** (boundary integral method [124, 125]) differs from FEM. Here volume objects are created and material properties are applied to these objects. After subdivision into a number of smaller objects, the solution is performed by building a large matrix in memory which represents mutual interactions between the object parts. The final magnetization in each small object is obtained iteratively, but contrary to the FEM approach, meshing the vacuum is not needed and outer boundaries have not to be defined.

In comparison each software shows advantages and disadvantages:

- RADIA offers better computational speed because the number of elements required for a given precision on the prediction of the central field of an undulator is typically 20 times smaller in RADIA compared to an FEM code and the CPU time required is also typically 20 times smaller. In general, the peak field of a hybrid undulator can be obtained with a precision better than 1% in less than 10 seconds on desktop PC, while it would take a few minutes to hours with the FEM code. Thus scans over large parameter spaces are better done by RADIA as well as open box simulations.

A further advantage of RADIA is: once the Relaxation is done, the magnetic flux density and field integrals can be computed instantly anywhere in space independent from the distance to the field-producing objects since the field integrals are determined as analytical formulas. The precision on a field integral computed with RADIA only depends on the level of segmentation of the iron but not on the field sampling and boundary conditions at infinity as it is the case with FEM codes.

- The essential drawback of RADIA compared to a FEM code is the fast divergence of memory required for a given number of elements. In the present version of RADIA, the memory scales proportionally to the square of the number of elements. For example, one roughly needs 50 (13) MB of memory to solve a geometry made of 1000 (500) elements (which roughly corresponds to 20000 elements in a FEM code for a similar precision on the field).

  The other drawback is RADIA's complicated geometric modeling, which leads often to errors and time consuming programming.

In the end the Infolytica software was used for the optimization due to the possibility to generate more exact undulator geometries, with detailed chamfers and notches, which can be parametrized in a simple way. The results were then crosschecked afterwards by RADIA for the optimized case.

3.8.1.1 Boundary conditions

A way to decrease the numerical effort of the FEM simulations is, to limit the simulation volume. This can be effectively done using symmetries of the model and setting adequate boundary conditions. In case of an undulator, several symmetries can be used:

- A planar undulator is symmetric along the horizontal and the vertical axis. Thus the device can be divided in left and right, upper and lower girder, and only one part of each must be calculated.

- Since the undulator has an overall length significantly longer than a single period length, the problem can be treated as infinitely long along the axis, as long as only the central part of the field is of interest, neglecting fringe fields or in- and out-coupling of the electron beam.

- Since the undulator is a periodic device, only one period has to be considered. And even within a single undulator period symmetry exists, since the first half of the magnetic field slope is the same as the last half except for the algebraic sign of the magnetization.

- After all only a quarter pole and magnet has to be simulated, the 8th part of an period, reducing CPU efforts drastically.

To implement these symmetries, adequate boundary conditions must be set. In general there are two possibilities:

- *Dirichlet* or flux tangential boundary conditions - The magnetic field lines at the chosen surface have no vector component perpendicular to the mirror plane.

- *Neumann* or field normal boundary conditions - The magnetic field lines at the chosen surface have only a vector component perpendicular to the mirror plane.

3.8.1.2 Maximum and effective magnetic field

The optimizations first aimed for maximizing the magnetic field amplitude which is called peak field in the following. The photon yield in fact depends more critically on the so-called effective undulator field B_{eff} described in section 2.3.1. The magnetic field map used for the calculation of the effective field B_{eff} is shown in figure 3.22. Only a quarter period length is simulated due
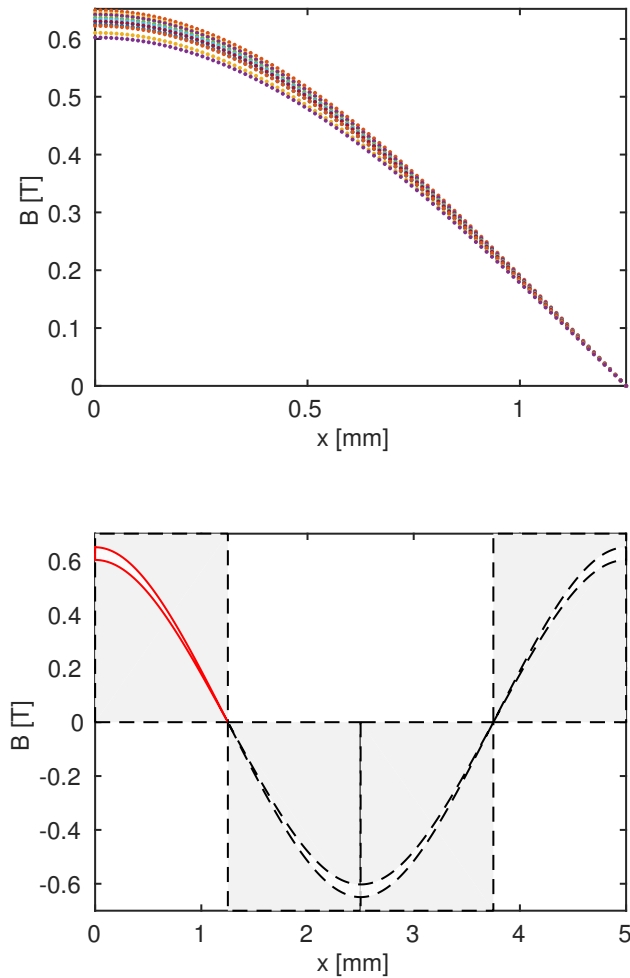
FIGURE 3.22: Magnetic field map used for the calculation of the effective undulator field B_{eff}. Only a quarter period length is simulated, the missing parts are completed with the data of the first quarter (permutation and change of algebraic sign).

to performance reasons, using boundary conditions which follow from symmetry, as described in the last section. Indeed, for the numerical calculation of the Fourier series, using Fast Fourier Transformation (FFT), one needs a continuous or rather periodic signal. The missing parts in the signal were completed by the data of the first quarter itself, by mirroring with appropriate algebraic signs.

3.8.2 Optimization of the LUX undulator

The idea of the optimization is to maximize the effective field B_{eff} of the undulator with 2 mm gap size and 5 mm period length. The optimization was first performed in 2D to further prune the optimization parameter range thus saving computational time.

3.8.2.1 2D optimization

First step was a 2D simulation to find the vertical extents of magnets and poles and the so-called overhang. For the given undulator period length of 5 mm, the magnetic on-axis flux density strength reaches a certain limit, and increasing the magnet size above a certain value yields only little gain. This is associated with the fact that the magnetic flux density of the pole material can exceed the magnetic flux density of the magnets but reaches saturation at a value of 2.35 T (see figure 3.8). Since the magnetization of the magnet material is only $B_{\text{r}} \approx 1.19$ T, the size of the magnets must be chosen greater than the extent of the poles in a specific ratio, to concentrate as much field flux as possible. This ratio is called overhang in the following, which is actually the ratio of the vertical or horizontal extent between poles and magnets.

2D model

In the figure 3.23 one can see the simulation model consisting of a quarter period length (more information about that can be found in section 3.8.1.1). The figure shows magnet (blue) and pole (red) and their corresponding FEM mesh. The horizontal width of both parts are neglected in the 2D case, or more precisely: assumed to be infinite. As in reality, the model features chamfers, which are presented inordinately scaled in figure 3.23 to better reveal their actual shape. The simulation mesh is adapted that way that regions where the magnetic flux density is expected to change rapidly in space are covered by a finer mesh. The simulation air box with their boundary conditions is not depicted to ensure a better view to the undulator model. They are directly attached on the outer faces on the left and right side of pole and magnet respectively. Vertically the lower boundary is situated at the middle of the gap, directly on the beam axis, in this case 1 mm below the pole tip. The upper border is set at the distance of three times the height of the magnet, measured from the upper side of the magnet. Thus only the upper part of a quarter period is simulated, as described in section 3.8.1.1. The model was proofed to be invariant with respect to a variation of the extent of the air box boundaries in the y-axis (vertical axis, see figure 3.23) and also to a further mesh refinement.
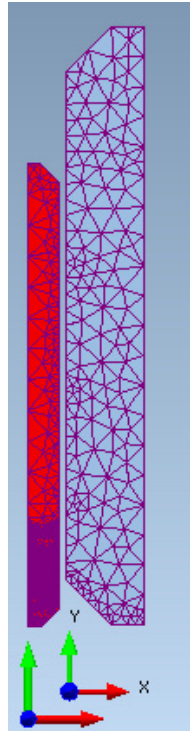
FIGURE 3.23: Meshed 2D model

3.8.2.2 3D optimization

The 3D scan start parameters were based on the results found by the much faster 2D simulations, to initially constrain the parameter space of the CPU-intensive 3D scan. Thus an assessment of the vertical dimensions could be made, as well as an estimation of the optimum overhang.

3D model

The used model is shown in fig. 3.24. The simulation mesh is adapted that way that regions where the magnetic flux density is expected to change rapidly in space, are covered by a finer mesh. Thus, especially at edges and corners, the meshing is fine. Again, the boundary conditions are not depicted. As in the 2D model, they are directly attached on the outer faces of on the left and right side of pole and magnet along the x-axis. Also along the y-axis the vertical boundaries set as in the 2D case. Along the z-axis, the boundary is on one side placed directly on the sectional plane on the left side, and at three times the distance of the magnets width on the right side.

3.8.2.3 Optimization method

It was found by Vilfredo Pareto in the 19th century [127] that in general one can find states of a system, where it is impossible to increase one of a selection of optimization goals without decreasing another of these selection. These states are known as Pareto efficient and can be
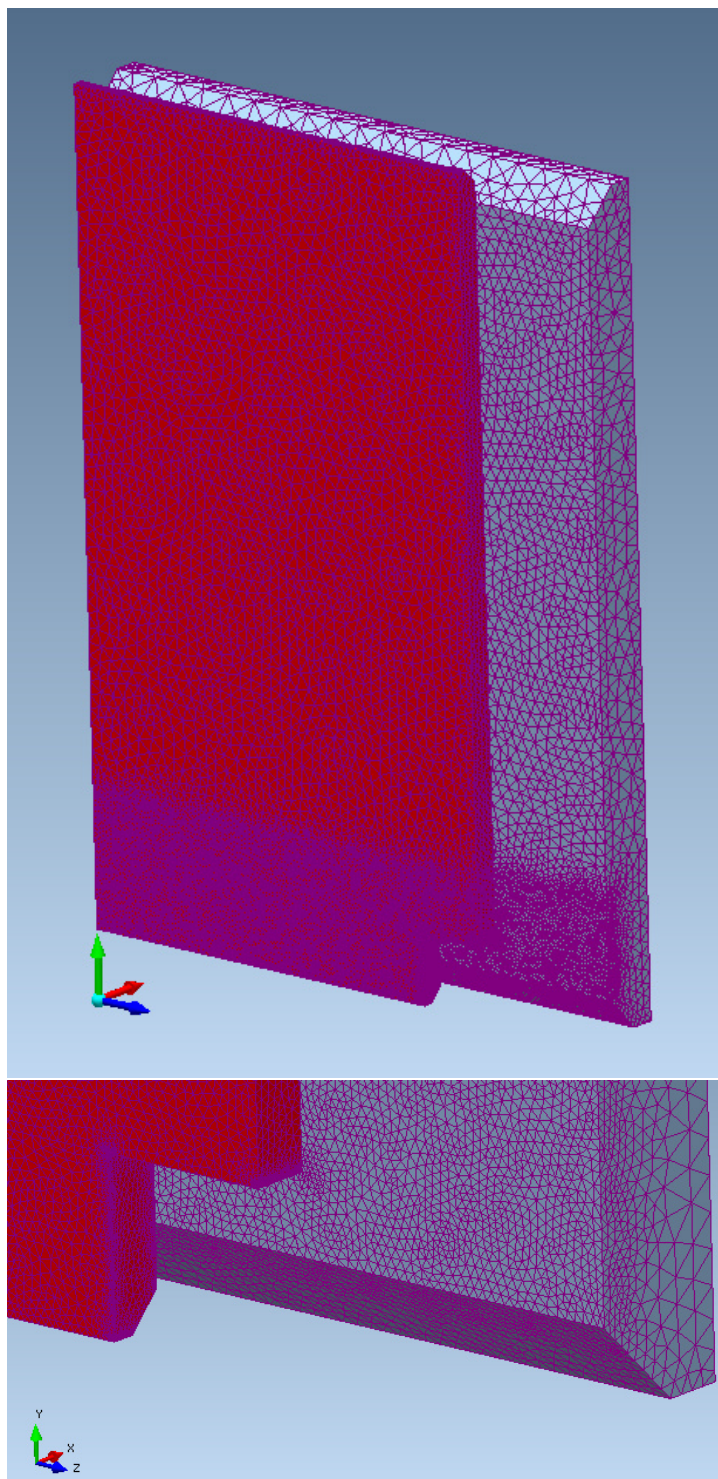
FIGURE 3.24: Meshed 3D model with a magnification of the chamfered edges with set manual mesh-refinement.

model parameter	lower limit [mm]	upper limit [mm]
Lx_{Mag}	1.6	1.7
Lx_{Pol}	0.67	0.74
Ly_{Mag}	20.9	29.9
Ly_{Pol}	19.0	23.0
Lz_{Mag}	8.8	15.6
Lz_{Pol}	8.0	12.0
volume	[mm^3]	[mm^3]
V_{Mag}	293.54	777.01
V_{Pol}	101.84	204.24
weight	[g]	[g]
m_{Mag}	2.26	5.98
m_{Pol}	0.83	1.66

TABLE 3.7: Parameter space of the 3D scan. Weight is calculated from the actual volume with densities of 7.7 g/cm^3 and 8.12 g/cm^3. The transverse (y/z-axis) dimensions are limited by the manufacturers die (mold) used for the production of the magnets - smaller geometries can not be produced and thus would not save resources.

represented by the outer boundary in the optimization parameter space, the so-called Pareto frontier.

The optimization goals for the planned undulator were to find a design case with a preferably high effective on-axis magnetic flux density using only small magnets minimizing the material costs this way. This case is represented by a 2D parameter space.

In the following it was found that it is possible to reach 98% of the effective field using magnets with a volume of only 50% from that value where the magnetic flux density on-axis first reaches its maximum.

The corresponding parameter range, which was scanned to find the Pareto frontier, was chosen on the basis of the results of a preliminary 2D scan. The resulting parameter range for each optimization parameter of the final 3D scan is given in table 3.7. These parameters where used then for a broadly conceived scan, where all geometric dimensions of the system were varied. Lx_{Mag} describes the extent of the magnet in x direction, which is in this case the direction of flight of the electrons. Lz_{Mag} describes the horizontal extent and Ly_{Mag} the vertical extent, as depicted in figure 3.24. The chamfers of the magnets were set to 0.2 to 0.4 mm due to manufacturing reasons. The parameters for the poles are tagged accordingly. Their chamfers were planned with 0.1 mm since the manufacturing of the pole material is more easy and tolerances can be kept tighter.

3.8.2.4 3D scans

In figure 3.25 & 3.26 the simulation results are presented in such way that the main figures of merit: the field flux and the volume of the magnets are plotted against each other.
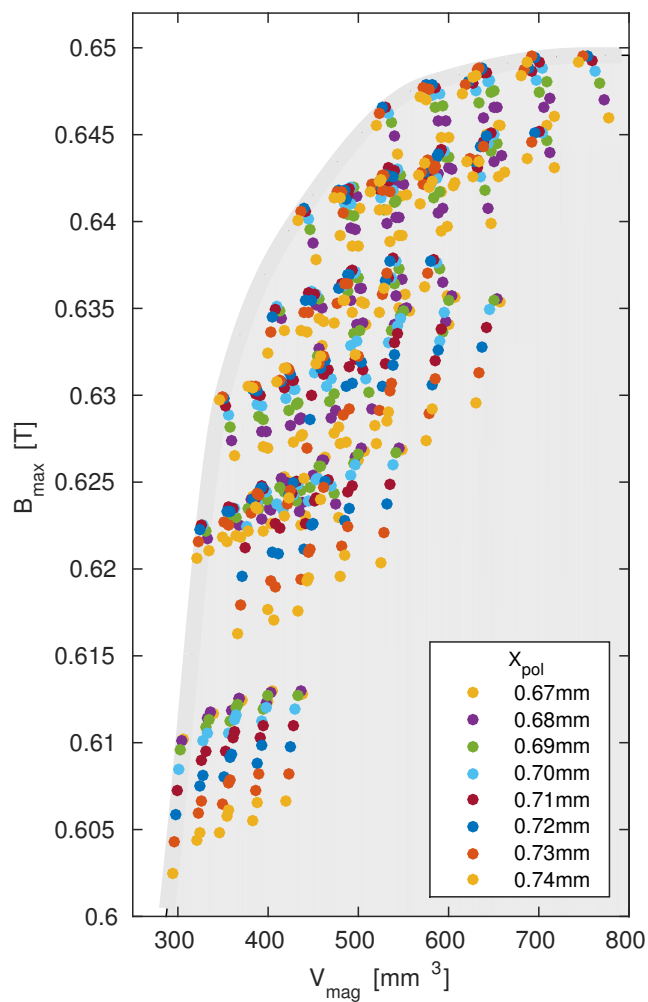
FIGURE 3.25: Volume optimization in 3D regarding the maximum undulator field $B_{\max}$. The colors represent the longitudinal extent of the poles while the undulator period length is hold constant at 5 mm. Therefore a thicker pole, implies a thinner magnet. The optimized setups are lying along the Pareto frontier (border of the Grey area). One can see that the optimal pole thickness of undulators with smaller magnet volumes shift from 0.73 mm to 0.67 mm. The upper 8% in terms of the maximum magnetic flux density were simulated and by conserving almost two third of the magnets volume only these 8% of field flux density is lost choosing the right magnet geometry.
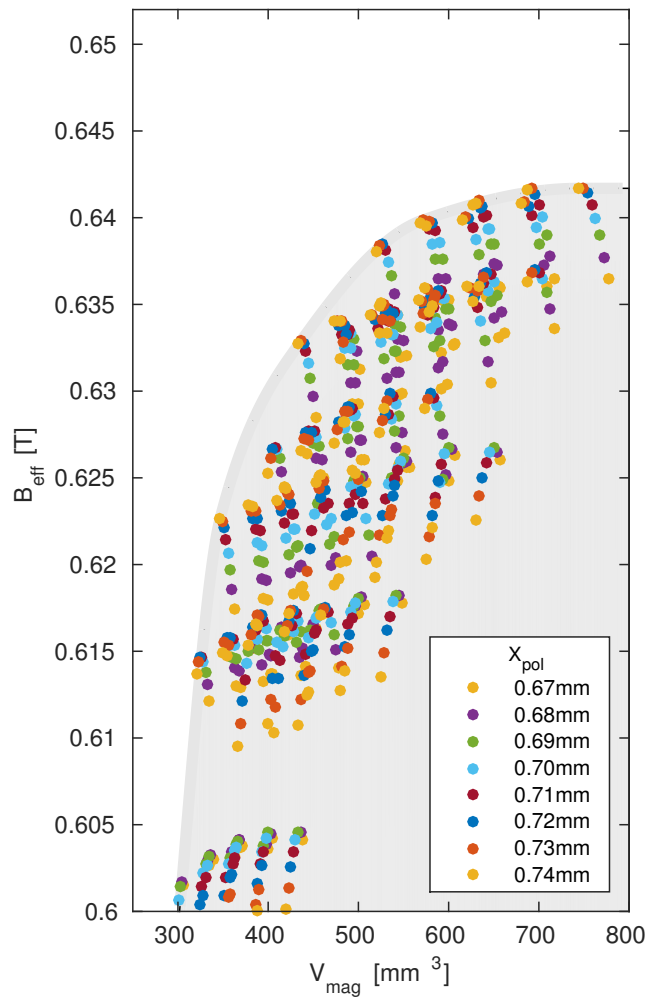
FIGURE 3.26: Volume optimization in 3D regarding the effective undulator field B_{eff}. The colors represent the longitudinal extent of the poles while the undulator period length is hold constant at 5 mm. Therefore a thicker pole, implies a thinner magnet. The optimized setups are lying along the Pareto frontier (border of the Grey area). One can see that the optimal pole thickness of undulators with smaller magnet volumes shift from 0.73 mm to 0.68 mm. The longitudinal pole extent is slightly broader compared to the maximum undulator field optimization. As seen in figure 3.25 also here the upper 8% in terms of the effective magnetic field strength were simulated and by conserving almost two third of the magnets volume only these 8% of flux density is lost choosing the right magnet geometry.

The undulators magnetic performance is on one case described by its maximum field flux, and on the other case by its effective field, which is in fact the sum of the first few coefficients of the Fourier series expansion of the magnetic field along the undulator axis. One can see that the maximum field is about 1.5% higher than the effective field, but it shows the same trend for a variation of the magnets volume.

Every simulation result is color-coded. The colors represent the longitudinal extent of the poles. The pole thickness is varied this way that the undulator period length is hold constant at 5 mm. Therefore a thicker pole, implies a thinner magnet. Since the pole (magnet) thickness is one of the key parameters, the simulation results show clusters of multicolored points, where a specific geometric configuration varies drastically with its corresponding pole (magnet) thickness.

One can see that for every configuration (a specific magnet geometry together with a specific pole geometry), there is an optimal ratio of magnets and poles longitudinal thickness. One can also see that for lower flux densities the optimal pole thickness becomes thinner. Along the Pareto frontier the pole thickness varies from almost 0.74 mm to 0.68 mm. This shift of the optimum is supposedly given by the fact that magnets with increased volume generate simply more absolute field flux. Thus more flux can be induced into the poles increasing the flux density inside the poles. However, at a certain flux density the magnetization of the pole material reaches saturation. If one increases the magnets volume further, ipso facto the pole volume decreases and less field flux is lead into the undulator gap. Thus the optimum ratio between the longitudinal thickness of poles and magnets shifts from thinner poles and thicker magnets at lower field flux values to thicker poles and thinner magnets at higher field fluxes. This is described in figures 3.25 & 3.26 by the value of the pole thickness, which is connected to a corresponding magnet thickness.

The highest field flux is reached by configurations consisting of magnets which have at the same time higher volumes but also lower longitudinal extents. This means that the optimal geometric design tends towards large and flat magnets. This kind of geometry can be problematic, since the dipole field of the magnet impends to demagnetize parts of the magnet itself. Therefore a stability check for the magnet material 3.8.3 was necessary.

3.8.2.5 Optimization results

To allow a better understanding of the data, specific setups along the Pareto frontier are exemplified in the following. The chosen setups are marked by red circles in the parameter space in figure 3.27 & 3.28. The exact values of the corresponding geometric properties can be found in the appendix D.

The range of the optimization parameters was chosen regarding the following considerations: Due to the fact that the manufacturer used the smallest available die (mold) for the manufacture of the magnets, the parameter ranges of the longitudinal and vertical extents were limited to 8.8 mm horizontally and 20.9 mm vertically as a lower limit. Smaller magnets below that values could be produced, but only by cutting of large parts of the magnets after fabrication, which does not reduce the price. As upper limit 15.6 mm was chosen horizontally and 29.9 mm in the vertical

dimension. A preliminary 2D simulation set the starting point of the pole thickness to 0.7 mm. A range of plus minus 50% from that value seemed appropriate and was varied with steps of 10 µm. In general the magnetization saturation of the pole material is higher (in this case 2.35 T compared to 1.19 T) than the remanence of permanent magnets. Thus a design was chosen which uses greater magnets than poles in the transverse (horizontal and vertical) direction, to induce as much magnetic field flux as possible into the poles. The range of the pole extents were set ranging from 8.0 mm horizontally and 19 mm vertically as a lower limit to 12 mm and 23 mm, thus leading to an overhang of the magnets of 10-30% above the poles in each transverse direction.

The simulated parameter space covers a selection of undulator setups generating 0.6 T to 0.65 T of magnetic flux density. Thus the upper 8% in terms of flux density were simulated and compared to each other by the performed parameter scan. Looking and comparing figures 3.25 & 3.26 a few general facts become apparent.

It does not matter if the maximum or the effective magnetic field is the optimization goal, the selected setups along the Pareto frontier show the same vertical and horizontal extents of both magnets and poles. On the right-hand side (greater volumes) of setup 5 both of the magnetic field measures, the effective and maximum measure, reach a maximum as the poles reach their saturation magnetization of 2.35 T. As a result setup 4 (see table 3.8) was chosen as geometry for the new 5 mm period length undulator saving almost 50% of the magnet material providing nevertheless 99.7% of the maximum magnetic flux density and the effective field compared to the reference setup. Thereby only a very small loss in magnetic flux density (0.3%) is expected while using a reasonable amount of resources. The regarding parameters of the geometric model are listed in appendix D.
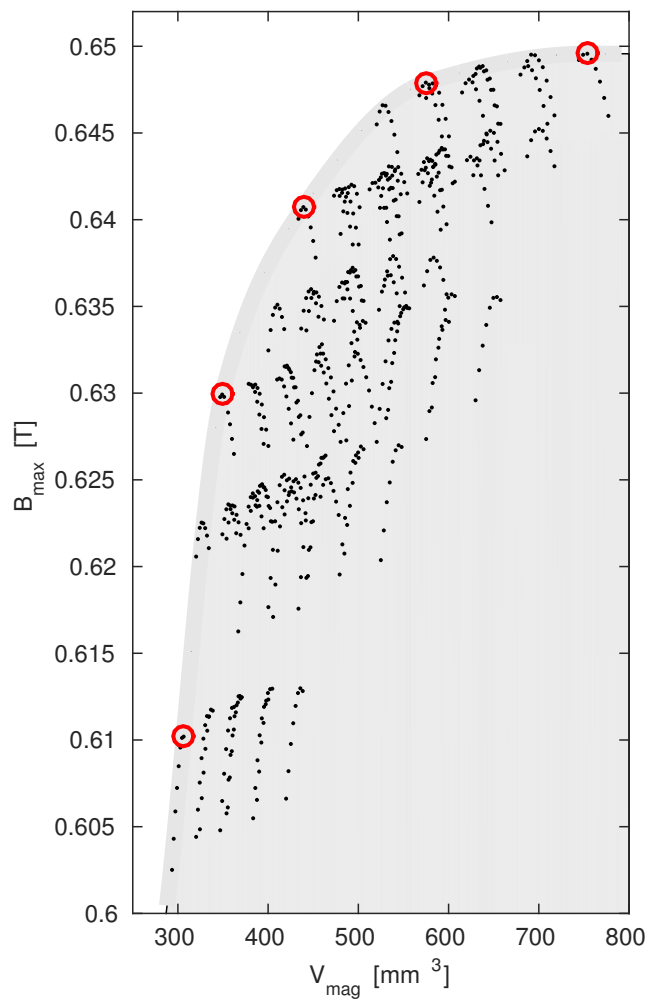
FIGURE 3.27: The optimized setups are directly located along the Pareto frontier (border of the Grey area). Five setups were chosen for a direct comparison and a closer analysis. The corresponding geometric parameters are listed in appendix D.
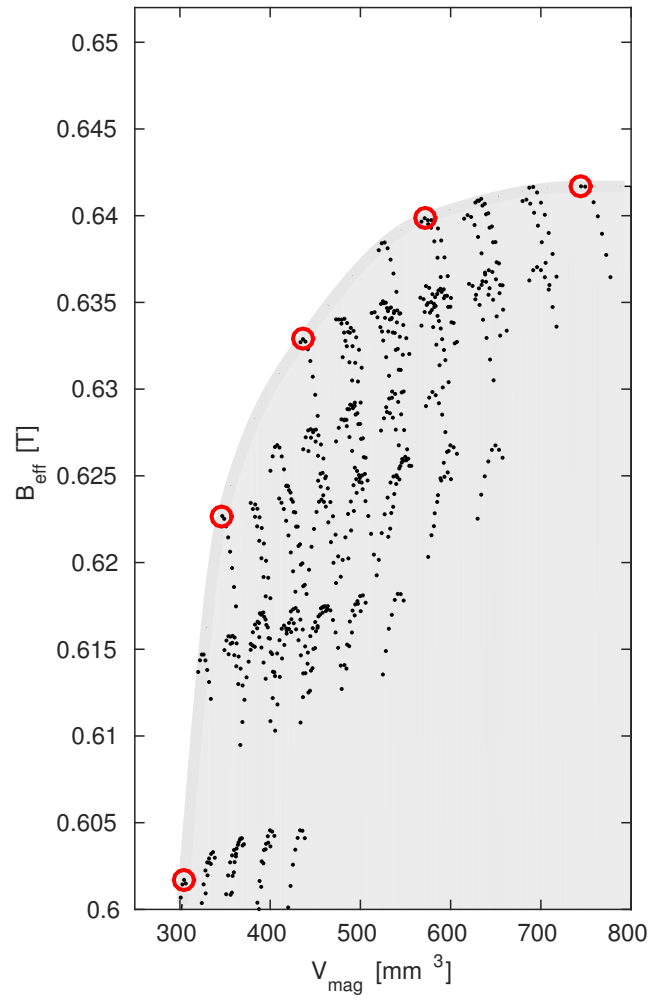
FIGURE 3.28: The optimized setups are lying along the Pareto frontier (border of the Grey area). Five different were chosen for a direct comparison. The corresponding geometric parameters are listed in appendix D.

3.8.3　Magnet stability check - operation point and permeance

Finally the chosen magnetic design must be reviewed, in terms of demagnetization stability of the system itself. Therefore the model with the final parameter setup was analyzed regarding magnetic flux density B and the actual field strength H on the center plane (where the flux density B is parallel to the plane normal of the simulation boundary) inside the magnet thus specifying the operation point of the system. The operation point was then marked along the demagnetization curve (also called normal curve, which is in fact the second quadrant of the hysteresis loop) of the used material (VACODYM 890 TP). The result is shown in figure 3.29 with data provided by the manufacturer *Vacuumschmelze*.

One can see that the operation point is far away from the edge of the curve, also called knee, where the slope of the curve becomes nonlinear (at about 2600 kA/m). This implies a high stability of the magnetization of the magnet. The situation of the operation point is not surprising since the used magnet material has one of the highest coercivities (2625 kA/m) of all commercially available magnet materials and thus it should be of high stability.

Simulation data revealed that the mean opposing field strength is about $H_{mean} = 823$ kA/m, shown in figure 3.29, with a maximum value of $H_{max} = 920$ kA/m. This defines together with a magnetic flux density B of 0.12 T the operating point of the magnet, shown as red dot in the figure. The resulting averaged permeance coefficient P_c is -1.8271×10^{-5}.
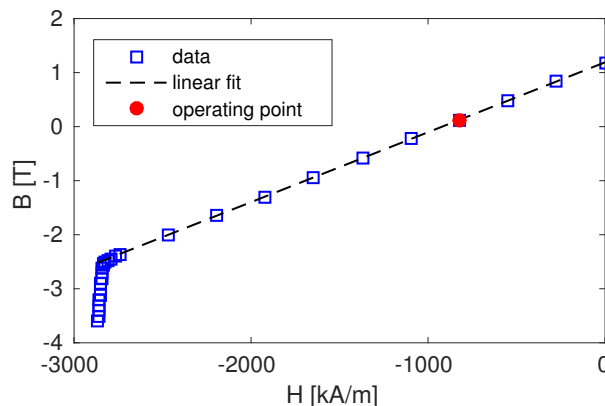
FIGURE 3.29: VACODYM 890 TP - fit to material data see appendix C, measured by *Vacuumschmelze*. Simulation data reveals that the mean oposing field strength is about $H_{mean} = 823$ kA/m with a maximum value of $H_{max} = 920$ kA/m. Together with the magnetic flux density (B) of 0.12 T it defines the operating point of the magnet, shown as red dot in the figure. In this case the operating point is located within the linear (reversible) region of the normal curve. The resulting averaged permeance coefficient P_c is -1.8271×10^{-5}.
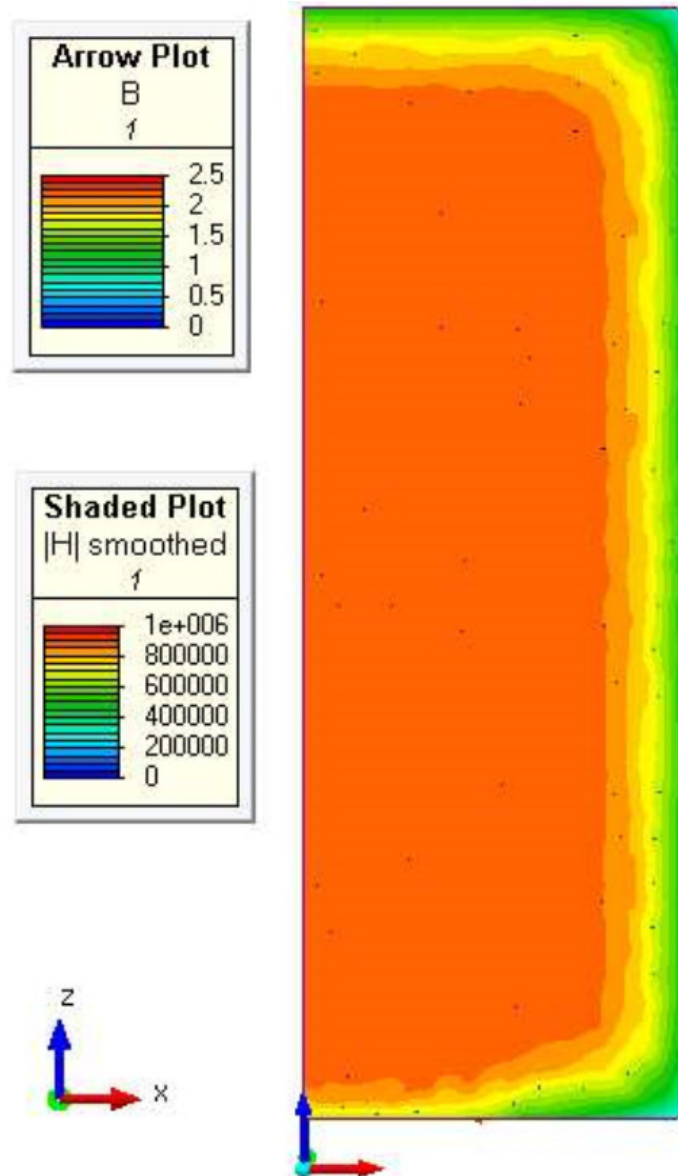
FIGURE 3.30: Magnetic flux density B and field strength H simulated with software from *Infolytica*. The model matches figure 3.24. The viewing angle is set from outside directly onto the center plane of the magnet. Thus one can see flux density and magnetic strength inside the magnet. The simulation visualizes that the maximum value of the magnetic strength is about $H_{max} = 920$ kA/m here. The magnetic flux density B is depicted as arrows with the length proportional to the value of B. As the value is only about 0.12 T inside the magnet the arrows are small.
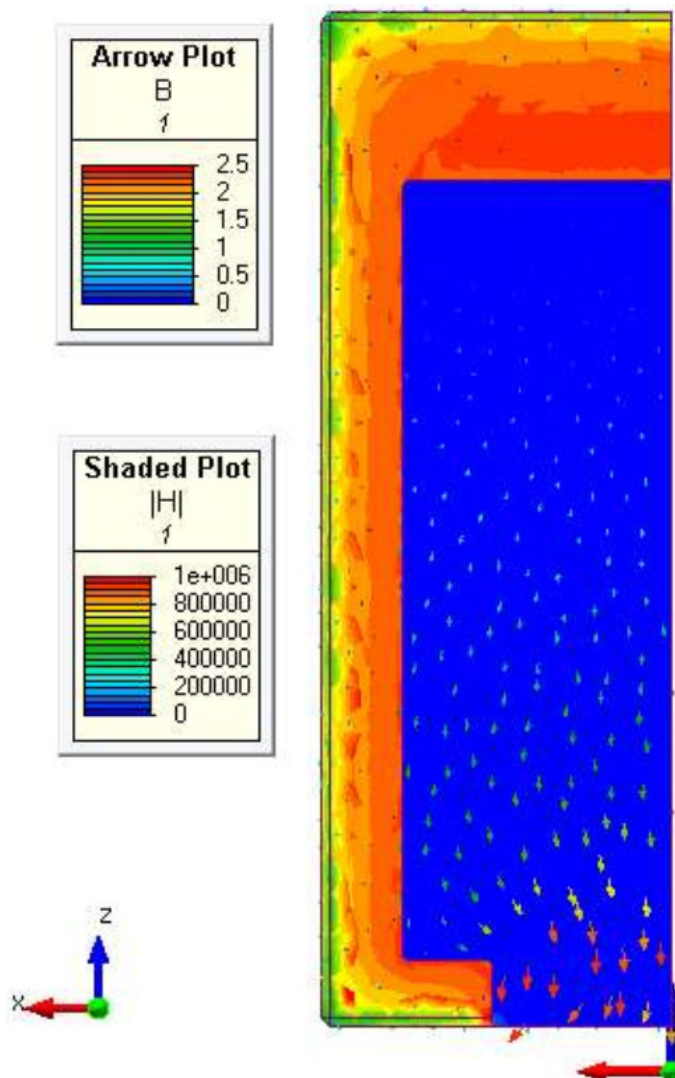
FIGURE 3.31: Magnetic flux density B and field strength H simulated with software from *Infolytica*. The model matches figure 3.24, but this time the other side of the model is shown and one can see flux density and strength on the central plane of the pole. Parts of the pole are in saturation as the magnetic flux density B is above 2 T. The direction of B points towards the undulator gap, which is at the bottom of the picture. H also called magnetic potential is small inside the pole since the permeability of the pole material is very high.

3.9 Discussion of the resulting geometric design

In this chapter the design of an undulator dedicated for the generation of synchrotron radiation at an PWA electron beam line was planned. In the first sections an empiric formula describing the undulators on axis flux density and thus the K parameter was used to find an optimal period length for a gap size of 1 mm and a magnet material providing a strong remanent field strength as long as a good demagnetization resistivity.

The final decision came to an undulator design with 5 mm period length, to maximize the photon flux of the fundamental wavelength at a short wavelength. The magnetic material (VACODYM 890 TP) from *Vacuumschmelze* was chosen on the basis of its high coercivity $H_{cJ} = 2625$ kA/m. A GBD treatment was arranged to further increase the magnets resistivity against demagnetization from incident particles. This demagnetization loss was estimated roughly to about 2.5 % after one year of intensive daily operation of the undulator beamline with a PWA.

In the second part of the chapter the simulations and optimizations of the physical undulator model and its magnetic flux density were described. The final setup reached about 99% of the possible magnetic flux density saving almost a quarter (23%) of the magnet material, reducing thereby the costs of the undulator drastically. The final setup has the parameters shown in table 3.8.

Magnets and poles with geometries matching this setup were ordered and manufactured. The undulator will be assembled and commissioned at the PWA electron beam line at *DESY* Hamburg a commissioning was intended for 2017.

final setup: model parameter	optimization goal	
	maximum field [mm]	effective field [mm]
Lx_{Mag}	1.616	1.606
Lx_{Pol}	0.72	0.73
Ly_{Mag}	22.8	22.8
Ly_{Pol}	19.0	19.0
Lz_{Mag}	15.6	15.6
Lz_{Pol}	12.0	12.0
volume	[mm^3]	[mm^3]
V_{Mag}	574.78	571.22
V_{Pol}	164.16	166.44
result:	$B_{\max}$	B_{eff}
field	0.648 T	0.640 T
$\Delta B/B$	0.997	0.997

TABLE 3.8: Optimization result - final setup.

3.10   Outlook

Another PWA electron beam line of our group is currently under construction at the Center for Advanced Laser Applications *CALA* in Munich. The heart of this research institute will be a high power laser system at the Petawatt class. Electron energies of more than one GeV are proposed and especially for this beam line another light source will be planned.

Thanks to the fact of the higher electron power one can consider longer undulator period lengths for this beam line, yielding more photons. The used models could serve again with a modified electron energy but the optimizing strategy in general could remain the same.

First experiences of the commissioning of the undulator at *DESY* should serve for further optimizations of the design, especially of the support structure of the undulator.

The idea described in section 3.3.4 of a over-saturation of the poles to compensate a possible loss of magnetization due to irradiation of the magnets should be considered for more irradiation tolerance. Even if the design of the undulator is aimed for stability against demagnetization it seems possible that the magnets will be damaged by the time. Electrons can not always be perfectly guided when electron bunches with large absolute energy spreads from PWA's are used. These highly divergent sources must be caught by beam optics (in most cases quadrupole lenses) intrinsically featuring chromaticism.

If these kind of demagnetization damages become apparent another idea to prevent the demagnetization is to place a collimator in front of the undulator.

Chapter 4

Evaluation of manufacturing tolerances of a PWA based FEL undulator

4.1 Introduction

This chapter presents a tolerance study, which was made against the background of a proof of concept lab scale XUV Free Electron Laser experiment based on a Plasma-Wakefield Accelerator (PWA) being planned. First the main concepts of the technologies are shortly introduced, for more background information see section 2.5.

A **Free Electron Laser (FEL)** is an ultra brilliant, highly coherent, tunable light source. The basic principle is the same as in conventional undulators but due to the stimulation of interactions between light and electrons self-amplification processes are enabled.

Also here a relativistic electron beam is used generated by a particle accelerator as a source medium for the creation of light. The electrons emit light while being transversally accelerated by the Lorentz force which is generated by alternating magnetic fields. These fields are oriented perpendicular to the direction of flight, provided by magnetic devices called undulators. Inside of these devices the electrons are thus forced to a sinusoidal track. During their flight the electrons interact with light previously emitted from electrons lying more rearward. This interaction modulates the distribution of the electrons and a clustering which is called micro bunching of the electrons evolves. This way the electrons order themselves in slices equally separated at the distance of one wavelength of the emitted light. As a result, constructive interference takes place and spatially (longitudinally and transversally) coherent light is emitted. A short introduction is given in 2.4 and more detailed information can be found in [128, 129].

As mentioned before, in the case at issue, the used electrons are accelerated by an alternative accelerator concept, a **Plasma-Wakefield Accelerator (PWA)**. The idea of this type of particle

accelerator is using the electric fields of a plasma for the acceleration and was first suggested by Tajima [28] in 1979. With the development of high power laser systems the experimental realization become possible several years later. Focusing a high power short pulse laser into a gas and thus ionizing it, a highly ionized plasma bubble is generated. Due to the ponderomotive force of the laser, the electrons are driven out of the bubble and an electron free space is emerging, providing strong electric fields. Within the electric field of the plasma bubble, which is about three orders of magnitude higher than the electric fields of conventional electron accelerators (about several 10 MV/m compared to hundreds of GV/m), the particles reach energies above 1 GeV at distances of a few centimeters. A more detailed description about mechanisms and properties of PWA is given in [130–132].

The relativistic electrons are then inserted into undulators as described above. To guarantee an undisturbed interaction between electrons and photons, the electron motion and the light wave must be phase matched. This demands a homogeneous electron bunch in terms of energy and direction of motion, with a high density in phase space. On the other hand the magnetic field should be ideally sinusoidal with a constant amplitude and a periodicity as accurate as possible. The aim of this work is therefore to check if the achievable manufacturing accuracy of the undulator would be sufficient for the success of the planned proof of concept lab scale XUV Free Electron Laser experiment based on a PWA.

For this purpose, a statistic ensemble of undulators with main parameters matching the requirements for the mentioned PWA FEL's experimental setup described by [133, 134] was simulated, involving all mechanical manufacturing tolerances with significant impact to the field quality.

Two magnetic error characteristics established as key parameters for the undulator design [84]. One affects the radiation bandwidth of the spontaneous undulator radiation, the other the FEL gain length and saturation power of the evolving FEL signal. These key figures are:

1. The relative deviation of the K parameter $\Delta K/K$ describing the relative variation of the magnetic peak field and the bandwidth of the spontaneously generated light pulse.

2. The RMS phase shake Ψ_n, which describes the quality of the longitudinal synchronization between electrons and radiation and thus the quality of the interaction between light and electron bunch.

The ambitious aim of the final experiment is the demonstration of an FEL signal in the undulator radiation spectrum produced from PWA electron bunches. These electron bunches are generally affected by an energy spread of a few percent. Recent studies [133] have shown that the slice energy spread can be reduced by longitudinal decompressing the electron bunch in a chicane. If the slice energy spread could be reduced below 0.25% a successful proof of principle experiment comes within reach, as theoretically shown by [135]. Seggebrock [4] states in his work, that the slice energy spread itself can be interpret as an RMS phase shake by the following expression :
$\sigma_{\Psi_{\Delta\gamma}} = \frac{4\pi}{\lambda_u} \frac{\sigma_\gamma}{\gamma} L_g.$

This defines a natural limit for the RMS phase shake of the FEL undulator: If the phase shake can be reduced below 0.35 mrad (or 20°) the gain reduction is dominated by the slice energy

spread induced phase error. The simulations following in the next sections were performed to check if the mechanical tolerances due to the manufacturing of the undulator hold this limit or not.

4.2   Model generation

For the simulation of the magnetic field and the field errors inside the undulator RADIA is used. This code allows for a fast and robust calculation of a fully parameterized model undulator containing all major mechanical sources of undulator field errors.

This model includes:

- Magnet size deviations in all three dimensions. The size of the magnet was varied up to 35 µm in each direction.

- Magnetization errors in terms of magnitude and angle variations. The magnitude is varied up to 5% and the angle deviations up to 2 deg.

- Pole size deviations in all three dimensions to an extent of up to 10 µm.

- Positioning errors of poles and magnets along the longitudinal and the vertical direction of up to 50 µm.

In a first step every kind of error was treated separately to analyze the impact on the field quality of each error type. For this purpose 7 ensembles of undulators were generated, each containing 10 randomly generated undulators sharing the same standard deviation of the observed defect. The standard deviations were chosen to be in the range of realistic manufacturing tolerances. The randomly generated undulators hold 33 periods and not the proposed, full length of 133 periods. This is necessary due to a lack of computer power, but in the following a phenomenon is described that ensures that the simulating of a longer device is not necessary.

Light emitted by the electron bunch propagating through the undulator is faster than the electron bunch itself, resulting in a certain distance at which the light pulse overtakes the electron bunch and leaves it completely behind. In the described decompression lab-scale FEL scenario the longitudinal bunch length σ_z is about 2 µm, and the wavelength of the light is about 135 nm. Thus it takes 30 ($\widehat{=}2\sigma_z$) periods until a photon from the previously emitted light from the tail of the bunch overtakes the electrons at the first position in the bunch as the photon travels with the speed of light. Hence after 30 periods, the spatial overlap between the light pulse and the electrons is lost completely. This distance is also called interaction length [4] and information cannot be passed further than 30 periods and with it, the phase error before and after that interval is without any consequence.

Two other accuracy relevant options for the RADIA simulation were set to the following limits: The accuracy of the relaxation method is set to 0.5 mT. The step size of the tracking routine is set to 500 µm.
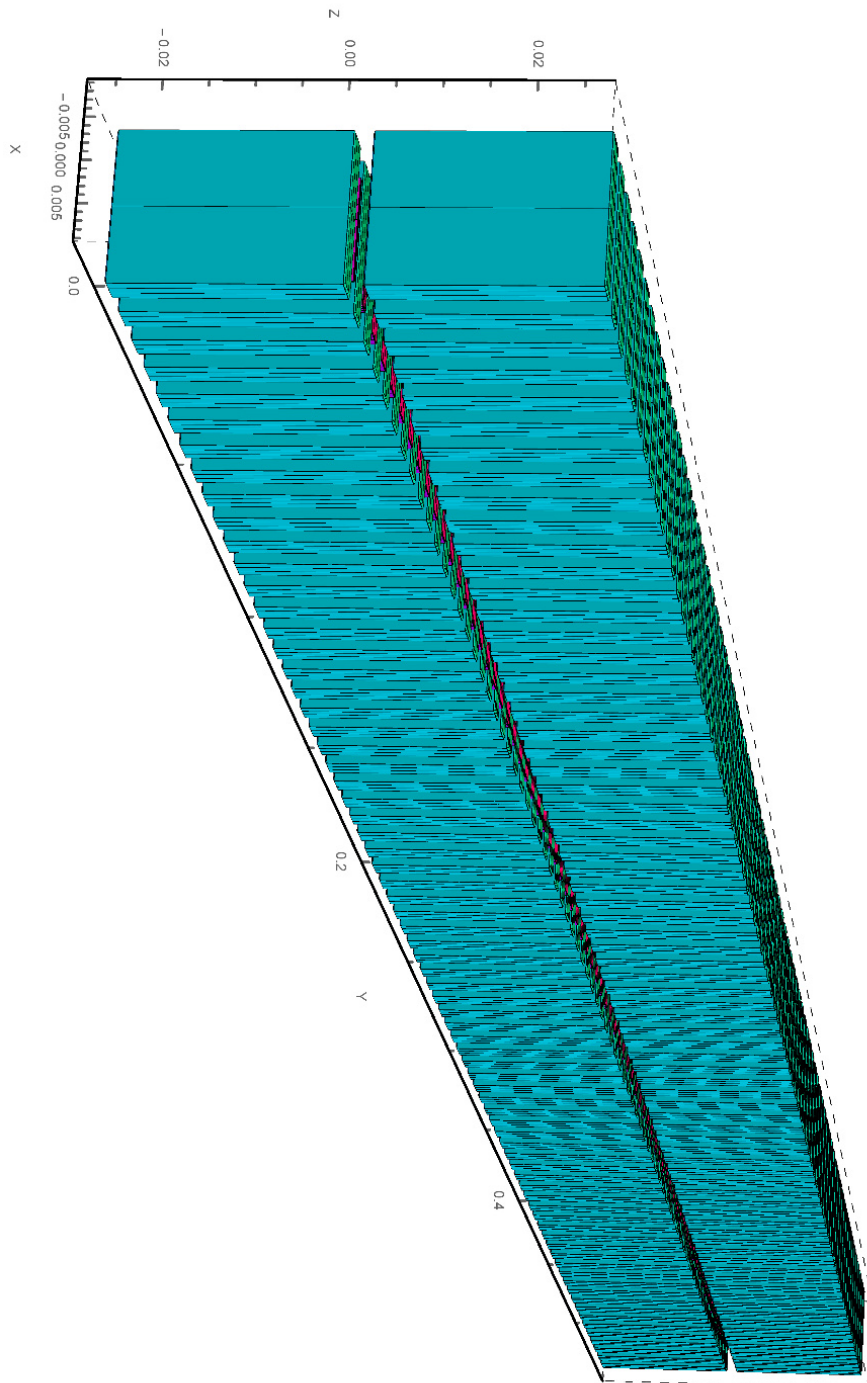
FIGURE 4.1: RADIA model of an undulator with 33 periods including parameterizations for magnet size deviations in all three dimensions, magnetization errors in terms of magnitude and angle variations, pole size deviations in all three dimensions and positioning errors of poles and magnets along the longitudinal and the vertical direction.
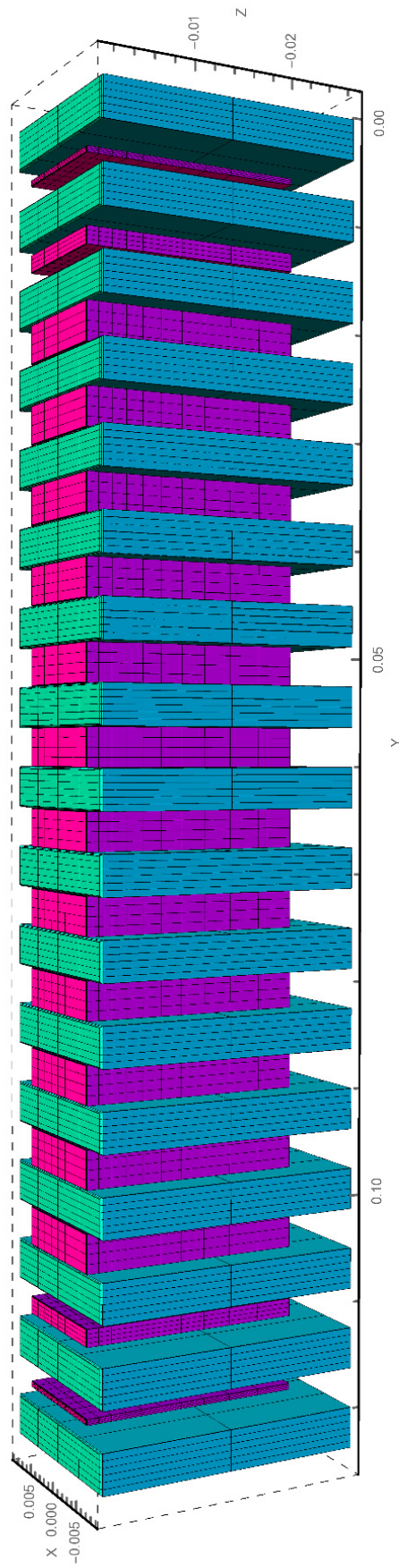
FIGURE 4.2: RADIA model of the lower array of an undulator with 8 1/2 periods used for testing the robustness of the actual undulator model, which has 33 periods, shown in figure 4.1.
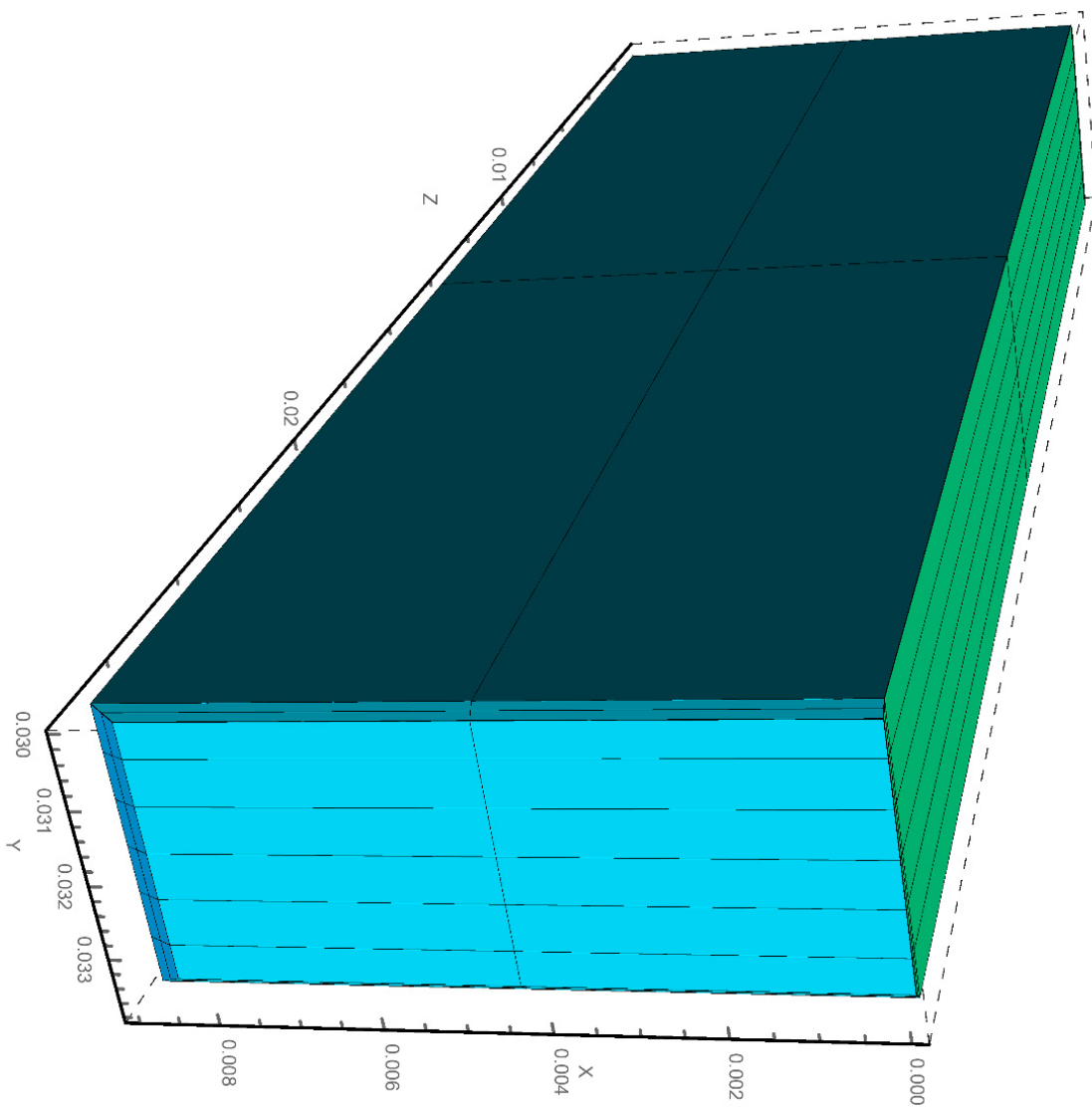
FIGURE 4.3: RADIA model of the magnet used as reference in the robustness test model. Since the magnet is mirrored along the X-axis at the Y-Z plane the magnet is composed in X,Y,Z of 4,6,2 segments. The top and bottom (at Z=0 mm and Z=28 mm) has a chamfer with a finer segmentation to resolve fringe effects at the edges.
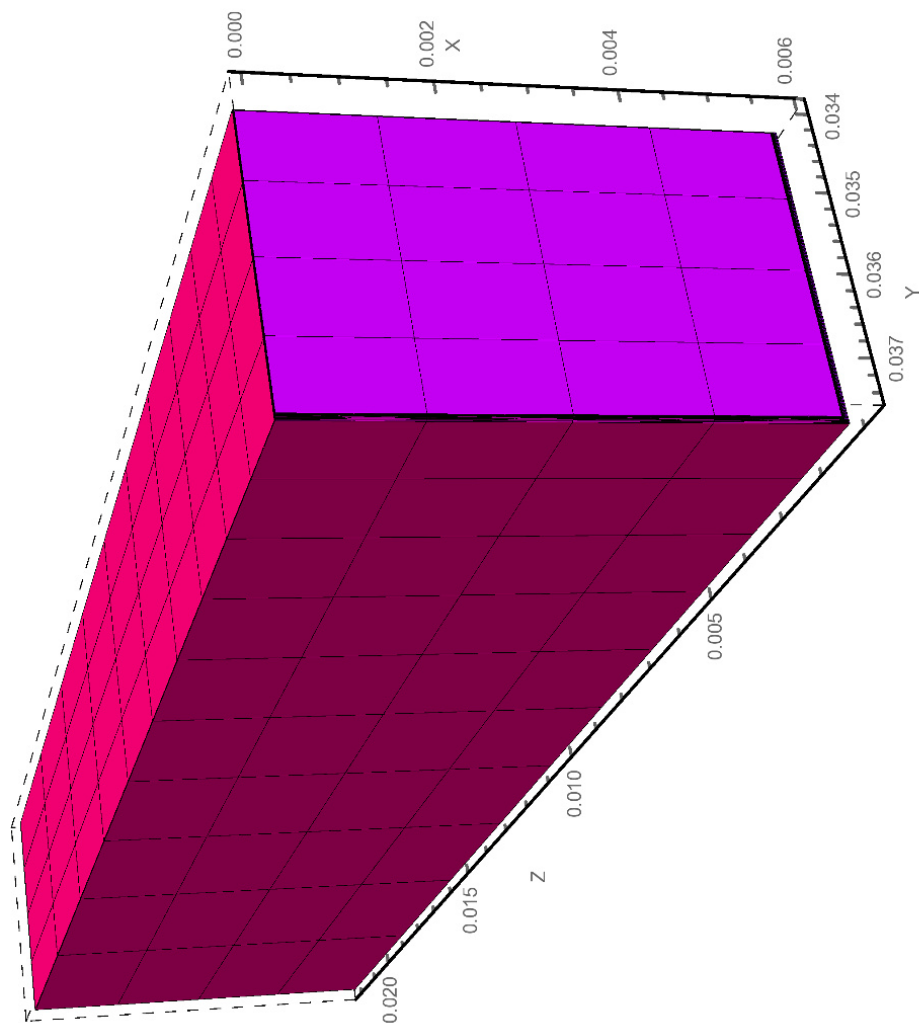
FIGURE 4.4: RADIA model of the pole used as reference in the robustness test model. Since the pole is mirrored along the X-axis at the Y-Z plane the magnet is composed in X,Y,Z of 8,4,10 segments. The top and bottom (at Z=0 mm and Z=20 mm) has a fine chamfer with an additional layer to increase the segmentation locally in order to resolve the higher field gradients at the edges of the poles.

Another important parameter of the simulations is the segmentation of the model, which defines a grid of nodes where the actual field values are calculated. The robustness of the simulations concerning a variation of the segmentation was tested before the simulations were carried out. The results of the tests are presented in the next section. Before that the model is shown in figures 4.1 to 4.4. In figure 4.1 one can see the complete undulator model with 33 periods consisting of two arrays with two magnets (blue) and poles (red) on each side. Figure 4.2 shows one array with 6 and a half undulator periods plus in- and out-coupling period for a better view. The segmentation is finer than in the final undulator model. In figure 4.3 the geometry of the undulator magnets is shown. Only one half of the magnet is simulated using symmetry to optimize the performance of the calculation. One can see that the edges of the magnet are radiused as in reality. The radii of the poles shown in figure 4.4 are smaller than these of the magnets due to manufacturing reasons.

4.3 Test of simulation robustness

The robustness of the model is tested by comparing differently segmented undulator models. The undulator model used for the robustness tests consisted of only three periods (six magnets and poles in each girder). This helped minimizing CPU time and main memory resources, in general the memory was limited to 32 GB in our case. RAM was fully used in case of the fine segmentation tests with the three period undulator as well as for the tolerance studies with undulator models holding 33 periods. During the test magnet and pole segmentations were varied separately according to table 4.1. While the segmentation of the magnets did not have a significant impact on the on-axis field simulations the segmentation of the poles is more critical. In figure 4.5 the resulting magnetic fields and their deviations are shown.

Three color groups are used, blue, green and red. These basic colors tag the pole segmentation according to table 4.1. The segmentation of the magnets is tagged varying the brightness of the used basic colors, but except for the roughest pole segmentation, visible as dark red curve, the field maps overlap each other, and almost no variation of the field could be recognized for the magnet's segmentation variation test.

In figure 4.5 the difference of the undulators magnetic field to the reference case (finest segmentation) is shown. Here one can see that the segmentation used in the further simulations, called standard and marked with green color, has a mean relative deviation from the reference of about

Segmentation X,Y,Z	fine	standard	rough
Magnets	4,6,2	2,3,1	2,1,1
Poles	8,4,10	4,2,5	2,1,1

TABLE 4.1: Segmentation of the robustness-test undulator model. The software used for all simulations is RADIA [124, 125] developed by the ESRF. The minimum segmentation in the X-direction is 2 since in this direction the model is mirrored to save computer resources. In the other directions mirroring was not an option since in these directions every magnet and poles was randomly modified in its size and position.
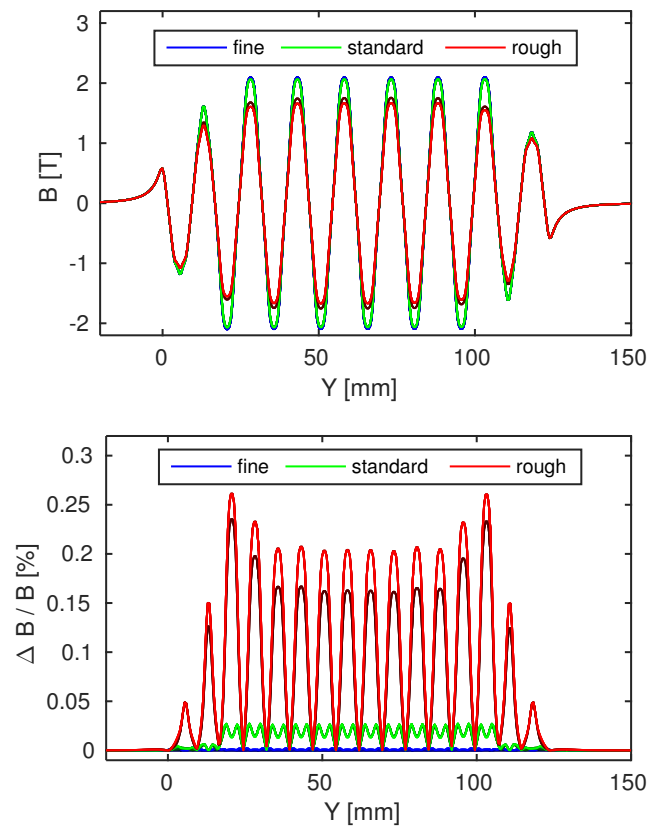
FIGURE 4.5: A variation of the segmentation described in table 4.1 leads to numerical errors of the undulator field. In the upper figure the absolute values of the undulator field are presented, in the lower graph the relative deviations are plotted. Both, the segmentation of the magnets and the poles, were varied and visualized by color. Whereas the base colors (red, green, blue) distinguish between the three grades of the pole segmentation, the brightness of each color shows the quantity of segments of the magnets. The darker, the finer the magnets were divided. The exact quantity of segments for both magnets and poles, is described by numbers in table 4.1. One can see that the magnets segmentation is less important for accuracy. Only in case of the rough pole segmentation (red), there is a notable difference in the field values. The rough magnet segmentation becomes distinct in that case, as dark red line. In all other cases the magnet's segmentation is insignificant and all differently bright lines overlay each other. The used segmentation for the tolerance study is called standard (see table 4.1) and shows a systematic deviation of about 0.025% to the finest segmented model (blue).

0.025%. The deviation fluctuates around that value, in the wake of numerical artifacts which are not significant for the following investigations.

4.4 Variation of magnet size

The first variation test regards the magnet size which can vary about 30 µm due to the manufacturing process. The magnets are usually produced in a die press. The workpiece, a long cylindrical bar, is exposed to a strong magnetic field then, and simultaneously heated. This way, the powder grains are magnetically aligned along the external magnetic field and fixed in that orientation by a sintering process of the material. Afterwards the particular magnet blocks are cut from the rough cast, ground by rotofinishing and coated with a TiN layer. This coating is
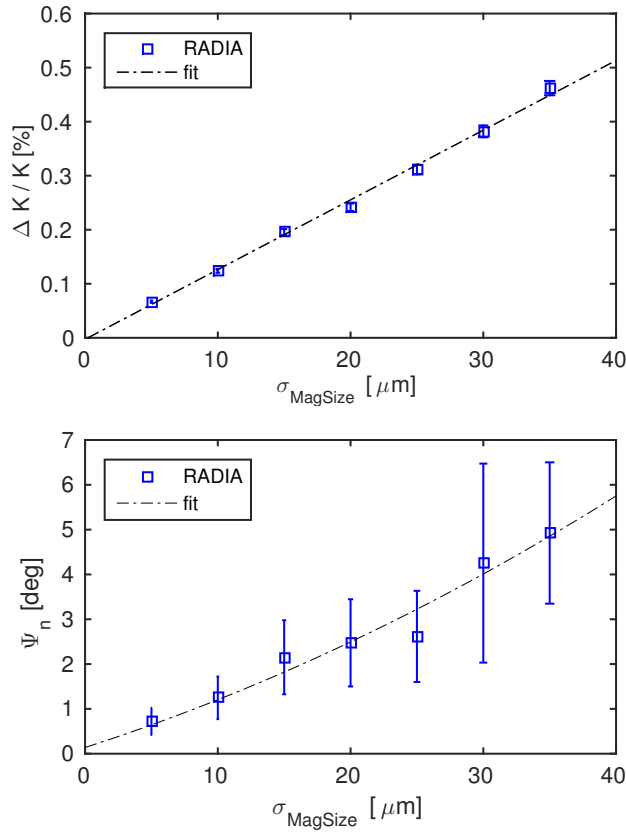
FIGURE 4.6: A typical manufacturing tolerance for the sintered magnet blocks is about 30 µm. This results from surface treatment, the grinding process and the surface coating with TiN. Whereas the relative variation of the undulator parameter $\Delta K/K$ scales linearly with the increasing standard deviation of the magnets sizes, the RMS phase error Ψ_n calculated for each half period of the undulator grows quadratically, as expected by equation (2.62). Error bars show the standard deviation of the ensemble.

expensive but provides several advantages over others. Due to its low thickness and high resistivity (mechanically and chemically) it is best suited for the use on undulator magnets, preventing the magnets from corrosion and outgassing with a layer thickness of about 4 µm. And since the coating can not be magnetized the choice of a preferably thin layer was important.

Due to these manufacturing processes each side of the magnet varies in its length to a certain value. This results in a variation of the magnets volume, and thus in the achieved magnetic field flux through the poles inside the undulator. A typical manufacturing tolerance for the sintered magnet blocks is about 30 µm.

Typ. deviation of magnet size	corresponding field errors	
$\sigma_{\mathrm{MagSize}}$	$\Delta K/K$	Ψ_n
30 µm	0.4%	4°

TABLE 4.2: The typical deviation of the absolute size in all three dimensions of the magnets, which are pressed in a die and then cut and ground to the final geometry, and the resulting field errors.

The resulting undulator field errors generated by a typical variation of the magnet size are summed up in table 4.2.

In figure 4.6 the relative deviation of the K parameter is shown. One can see a linear increase of $\Delta K/K$ with the increasing standard deviation of the magnets size $\sigma_{\mathrm{MagSize}}$. Whereas the relative variation of the K parameter scales linearly with the increasing standard deviation of the magnets sizes, a fit to the simulation data shows that the RMS phase error Ψ_n calculated for each half period of the undulator grows quadratically.

4.5 Variation of the magnetization direction

The consequences of a variation of the magnetization direction in terms of undulator field errors are analyzed in this section. If the magnets are ordered from the manufacturer, one has to pay attention to the fact that the typical geometrical plane alignment tolerance for the sintered
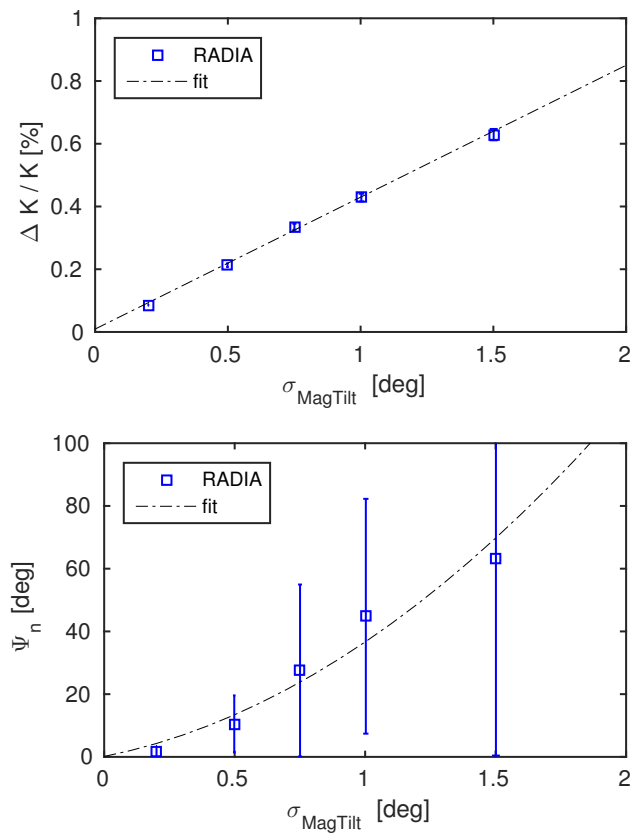
FIGURE 4.7: A typical manufacturing tolerance for the magnetization direction is about 1°. However, a more accurate determination of the magnetization direction is (in the majority of cases) not possible due to measurement errors. Thus a greater production volume (picking out the most accurate magnets) could not help minimize this tolerance. Also in this case, the relative variation of the undulator parameter $\Delta K/K$ scales linearly with the increasing standard deviation of the magnets sizes, whereas the RMS phase error Ψ_n calculated for each half period of the undulator grows quadratically. Moreover, the variation of the magnetization is more strongly linked to the RMS phase error, as can be seen in comparison to the magnet size described in section 4.4. Error bars show the standard deviation of the ensemble.

Typ. deviation of magnetization direction	corresponding field errors	
$\sigma_{\mathrm{MagTilt}}$	$\Delta K/K$	Ψ_n
1°	0.4%	34°

TABLE 4.3: Typical deviation of the magnetization direction from the ideal axis and the resulting field errors.

magnet block surfaces is 5 mrad (0.3 degree) which is small compared to the variation of the magnetization direction itself. The magnetization vector varies up to 17.5 mrad or 1° and has a significant impact on the quality of the magnetic field. In fact it is the most important source of errors for an insertion device, especially the contribution to the phase error is significant. Also here one can see, that the relative variation of the K parameter increases linearly with the increasing standard deviation of the magnetization tilt and the RMS phase error Ψ_n calculated from each half period of the undulator grows quadratically. However, the phase error increases more drastically. Compared to the variation of the magnet size the same relative error in K is correlated to a significantly higher phase shake Ψ_n. For example a $\Delta K/K$ of about 0.4% is correlated to an RMS phase shake of 4° for the size variation, but in case of the tilt variation a $\Delta K/K$ of about 0.4% is related to an more than tenfold RMS phase shake of 40°. It follows therefor that the tilted magnetization has a higher impact on the RMS phase shake than on the relative magnetization. It seems not only to shift the amplitude of the field, but also the position of the peaks and the zero-crossings.

4.6   Variation of magnet remanence

The manufacturing tolerances of the magnetization magnitude (measured by the magnets remanence) is analyzed in this section. Together with the magnetization direction, this is another important parameter, significantly influencing the quality of the magnetic field of the undulator.

Since this value could be measured more precisely, it can be decreased by producing a greater charge of magnets and sorting out the ones which exceed the limit. A typical manufacturing tolerance for the sintered magnet blocks is about 1%, also depending on the magnets size and geometry. In contrast to the linearly growing deviation in K, also here the RMS phase error grows quadratically.

Typ. deviation of magnet remanence	corresponding field errors	
$\Delta B_{\mathrm{r}}/B_{\mathrm{r}}$	$\Delta K/K$	Ψ_n
2%	1%	12°

TABLE 4.4: Typical deviation of the magnet's remanence $\Delta B_{\mathrm{r}}/B_{\mathrm{r}}$ from the ideal value and the resulting field errors. One can see here that the deviation of the magnet's remanence generates an error of the on-axis magnetic flux density ($\Delta B/B \propto \Delta K/K$ if a variation of the undulator period length λ_{u} is neglected) of the undulator which is only about half as large.
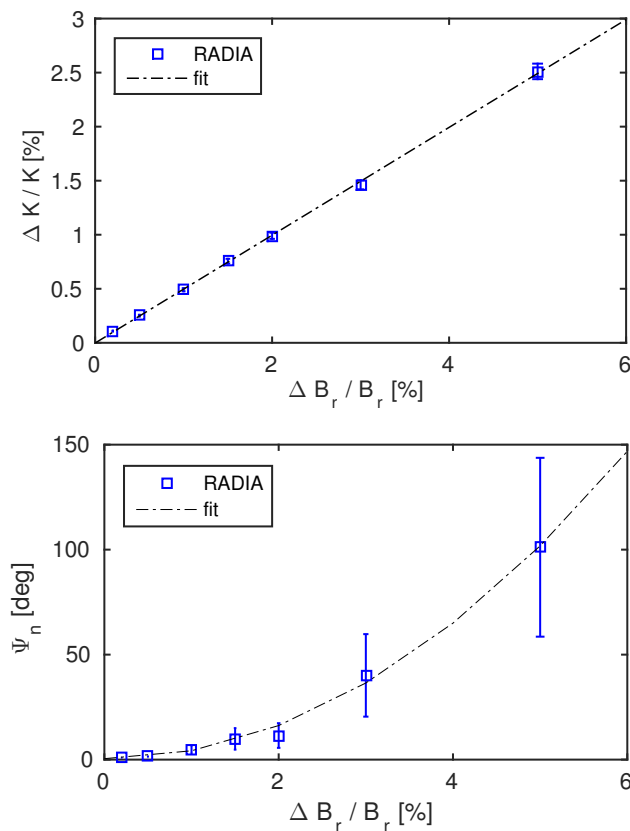
FIGURE 4.8: A typical manufacturing tolerance for the remanence is about 1-2%. Also in this case, the relative variation of the undulator parameter $\Delta K/K$ scales linearly with the increasing standard deviation of the magnets sizes, whereas the RMS phase error Ψ_n calculated for each half period of the undulator grows quadratically. The variation of the magnet's remanence is linked as strongly to the RMS phase error, as the previously discussed magnetization direction (4.5). Both show more crucial impact on the RMS phase shake than the variation of the magnet size described in section 4.4. Error bars show the standard deviation of the ensemble.

4.7   Variation of pole size

The poles can be processed more accurate than the magnets since the type of production is completely different. The poles are cut from a rolled sheet by wire erosion, plasma or waterjet cutting. The manufacturing accuracy depends on the quality of the sheet and the processing method, and is not far from 5 µm in each direction.

Only small pole pieces with a longitudinal thickness below 1 mm suffer from manufacturing problems as the material tends to distort under the action of heat. Especially for the design of short period high field undulators, as described in chapter 3, that is a crucial fact. All tolerances must be chosen with more clearance, for that purpose. In contrast to the linearly growing deviation in K, the RMS phase error grows quadratically.
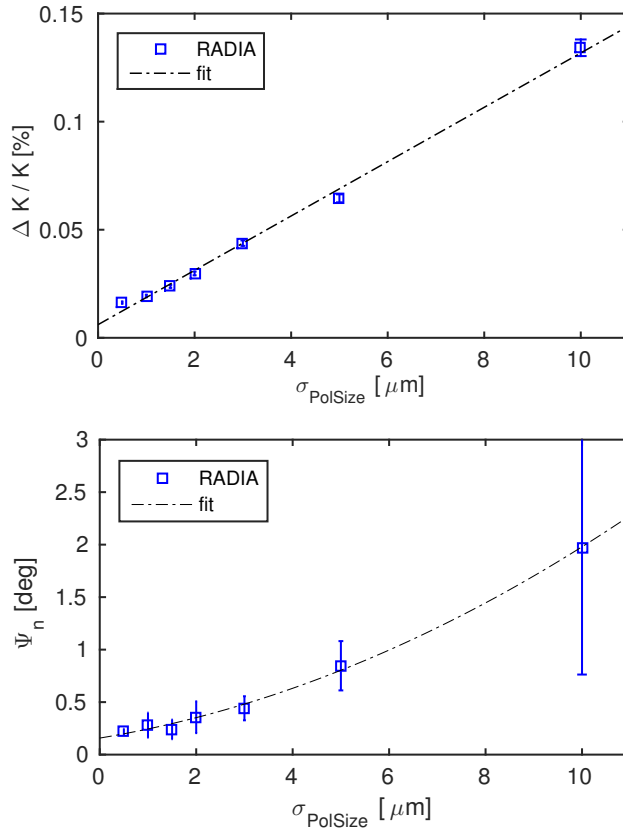
FIGURE 4.9: Deviation of the pole size from the ideal value and the resulting error in $\Delta K/K$ (top) and the resulting phase error Ψ_n (bottom).

Typ. deviation of pole size	corresponding field errors	
σ_{PolSize}	$\Delta K/K$	Ψ_n
10 µm	0.14%	2°

TABLE 4.5: Typical deviation of the pole size from the ideal value and the resulting field errors.

4.8 Variation of the longitudinal positions of poles and magnets

According to the simulations the variation of the longitudinal positions of poles and magnets is uncritical. In fact the variation of the magnets positions showed no significant effect on the field quality and is therefore not considered in this work.

The results for the pole variation showed that even if the standard variation of the longitudinal positioning accuracy exceeds 10 µm, the induced relative errors stay below 0.05%. Also the RMS phase errors which are intuitively more sensitive to the longitudinal position of the poles stay below 0.3° and will not contribute much to the total phase error of the device. This is also not surprising if one considers the relatively small deviation compared to the value of the period
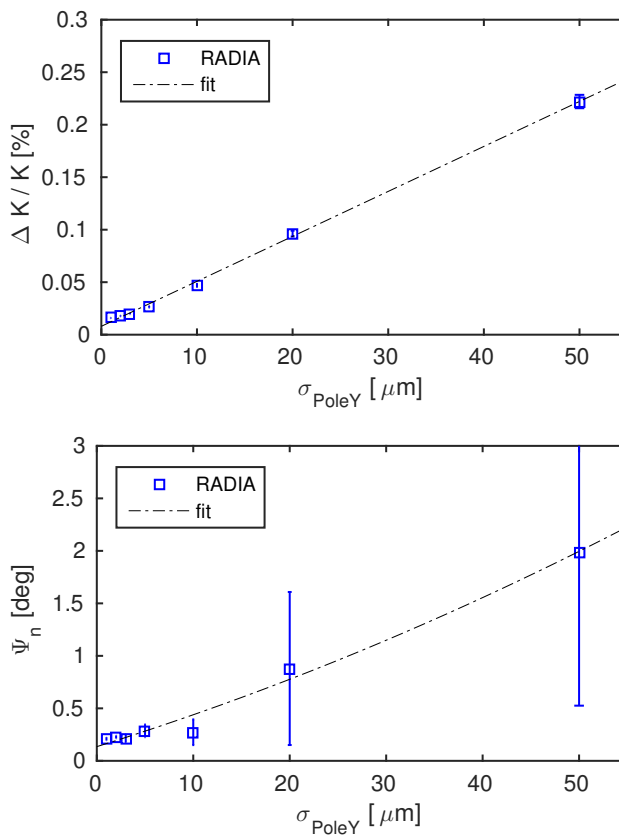
FIGURE 4.10: The deviation of the pole position (longitudinal) results in relative deviations of the K parameter (top) and an RMS phase shake (bottom). It is intuitively clear that the variation of the longitudinal position affects primarily the RMS phase shake, whereas $\Delta K/K$ is below .25% even for large deviations of up to 50 µm.

Typ. deviation in Y	corresponding field errors	
σ_{PoleY}	$\Delta K/K$	Ψ_n
10 µm	0.05%	0.29°

TABLE 4.6: Typical deviation of the longitudinal (Y) pole position from the ideal value and the resulting field errors.

length. A rough estimation shows: 50 µm is just about 6.7‰ of the undulator half period and thus only a phase shift of 2.4°. This is consistent with the simulations shown in figure 4.10

4.9 Variation of the vertical positions of poles and magnets

More crucial is the variation of the vertical position. This becomes apparent considering the analytic approach to the so-called pole height adjustment method for the tuning of the undulator field. This uses the dependence of the on-axis magnetic field on the gap size, which can be analytically deduced resulting in the following expression for the on-axis peak field [79]:

$$\tilde{B}(g) = \frac{B_0}{\cosh\left(\pi \frac{g}{\lambda_{\mathrm{u}}}\right)} \ .$$

(4.1)

With B_0 the magnetic flux density at the pole tip of the undulator, g the gap size and λ_{u} the undulator period length. If one assumes $\Delta g/g \ll 1$, one can suppose that B_0 will not change significantly, especially if the pole material is in saturation.
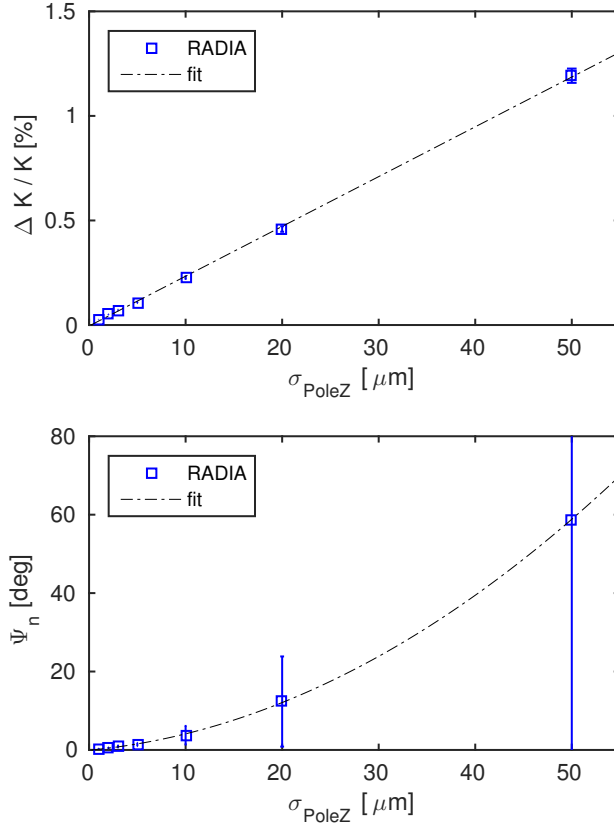
FIGURE 4.11: The deviation of the pole position (vertical) results in more significant changes of the magnetic field shown for both the relative deviations of the K parameter (top) and the RMS phase shake (bottom). It affects both field quality measures more significantly than the longitudinal position error.

Typ. deviation in Z	corresponding field errors	
σ_{PoleZ}	$\Delta K/K$	Ψ_n
10 µm	0.22%	3.5°

TABLE 4.7: Typical deviation of the vertical pole position (Z) from the ideal value and the resulting field errors.

$$
\begin{aligned}
\frac{\Delta K}{K} \approx \frac{\Delta \tilde{B}}{\tilde{B}} \;=\;& \frac{\left| \tilde{B}(g - \Delta g) - \tilde{B}(g + \Delta g) \right|}{\tilde{B}(g)} \\
=\;& \cosh\left(\pi \frac{g}{\lambda_\mathrm{u}} \right) \left| \frac{1}{\cosh\left(\pi \frac{g - \Delta g}{\lambda_\mathrm{u}} \right)} - \frac{1}{\cosh\left(\pi \frac{g + \Delta g}{\lambda_\mathrm{u}} \right)} \right| .
\end{aligned}
\tag{4.2}
$$

This approximation is consistent with the simulated data, as can be shown by the following comparison. A vertical pole position error with a standard deviation of 50 µm for instance, corresponding to a gap error of $\Delta g = 50$ µm would generate a relative on-axis field error of about $\Delta B/B \approx 1\%$ for our undulator with a 15 mm period length λ_u and a mean gap size of 2.5 mm if one assumes B_0, the field at the pole top near saturation (2.35 T).

The simulations shown in figure 4.11 resulted in $\Delta K/K \approx 1\%$ and again due to equation (2.39) it is clear that $\Delta K/K \propto \Delta B/B$.

4.10 Variation of the complete error set

For the analysis of a real undulator containing the introduced types of errors, all parameters were varied at the same time. For this purpose two setups were chosen, each with a distinct standard deviations in every discussed property. All parameters and their standard deviation are summarized in table 4.8.

With these standards two ensembles were generated, each consisting of 100 undulators with 33 periods and thus 132 magnets and 132 poles. Every discussed undulator component was randomly manipulated in its size and position and all magnets were additionally modified in their magnetic field's magnitude and direction. The parameters of the first ensemble Ω_1 had a standard deviation which is achievable for the manufacturer but very costly due to the required overproduction and selection process. The second ensemble Ω_2 is economically more reasonable.

Parameters	Ensemble Ω_1	Ensemble Ω_2
Magnet size σ_MagSize	10 µm	50 µm
Magnetization tilt σ_MagTilt	$1° \mathrel{\hat{=}} 17.5$ mrad	$1,4° \mathrel{\hat{=}} 25$ mrad
Magnet remanence $\Delta B/B$	1%	1%
Pole size σ_PolSize	1 µm	5 µm
Pole position (long.) σ_PoleY	3 µm	10 µm
Pole position (vert.) σ_PoleZ	3 µm	10 µm

TABLE 4.8: Comparison of the tolerances used in setup Ω_1 and setup Ω_2. Tolerances are given as standard deviation for an ensemble of 100 simulated undulators. Whereas Ω_1 is technically possible only if suitable components (magnets and poles) are selected from an larger stack discarding the overproduction, accepting higher efforts and costs, and the undulator girder is manufactured by a CNC machine especially dedicated for higher precision. In contrast to that, Ω_2 should be attainable without extra costs. The remanence tolerance in both cases is tough, but should be achievable.

A comparison of the resulting undulator field errors $\Delta K / K$ and the RMS phase error are presented in figure 4.12 & 4.13. On the left hand side one can see the results of the single runs and their frequency is plotted in the histograms on the right hand side.

4.10.1 Relative error of the K parameter

The viability of $\Delta K / K$ as a quality measure is limited to the spontaneous generation of undulator radiation, but should be discussed here nevertheless, since the planned undulator will also work as a source of light from spontaneous emission as long as the used PWA electrons do not meet the requirements for an FEL experiment. Looking to figure 4.12 one can see that even for ensemble Ω_2 with greater tolerances $\Delta K / K$ stays for more than 80% of all cases below 1% even without using any field correction method. The actually lowest measured energy spread of PWA generated electron beams is in the same order of magnitude. Therefore the undulator radiation bandwidth is not increased significantly. Thus it is not critical for PWA driven undulator light sources, other than for conventionally driven light sources, where the energy spread is in the order of 10^{-5}.
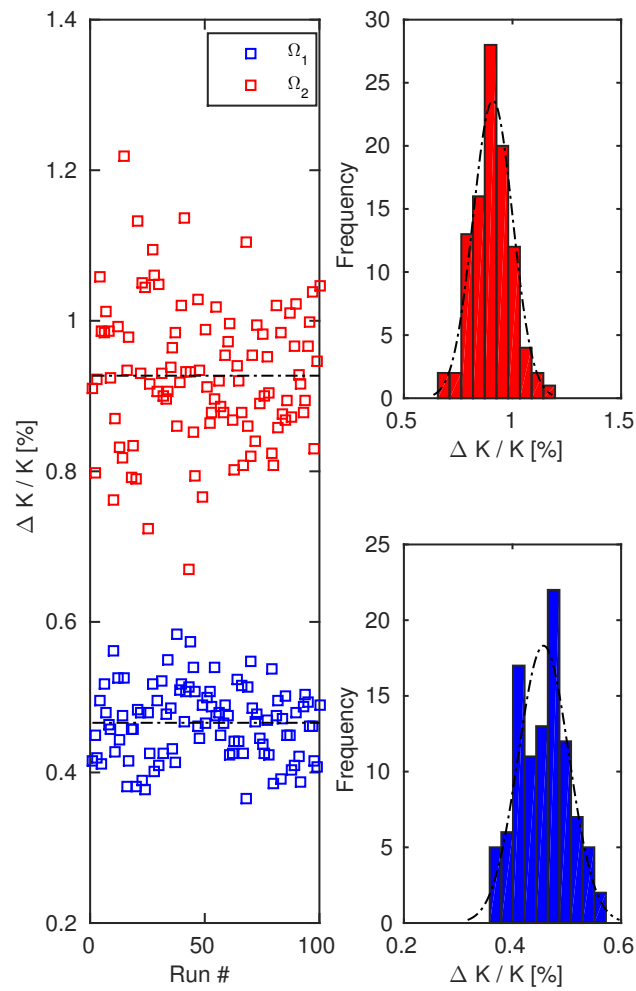
FIGURE 4.12: $\Delta K/K$ is shown for two distinct setups with tolerances according to tab. 4.8. Even for ensemble Ω_2 with greater tolerances $\Delta K/K$ stays for more than 80% of all cases below 1% although no field correction method was used in the simulation so far. Since state of the art PWA electron bunches have still more than 1% of energy spread, a broadening of the spectral bandwidth is not expected.

4.10.2   Undulator RMS phase error

In this section the RMS phase error Ψ_n (also called phase shake) is analyzed for non ideal undulators which are affected by manufacturing tolerances. In the simulated case of a PWA based FEL proof of principle experiment the electron bunch is extended by a longitudinal bunch decompression concept described in more detail in [133, 135]. In the related doctoral thesis of Seggebrock [134] it could be shown that the RMS value of the phase error is a key factor for the success of the experiment.

This FEL scenario requires an RMS phase error of the undulator which should not exceed 0.35 mrad or 20°. Ensemble Ω_1 shows a mean phase shake of 38°, ensemble Ω_2 even a mean phase shake of 84° averaged over all sample undulators. However, the histograms reveal that almost half of all simulated undulators (47%) show a phase shake below 20° for Ω_1 and 19% of Ω_2, even if the fields are not shimmed or corrected and even if no magnet sorting were performed before assembly.
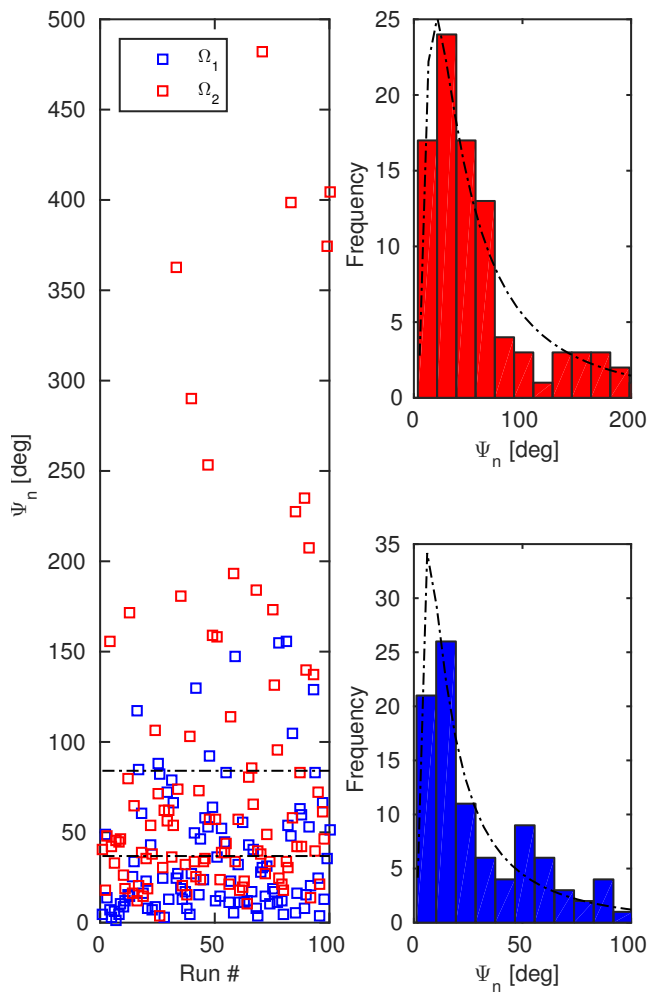
FIGURE 4.13: The RMS phase error Ψ_n should not exceed 0.35 mrad or 20° for the PWA FEL experiment. Ensemble Ω_1 shows a mean phase shake of 38°, ensemble Ω_2 even more, up to 84°. However, almost half of all simulated undulators (47%) show a phase shake below 20° for Ω_1 and 19% of Ω_2 without shimming or magnet sorting.

4.11 Discussion

Analyzing the manufacturing tolerances it was found that magnetization tilt, variation of the magnets remanence dB/B and the offset of the poles vertical position (Z-axis) are the most crucial deviances regarding the effects to the undulator field.

Two ensembles combining all tolerances with typical manufacturing tolerances were performed, analyzing two undulator field error types, the relative error of the undulator parameter $\Delta K/K$ and the RMS phase shake Ψ_n.

Even in ensemble Ω_2, where the variation of the tolerances are more relaxed and thus deviations are higher, the relative deviation $\Delta K/K$ stays for more than 80% of all simulated cases below 1%. This could be considered as not significant, as its effect on the bandwidth of the undulator radiation of PWA based light sources, with energy spreads of typically more than 1%, is negligible.

Analyzing the phase shake Ψ_n, histograms reveal that almost half of all simulated undulators (47%) for Ω_1 and 19% of Ω_2 show a phase shake below 20°, even if no field correction methods are used. A feasibility study of a proof of concept PWA based FEL experiment [133] claims a phase shake below 0.35 mrad (or 20°) which is thereby not strictly complied with in any case.

As a result, shimming (magnetic and spectral) and magnet sorting must be recommended. These methods are not included into the simulations. For more informations about the methods and processes it is recommended to consult the book of P.Elleaume [68]. Typically phase errors between 1° and 2° can be achieved after these kind of corrections.

4.12 Outlook

The start to end simulations of T. Seggebrock [4] have shown that the use of a PWA instead of a conventionel linear accellerator becomes more and more possible. Using the interplay of the proposed decompression concept, the actual design of a chicane used for the decompression and a set of taylored quadrupol beam optics, the actual design tolerances of the undulator design (determining one of several degrading effects) became manageble. This confirms the hope to realize a first proof-of-principle experiment for a PWA driven soft X-ray FEL.

Chapter 5

Spectral analysis of a CPMU prototype

The acceleration of charged particles in plasma generated, ultra high electric fields (up to TV/m), induced by intense light pulses, focused into gases or on thin foils, was already theoretically proposed in 1979 [28]. However, it took several decades to develop lasers which provide the required power. Yet, in recent years the Plasma-Wakefield Accelerator (PWA) scheme has rapidly gained in significance since experiments showed continuous improvements in the properties of the generated electron beam. In 2004 electron spectra with bunch charges of a few nC with several percent energy spread and energies around 200 MeV [131, 132, 136] were achieved. Now, in 2014, energies of up to 4.2 GeV are reached with an energy spread of 6% [98]. Although, these PWA sources provide a remarkably low emittance (normalized transverse beam emittance of 0.21 π mm mrad [99] in 2012 and even less, few tens of nm rad [137], using ionizing electron injection in 2014), PWA electron beams are still suffering from several drawbacks compared to conventional accelerator types. And even though the reliably achieved electron energies are continuously increasing, the electron beams are still endued with broad energy spreads of several percent. In addition to that, significant electron beam instabilities are induced by the high power laser systems. Thus, in order to use PWA electron beams to produce VUV-radiation and soft X-rays by insertion devices, despite the properties named above, it is vitally important to adapt the experimental setup and especially the design of the used devices [71–73].

One of these adjustments to PWA beam lines is the development of undulators with a short period length which nevertheless provide high magnetic fields. By doing so, it is possible to generate high energy photon beams with a sufficient photon flux using PWA electron beams, which still provide relatively low energy and only a few pC bunch charge. For more information about interrelations between undulator period length, magnetic field, photon energy and flux, see chapter 3.

One possibility aiming for short periods and high fields is to cool down the undulator magnets. Therefor a new material is used which increases its remanent magnetic field by 20% being cooled
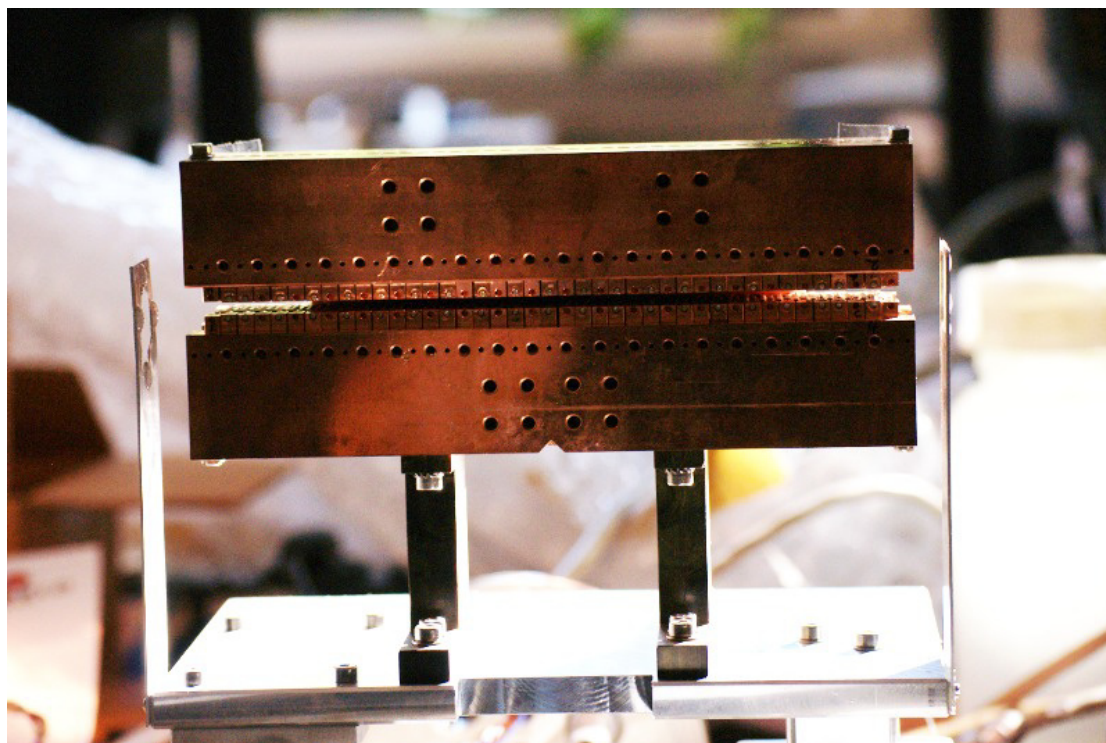
FIGURE 5.1: Cryogenic undulator on insulating teflon mounts with 9 mm period length, 20 periods and a gap size of 2.5 mm. The support structure is made of OFHC copper to optimize heat flow thus avoiding temperature gradients along the structure. Cooling the undulator down to temperatures below 30 K the on-axis peak field increases from 0.966 T to 1.149 T. At the front and the back side of the undulator a cross hair is installed for a wire scan to measure the electron beam properties.

down to cryogenic temperatures. It outperforms previously used cooled permanent magnet materials, and for small undulator periods (below 10 mm) even superconducting undulator materials [69].

Hence, the commissioning of a cryogenic prototype undulator based on a new rare earth magnet material [138] was the first step towards the development of small-period high-field undulators, specifically designed for operation at PWA driven electron beam lines.

The aim of the first UR measurements with the new prototype was to characterize its spectral properties at warm and cold temperatures. From these measurements it was planned to deduce to the magnetic field properties of the undulator under operating conditions at an electron accelerator. However, the analysis of the data, measured during an external beam time at the *Mainzer Mikrotron* MaMi, revealed contradictory spectral characteristics. The measured gain of the on-axis flux density, which was perfectly agreeing to theoretic predictions concerning a low electron divergence, seemed to be inconsistent with the fact that radiation from the second harmonic appeared directly on-axis, which shall be possible only for highly divergent electron beams.

A posteriori analysis of additional data revealed that the initially presumed electron divergence of the accelerator changed during the measurement campaigns. Subsequently the previously used equation (2.51) was extended to include the impact of the actual electron divergence. As

a result equation (2.52) was found and thereby the paradox could be resolved. The data was published subsequently in 2014 [139].

In the following chapter, the spectral measurement of the cryogenic undulator prototype will be discussed in detail. First, the cryogenic undulator is introduced in section 5.1. In section 5.2 the experimental setup of the spectrometer is described and in section 5.3 the spectral data is presented. In the following section 5.4 the conflict between the spectral characteristics is illustrated and a detailed explanation is presented. In the last section 5.6 the results are summed up and an outlook on the future use of cryogenic undulators at the PWA electron beam line at the *Deutsches Elektronen-Synchrotron* DESY and the *Centre for Advanced Laser Applications* CALA is given.

5.1 The cryogenic undulator prototype

In figure 5.1 a picture of the cryogenic undulator prototype based on the new developed advanced magnet material is shown. The undulator is built as a hybrid device (see section 2.2) and consists of 20 periods with a 9 mm period length. The magnetic material itself is a rare earth alloy based on Praseodymium and Neodymium: $(Pr_{0.8}, Nd_{0.2})_2Fe_{14}B$ with an unprecedented energy product of 540 kJ/m^3 at a temperature of 35 K.

The materials specific mixture ratio of 80% Pr and 20% Nd in the rare earth content was chosen in order to maximize the magnetic field at cryogenic temperatures. Thereby it was achieved that the magnets show an untypical monotonic increase of both remanence and coercivity, for temperatures down to absolute zero. In figure 5.2 a comparison between typical undulator magnet materials and the new magnets is shown (data taken from [70]). One can see that commonly used magnets reach a maximum field strength around a temperature of 140 K, except samarium cobalt magnets (SmCo) which are generally lower in their remanent field and thus not competitive with modern materials. The loss of remanence below 140 K is due to an effect called spin reorientation transition SRT, which leads in common rare earth magnets to a limited gain of remanence. This opposing effect does not affect the new material. A comprehensive description of SRT can be found in [140, 141].

The magnetic design of the undulator was optimized to reach the highest possible magnetic field inside the undulator using cryogenic cooling technology. However, this also meant that the magnet and pole geometry was set to an extreme limit. As a result, the stability of the undulator magnet's magnetization was barely guaranteed at room temperature. Still, demagnetizing opposing fields are the highest during assembly, when the magnet is moved from outside to inside the undulator girder. Therefor the manufacture was located in a cold house at −20 °C. At this temperature the coercivity of the magnets, which also increases with lower temperatures, was sufficient to avoid demagnetization. Later, it has been demonstrated that the magnets can be treated by a new processing method called Grain Boundary Diffusion (GBD) [142]. During this procedure Dy or terbium, which have higher coercivities compared to Nd or Pr, are induced by diffusion through the magnets surface to the grain boundaries, thus enhancing the magnet's coercivity up to 7 kOe or 560 kA/m [62]. Thereby an assembly at room temperature [142] would
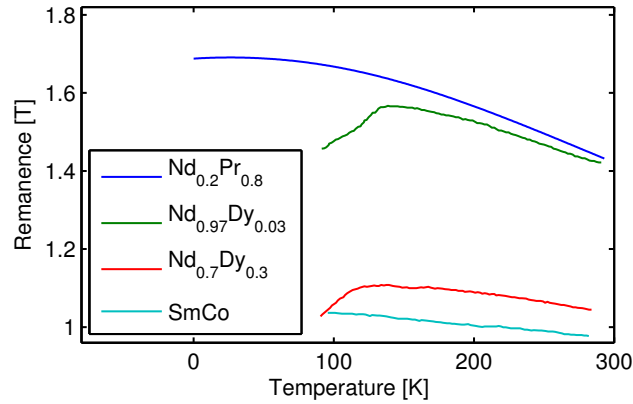
FIGURE 5.2: Performance comparison of magnet materials at low temperatures [70]. The remanent magnetic field is plotted against the temperature for two standard rare earth magnet alloys based on Nd and Dy, SmCo and the new Pr based alloy. The mixing ratios are given as index. The Pr as well as SmCo based materials show now spin reorientation effect and increase their remanence monotonically towards absolute zero.

become possible. This processing method was also used for another undulator, designed for use at room temperature with 5 mm period length, which is described in detail in chapter 3.

The support structure of the prototype is made of Oxygen Free High Conductivity (OFHC) copper to maximize the thermal conductivity and thereby reduce the temperature gradient along the structure to a minimum. When the temperature lowers, heat transfer by phonon scattering becomes less efficient for most materials. But for highly purified OFHC copper, the electric conductivity at cryogenic temperatures increases by three orders of magnitude (depending on the purity of the copper, see figure 5.3). At these temperatures, electrons from the conduction band are no longer scattered at thermal oscillations of the metal's crystal lattice, known as phonons, and thus electric conductivity is increased dramatically. Instead of phonon scattering heat transfer is proceeded then mainly by free moving electrons [39]. The low electric resistance
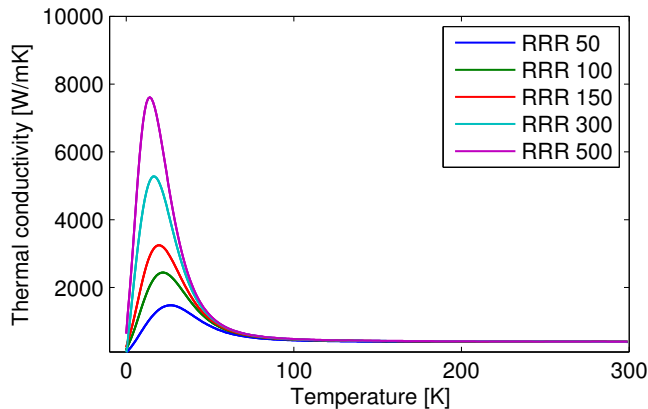
FIGURE 5.3: Thermal conductivity κ of highly purified copper. The residual-resistance ratio is defined as the ratio between the resistance at room temperature and at 0 K, written as RRR:$= \rho_{294K}/\rho_{0K}$. At temperatures below 100 K the resistivity of copper decreases since the phonon excitement decreases too. The less impurities are contained in the material the less is the remaining resistance. At these temperatures heat is transferred by electrons from the conduction band. Thus the thermal conductivity increases significantly.

Undulator	T	B_r	$\tilde{B}$	K	λ_u	N	gap
	[K]	[T]	[T]		[mm]	#	[mm]
warm	294	1.42	0.996	0.837	9	20	2.5
cold	25	1.69	1.149	0.966			

TABLE 5.1: Specifications of the CPMU09 prototype undulator. The magnetic peak field $\tilde{B}$ is measured at HZB with a Hall probe bench [143], the magnet's remanence B_r was measured by the manufacturer [70].

of the support structure at low temperatures helps thereby to avoid thermal gradients along the undulator and enables a fast cooling process.

An equalized temperature distribution along the undulator girder is necessary for two reasons. First, the remanence of the magnets depends on their temperature. A variation of the magnets temperatures along the structure would therefore induce a magnetic field error to the undulator. A second reason is given by the thermal expansion coefficient of the support material, in our case copper. A variation of the temperature would generate mechanical strains and distortions which again would induce magnetic field errors to the undulator.

In order to minimize field errors in general from the beginning, a specific sequencing and assembling method applied. Measurements of each undulator magnet's 3-dimensional magnetization vector were performed before they were inserted into the support structure. A subsequent matching of neighboring magnets and elaborate processing of the undulator girder with sub micrometer accuracy lead to a relative RMS field error below 1.75%. This corresponds to a phase error below 3.7° [83]. The field maps of the undulator were measured at room temperature and at 15 K for the assembled device. The measurements were performed with an in vacuum Hall probe bench [143] at the *Helmholtz-Zentrum Berlin für Materialien und Energie* (HZB). The results of these measurements are listed in table 5.1.

calculated assuming a normalized beam emittance of (0.5/7.8) π nm rad (vertical/horizontal) at 855.1 MeV energy [144].

5.2 Experimental setup

A schematic view of the experimental setup is shown in figure 5.4. Two independent detector systems were used, a low noise, high resolution Germanium diode Detector (GeD) [145] and a Transmission Grating Spectrometer (TGS) [146], with a free standing gold wire grating with 1000 lines per millimeter [147]. The specific setups for both detectors are described separately in the next two sections.

5.2.1 Germanium detector

The GeD was placed at $L_{Ge} = 13.4$ m behind the undulator, equipped with a pinhole of $A_{Ge} = 500$ μm diameter. Pinhole and radiation source size Σ_r defined the angular acceptance of the
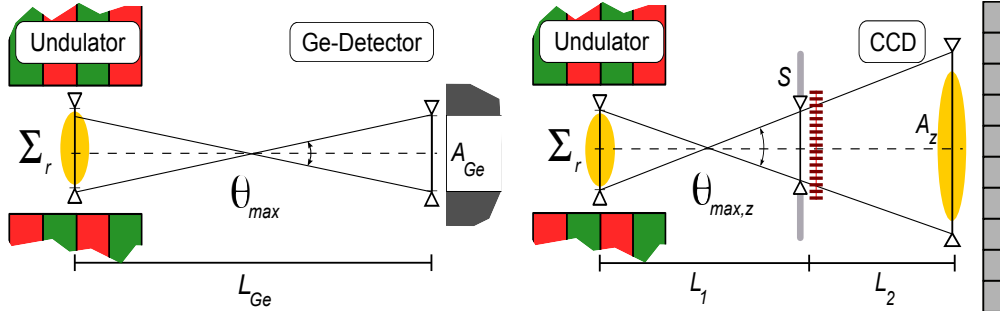
FIGURE 5.4: Experimental Setup: two independent detector systems were used, a Germanium diode detector (left) and a transmission grating spectrometer (right). In both schemes the radiation source size is represented by Σ_r. A is the detector aperture and θ_{max} the resulting acceptance angle. The transmission grating spectrometer on the right hand has a variable entrance slit of size S which restricts the angle of incidence $\theta_{max,z}$ thus optimizing the spectral resolution. The distances between the detector components, represented by L_{Ge}, L_1, and L_2 are specified in sections 5.2.1 and 5.2.2.

detector: $\theta_{max} \approx 39$ μrad, as can be seen in fig. 5.4. Thereby a spatially resolved detection of the radiation was possible, proofed by equation (2.43) one gets about 300 μrad as radiation divergence. The energy resolution for a single photon Δ_{Ge} is about 150 eV (FWHM) [145] for this detector type, which is smaller than the spectral separation between two harmonic peaks ($\Delta_{E_n} \approx 500$ eV). Thereby the harmonic structure of the spectrum could be resolved.

However, the bandwidth of the spectral lines is about six times smaller than Δ_{Ge} and thus not resolvable. The absolute energy calibration was done using decay spectra emitted by two different radioactive probes, Fe_{26}^{55} and Am_{95}^{243}. To minimize the detector's dead time and also the number of multi-photon events, the electron beam current and thereby the photon flux, was limited to a maximum of 10 pA.
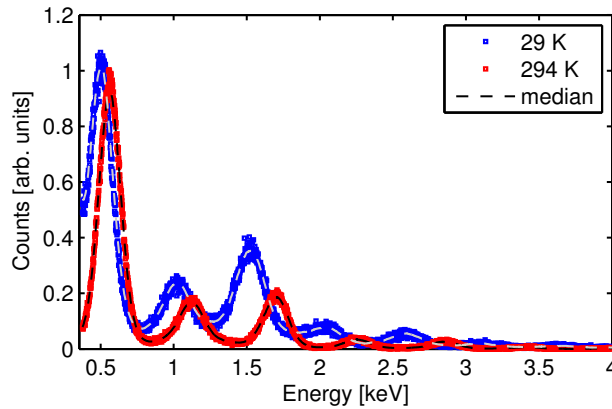
FIGURE 5.5: Comparison of the undulator's spectral output at room temperature and at 29 K measured by a Germanium detector. The spectra are normalized to the peak count of the fundamental's flux density at room temperature, like in figure 5.7. A shift of the peak energies and a gain in the on-axis flux density due to the increasing K parameter is observed which is in good agreement with the theory, given by equation (2.51) and visualized in figure 5.7 respectively.

5.2.2 Transmission grating spectrometer

The transmission grating spectrometer was based on a gold wire grating, which originates from the NASA's Chandra Observatory program and is exactly specified in [147]. An entrance slit with variable size S, attached directly in front, restricted the angle of incidence towards the dispersion axis. Grating and slit were placed 7.55 m (L_1) behind the undulator's center which was assumed as source position, leaving a dispersion drift of 5.85 m (L_2) to the X-ray CCD, as can be seen in the arrangement sketch in fig. 5.4.

The used CCD was a back illuminated device with a VUV (Vacuum UltraViolet) adapted coating, cooled to -70°C. Due to the low operation temperature, which reduces the thermal noise of the chip to a minimum, rest gases froze out on the CCD's surface visible at the low energy tails of the fundamental radiation of the 294 K measurement. The measurements at this temperature where performed after the cold measurements, which is why the features are invisible in the above picture of figure 5.6. Due to the specific wavelength range, at which these droplets are visible (between 2.3 nm and 2.5 nm) the drops consist most probably of water, since oxygen has its K-absorption edge at 2.34 nm. The CCD itself is manufactured by Andor [146], with a pixel size of $S_{pix} = 22.5$ µm. The spectral resolution of this instrument is largely dominated by the projection
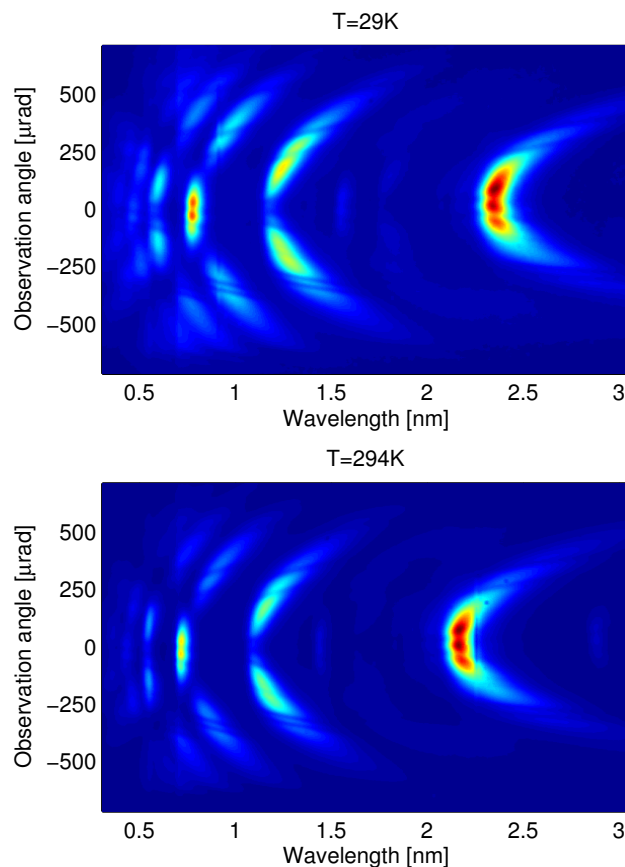
FIGURE 5.6: CCD data from the TGS. The images compare the cooled case (top) with the room temperature case (bottom). The entrance slit sizes 75 µm and 100 µm were adapted to optimize the resolution of the spectrometer for the specific wavelength of the first harmonic. The color scale is normalized to the maximum count number of the fundamental peak of each temperature case. Shadows of the grating's support structure [147] are visible.

of the radiation source with the size Σ_r onto the CCD. Thereby, a spatially broad signal arrives at the CCD screen overlaying the dispersion patterns. This results from the simplicity of the used setup, which works similar to a pinhole camera, without further imaging features. An estimation of the spectral resolution of the transmission grating spectrometer has been made, considering geometric optics, Rayleigh's criterion and diffraction. Considering these effects, the size of the pixels itself and positioning uncertainties, the absolute wavelength accuracy ranges between 2.5% at a wavelength of 0.4 nm (which corresponds to the 5th UR's harmonic) and 1% at 2 nm wavelength (corresponding to the UR's fundamental for the used electron energy of 855.1 MeV). A more detailed description of the accuracy assessment can be found in appendix B.

According to the expected accuracy of the spectrometer, an increase of the magnetic field error due to thermally induced mechanical distortions should be detectable, if the RMS field error becomes greater than 2%. To confirm this was the main target of the beam time. The measured spectra are shown in figure 5.6.

5.2.3 Wire scanner - electron divergence

In order to determine the electron beam divergence during the measurement campaign, the electron beam cross section at the focus-position was measured by a wire scan, performed at the end of the MAMI beam time. Cross hairs used for this purpose were mounted onto the undulator stage, visible in figure 5.1. The divergence was calculated using the emittance of the accelerator, assuming accelerator parameters as explicitly described in [144]. The results of the wire scans are summed up in table 5.2.

The calculated horizontal and vertical electron beam divergence of 21 and 3 μrad respectively, seemed small enough to legitimate the comparison of the measured photon flux density to a simple theoretic approximation, given by equation (2.51), particularized in the following section. As mentioned before equation (2.51) is an approximation, which neglects electron beam divergence effects, and is thus applicable only in case of low divergence (idealized) electron beams, also called pencil beams.

MAMI B (III RTM 3)		vertical	horizontal
		z	x
beam emittance	[$\pi\,\mu$m rad]	13 ± 5	0.84 ± 0.06
norm. beam emittance	[$\pi\,\mu$m mrad]	7.8 ± 0.06	0.5 ± 0.03
divergence	[μrad]	3 ± 1	21 ± 1
beam size	[µm]	160 ± 3	367 ± 7

TABLE 5.2: Electron beam parameters measured by a wire scan during the beam time at MAMI.

5.3   Spectral analysis

In figure 5.7 the expected gain of the on-axis photon flux density is shown in the specific region of the used undulator's K parameter, calculated by equation (2.51). The K parameter of the cryogenic device is expected to increase from 0.837 to 0.966 according to the previously measured magnetic field of the undulator at warm and cold operating temperatures. This corresponds to a gain of $(15.4 \pm 0.6)\%$ due to the cryogenic cooling.

From the measured spectrum, shown in figure 5.5, one can deduce the undulator's K parameter by the following method. Plotting the peak energies of the harmonic spectrum against their harmonic number n one obtains two best-fit lines for the warm and the cold measurements respectively (visible in figure 5.8) if the following effect is taken into account. Due to the relativistic Doppler-effect, described by equation (2.41), the low energy edge of the measured spectral lines are broadened which causes a shift of the center of the spectral peaks towards lower energies. The slope of the found best-fit lines $\mathrm{d}E/\mathrm{d}n$ can be inserted into a variation of the undulator resonance equation (2.40) given by the following equation:

$$K_{\mathrm{eff}} = \sqrt{\frac{4\gamma^2\,hc}{\lambda_u\,\mathrm{d}E/\mathrm{d}n} - 2}. \tag{5.1}$$

With λ_u, the period length of the undulator, the Lorentz factor $\gamma = 1 + E/(m_0 c^2)$ describing the total energy of the electrons in the beam, the harmonic number $n = 1, 2, 3, \ldots$ and the energy E of the UR. Thus, one obtains the effective K parameter, hereinafter called K_{eff}, which is, applying this method, spectrally determined. The result is 0.83 ± 0.02 at 294 K and 0.97 ± 0.01 at 29 K, corresponding to a gain of $(16.6 \pm 2.8)\%$, comparing the warm and cold operation modes respectively. These values of K_{eff} and the resulting gain agreed well with the K parameter calculated from the magnetic on-axis field of the undulator K_{field}, measured at the HZB. The results are summed up in table 5.3.
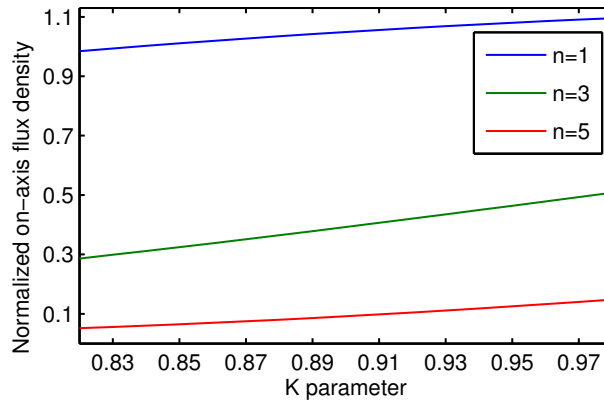
FIGURE 5.7: Theoretic on-axis photon flux density of UR, according to equation (2.51), normalized to the measured K parameter at room temperature. Theory predicts a relative gain of the on-axis photon flux density of 9%, 66% and 100% for the 1st, 3rd and 5th harmonic respectively, if K is increased from 0.837 at room temperature to 0.966 at 29 K. The plot is normalized to the flux density of the fundamental corresponding to the warm K parameter.
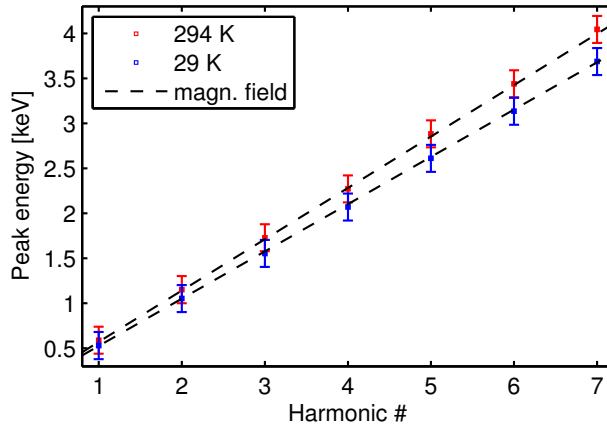
FIGURE 5.8: The peak energies of the undulator spectrum measurement plotted against the corresponding harmonic number n. The data is detuning corrected, see equation (2.41), to compensate the red-shift caused by the detector aperture. The dashed lines show the expected peak energies resulting from a magnetic field Hall probe measurement done by the HZB. The error bars are given by the energy resolution of the Germanium detector of 150 eV (FWHM).

The second detector system, the TGS, could not be absolutely calibrated like the GeD, due to the absence of appropriate gauging sources (only a rough approval was possible due to the described water droplets on the CCD and their specific K-absorption edge). It delivered nevertheless a better relative resolution of the spectral lines. Thus it was used to analyze the bandwidth of the UR harmonics. From the measured spectra, shown in figure 5.6, line outs were taken at the center of the radiation cones, where the observation angle is zero. These line outs, shown in figure 5.9 were averaged over the ten innermost pixel rows smoothing the noise and then used to determine the bandwidth of the UR.

Within the limits of accuracy of the spectrometer, which is explained in detail in appendix B, the measured bandwidth of the harmonic peaks agreed perfectly to the theory. The results are listed in table 5.4. No significant additional broadening of the spectral spikes due to magnetic field deviations of the undulator caused by the cryogenic cooling were noticed. Over all, the experiments seemed successful and a subsequent publication was planned. However, a serious irregularity showed up in the aftermath.

On closer examination the measured spectra revealed the fact, that the second harmonic was visible directly at the center of the radiation cone, at a position where only odd harmonics should be visible whereas even harmonics are canceled out due to destructive interference. This was measured, although the electron divergence was evidently low (measured by the wire scan, presented in table 5.2). Hence, a further investigation of the data was necessary. A

K parameter	warm (294 K)	cold (29 K)	gain [%]
K_{field}	0.837 ± 0.009	0.965 ± 0.009	15.4 ± 0.6
K_{eff}	0.83 ± 0.02	0.97 ± 0.01	16.6 ± 2.8

TABLE 5.3: Comparison of the K parameters deduced from a Hall probe measurement: K_{field}, and spectrally deduced from the energies of the harmonic peaks: K_{eff}.

Bandwidth	warm (294 K)		cold (29 K)	
harmonic #	expected	measured	expected	measured
1	5.2%	5.2%	5.4%	5.4%
3	13%	7.6%	14%	7.8%
5	22%	17.3%	24%	19.7%

TABLE 5.4: Bandwidth of the UR measured with the TGS. The fundamental is measured with spectrometer slit widths of 75 µm and 100 µm (warm and cold), the higher order UR bandwidths with a 50 µm slit for both temperatures. The expected bandwidth of the higher harmonics is overestimated by the used approximations (Fresnel vs. Fraunhofer diffraction) - for details see appendix B.

detailed description of the indicated problems together with an explanation for these problems is presented in the following section.
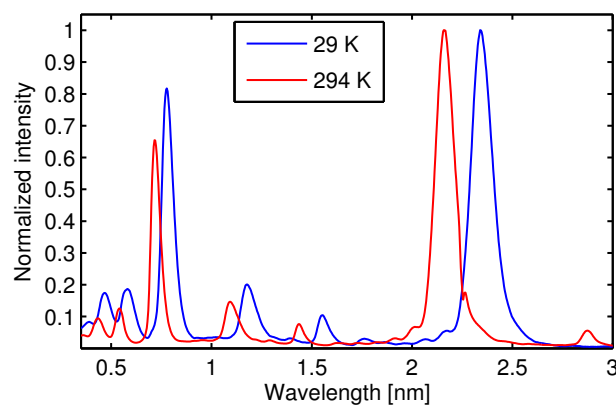
FIGURE 5.9: Line-outs made at the center of the CCD images (observation angle = 0 rad, fig. 5.6) of the cold (blue) and the warm (red) case. The absolute flux is not comparable since the entrance slits of the spectrometer is not the same in both cases. From these line-outs the bandwidth of the harmonics are determined and compared to the expected values, to examine a possible increase of field errors due to the temperature drop. The resulting bandwidths are given in table 5.4. Both spectra show small peaks at two-thirds of the fundamental wavelength. These features are the third undulator harmonic diffracted into second diffraction order of the grating.

5.4 Electron beam analysis

The crux of the matter was, that the experimental results seemed reasonable per se, but conflicting if they were put in context. Or, to address the problem specifically, the wire scan measurement data seemed to be conflicting with the data of the GeD measurement. An electron divergence as measured by the wire scan (shown in table 5.2) would not explain the fact that the second harmonic appeared in the on-axis spectrum, where the observation angle is delimited to the detectors aperture. However, the GeD data showed explicit spikes slightly above energies of 1 keV, which is the second harmonic's energy considering the electron energy and the undulator parameters, visible e.g. in figure 5.5.

These facts are inconsistent since the detector was approved to be at the center position of the radiation cone with an uncertainty of 2.5 μrad horizontally and 7.3 μrad vertically, while the acceptance angle $\theta_{\max}$ of the GeD was below 40 μrad (defined by the pinhole with 500 µm diameter and the radiation source size Σ_r). That angle is significantly smaller than the angle in which the second harmonic is emitted by a low divergent electron beam. Peaks of the second harmonic radiation should appear at an angle of about 350 μrad from the central axis for the given parameters (undulator K parameter 1, electron energy 855.1 MeV) calculated by equation (2.23). The expected radiation distribution for these parameters at the position of the detector window is shown in figure 5.10. Here one sees clearly that in the range of the detector's entrance window (diameter 500 µm) no significant contribution from the second harmonics radiation is expected.

To solve this paradox, a more specific investigation of the measured data was necessary. Mainly three characteristic features were visible in the presented data:
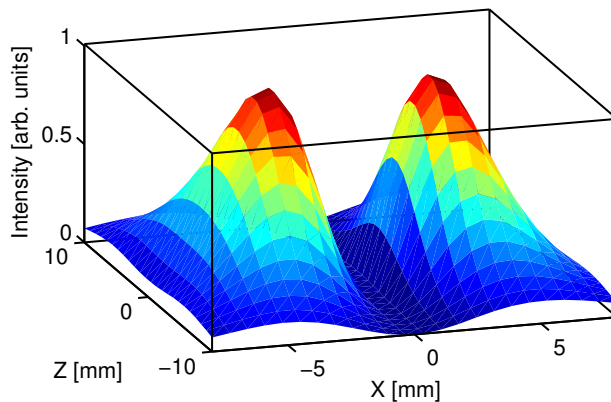
FIGURE 5.10: Intensity distribution for the second harmonic UR. Equation (2.23) was used to calculate the intensity distribution at the position of the detector for a low divergent electron beam regarding the characteristics of the undulator prototype operated at 294 K. The detector had a pinhole with a diameter of 500 µm, thus almost no contribution to the measured UR spectrum is expected since the intensity is greatest around 5 mm off axis. At cryogenic temperatures the K parameter of the undulator increases further and the positions of the intensity peaks move further apart from the center. Thus even less radiation would reach through the entrance window of the GeD.

(a) The harmonic peak-energies indicate an increase of the effective undulator parameter K_{eff} and for the warm and the cold undulator a K_{eff} of 0.83 and 0.97 was determined.

(b) An increase of the on-axis flux-density of 9% for the 1st, 70% for the 3rd and 100% for the 5th harmonic peak was measured.

(c) The appearance of the second harmonic in the measured on-axis spectrum at an intensity ratio of about 1/6-th of the fundamental's peak height was detected.

Whereas (a) was independently confirmed by a Hall probe measurement and thus could be assumed as ensured, (b) if combined with the results of (a) was not consistent with (c).

At first glance, the combination of (a) and (b) was consistent to the theory given by equation (2.51) explained in chapter 2. Equation (2.51) and figure 5.7 respectively, predicted an increase of the peak flux-density for the 1st, 3rd and 5th harmonic of 10%, 66% and 100% according to the specific undulator parameters. These undulator K parameters were spectrally observed by the peak shift (a) and independently confirmed by the Hall probe measurement. Furthermore, the measured flux-density agreed with the measured values of 9%, 70% and 100% stated in (b). The constraint of equation (2.51) discussed in chapter 2 is, that this approximation is valid only for pencil beams. However, assuming of a negligible divergence seemed reasonable, regarding the divergence data calculated from the cross section measurement, resulting in 21 and 3 μrad (horizontal and vertical electron divergence respectively).

In contrast to the small divergence assumed in (b), feature (c) indicated that either, the position of the detector was not on-axis or, the horizontal divergence must have been significantly higher (approx. 200 μrad). Otherwise, the intensity of the second harmonic would have been less distinctive in the on-axis spectrum. This can be shown by a comparison to calculations done with UR simulation codes (e.g. SPECTRA [78] or URGENT [76]) executed with the parameters of the experiment. Since the on-axis position of the GeD was approved to be centered with an accuracy of 2.5 μrad horizontally and 7.3 μrad vertically by transverse scans over the radiation cone, it followed that only a deviance from the electron divergence measured by the wire scan can explain the observed data. The analysis of transverse scans, initially performed to align the GeD, delivered also information about the spatial distribution of the undulator radiation. The observation of the radiation intensity at the resonance energy of the fundamental, scanning over the transverse position of the detector gave the opening angle of the undulator radiation (the detector window was deconvolved from the dataset. Then the electron divergence was deduced, assuming the measured opening angle as a convolution of the unknown electron divergence, the intrinsic opening angle of undulator radiation and a contribution due to diffraction. As a result, these scans confirmed indeed that the electron beam divergence during the GeD measurements was higher than expected initially from the wire scan. Compared to the wire scan a ten times higher value for the divergence was found. The results are summed up in table 5.5.

The uncertainty of this measurement was determined from the fitting curve, which resulted from the flux density distribution (at the fundamental's resonance energy) plotted against the associated transverse detector positions. One standard deviation, which corresponded to a confidence interval of 66% was taken as error margin for these divergence measurements. The large uncertainty of the resulting divergence, determined by the transverse scans of the radiation cone,

GeD Scan of Radiation Cone		warm (294K)		cold (29K)	
		vertical	horizontal	vertical	horizontal
divergence	[μrad]	190 ± 6	264 ± 13	190 ± 18	299 ± 17
beam size	[µm]	26 ± 2	3 ± 1	30 ± 2	3 ± 1

TABLE 5.5: Electron beam parameters during the GeD measurements deduced from transverse scans over the radiation cone.

was mainly caused by the low sampling rate. Only 5 to 10 transverse detector positions were measured due to a tight beam time schedule. Another contribution came from the statistical uncertainty of the detector's count rate itself which has to be mentioned here.

5.5   Flux considering electron divergence

Thus, it became apparent that the divergence during the GeD measurements was significantly higher than thought at first and furthermore significantly changed during the campaign. The used theory, valid only for ideal electron beams without divergence, had to be reconsidered. A modification of equation (2.51) was used then, to include the effect of electron divergence to the simple flux density approximation. The extended equation (5.2) can also be found in the literature, see e.g. P. Elleaume [68]. Following his reasoning, a divergence dependent factor is introduced. The revised equation (2.52) can be used then to compare the expected theoretic gain of the 1st, 3rd and 5th harmonic flux density with the measured data, regarding an increase of the undulator parameter K_{eff} from 0.837 to 0.966 (field measurements) and the actual divergence determined by the transverse scans. The impact of the divergence measurement uncertainty on the expected flux gain is huge and thus the theoretically predicted gain of flux is only poorly determined:

$(1 \pm 24)\%$, $(46 \pm 33)\%$ and $(114 \pm 47)\%$ respectively, based on the measured divergences.

The measured gain values were 9% for the 1st harmonic, 70% for the 3rd and 100% for the 5th respectively. These except for the third harmonic, the values lay more or less centered within the predicted values and all within the range of accuracy.

In order to give a better understanding of the measured gain of the on-axis flux density, the data is visualized and compared to theoretic expectations in the following, thus illustrating effects and interrelations of the involved parameters. For this purpose, it was necessary to simplify equation (2.52) in order to reduce the number of free variables from four to two comparable variables (two divergences along both transversal axes, x and z, for each measurement, at warm and cold undulator temperatures). This was achieved performing a Taylor series approximation around the measured mean divergence values, hereinafter called $\sigma_{x_0'}$ and $\sigma_{z_0'}$. It revealed that directly on-axis small changes from the mean divergences of each direction x and z generate approximately the same change in flux density, thus having almost the same impact. Hence it would seem natural, to combine these deviations from the measured mean values in both directions to one single expression. This expression depends then on a weighted sum of the

deviations from the measured mean values ($\sigma_{x'_0}$ and $\sigma_{z'_0}$) for both axes. It is therefore taken as a commensurate variable to describe the effect of the electron divergence on the gain of the flux density. In the following paragraphs the calculation of the Taylor approximation is presented. Deviances from the measured mean values are written as $\Delta\sigma_{x'} = \sigma_{x'} - \sigma_{x'_0}$ and $\Delta\sigma_{z'} = \sigma_{z'} - \sigma_{z'_0}$. With these notations the first order Taylor approximation of equation (2.52) can be written as:

$$
\begin{aligned}
\left.\frac{d\dot{N}\left(\sigma_{x'}, \sigma_{z'}\right)}{d\Omega}\right|_{\theta=0} &\approx \left.\frac{d\dot{N}_0}{d\Omega}\right|_{\theta=0} \times \left[\left(1 + \frac{L\sigma_{x'}^2}{2\lambda_{ph}}\right)\left(1 + \frac{L\sigma_{z'}^2}{2\lambda_{ph}}\right)\right]^{-1} \\
&\approx \underbrace{\left.\frac{d\dot{N}_0}{d\Omega}\right|_{\theta=0}}_{\text{const.}} \times \underbrace{\frac{4\lambda^2}{\left(2\lambda + L\sigma_{x'}^2\right)\left(2\lambda + L\sigma_{z'}^2\right)}}_{:=f_{\text{div}}}
\end{aligned}
\tag{5.2}
$$

Since the first factor is constant, only the second factor has to be calculated. The first order Taylor expansion T_1 for small deviations $\Delta\sigma_{x'}, \Delta\sigma_{z'}$ from $\sigma_{x'_0}, \sigma_{z'_0}$ of the factor f_{div} reads then:

$$
\begin{aligned}
&T_1[f_{\text{div}}(\sigma_{x'_0} + \Delta\sigma_{x'}, \sigma_{z'_0} + \Delta\sigma_{z'})] \\
&= \frac{4\lambda^2}{\left(2\lambda + L\sigma_{x'_0}^2\right)\left(2\lambda + L\sigma_{z'_0}^2\right)} \\
&\quad - \frac{8\lambda^2 L\sigma_{x'_0}}{\left(2\lambda + L\sigma_{x'_0}^2\right)^2\left(2\lambda + L\sigma_{z'_0}^2\right)}\Delta\sigma_{x'} - \frac{8\lambda^2 L\sigma_{z'_0}}{\left(2\lambda + L\sigma_{x'_0}^2\right)\left(2\lambda + L\sigma_{z'_0}^2\right)^2}\Delta\sigma_{z'} \\
&\quad + \frac{16\lambda^2 L^2\sigma_{x'_0}\sigma_{z'_0}}{\left(2\lambda + L\sigma_{x'_0}^2\right)^2\left(2\lambda + L\sigma_{z'_0}^2\right)^2}\Delta\sigma_{x'}\Delta\sigma_{z'} + \mathcal{O}(\Delta\sigma_{x'}^2) + \mathcal{O}(\Delta\sigma_{z'}^2) \\
&= \frac{4\lambda^2}{\left(2\lambda + L\sigma_{x'_0}^2\right)\left(2\lambda + L\sigma_{z'_0}^2\right)} \\
&\quad - \frac{8\lambda^2 L\sigma_{x'_0}}{\left(2\lambda + L\sigma_{x'_0}^2\right)^2\left(2\lambda + L\sigma_{z'_0}^2\right)}\underbrace{\left(\Delta\sigma_{x'} + \underbrace{\frac{\sigma_{z'_0}\left(2\lambda + L\sigma_{x'_0}^2\right)}{\sigma_{x'_0}\left(2\lambda + L\sigma_{z'_0}^2\right)}}_{\approx 9/10}\Delta\sigma_{z'}\right)}_{\approx \Delta\sigma_{x'} + 9/10\,\Delta\sigma_{z'} := \Delta\Sigma_{x'z'}} \\
&\quad + \mathcal{O}(\Delta\sigma_{x'}\Delta\sigma_{z'}) + \mathcal{O}(\Delta\sigma_{x'}^2) + \mathcal{O}(\Delta\sigma_{z'}^2)
\end{aligned}
$$

With this expression, the expected gain for an increase of the K parameter from 0.837 to 0.966 can be plotted as a function of the summed deviations $\Delta\Sigma_{x'z'}$ from the mean divergences σ_{x0} and σ_{z0}, for each flux-density measurement at both temperatures, warm and cold.

In the following figures 5.11 & 5.12, the expected gain depending on the electron beam divergence is color coded using equation (2.52), and observed separately for the 1st, the 3rd and the 5th harmonic. The green line marks the actual gain of 9%, 70% and 100% measured with the GeD. The probability distribution of the electron divergence measurements is plotted as height along

the z-axis. In this case, the divergence is determined by the described transverse scans over the UR radiation cone and not by the wire scan. The measured mean divergences can be found at the center of the divergence axes along the bottom plane where the deviation from σ_{x0} and σ_{z0} is zero. One can see in figures 5.11 & 5.12 that the actual measured gain in flux-density (green line) crosses the region around the mean values of the measured divergences within a 10 μrad radius.
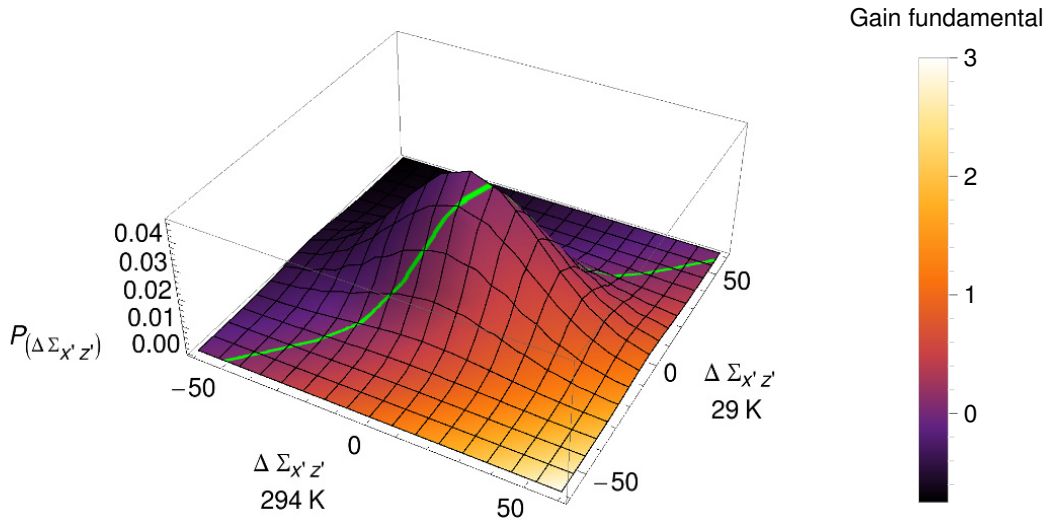
FIGURE 5.11: Analysis of the fundamental on-axis flux density. The 3D contour plot presents two characteristics of the GeD data combined in one graphic. The aim is to confirm the gain of the K-parameter of the cryogenic undulator due to the cooling, even if the electron divergence was changing during the measurement campaign and a simple, direct comparison of the data was not possible. In the graph the measured divergence of the electron beam at MAMI is visualized as a gaussian probability distribution. The data was generated by transverse scans over the radiation cone measuring the radiation intensity with the GeD itself. From these 2D radiation intensity patterns the particular electron divergence during cold and warm operation along both axes was deduced. For ease of exposition the horizontal and vertical divergences are combined to a general divergence parameter $\Delta\Sigma_{x'z'}$. This was done for both the cold and the warm operation mode (further information in the text). The divergence parameter $\Delta\Sigma_{x'z'}$ is zero when the divergences match the measured mean values σ_{x0} and σ_{z0} and alters with deviations from that. The mean values are given in table 5.5. On the other hand the theoretical gain of the on-axis flux density was calculated by equation (2.52) for the corresponding electron divergences. The result is color coded, represented by the legend on the right side of the plot. The green line marks the value of the actual measured gain, which is 9% for the 1st harmonic. One can see, that the green line, representing the measured flux gain, crosses the area near the mean values of the divergence measurements within a distance of about 10 μrad, showing that theory and measurement agree in the range of the measurement uncertainties.

This way the conflict within the data could have been solved. It could be shown that the measured gains agree with the theoretically predicted gains, regarding the electron beam divergences and their range of accuracy. Hence, the data is consistent to the extended theory, given by equation (2.52), and without contradiction, if the changing electron beam divergence is considered correctly.
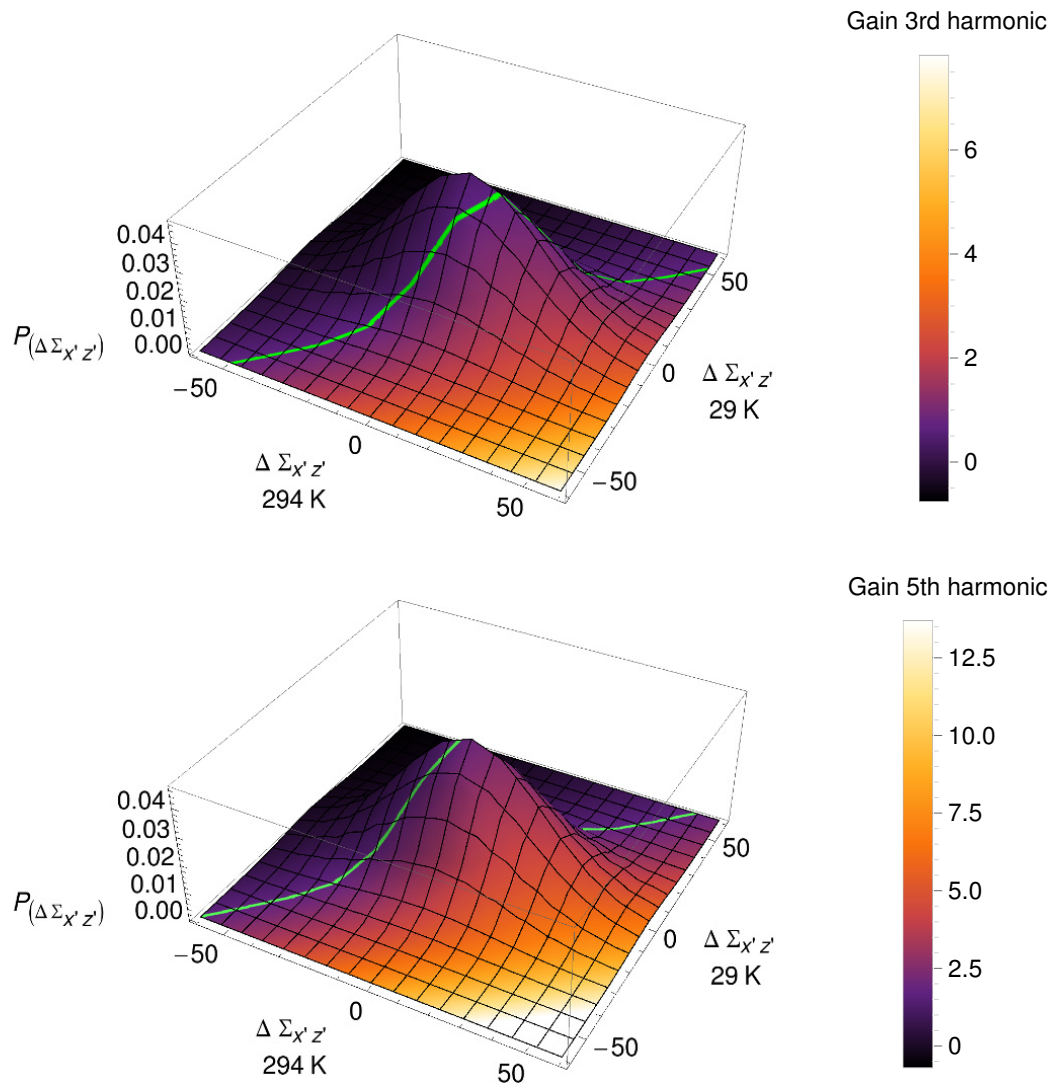
FIGURE 5.12: Analysis of the 3rd and 5th harmonics on-axis flux density. For a detailed description of the presented data read the caption of figure 5.11. The green line, representing the measured gain of 70% and 100% for the 3rd and the 5th harmonic, crosses the area near the mean values of the divergence measurements within a distance of about 10 μrad, showing that theory, given by equation (2.52), and measurement agree in the range of the measurement uncertainties, if the electron beam divergence is considered, which was measured by transverse scans over the UR cone.

5.6   Conclusion and outlook

The spectral measurements confirm the expected gain of the *K* parameter of more than 15%. Any additional source of field errors generated by mechanical distortion due to the temperature drop of more than 260 K or produced by thermal gradients along the undulator are below 2% (corresponding to the resolution limit of our spectrometer, see appendix B). A significant gain of the photon flux density was achieved (9%, 70% and over 100% increase for the 1st, 3rd and 5th harmonic) in good agreement with theoretical expectations.

The experiments with the prototype confirmed the expectations and the feasibility of the cryogenic undulator technology. The achieved increase of the magnet's remanent field strength enables new technical realizations and enhancements for future UR sources. Existing third generation synchrotrons rely on the development of short-period undulators with high magnetic fields to increase their attainable photon energy range [148–151]. Furthermore, the use of the new permanent magnet material paves the way for the application of PWA accelerated electrons as source for UR and even as drivers for PWA based FELs.

Since these newly developed PWA sources suffer from electron beam instabilities and a broad energy spread, which makes proper electron beam transport challenging, the significantly increased coercivity (up to 300%) of the cooled magnets and a correspondingly increased resistivity against demagnetization due to irradiation by electrons and laser light is vitally important.

Furthermore, a high *K* parameter in combination with a relatively short period is essential for the PWA-FEL scenario. The interaction between electrons and light-field is thereby amplified and slippage effects are reduced. As a consequence the acceptance of the electron energy spread is increased [135], which is as mentioned before a crucial drawback of todays PWA technology.

Until now the described CPMU prototype was successfully used during two different beam times at MAMI and SLAC [152]. The next step will be the implementation into a PWA beam line. The experiences and the lessons we learned inspired the development of two new undulators designed for the PWA beam lines at DESY and CALA. The first device will have 100 periods with 5 mm length, hence a total length of 0.5 m. This device will be a conventional non cryogenic undulator which provides a prompt readiness and a simple use without cooling and defrosting procedures. The specific design of the new undulator is described and field optimization simulations are presented in detail in chapter 3. The other device will be an 2-m-long cryogenic undulator with a 15 mm period which will be used as a proof of principle PWA VUV-FEL experiment. This undulator period length was the optimum result of a start to end simulation including beam optics and realistic electron beam properties. Both new undulators will be milestones on the way to establish new kinds of ultra-brilliant and tunable X-ray sources for scientific purposes.

Appendix A

Electron bunch transverse motion and alignment tolerance

To estimate the irradiation dose induced into the undulator magnets during a lifelong operation, preliminary considerations were made, considering typical LPA electron beam instabilities. With two assumptions concerning the undulators self focusing properties of an undulator with typical horizontal pole width [82] and typical vertical magnetic field slope [79]:

$$k_x = \frac{1}{3\lambda_u} \text{ and } k_z = \frac{2\pi}{\lambda_u} \,,$$

the propagation of the bunch in the undulator can be described as:

$$x(s, x_0, \theta_{x0}) = x_0 \cosh(\kappa_x s) + \frac{\theta_{x0}}{\kappa_x} \sinh(\kappa_x s) \tag{A.1}$$

$$z(s, z_0, \theta_{z0}) = z_0 \cos(\kappa_z s) + \frac{\theta_{z0}}{\kappa_z} \sin(\kappa_z s) \,, \tag{A.2}$$

using the following expressions for κ_x and κ_z

$$\kappa_x = \frac{K k_x}{\sqrt{2}\gamma} \text{ and } \kappa_z = \frac{K k_z}{\sqrt{2}\gamma} \,.$$

Thereby, one gets the maximum offset of an electron bunch inside the undulator depending on its tilt and offset parameters at the beginning of the undulator. In figure A.1 the motion of the electron bunch center through an undulator for two special cases is shown. The blue line shows an electron bunch which has an 500 µm offset at the undulator start. The motion is shown for
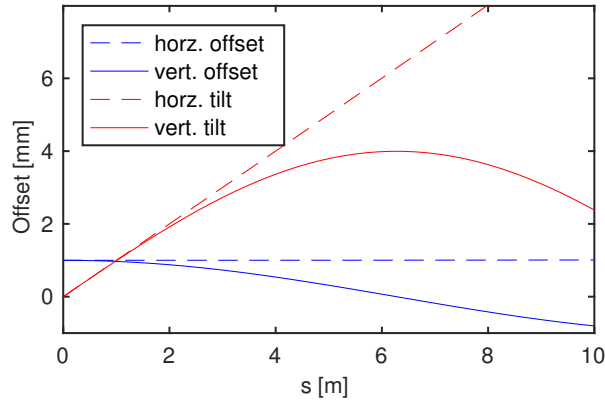
FIGURE A.1: Focusing effects of the planar undulator with a 5 mm period length and a *K* parameter of 0.4 (as expected in our case) on the electron beam. Calculations are made for rather unrealistic offsets of 1 mm and tilts of 1 mrad along both axis, horizontally and vertically to highlight the effects. One sees that the undulator has weak focusing abilities, which only would be significant for longer insertion devices of several meters. A 10 m device as shown here may be a future design case one day.

both planes the horizontal (dashed line) and the vertical (solid line). The red line shows the case where the bunch is tilted by 0.1 mrad with respect to the undulator axis.

The self focusing of the undulator in the vertical plane is weak, which is also due to the fact that the assumed undulator has a period length of 5 mm and a *K* parameter of only 0.4 . All values are orientated towards the targeted undulator design, except for the fact, that the actual undulator will have a length of only 0.5 m instead of 10 m, as depicted. This was done consciously for two reasons. First to make the weak focusing apparent, second to take future undulator extensions into account.

What becomes clear is that for short undulators the alignment tolerances are easily compliable. Combining both alignment issues one gets a parameter space in which the bunch must be located A.2. The spectral output of an undulator is maximized for an electron bunch with $\beta = D$, where β is the TWISS parameter of the bunch at the center of the undulator and D is the distance from the undulator center to the point of observation [68]. With D one gets a bunch cross section within the undulator and thus a maximum offset and tilt from the undulator axis at the undulator front. However, this is only important for long undulators.
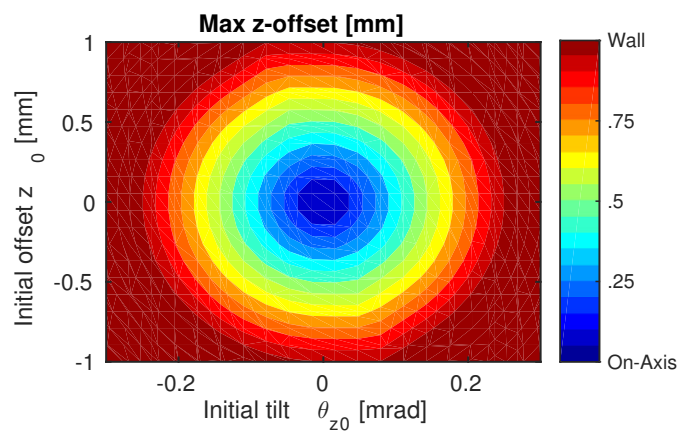
FIGURE A.2: Maximum vertical electron beam offset from the central axis inside a 10 m long 5 mm period length planar undulator, with a K parameter of 0.4 (as expected in our case). The maximum offset is calculated for initial vertical misalignments up to 1 mm and initial tilts up to 0.3 mrad.

Appendix B

Spectral resolution of the transmission grating spectrometer

The spectral resolution of the TGS is dominated by the size of the image of the spectrometers entrance slit, projected onto the CCD - see figure 5.4. This size depends on the maximum divergence of the incident light along the dispersion axis. The maximum angle is given by: $\theta_{max,z} = (\Sigma_{r,z} + S)/L_1$ with the slit size S and the standard deviation of the source size $\Sigma_{r,z}$. The spectral resolution depends therefore among other parameters on the size of the entrance slit S. If the size of the entrance slit S is wide, the value of A_z, the projection of the source Σ_r, z through the slit onto the CCD, becomes wide and overlapping of two nearby signals limits the resolution. On the other hand, Rayleigh's criterion limits the resolution for small entrance slits, since the number of illuminated grating grooves depends on S. Further, for small entrance slits S and long wavelengths of the incident photons one has to take diffraction into account. For our case a Fresnel number F around 1 indicates that near field effects and with it Fresnel diffraction dominates. The Fresnel number is given by $F = S^2/(4\lambda_{ph}L_2)$. Now a simple approximation of the single slit diffraction can be made:

$$\left(\frac{d\lambda_{ph}}{\lambda_{ph}}\right)_{tot} \approx \sqrt{\left(\frac{d}{\lambda_{ph}}\left(\frac{S}{L2} + \frac{S+\Sigma_{r,x}}{L1}\right)\right)^2 + \left(\frac{1}{n_g N_g}\right)^2 + \left(\frac{1}{n_u N_u}\right)^2 + \left(2.78\frac{d}{\pi S}\right)^2} \quad \text{(B.1)}$$

All mentioned effects are summarized by the following Gaussian sum which approximates the bandwidth measured by the TGS. The first summand of the Gaussian sum originates from geometric optics [153] as described above. The second term represents Rayleigh's criterion with the diffraction order n_g and the number of illuminated slits N_g, while the third summand describes the intrinsic undulator bandwidth with harmonic number n_u and the number of undulator periods N_u. The last term estimates the contribution due to single slit Fresnel diffraction. Two other contributions are neglected. The electrons energy spread, below 0.2%, is neglected as well as the contribution due to UR redshift, both described in section 2.2.5.4. The redshift is limited by the acceptance angle of the spectrometer, which is set much smaller than the UR opening angle.
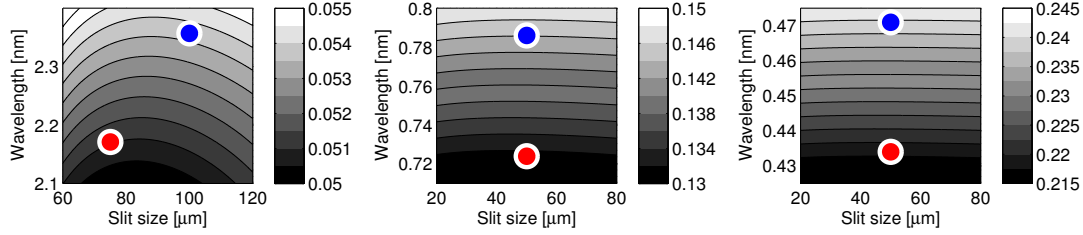
FIGURE B.1: Expected spectral resolution (color coded) as a function of wavelength and slit size as discussed in the setup section. The red and blue dots mark the chosen slit width for the warm and the cold undulator spectrum measurement respectively. From left to right the best spectral resolution according to the wavelengths of the fundamental, third and fifth harmonic is shown. The higher harmonics intrinsic undulator bandwidth of 1.67% and 1% for the third and the fifth harmonic respectively is overlaid by the spectrometers resolution and thereby not resolvable.

The spectrometers' slit limits the acceptance angle $\theta_{max,z}$ in the z direction (see figure 5.4). The acceptance angle in the x direction is given by the size of a single pixel and the distance between undulator and CCD. This is due to the fact that the bandwidth is determined by a line-out of the CCD data with a single pixel width. Therefor the acceptance angle in x is given by $\theta_{max,x} = (S_{pix} + \Sigma_{r,x})/(L_1 + L_2)$. These two angles, $\theta_{max,z} \approx 44$ μrad for a 100 μrad slit and $\theta_{max,x} \approx 30$ μrad for a source size $\Sigma_{r,x} \approx 370$ µm, determine an additional contribution to the measured line width due to a certain amount of tilted radiation, which is also redshifted - see equation (2.40). The resulting contribution to the bandwidth is far below 0.5%, and therefor also neglected.

This approximation overestimates the diffraction broadening for the shorter wavelength of the higher harmonics, where a transition to the far field or rather Fraunhofer diffraction occurs, which is not considered in our approximation. The resolution of the spectrometer according to equation (B.1) is plotted in figure B.1. The blue and red dots (cooled and RT) mark the bandwidth of an ideal undulator detected by the TGS. A slit size of 75 µm for the wavelength of the uncooled device's fundamental and 100 µm for the cooled undulator's fundamental was chosen to optimize the spectrometers resolution whereas 50 µm was chosen for the higher orders. An increase of the magnetic field error due to thermally induced mechanical distortions gives an additional summand in equation (B.1). This effect should be detectable if the field error (RMS) becomes greater than 2%. The bandwidths of the higher harmonics, intrinsically 1.67% and 1% for the third and the fifth harmonic, are dominated by the spectrometers resolution and could not be analyzed, see figure B.1.

Appendix C

Magnetization data

This section shows the magnetization curves of the all materials used in the simulations in section 3.8.2. Only the first quadrant is needed and listed in the tables.

H [kOe]	**B** [T]
0.00	1.19034
-3.45	0.8351891377
-6.90	0.4800382753
-10.34	0.124887413
-13.79	-0.2302634494
-17.24	-0.5854143117
-20.69	-0.9405651741
-24.14	-1.2957160364
-27.58	-1.6508668988
-31.03	-2.0060177611
-34.48	-2.3611686234
-34.79	-2.3982688546
-35.09	-2.4406491396
-35.33	-2.4835294591
-35.46	-2.5128896996
-35.58	-2.5475299939
-35.64	-2.5707902016
-35.70	-2.6151706246
-35.73	-2.7136602902
-35.76	-2.8121499557
-35.79	-2.9106396213
-35.82	-3.0091292868
-35.85	-3.1076189524
-35.88	-3.206108618
-35.91	-3.3045982835
-35.94	-3.4030879491
-35.97	-3.5015776147
-36.00	-3.6000672802

TABLE C.1: Magnetization data (first quadrant) of *VacoDym890TP*, used for the optimization simulations. These data was measured by *VACUUMSCHMELZE*.

H [A/m]	**B** [T]
0	0
10.151	0.016
11.676	0.019
13.431	0.023
15.449	0.027
17.770	0.033
20.438	0.040
23.507	0.049
27.037	0.060
31.095	0.076
35.763	0.099
41.129	0.134
47.302	0.178
54.402	0.232
62.564	0.298
71.962	0.375
82.743	0.476
95.156	0.617
109.443	0.812
125.868	1.056
144.718	1.284
166.435	1.463
191.414	1.589
220.120	1.678
253.147	1.750
291.112	1.810
334.765	1.858
384.989	1.900
442.731	1.936
509.181	1.966
585.553	1.996
673.389	2.025
774.299	2.049
890.488	2.079
921.134	2.085
1059.370	2.103
1218.331	2.126
1401.323	2.144
1611.433	2.161
1853.071	2.179
2130.866	2.196
2450.110	2.207

TABLE C.2: Magnetization data of *VacoFlux50*, used as pole material for the optimization simulations. These data was measured by *VACUUMSCHMELZE*.

Appendix D

Geometric parameters of the optimization setups

Within this section a number of geometrical setups are listed which are situated along the Pareto frontiers discussed in section 3.8.2.5. These setups reach the highest possible magnetic peak and effective fields minimizing the material costs of the undulator.

setup 1:	optimization goal	
model	maximum field	effective field
parameter	[mm]	[mm]
Lx_{Mag}	1.666	1.656
Lx_{Pol}	0.67	0.68
Ly_{Mag}	20.9	20.9
Ly_{Pol}	19.0	19.0
Lz_{Mag}	8.8	8.8
Lz_{Pol}	8.0	8.0
volume	[mm^3]	[mm^3]
V_{Mag}	306.41	304.57
V_{Pol}	101.84	103.36
result:	B_{max}	B_{eff}
field	0.610 T	0.601 T
$\Delta B/B$	0.939	0.938

TABLE D.1: Optimization result of setup 1.

setup 2:	optimization goal	
model	maximum field	effective field
parameter	[mm]	[mm]
Lx_{Mag}	1.606	1.596
Lx_{Pol}	0.73	0.74
Ly_{Mag}	20.9	20.9
Ly_{Pol}	19.0	19.0
Lz_{Mag}	10.4	10.4
Lz_{Pol}	8.0	8.0
volume	[mm^3]	[mm^3]
V_{Mag}	349.08	346.91
V_{Pol}	110.96	112.48
result:	B_{max}	B_{eff}
field	0.630 T	0.623 T
$\Delta B/B$	0.970	0.970

TABLE D.2: Optimization result of undulator setup 2.

setup 3:	optimization goal	
model	maximum field	effective field
parameter	[mm]	[mm]
Lx_{Mag}	1.616	1.606
Lx_{Pol}	0.72	0.73
Ly_{Mag}	20.9	20.9
Ly_{Pol}	19.0	19.0
Lz_{Mag}	13.0	13.0
Lz_{Pol}	10.0	10.0
volume	[mm^3]	[mm^3]
V_{Mag}	439.07	436.35
V_{Pol}	136.8	138.7
result:	B_{max}	B_{eff}
field	0.641 T	0.633 T
$\Delta B/B$	0.986	0.986

TABLE D.3: Optimization result of undulator setup 3.

setup 4:	optimization goal	
model	maximum field	effective field
parameter	[mm]	[mm]
Lx_{Mag}	1.616	1.606
Lx_{Pol}	0.72	0.73
Ly_{Mag}	22.8	22.8
Ly_{Pol}	19.0	19.0
Lz_{Mag}	15.6	15.6
Lz_{Pol}	12.0	12.0
volume	[mm^3]	[mm^3]
V_{Mag}	574.78	571.22
V_{Pol}	164.16	166.44
result:	B_{max}	B_{eff}
field	0.648 T	0.640 T
$\Delta B/B$	0.997	0.997

TABLE D.4: Optimization result of undulator setup 4.

setup 5:	optimization goal	
model	maximum field	effective field
parameter	[mm]	[mm]
Lx_{Mag}	1.616	1.596
Lx_{Pol}	0.72	0.74
Ly_{Mag}	29.9	29.9
Ly_{Pol}	23.0	23.0
Lz_{Mag}	15.6	15.6
Lz_{Pol}	12.0	12.0
volume	[mm^3]	[mm^3]
V_{Mag}	753.77	744.44
V_{Pol}	198.72	204.24
result:	B_{max}	B_{eff}
field	0.650 T	0.642 T
$\Delta B/B$	1	1

TABLE D.5: Optimization result of setup 5. The values are taken as reference for the maximum on-axis magnetic induction as the field reaches saturation. A significant growth beyond this magnetic induction is not possible with the used magnet and pole material.

Acknowledgements

Bibliography

[1] Uwe Bergmann, John Corlett, Steve Dierker, Roger Falcone, John Galayda, Murray Gibson, Jerry Hastings, Bob Hettel, John Hill, Zahid Hussain, et al. Science and technology of future light sources: A white paper. Technical report, Stanford Linear Accelerator Center (SLAC), 2009.

[2] James Benjamine Rosenzweig, DB Cline, B Cole, H Figueroa, W Gai, R Konecny, J Norem, P Schoessow, and J Simpson. Experimental observation of plasma wake-field acceleration. *Physical review letters*, 61(1):98, 1988.

[3] B. Hidding, T. Königstein, J. Osterholz, S. Karsch, O. Willi, and G. Pretzler. Monoenergetic energy doubling in a hybrid laser-plasma wakefield accelerator. *Phys. Rev. Lett.*, 104: 195002, May 2010. doi: 10.1103/PhysRevLett.104.195002. URL http://link.aps.org/doi/10.1103/PhysRevLett.104.195002.

[4] Thorben Seggebrock. *Conceptual design of a laser-plasma driven free-electron laser*. PhD thesis, Ludwig-Maximilians-Universität München, Fakultät für Physik, Schellingstraße 4, D-80799 München, 2015.

[5] Picture taken from Website, 2018. <http://home.slac.stanford.edu/pressreleases/2011/20110202.htm>, originated on 2011.

[6] J Clerk Maxwell. A dynamical theory of the electromagnetic field. *Philosophical transactions of the Royal Society of London*, 155:459–512, 1865.

[7] Picture taken from Website, 2018. <https://en.wikipedia.org/wiki/James_Clerk_Maxwell>, originated on 1890.

[8] Picture taken from Website, 2018. <https://de.wikipedia.org/wiki/Hendrik_Antoon_Lorentz>, originated on 1921.

[9] Picture taken from Website, 2018. <https://en.wikipedia.org/wiki/Michelson\T1\textendashMorley_experiment>, originated on 1887.

[10] A Liénard. Champ électrique et magnétique produit par une charge électrique contentreé en un point et animée d'un mouvement quelconque. *L'Éclairage Électrique*, 16(5):53, 1898.

[11] E Wiechert. *Archives Neerlandaises des Sciences exactes et naturelles*, II.5:1900.

[12] Albert Einstein. Zur elektrodynamik bewegter körper. *Annalen der physik*, 322(10):891–921, 1905.

[13] JP Blewett. Radiation losses in the induction electron accelerator. *Physical Review*, 69 (3-4):87, 1946.

[14] FR Elder, RV Langmuir, and HC Pollock. Radiation from electrons accelerated in a synchrotron. *Physical Review*, 74(1):52, 1948.

[15] Picture taken from Website, 2018. <https://en.wikipedia.org/wiki/Betatron>, originated on 1940.

[16] Wilhelm Conrad Röntgen. Über eine neue art von strahlen. *Annalen der Physik*, 300(1): 1–11, 1898.

[17] Picture taken from Website, 2018. <http://photon-science.desy.de/facilities/petra_iii/beamlines/index_eng.html>, originated on 2009.

[18] J Schwinger. On the classical radiation of accelerated electrons. *Physical Review*, 75(12): 1912, 1949.

[19] H Motz. Applications of the radiation from fast electron beams. *Journal of Applied Physics*, 22(5):527–535, 1951.

[20] H Motz, W Thon, and RN Whitehurst. Experiments on radiation by fast electron beams. *Journal of Applied Physics*, 24(7):826–833, 1953.

[21] DF Alferov, Yu A Bashmakov, KA Belovintsev, EG Bessonov, and PA Cherenkov. Observation of undulating radiation with the "pakhra" synchrotron. *JETP Lett*, 26(7):385–388, 1977.

[22] DF Alferov, Iu A Bashmakov, and EG Bessonov. Theory of undulator radiation. i, ii. *Soviet Physics Technical Physics*, 23:902–909, 1978.

[23] VL Ginzburg and IM Frank. On a doppler efffect at the superlight velocity. In *Dokl. Akadem. Nauk SSSR*, volume 56, page 583, 1947.

[24] IM Frank and VL Ginzburg. Radiation of a uniform moving electron due to its transition from one medium into another. *J. Phys.(USSR)*, 9:353, 1945.

[25] Gwyn P Williams. X-ray data booklet. *X-RAY DATA BOOKLET*, 2001.

[26] Picture taken from Website, 2018. <https://www.nature.com/news/europe-s-x-ray-laser-fires-up-1.22519>, originated on 2017.

[27] Picture taken from Website, 2018. <https://www.xfel.eu/facility/overview/index_eng.html>, originated on 2017.

[28] T Tajima and JM Dawson. Laser electron accelerator. *Physical Review Letters*, 43(4):267, 1979.

[29] C Joshi, WB Mori, T Katsouleas, JM Dawson, JM Kindel, and DW Forslund. Ultrahigh gradient particle acceleration by intense laser-driven plasma density waves. *Nature*, 311 (5986):525–529, 1984.

[30] KA Marsh. Trapped electron acceleration by a laser-driven relativistic plasma wave. *Nature*, 368:7, 1994.

[31] A Modena, Z Najmudin, AE Dangor, CE Clayton, et al. Electron acceleration from the breaking of relativistic plasma waves. *nature*, 377(6550):606, 1995.

[32] Jalas Sören, 2016. <https://www.cfel.de/news_archive/2016/news_2016/accelerator_produces_first_particle_beam/index_eng.html>.

[33] W. P. Leemans, A. J. Gonsalves, H.-S. Mao, K. Nakamura, C. Benedetti, C. B. Schroeder, Cs. Tóth, J. Daniels, D. E. Mittelberger, S. S. Bulanov, J.-L. Vay, C. G. R. Geddes, and E. Esarey. Multi-gev electron beams from capillary-discharge-guided subpetawatt laser pulses in the self-trapping regime. *Phys. Rev. Lett.*, 113:245002, Dec 2014. doi: 10.1103/PhysRevLett.113.245002. URL http://link.aps.org/doi/10.1103/PhysRevLett.113.245002.

[34] Matthias Fuchs, Raphael Weingartner, Antonia Popp, Zsuzsanna Major, Stefan Becker, Jens Osterhoff, Isabella Cortrie, Benno Zeitler, Rainer Hörlein, George D Tsakiris, et al. Laser-driven soft-x-ray undulator source. *Nature physics*, 5(11):826–829, 2009.

[35] JA Clarke. *The Science and Technology of Undulators and Wigglers*. Oxford University Press, 2004.

[36] Peter Campbell. *Permanent Magnet Materials and their Application*. Cambridge University Press, 1994. ISBN 9780511623073. URL http://dx.doi.org/10.1017/CBO9780511623073. Cambridge Books Online.

[37] HR Kirchmayr. Permanent magnets and hard magnetic materials. *Journal of Physics D: Applied Physics*, 29(11):2763, 1996.

[38] Lev Davidovič Landau and Evgenii Mikhailovich Lifshitz. *Mechanics and electrodynamics*. Elsevier, 2013.

[39] Charles Kittel. *Introduction to solid state physics*. Wiley & Sons, 1996.

[40] Teruhiko Bizen, T Tanaka, Y Asano, DE Kim, JS Bak, HS Lee, and H Kitamura. Demagnetization of undulator magnets irradiated high energy electrons. *Nuclear Instruments and Methods in Physics Research Section A: Accelerators, Spectrometers, Detectors and Associated Equipment*, 467:185–189, 2001.

[41] T Bizen, X-M Maréchal, T Seike, H Kitamura, T Hara, T Tanaka, Y Asano, DE Kim, and HS Lee. Radiation damage in permanent magnets for id. *Radiation measurements*, 41:S260–S264, 2006.

[42] Teruhiko Bizen, Yoshihiro Asano, Xavier-Marie Maréchal, Takamitsu Seike, Tsuyoshi Aoki, Kenji Fukami, Naoyasu Hosoda, Hiroto Yonehara, Tetsuya Takagi, Toru Hara, et al. High-energy electron irradiation of ndfeb permanent magnets: Dependence of radiation damage on the electron energy. *Nuclear Instruments and Methods in Physics Research Section A: Accelerators, Spectrometers, Detectors and Associated Equipment*, 574(3):401–406, 2007.

[43] Rui Qiu, Hee-Seock Lee, Junli Li, Tae-Yeong Koo, and Tae Hwan Jang. Radiation damage of nd 2 fe 14 b permanent magnets at 2.5 gev electron accelerator. *Nuclear Instruments and Methods in Physics Research Section A: Accelerators, Spectrometers, Detectors and Associated Equipment*, 594(2):111–118, 2008.

[44] Jochen Skupin, Y Li, J Pflüger, B Faatz, T Vielitz, and Deutsches Elektronen-Synchrotron. Undulator demagnetization due to radiation losses at flash. *Proceedings of EPAC08, Genoa, Italy*, pages 2308–2310, 2008.

[45] AB Temnykh. Measurement of NdFeB permanent magnets demagnetization induced by high energy electron radiation. *Nuclear Instruments and Methods in Physics Research Section A: Accelerators, Spectrometers, Detectors and Associated Equipment*, 587(1):13–19, 2008.

[46] Adib Samin, Michael Kurth, and Lei R Cao. An analysis of radiation effects on ndfeb permanent magnets. *Nuclear Instruments and Methods in Physics Research Section B: Beam Interactions with Materials and Atoms*, 342:200–205, 2015.

[47] Teruhiko Bizen. Brief review of the approaches to elucidate the mechanism of the radiation-induced demagnetization. In *Proc. ERL*, pages 121–126, 2011.

[48] Burton L Henke, Eric M Gullikson, and John C Davis. X-ray interactions: photoabsorption, scattering, transmission, and reflection at e= 50-30,000 ev, z= 1-92. *Atomic data and nuclear data tables*, 54(2):181–342, 1993.

[49] Hans Bichsel. A method to improve tracking and particle identification in tpcs and silicon detectors. *Nuclear Instruments and Methods in Physics Research Section A: Accelerators, Spectrometers, Detectors and Associated Equipment*, 562(1):154–197, 2006.

[50] MJ Berger. Estar. 2002.

[51] Gregory Wilson and JR Dennison. Approximation of range in materials as a function of incident electron energy. *Plasma Science, IEEE Transactions on*, 40(2):291–297, 2012.

[52] William Duane and Franklin L Hunt. American physical society. *Physical Review*, 23(24):I9IS, 1913.

[53] TT Böhlen, F Cerutti, MPW Chin, A Fasso, A Ferrari, PG Ortega, A Mairani, PR Sala, G Smirnov, and V Vlachoudis. The fluka code: developments and challenges for high energy and medical applications. *Nuclear Data Sheets*, 120:211–214, 2014.

[54] Alfredo Ferrari, Paola R Sala, Alberto Fasso, and Johannes Ranft. Fluka: A multi-particle transport code (program version 2005). Technical report, 2005.

[55] Rene Brun, Federico Carminati, Simone Giani, et al. Geant detector description and simulation tool. *CERN program library long writeup W*, 5013:1993, 1993.

[56] T Bizen, Y Asano, T Hara, X Marechal, T Seike, T Tanaka, HS Lee, DE Kim, CW Chung, and H Kitamura. Baking effect for NdFeB magnets against demagnetization induced by high-energy electrons. *Nuclear Instruments and Methods in Physics Research Section A: Accelerators, Spectrometers, Detectors and Associated Equipment*, 515(3):850–852, 2003.

[57] T. Diaz de la Rubia, R. S. Averback, R. Benedek, and W. E. King. Role of thermal spikes in energetic displacement cascades. *Phys. Rev. Lett.*, 59:1930–1933, Oct 1987. doi: 10.1103/PhysRevLett.59.1930. URL http://link.aps.org/doi/10.1103/PhysRevLett.59.1930.

[58] A Meldrum, SJ Zinkle, LA Boatner, and Rodney C Ewing. A transient liquid-like phase in the displacement cascades of zircon, hafnon and thorite. *Nature*, 395(6697):56–58, 1998.

[59] ES Gorkunov and Yu N Dragoshansky. Interaction between domain walls and structural defects as a background for magnetic inspection of steel structures. In *Proceedings of the 15th World Conference on Nondestructive Testing, Roma, Italy*, 2000.

[60] K Uestuener, M Katter, and W Rodewald. Dependence of the mean grain size and coercivity of sintered nd–fe–b magnets on the initial powder particle size. *IEEE transactions on magnetics*, 42(10):2897–2899, 2006.

[61] K Moriyama. Coatings for improved vacuum materials. *MRS Bulletin*, 15:32–34, 7 1990. ISSN 1938-1425. doi: 10.1557/S0883769400059224. URL http://journals.cambridge.org/article_S0883769400059224.

[62] Vacuumschmelze Roland Zoller, 2016. Private communication.

[63] K Hirota, H Nakamura, T Minowa, and M Honshima. Coercivity enhancement by the grain boundary diffusion process to NdFeB sintered magnets. *Magnetics, IEEE Transactions on*, 42(10):2909–2911, Oct 2006. ISSN 0018-9464. doi: 10.1109/TMAG.2006.879906.

[64] H Nakamura, K Hirota, T Ohashi, and T Minowa. Coercivity distributions in NdFeB sintered magnets produced by the grain boundary diffusion process. *Journal of Physics D: Applied Physics*, 44(6):064003, 2011. URL http://stacks.iop.org/0022-3727/44/i=6/a=064003.

[65] H Sepehri-Amin, T Ohkubo, and K Hono. The mechanism of coercivity enhancement by the grain boundary diffusion process of nd–fe–b sintered magnets. *Acta Materialia*, 61(6): 1982 – 1990, 2013. ISSN 1359-6454. doi: http://dx.doi.org/10.1016/j.actamat.2012.12.018. URL http://www.sciencedirect.com/science/article/pii/S1359645412008762.

[66] K. Löewe, C. Brombacher, M. Katter, and O. Gutfleisch. Temperature-dependent dy diffusion processes in nd–fe–b permanent magnets. *Acta Materialia*, 83(0):248 – 255, 2015. ISSN 1359-6454. doi: http://dx.doi.org/10.1016/j.actamat.2014.09.039. URL http://www.sciencedirect.com/science/article/pii/S1359645414007198.

[67] Picture taken from Website, 2018. <http://photon-science.desy.de/facilities/flash/the_free_electron_laser/undulator/index_eng.html>.

[68] H Onuki and P Elleaume. *Undulators, Wigglers and their Applications*. Taylor and Francis, New York, 2003.

[69] Erik Wallén, J Chavanne, and P Elleaume. Magnetic calculations of a superconducting undulator at the esrf. *Nuclear Instruments and Methods in Physics Research Section A: Accelerators, Spectrometers, Detectors and Associated Equipment*, 541(3):630–650, 2005.

[70] K. Uestuener, M. Katter, R. Blank, D. Benedikt, J. Bahrdt, A. Gaupp, B. Klemke, F. Grüner, and R. Weingartner. Sintered (Pr,Nd)-Fe-B permanent magnets with $(BH)_{max}$ of 520 kJ / m^3 at 85K for cryogenic applications. *J. Synchrotron Rad.*, 8:1221, 2001.

[71] T Eichner, F Grüner, S Becker, Matthias Fuchs, D Habs, R Weingartner, U Schramm, H Backe, P Kunz, and W Lauth. Miniature magnetic devices for laser-based, table-top free-electron lasers. *Physical Review Special Topics-Accelerators and Beams*, 10(8):082401, 2007.

[72] F O'Shea, G Marcus, J Rosenzweig, F Gruener, R Weingartner, A Gaupp, and J Bahrdt. A short period undulator utilizing a novel material. In *Proc. of PAC09, Vancouver, BC, Canada.* PAC09, 2009.

[73] FH O'Shea, G Marcus, JB Rosenzweig, M Scheer, J Bahrdt, R Weingartner, A Gaupp, and F Grüner. Short period, high field cryogenic undulator for extreme performance x-ray free electron lasers. *Physical Review Special Topics-Accelerators and Beams*, 13(7):070702, 2010.

[74] JD Jackson. *Classical electrodynamics*, volume 3. Wiley New York etc., 1962.

[75] LD Landau and EM Lifshitz. *The classical theory of fields*, volume 2. Butterworth-Heinemann, 1975.

[76] RP Walker and B Diviacco. Urgent- a computer program for calculating undulator radiation spectral, angular, polarization, and power density properties. *Review of scientific instruments*, 63(1):392–395, 1992.

[77] O Chubar and P Elleaume. Accurate and efficient computation of synchrotron radiation in the near field region. In *proc. of the EPAC98 Conference*, pages 1177–1179, 1998.

[78] T. Tanaka and H. Kitamura. Spectra: a synchrotron radiation calculation code. *J. Synchrotron Rad.*, 8:1221, 2001.

[79] K Wille. *The Physics of Particle Accelerators - an introduction.* Oxford University Press, 1996.

[80] Peter P Ilinski, Roger J Dejus, Efim S Gluskin, and Timothy I Morrison. Practical aspects of undulator radiation properties. In *SPIE's 1996 International Symposium on Optical Science, Engineering, and Instrumentation*, pages 16–25. International Society for Optics and Photonics, 1996.

[81] R Dejus, Isaac B Vasserman, Shigemi Sasaki, and Elizabeth R Moog. Undulator a magnetic properties and spectral performance. *ANL/APS/Tech. Bull*, 45:1–51, 2002.

[82] Andreas Gaupp, 2013. Private communication.

[83] Johannes Bahrdt, 2013. Private communication.

[84] BL Bobbs, G Rakowsky, P Kennedy, RA Cover, and D Slater. In search of a meaningful field-error specification for wigglers. *Nuclear Instruments and Methods in Physics Research Section A: Accelerators, Spectrometers, Detectors and Associated Equipment*, 296(1):574–578, 1990.

[85] BM Kincaid. Random errors in undulators and their effects on the radiation spectrum. *J. Opt. Soc. Am. B*, 2(8):1294–1306, Aug 1985. doi: 10.1364/JOSAB.2.001294. URL http://josab.osa.org/abstract.cfm?URI=josab-2-8-1294.

[86] RP Walker. Interference effects in undulator and wiggler radiation sources. *Nuclear Instruments and Methods in Physics Research Section A: Accelerators, Spectrometers, Detectors and Associated Equipment*, 335(1–2):328 – 337, 1993. ISSN 0168-9002. doi: http://dx.doi.org/10.1016/0168-9002(93)90288-S. URL http://www.sciencedirect.com/science/article/pii/016890029390288S.

[87] Matthias Fuchs. *Laser-driven soft-X-ray undulator source.* PhD thesis, Ludwig-Maximilians-Universität München, Fakultät für Physik, Schellingstraße 4, D-80799 München, 2010.

[88] Peter Schmüser, Martin Dohlus, and Jörg Rossbach. *Ultraviolet and soft X-ray free-electron lasers: introduction to physical principles, experimental results, technological challenges*, volume 229. Springer Science & Business Media, 2008.

[89] Picture taken from Website, 2018. <http://photon-science.desy.de/facilities/flash/the_free_electron_laser/how_it_works/high_gain_fel/index_eng.html>.

[90] Picture taken from Website, 2018. <http://lux.cfel.de/researchtopics#angus-laser-system>.

[91] Lars Goldberg, Lucas Schaper, Tobias Kleinwächter, Jan-Patrick Schwinkendorf, Charlotte Palmer, Jens Osterhoff, and Gas Target Design. Characterization of gas targets for plasma-wakefield acceleration. In *5th International Particle Accelerator Conference*, number DESY-2014-03115. Forschung Linear Accelerator, 2014.

[92] E Esarey, CB Schroeder, and WP Leemans. Physics of laser-driven plasma-based electron accelerators. *Reviews of Modern Physics*, 81(3):1229, 2009.

[93] Victor Malka, Jérôme Faure, Yann A Gauduel, Erik Lefebvre, Antoine Rousse, and Kim Ta Phuoc. Principles and applications of compact laser–plasma accelerators. *Nature Physics*, 4(6):447–453, 2008.

[94] CALA. Centre for Advanced Laser Applications. Website, 2016. URL:http://www.lex-photonics.de/cala/index.html.

[95] CFEL-LUX. Center for Free Electron Laser science. Website, 2015. URL:http://uni-hamburg.cfel.de/asg/lux/.

[96] C Benabderrahmane, M Labat, A Loulergue, F Marteau, M Valléau, ME Couprie, G Le Bec, J Chavanne, and C Evain. Lunex5 fel line undulators and magnetic elements. In *International Free Electron Laser Conference, Nara, Japan*, pages 26–31, 2012.

[97] H-P Schlenvoigt, K Haupt, A Debus, F Budde, O Jäckel, S Pfotenhauer, H Schwoerer, E Rohwer, JG Gallacher, E Brunetti, et al. A compact synchrotron radiation source driven by a laser-plasma wakefield accelerator. *Nature Physics*, 4(2):130–133, 2008.

[98] Wim Leemans. Multi-gev electron beams from capillary discharge guided sub-petawatt class laser pulses in the self-trapping regime. *Bulletin of the American Physical Society*, 59, 2014.

[99] R Weingartner, Sebastian Raith, A Popp, S Chou, J Wenz, K Khrennikov, M Heigoldt, AR Maier, N Kajumba, Matthias Fuchs, et al. Ultralow emittance electron beams from a laser-wakefield accelerator. *Physical Review Special Topics-Accelerators and Beams*, 15 (11):111302, 2012.

[100] S. Karsch. Cala and garching plans. In *EuroNNAc Workshop, CERN, Geneva*, 2011.

[101] LMU Raphael Weingartner, MPQ, 2012. Private communication.

[102] P Colomp, T Oddolaye, and P Ellaeume. Demagnetization of permanent magnets to 180 mev electron beam. *ESRF Internal Note, ESRF/MACH-ID/93-09 and J. Chavanne, P. Elleaume, P. Van Vaerenbergh,"Ageing of Permanent Magnet Devices at the ESRF", to be published at RADECS*, 99, 1993.

[103] S Okuda, K Ohashi, and N Kobayashi. Effects of electron-beam and γ-ray irradiation on the magnetic flux of $Nd_2Fe_{12}B$ and $SmCo_5$ permanent magnets. *Nuclear Instruments and Methods in Physics Research Section B: Beam Interactions with Materials and Atoms*, 94 (3):227–230, 1994.

[104] Mario Santana-Leitner, A Fass, J Vollaire, S Mao, HD Nuhn, S Rokni, and S Roesler. Radiation protection studies for lcls tune up dump. Technical report, 2010.

[105] Yoshihiro Asano, Teruhiko Bizen, and Xavier Marechal. Analyses of the factors for the demagnetization of permanent magnets caused by high-energy electron irradiation. *Journal of synchrotron radiation*, 16(3):317–324, 2009.

[106] Y Asano, RIKEN XFEL, and T Bizen. Estimations for demagnetization of id permanent magnets due to installation of otr. *Star*, 10:8, 2010.

[107] Amikam Aharoni. Demagnetizing factors for rectangular ferromagnetic prisms. *Journal of applied physics*, 83(6):3432–3434, 1998.

[108] Toru Hara, Takashi Tanaka, Hideo Kitamura, Teruhiko Bizen, Xavier Maréchal, Takamitsu Seike, Tsutomu Kohda, and Yutaka Matsuura. Cryogenic permanent magnet undulators. *Physical Review Special Topics-Accelerators and Beams*, 7(5):050702, 2004.

[109] Helmut Mehrer. *Diffusion in solids: fundamentals, methods, materials, diffusion-controlled processes*, volume 155. Springer Science & Business Media, 2007.

[110] *Vacodym 890 TP*. Vacuumschmelze, 2013. from URL http://www.vacuumschmelze.de/de/produkte/dauermagnete-systeme/dauermagnete/nd-fe-b/vacodym/vacodym-890-tp.html.

[111] Alex Murokh, Vyacheslav Solovyov, Ron Agustsson, Finn H O'Shea, Oleg Chubar, Yung Chen, and Thomas Grandsaert. Textured dysprosium and gadolinium poles for high-field, short-period hybrid undulators. *Nuclear Instruments and Methods in Physics Research*

Section A: Accelerators, Spectrometers, Detectors and Associated Equipment, 735:521–527, 2014.

[112] *Soft Magnetic Materials and Semi-finished Products.* Vacuumschmelze, 2014. from URL http://www.vacuumschmelze.com/fileadmin/docroot/medialib/documents/broschueren/htbrosch/Pht-004_e.pdf.

[113] Klaus Halbach. Permanent magnet undulators. *Le Journal de Physique Colloques*, 44(C1): C1–211, 1983.

[114] Pascal Elleaume, J Chavanne, and Bart Faatz. Design considerations for a 1å sase undulator. *Nuclear Instruments and Methods in Physics Research Section A: Accelerators, Spectrometers, Detectors and Associated Equipment*, 455(3):503–523, 2000.

[115] Not Available. *7-GeV Advanced Photon Source Conceptual Design Report.* Apr 1987. doi: 10.2172/5732545. URL http://www.osti.gov/scitech/servlets/purl/5732545.

[116] DIAMOND Synchrotron Light Source. Report of the design specification. *CCLRC, June*, 2002.

[117] Jia Qi-ka, Zhang Shancai, Lu Shengkuan, He Duohui, Zhou Qiaogen, Cao Yun, and Zhao Zhentang Dai Zhimin. Design of undulator for the shanghai duv-fel. In *Proc. of the 2004 FEL Conference*, pages 494–497, 2004.

[118] Alexander Buck, Maria Nicolai, Karl Schmid, Chris MS Sears, Alexander Sävert, Julia M Mikhailova, Ferenc Krausz, Malte C Kaluza, and Laszlo Veisz. Real-time observation of laser-driven electron acceleration. *Nature Physics*, 7(7):543–548, 2011.

[119] O Lundh, J Lim, C Rechatin, L Ammoura, A Ben-Ismail, X Davoine, Guilhem Gallot, JP Goddet, E Lefebvre, V Malka, et al. Few femtosecond, few kiloampere electron bunch produced by a laser-plasma accelerator. *Nature Physics*, 7(3):219–222, 2011.

[120] Florian Grüner, Stefan Becker, U Schramm, T Eichner, M Fuchs, R Weingartner, Dietrich Habs, Jürgen Meyer-ter Vehn, Michael Geissler, M Ferrario, et al. Design considerations for table-top, laser-based vuv and x-ray free electron lasers. *Applied Physics B*, 86(3): 431–435, 2007.

[121] Kwang-Je Kim. Brightness, coherence and propagation characteristics of synchrotron radiation. *Nuclear Instruments and Methods in Physics Research Section A: Accelerators, Spectrometers, Detectors and Associated Equipment*, 246(1):71–76, 1986.

[122] Jean Buon. Beam phase space and emittance. Technical report, 1992.

[123] K-J Kim and RG Littlejohn. Entropy and emittance of particle and photon beams. In *Particle Accelerator Conference, 1995., Proceedings of the 1995*, volume 5, pages 3358–3360. IEEE, 1995.

[124] Oleg Chubar, Pascal Elleaume, and Joel Chavanne. A three-dimensional magnetostatics computer code for insertion devices. *Journal of synchrotron radiation*, 5(3):481–484, 1998.

[125] P. Elleaume, O. Chubar, and J. Chavanne. Computing 3d magnetic field from insertion devices. *proc. of the PAC97 Conference*, page 3509, 1997.

[126] Peter P Silvester and Ronald L Ferrari. *Finite elements for electrical engineers.* Cambridge university press, 1996.

[127] Vilfredo Pareto. La legge della domanda. *Giornale degli economisti*, pages 59–68, 1895.

[128] John MJ Madey and David AG Deacon. *Free electron lasers.* Springer, 1977.

[129] Evgenij L Saldin, Evgeny A Schneidmiller, and Mikhail V Yurkov. The physics of free electron lasers. an introduction. *Physics reports*, 260(4):187–327, 1995.

[130] H Schwoerer, S Pfotenhauer, O Jäckel, K-U Amthor, B Liesfeld, W Ziegler, R Sauerbrey, KWD Ledingham, and T Esirkepov. Laser-plasma acceleration of quasi-monoenergetic protons from microstructured targets. *Nature*, 439(7075):445–448, 2006.

[131] Jérôme Faure, Yannick Glinec, A Pukhov, S Kiselev, S Gordienko, E Lefebvre, J-P Rousseau, F Burgy, and Victor Malka. A laser–plasma accelerator producing monoenergetic electron beams. *Nature*, 431(7008):541–544, 2004.

[132] SPD Mangles, CD Murphy, Z Najmudin, AGR Thomas, JL Collier, AE Dangor, EJ Divall, PS Foster, JG Gallacher, CJ Hooker, et al. Monoenergetic beams of relativistic electrons from intense laser–plasma interactions. *Nature*, 431(7008):535–538, 2004.

[133] T Seggebrock, AR Maier, I Dornmair, and F Grüner. Bunch decompression for laser-plasma driven free-electron laser demonstration schemes. *Physical Review Special Topics-Accelerators and Beams*, 16(7):070703, 2013.

[134] Thorben Seggebrock. Concepts for a laser-driven FEL demonstration by tailored electron bunches. Master's thesis, Ludwig-Maximilians-Universität München, Fakultät für Physik, Schellingstraße 4, D-80799 München, 2010.

[135] A. R. Maier, A. Meseck, S. Reiche, C. B. Schroeder, T. Seggebrock, and F. Grüner. Demonstration scheme for a laser-plasma-driven free-electron laser. *Phys. Rev. X*, 2:031019, Sep 2012. doi: 10.1103/PhysRevX.2.031019. URL http://link.aps.org/doi/10.1103/PhysRevX.2.031019.

[136] CGR Geddes, Cs Toth, J Van Tilborg, E Esarey, CB Schroeder, D Bruhwiler, C Nieter, J Cary, and WP Leemans. High-quality electron beams from a laser wakefield accelerator using plasma-channel guiding. *Nature*, 431(7008):538–541, 2004.

[137] XL Xu, YP Wu, CJ Zhang, F Li, Y Wan, JF Hua, C-H Pai, W Lu, P Yu, C Joshi, et al. Low emittance electron beam generation from a laser wakefield accelerator using two laser pulses with different wavelengths. *arXiv preprint arXiv:1402.5322*, 2014.

[138] Florian Holy. Development of a Cryogenic Undulator Prototype. Master's thesis, Ludwig-Maximilians-Universität München, Fakultät für Physik, Schellingstraße 4, D-80799 München, 2010.

[139] F. Holy, A. R. Maier, B. Zeitler, R. Weingartner, S. Raith, N. Kajumba, M. El Ghaz-aly, W. Lauth, D. Krambrich, A. Gaupp, M. Scheer, J. Bahrdt, and F. Grüner. First spectral measurements of a cryogenic high-field short-period undulator. *Phys. Rev. ST Accel. Beams*, 17:050704, May 2014. doi: 10.1103/PhysRevSTAB.17.050704. URL http://link.aps.org/doi/10.1103/PhysRevSTAB.17.050704.

[140] Konstantin P Belov, Anatolii K Zvezdin, Antonina M Kadomtseva, and R Z Levitin. Spin-reorientation transitions in rare-earth magnets. *Soviet Physics Uspekhi*, 19(7):574, 1976. URL http://stacks.iop.org/0038-5670/19/i=7/a=R03.

[141] M Sagawa, S Fujimura, H Yamamoto, Y Matsuura, and S Hirosawa. Magnetic properties of rare-earth-iron-boron permanent magnet materials. *Journal of applied physics*, 57(8): 4094–4096, 1985.

[142] J. Bahrdt. Pushing the limits of short period permanent magnet undulators. In *Proc. FEL*, pages 435–442, 2011.

[143] Carsten Kuhn, Hans-Juergen Baecker, Johannes Bahrdt, Andreas Gaupp, and Bodo Schulz. Hall-probe bench for cryogenic in-vacuum-undulators. *Proc. of IPAC2013, Shang-hai, China*, pages 2126–2128, 2013.

[144] H Euteneuer, F Hagenbuck, R Herr, J Herrmann, K Herter, MO Ihm, KH Kaiser, Ch Klüm-per, HP Krahn, HJ Kreidel, et al. Beam measurements and operating experience at mami. In *Proc. EPAC*, volume 94, page 506, 1994.

[145] *Ultra-LEGe Detector*. Canberra, 2002. from URL http://www.canberra.com/pdf/Products/Detectors_pdf/UltraLEGE.pdf.

[146] *Manual: iKon BR-DD DW432*. Andor, 2008. back illuminated X-ray CCD.

[147] Chandra X ray Center. The Chandra Proposers' Observatory Guide. Website, 2009. from URL:http://cxc.harvard.edu/proposer/POG/html/chap9.html.

[148] P He, P Cappadoro, T Corwin, D Harder, H Fernandes, CA Kitegi, M Kokole&, J Rank, G Rakowsky, and T Tanabe. Characterization of prfeb permanent magnet blocks with helmholtz coils at nsls-ii. pages 2304–2306, 2013.

[149] JL Revol, JC Biasci, JF Bouteille, F Ewald, L Farvacque, A Franchi, G Gautier, L Goirand, M Hahn, L Hardy, et al. Esrf operation and upgrade status. pages 82–84, 2013.

[150] C Benabderrahmane, M Valléau, P Berteaud, K Tavakoli, J L Marlats, R Nagaoka, N Béchu, D Zerbib, P Brunelle, L Chapuis, D Dallé, C Herbeaux, A Lestrade, M Lou-vet, and M E Couprie. Development of a 2 m pr 2 fe 14 b cryogenic permanent magnet undulator at soleil. *Journal of Physics: Conference Series*, 425(3):032019, 2013. URL http://stacks.iop.org/1742-6596/425/i=3/a=032019.

[151] M Calvi, Th Schmidt, A Anghel, A Cervellino, S J Leake, P R Willmott, and T Tanaka. Commissioning results of the u14 cryogenic undulator at sls. *Journal of Physics: Confer-ence Series*, 425(3):032017, 2013. URL http://stacks.iop.org/1742-6596/425/i=3/a=032017.

[152] F. O'Shea. Cryogenic permanent magnet undulators. In *Workshop on Physics and Applications of High Brightness Beams: Towards a Fifth Generation Light Source, Puerto Rico*, 2013.

[153] S Sailaja, V Arora, S R Kumbhare, P A Naik, P D Gupta, D A Fedin, A A Rupasov, and A S Shikanov. A simple xuv transmission grating spectrograph with sub-ångström resolution for laser-plasma interaction studies. *Measurement Science and Technology*, 9(9): 1462, 1998. URL http://stacks.iop.org/0957-0233/9/i=9/a=015.